Sitka spruce (*Picea sitchensis* (Bong.) Carr) drought monitoring using remotely sensed Vegetation Indices (VI) at multiple spatiotemporal scales

Gerrard English

Submitted to Swansea University in fulfilment of the requirements for the Degree of
Doctor of Philosophy
PhD

Swansea University
2024

Abstract

The environmental threats to UK forests due to the changing climate are unprecedented. However, the potential for remote sensing to assess, model, and monitor these threats at previously unattainable spatio-temporal scales has never been greater. Drought stress is among the greatest threats to forests, and Sitka spruce (*Picea sitchensis* (Bong.) Carr.), UK forestry's most important conifer species, can be susceptible to it. The present thesis explores potential ways that the UK forestry sector could adopt remotely sensed Vegetation Indices (VI) and transition towards more drought-resilient management. In the analysis presented in this thesis, VI associated with the xanthophyll cycle and anthocyanin concentrations (PRI, ARI, ARI2) detected early drought responses in Sitka spruce needles after about 10 days of mild drought stress. At the stand level, the xanthophyll cycle-associated VI (CCI and GPP_{VI}) detected drought-induced annual reductions during the 2018 drought year. Depending on the time interval, these reductions ranged between 5% and 15%, compared to the 5% GPP reduction estimated by the flux tower. Gross Primary Productivity (GPP) (within 0.5% of flux tower GPP) which were delectable from space. These VI also act as Vcmax proxies to improve model realism in process-based biophysical models. Traditional VI such as NDVI generally performed poorly at the needle and canopy scale for drought detection however, successfully tracked seasonal GPP patterns ($R^2 > 0.80$) when combined with a measure of PAR in the Light Use Efficiency Model (LUE). For the first time, intraspecific clonal differences in drought responses were detected with VI in conifers. This demonstrated the possibility of high-throughput phenotyping for drought tolerance and highlighted potential discrepancies in the drought tolerance of existing breeding population Sitka spruce trees. The results demonstrate how VI can directly aid in transitioning UK forestry to a drought-resilient sector. Xanthophyll reflectance, detectable with MODIS satellites at countywide scales, could facilitate Sitka spruce health monitoring and stress assessments, as well as be incorporated into the breeding program to future-proof progeny.

Declarations

This work has not previously been accepted in substance for any degree and is not being concurrently submitted in candidature for any degree.

17th June 2024

This thesis is the result of my own investigations, except where otherwise stated. Other sources are acknowledged by footnotes giving explicit references. A reference list is appended.

17th June 2024

I hereby give consent for my thesis, if accepted, to be available for electronic sharing after expiry of a bar on access approved by the Swansea University.

17th June 2024

The University's ethical procedures have been followed and, where appropriate, that ethical approval has been granted.

17th June 2024

Contents

Acknowledgements

My first thanks go to my supervisors, Dr. Jackie Rosette, Dr. Juan Suárez, and Dr. Sietse Los. Specifically, Jackie for her enthusiasm towards my work, support, and feedback; Juan for a memorable trip to Valencia and for agreeing to travel by car to satisfy my "morals"; and Sietse for his invaluable knowledge and insights during the first years of this venture.

I am grateful to everyone who contributed to making Forest Research a welcoming and productive environment. Special thanks to Dr. Georgios Xenakis for his generous contribution of data and expertise throughout, as well as Adam Ash for his aid in setting up, Dr. Richard Whittet for donating trees, Dr. Mike Perks, David Clark, and all the nursery staff. I am also grateful to Dr. Robbie Ramsey at the NERC Field Spectroscopy Facility for technical advice on hyperspectral measurements and for generously calibrating my reference panels. Additionally, thanks to Dr. Jochem Verrelst and Dr. Santiago Belda for welcoming us to Valencia and providing personal tutorials for ARTMO and DATimeS.

Thank you to my parents and family for their love and absolute trust in allowing me to pursue whatever in life I choose. Thank you to all those at Dafforne Road who kindly took me in over the pandemic and to Frankie for your support.

Most importantly, for providing me with community, support, laughter, distractions and food, I would like to thank my amazing friends, without whom 'trees from space' would not be possible. I cannot mention you all individually, but a special thank you goes to all associated with GCR who have made Sheffield my home. I am grateful to those completing their own theses for support and an active work email thread. Thank you, Eve, for everything you do and for almost a decade of proofreading. And finally, Pippa, for your love, support, company from afar, interest in my graphs, and future adventures.

List of Figures

List of Tables

Abbreviations

ABA Abscisic Acid.

BDRF Bidirectional Reflectance Distribution Function.

BL Big-Leaf.

CI Clumping Index.

CV-MVC Constrained View Maximum Value Composite.

DATimeS Decomposition and Analysis of Time Series software.

EC Eddy Covariance.

ECMWF European Centre for Medium-Range Weather Forecasts.

EMM Estimated Marginal Means.

ENF Evergreen Needleleaf Forest.

ERA5 ECMWF Forecasts Reanalysis v5.

FC Field Capacity.

ft Flux Tower.

ftGPP (Eddy covariance) Flux Tower Gross Primary Productivity.

Fv/Fm maximum quantum yield of photosystem II.

GEE Google Earth Engine.

GPP Gross Primary Productivity.

GPR Gaussian Process Regression.

IPCC Intergovernmental Panel on Climate Change.

IRGA Infrared Gas Analyser.

LAD Leaf Angle Distribution.

LAI Leaf Area Index.

LUE Light Use Efficiency (model).

LUT Look Up Table.

MAIAC Multi-Angle Implementation of Atmospheric Correction.

MERIS Medium Resolution Imaging Spectrometer.

ML Machine Learning.

MOD13 MODIS Vegetation Index Products (NDVI and EVI).

MODIS Moderate Resolution Imaging Spectroradiometer.

NIR Near-Infrared.

NPP Net Primary Productivity.

NPQ Non-Photochemical Quenching.

PAM Pulse-Amplitude-Modulation.

PFT Plant Functional Type.

PSII Photosystem II.

QA Quality Assessment (bands).

ROS Reactive Oxygen Species.

Rubisco Ribulose-1,5-bisphosphate carboxylase/oxygenase.

SiB Simple Biosphere Model.

SIF Solar-induced fluorescence.

SRS Satellite-Based Remote Sensing.

SWIR Short-Wave Infrared.

SZA Solar Zenith Angle.

Vcmax Maximum carboxylation rate or Rubisco-limited photosynthetic capacity.

VI Vegetation Indices.

VIS Visible (radiation).

VPD Vapor Pressure Deficit.

WUE Water Use Efficiency.

Chapter 1

General introduction

1.1 Overview

Globally, forests are facing a multitude of threats to their health including climate change, droughts, deforestation, pathogens, and poor management (Nemani et al., 2003; Foley et al., 2005; Somers & Asner, 2012; Gauthier et al., 2015; Lewis et al., 2015; Wingfield et al., 2015; Lausch et al., 2016). The healthy functioning of forests is of high importance due to their extensive global coverage (around 30% of the Earth's terrestrial surface (Bonan, 2008)) and vital ecosystem services e.g. carbon sequestration, climate change mitigation, water filtration, flood regulation, air purification, erosion control, nutrient cycling, habitat for maintaining biodiversity as well as timber and medicinal resources (Lausch et al., 2016; Aznar-Sánchez et al., 2018). Monitoring forest function and health, to alleviate the threats and maintain ecosystem services, is therefore of paramount importance. Satellite based remote sensing (SRS) offers unprecedented potential for forest health monitoring owing to global coverage, frequent observation revisits and systematic data retrieval (Huete, 2012; Ma et al., 2015; Lausch et al., 2016).

Drought stress is a significant risk to UK forestry (Davies et al., 2020; Locatelli et al., 2021) which, due to climate change, is increasing in severity and frequency (Le et al., 2023). However, the potential for satellite-based remote sensing to assess drought stress in UK forests is great. For example, country-wide multiple daily over-passes of the Moderate Resolution Imaging Spectroradiometer (MODIS) and 10 m pixel size of the European Space Agency's (ERA) Sentinel-2 satellites provide high spatio-temporal resolution to assess stress. Sitka spruce (*Picea sitchensis* (Bong.) Carr) is arguably the dominant conifer species for UK forestry but, relative to other species, is susceptible to drought (Samuel et al., 2007; Krakau et al., 2013; Locatelli et al., 2021). Studying the drought response of Sitka spruce is therefore essential in

transitioning UK forestry into a more drought resilient sector. This thesis explores the role of remote sensing, specifically reflectance retrieval via Vegetation Indices (VI), to evaluate the effects of water limitation on Sitka spruce at differing spatiotemporal scales, to characterise and expand the current state of understanding, for UK forestry and the broader forest ecology community.

In this section, key concepts are introduced to summarise Sitka spruce, forest drought responses, and the driving mechanisms behind linking remotely sensed VI with plant biophysical processes. Primarily, it focuses on understanding the link between how plant pigments regulate photosynthesis and stress, and the (sometimes subtle) influence this has on reflectance, and therefore VI. This is followed by an outline of the primary research conducted in later chapters.

1.2 Sitka Spruce

Sitka Spruce is an extremely large, fast growing, coastal evergreen conifer species, which can grow to around 75 m (up to 100m ((Van Pelt, 2007)) tall and live for up to 500 years (Krakau et al., 2013). The natural range of Sitka spruce is along the west coast of the USA, spanning from northern California, to Kodiak Island in Alaska (Figure 1.1).

Sitka spruce is the most numerous planted tree species in the UK, covering around 700 thousand hectares, making up a third of all forest estate (Samuel et al., 2007; Krakau et al., 2013). Therefore, research that can better inform silvicultural practices, especially in the context of climate change, will greatly benefit the forestry community. The mild oceanic climate of northern and western parts of Britain and Ireland, provide preferable growing conditions for Sitka spruce. It is therefore favoured across much of the UK, as the fastest growing conifer species over a range of site types (waterlogged and exposed to high wind levels) and locations (Davies et al., 2020) owing in part to foliar morphology, which is adapted for high photosynthetic rates (Kramer et al., 2018). Sitka is easy to establish, has very high strength-to-weight ratios and provides high timber yields, suitable for multiple applications (Van Pelt, 2007; Cameron, 2015). Sitka spruce is traditionally managed in the UK as even aged monocultures on short (35 - 50 year) rotations (Cameron, 2015).

1.2.1 Susceptibility to drought

The high productivity of Sitka spruce, and relatively quick turnover, means its centrality to the forestry sector across the UK is likely to remain into the near

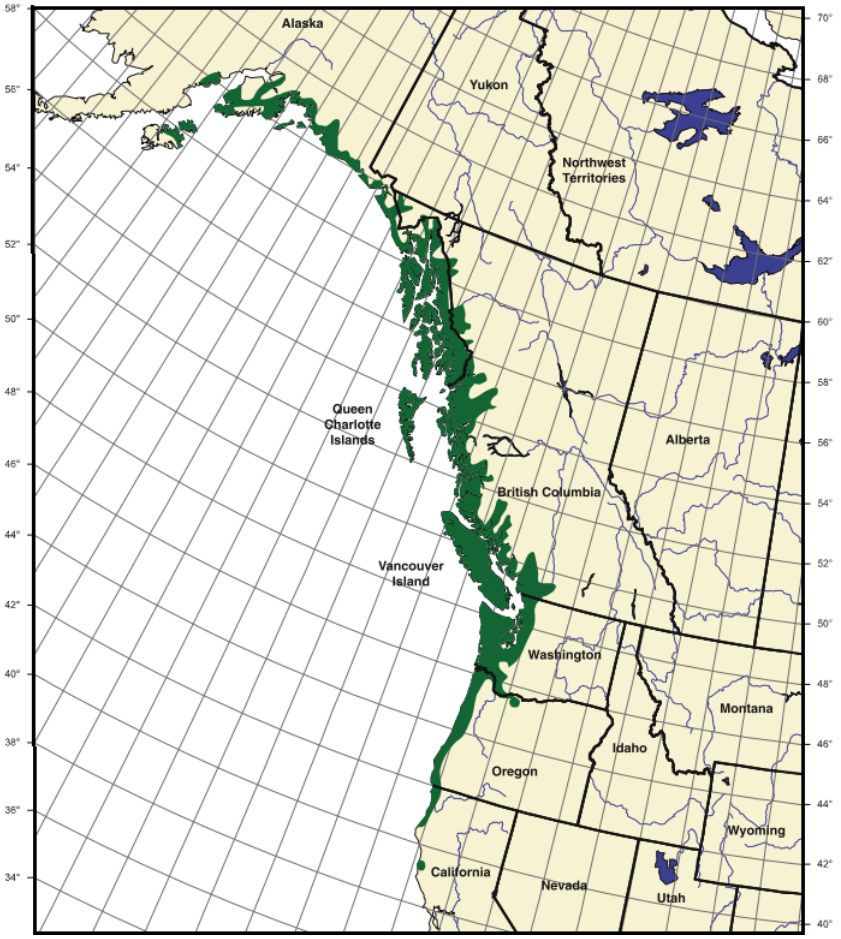

Figure 1.1: The natural distribution of Sitka spruce (*Picea sitchensis* (Bong.) Carr) along the west coast of the USA. Sitka spruce exists over a wide latitudinal range (around 3000 km) but, due to requirements for humid oceanic growing conditions, not more than 200 km from the coast. Adapted from Krakau et al. (2013).

future (Davies et al., 2020). However, due to its susceptibility to drought, relative to other commercial species in the UK, increasingly Sitka spruce forest sites will become at risk of moving beyond the species tolerance conditions (Samuel et al., 2007; Green & Ray, 2009; Locatelli et al., 2021). Naturally, Sitka spruce grows in humid regions which experience 1000 - 3000 mm annual precipitation (Krakau et al., 2013). Scottish planting guidelines state Sitka spruce performs poorly (reduced productivity) in areas with less than 1000 mm of annual precipitation, however it can sometimes perform adequately, where soil moisture is sufficient, at sites with 700 mm precipitation p.a. (Locatelli et al., 2021). Due to the effects of climate change, the UK is currently, and will continue to experience, increasingly hot and dry summers (Burke et al., 2010; Petr et al., 2014; Cameron, 2015; Betts & Brown, 2021; Met Office, 2021). Presently, low rainfall across parts of the UK, including eastern Scotland, limit the range of Sitka spruce (Krakau et al., 2013; Grant & O'Reilly, 2017), where over 120 existing Sitka forests are on moderate or high drought risk

sites (Green & Ray, 2009).

Recent drought events are already impacting Sitka spruce in the UK. In the extreme European drought of 2003, widespread damage and mortality of Sitka spruce was recorded across north-eastern Scotland (Green et al., 2008; Green & Ray, 2009). In the warm, dry spring and summer of 2018, net carbon sequestration of a mature even aged Sitka spruce plantation in Northern England reduced by 30%, due in part to a 5% reduction in photosynthesis and increased evapotranspiration, reducing soil moisture and accelerating soil respiration, due to increased aeration (Xenakis et al., 2021). However, soil respiration would likely decrease if soil moisture continued to decline as microbial activity declines (Yan et al., 2018). During this summer, mortality of seedlings at a clear-felled site also increased (Xenakis et al., 2021). Summers like that of 2018 are likely to become the norm in the UK by 2050 (Betts & Brown, 2021). This could transition areas beyond the tolerance range of Sitka spruce, highlighting a potential unsuitability for future plantations and forestry. The appropriateness of Sitka spruce across the UK may decrease as high drought risk areas expand, although research on this is limited. As such the research here aims to gain invaluable information on the responses of Sitka spruce to droughts akin to those the country will routinely experience in the coming decades. Drought response within species is important in understanding suitability to a changing climate. The Sitka spruce breeding programme, established in 1963, has successfully bred and proliferated trees with high timber quality (Lee, 1999). Screening or selecting for more drought resistance strains could be a useful tool in moving towards a more drought resilient UK forestry sector (Schiop et al., 2017). Remote sensing offers the potential for high throughput phenotyping (Plesa et al., 2019; Liming & Huichun, 2020; Baldi & La Porta, 2022), which will be explored in the present research.

1.3 Drought stress in forest

1.3.1 Definitions of drought

Droughts are heterogeneous and complex events which, due to slow gradual onset and spatio-temporal variability, are hard to specifically define (Du et al., 2013; AghaKouchak et al., 2015; West et al., 2019). Therefore, definitions of drought are varied, but can be classified into four types: meteorological, agricultural, hydrological, and socioeconomic (Heim, 2002). Whereby, (i) meteorological droughts occur as a precipitation deficit, or below average precipitation in a specific region, (ii) agricultural droughts are a deficit of soil moisture, insufficient to meet the water demands of crops and other vegetation, (iii) hydrological droughts are a deficit of surface water and groundwater levels and (iv) a socioeconomic drought impacts water scarcity

on human populations and communities, and can relate to the shortage of economic goods (Heim, 2002; Du et al., 2013; AghaKouchak et al., 2015). For the purposes of this thesis, drought is defined as the condition in which, a water deficit, in either the atmosphere (Vapour Pressure Deficit (VPD)), or soil, induces a physiological, biochemical or molecular response from a plant, to acclimate or survive the water deficit (Dalal & Tripathy, 2018; Gerhards et al., 2018; Le et al., 2023). For example, a reduction in vegetation productivity, as a direct response of low water availability, is considered a drought response.

1.3.2 Drought in forests

Globally, drought greatly limits forest's productivity potentially more than any other environmental factor (Ciais et al., 2005; Zhao & Running, 2010) and forest mortality, as a result of drought, has been recorded on every vegetation continent on Earth (Ciais et al., 2005; Phillips et al., 2008; Allen et al., 2010; Zhao & Running, 2010; McDowell et al., 2011; Anderegg et al., 2012; McDowell & Allen, 2015; Anderegg et al., 2019) although the exact mechanisms of forest mortality are unknown (McDowell et al., 2011; Anderegg et al., 2013, 2016; Klein et al., 2019). To avoid drought induced mortality, trees possess a multifaceted drought response (Ensminger et al., 2015). Many of these drought response mechanisms are conserved across the plant kingdom (Fang & Xiong, 2015). As a drought intensifies, plants will employ different strategies, to ameliorate the worst effects of drought. The conditions required to initiate a drought response from an individual plant are a function of many interplaying biotic (taxa, species, ecotypes, morphology, age, and development cycle) (Gallé & Feller, 2007; Pantin et al., 2013; Harrison et al., 2020)) and environmental (meteorological, edaphic and topographic) (Geßler et al., 2006; Kreuzwieser & Gessler, 2010; Anjum et al., 2011; Liu et al., 2017) factors.

The effects of drought on trees has been extensively studied (Ensminger et al., 2015; Fang & Xiong, 2015; Lausch et al., 2016). Responses can be broadly characterised into drought avoidance and drought tolerance strategies (Ensminger et al., 2015).

Drought avoidance strategies seek to increase water uptake and minimise water loss, in order to maintain adequate water content, to avoid the onset of drought stress. This can be done via investment into root biomass, to ensure a deeper or larger root system, which can access larger portions of available water, for example seen in maritime pine (*Pinus pinaster*) populations (Aranda et al., 2010). Water loss can be regulated through transpiration. Reductions in transpiration can be achieved with smaller total leaf area. For example, leaves grown in low water conditions are smaller due to less cell turgor, leading to reduced cell expansion. Wilting, heliotropism or senescence (in intense drought) also regulate transpiration in order to

avoid drought stress (Chaves et al., 2003; Marron et al., 2003; Poorter & Markesteijn, 2008; Takahashi & Badger, 2011; Khanna-Chopra, 2012; Juvany et al., 2013; Estiarte & Peñuelas, 2015; Fang & Xiong, 2015; Schuldt et al., 2020; Nadal-Sala et al., 2021). Stomatal regulation, via density on the leaf, or through changes in stomatal conductance are a primary response to drought, reducing water loss and maintaining hydraulic integrity (Hetherington & Woodward, 2003). When stomata are closed, the diffusion of carbon dioxide (CO_2) from the atmosphere is reduced, which limits carbon uptake (Chaves et al., 2003; Hetherington & Woodward, 2003; Harrison et al., 2020). Stomata close when guard cells lose turgor, which can occur passively with dropping water potential (Tombesi et al., 2015; Wang et al., 2018). This is regulated through various signalling pathways and chemical reactions (Saibo et al., 2009; Pessarakli, 2018). One of the major identified drought signalling molecules is abscisic acid (ABA), a phytohormone, which among other things decreases stomatal conductance and initiates a drought response (Gomes et al., 2004; Pantin et al., 2013).

Drought Tolerance mechanisms allow a plant to withstand water deficit conditions, and maintain physiological functions, under low water availability. Osmotic adjustment is an important mechanism to ensure that cells do not lose turgor, which is achieved through increasing solutes/ osmolytes, including amino acids, glycine, betaine, proline, soluble sugars or sugar alcohols (Ashraf & Foolad, 2007; Ensminger et al., 2015; Blum, 2017; Schönbeck et al., 2018). For example, proline is upregulated under drought stress in Scots pine (*Pinus sylvestris*) (MacAllister et al., 2019). A natural byproduct of photosynthesis are reactive oxygen species (ROS), formed by excess energy absorbed by leaves, causing electrons with a higher energy state to be transferred to molecular oxygen (Mittler et al., 2004; Nishiyama et al., 2006; Miller et al., 2010; Pintó-Marijuan & Munné-Bosch, 2014). ROS are highly reactive oxygen radicals and non-radical oxygen derivatives (Mittler et al., 2004; Patel et al., 2018), which can cause photo-inhibitory oxidative damage to proteins, lipids and DNA (Mittler, 2002). Antioxidants (including ascorbic acid and glutathione) (Saibo et al., 2009) or ROS scavenging enzymes (Kruk et al., 2005; Miller et al., 2010) are important to curb ROS acclimation during drought stress (Mittler et al., 2004; Cheeseman, 2007; Jubany-Marí et al., 2010). A rapid rise in the production of ROS, known as an oxidative burst, is important in the control of environmental stress response by triggering acclimation (Torres & Dangl, 2005; Miller et al., 2008, 2010).

1.3.3 Photosynthesis during drought

Down regulation or damage of the two major photosynthetic processes (the light reactions (photochemical) and the carbon fixation reactions are potential consequences of drought stress (Fang & Xiong, 2015; Harrison et al., 2020). The progressive downregulation of photosynthesis and carbon assimilation, during increasing drought stress, is characterised by Ensminger et al. (2015) into three phases: the first involves reductions in stomatal conductance, photosynthetic enzymes are unaffected, but photorespiration increases due to reduced internal CO_2; during phase 2, stomatal conductance is further reduced, the electron transport chain is disrupted, and energy dissipation mechanisms begin to operate; finally in phase 3, photochemistry and carboxylation is decreased (via RuBP/Rubisco reductions), which can leave permanent damage.

1.4 Pigments, reflectance and drought stress

The composition of leaf pigments is the key mechanism to evaluate plant biophysical processes via remote sensing, due to their dominance in the spectral signature of plants (Croft & Chen, 2018). Therefore, pigments are explored in depth throughout this thesis. The role of leaf pigments in drought stress responses are significant and varied and three major groups of pigments (chlorophylls, carotenoids, anthocyanins) are the focus of this section and the subsequent thesis.

1.4.1 Pigments overview

Chlorophylls are the primary photosynthetic pigments (chlorophyll a and chlorophyll b) which are responsible for harvesting light and transferring excitation energy to reaction centres (Chaves et al., 2003; Kiang et al., 2007; Govender et al., 2009; Croft & Chen, 2018; Plesa et al., 2019; Sonobe et al., 2020). Under drought stress, chlorophyll concentration is reduced via, (i) the accumulation of ROS which damage photosynthetic machinery, including chloroplasts (Rasheed et al., 2021), or (ii) photoinhibition related chlorosis and reduced chlorophyll biosynthesis (Grulke et al., 2020). Detecting chlorophyll related reductions is an established biomarker of stress and a primary mechanism to optically detect drought stress in plants (Plesa et al., 2019; Grulke et al., 2020; Walshe et al., 2020).

After chlorophylls, **Carotenoids** are considered to be the second major pigment group (Blackburn, 2007; Huang et al., 2018). Carotenoids have diverse functions including light capture and, when photosynthesis is compromised under drought stress, photoprotection, energy dissipation and antioxidation (Demmig-Adams & Adams,

1996; Gamon et al., 2016; Sonobe et al., 2020). The most abundant carotenoids in plant leaves are β-carotene and a group of five xanthophylls (lutein, zeaxanthin, violaxanthin, antheraxanthin, and neoxanthin) (Gitelson et al., 2002). β-carotene is the primary photosynthetic carotenoid pigment. It aids plants in maximising the available radiation by absorbing light in wavelengths (blue-green region of the spectrum) where absorption by chlorophyll is low (Ida, 1981; Hashimoto et al., 2016; Simkin et al., 2022). Dissipating excess light energy as thermal energy is a drought stress strategy used to ameliorate photo-oxidative damages. Energy dissipation is done via the xanthophyll cycle, in which de-epoxidation of xanthophylls and the reverse reactions, reduce the amount of energy that reaches vulnerable structures (García-Plazaola et al., 2007; Esteban et al., 2009; Takahashi & Badger, 2011). The dissipation of excess energy is known as non-photochemical quenching (NPQ) (Gulias et al., 2002), and is a highly important component of stress acclimation. Young leaves that are more susceptible to photoinhibition, due to lack of photosynthetic machinery, therefore have relatively large xanthophyll pools (Jiang et al., 2006). The xanthophyll cycle acts on rapid and longer timescales to regulate seasonal photosynthesis and stress responses (Gamon & Berry, 2012; Wong & Gamon, 2015b; Gamon et al., 2016). It is detectable via remote sensing and is therefore one of the most crucial processes within plant stress-remote sensing research (Demmig-Adams & Adams, 1996; Peguero-Pina et al., 2007; Filella et al., 2009; Hernández-Clemente et al., 2011; Gamon & Berry, 2012; Wong & Gamon, 2015a, 2015b; Gamon et al., 2016; Mõttus et al., 2017, 2019).

Anthocyanins are flavonoid pigments. They are actively synthesised during stress, however uncertainties surround the exact role the they play in drought stress (Steyn et al., 2002; Landi et al., 2015; Croft & Chen, 2018; Cirillo et al., 2021). Anthocyanins' role in stress responses is diverse and they have been termed 'nature's Swiss army knife' (Gould, 2004). Light screening properties are one role whereby anthocyanins absorb high energy photons, particularly excess UV-B radiation, directing them away from light saturated photosynthetic machinery (Gould, 2004; Kyparissis et al., 2007; Landi et al., 2015; Croft & Chen, 2018). Anthocyanin pigments may act as antioxidants during times of stress by scavenging ROS, although this is uncertain (Close & Beadle, 2003; Gould, 2004; Hernández et al., 2009; Croft & Chen, 2018; Cirillo et al., 2021).

All three pigment groups are characterised by strong absorption in the visible (VIS) portion of the spectrum (Figure 1.2). Chlorophylls reflect green light, which accounts for the characteristic green colour of plants. Chlorophyll a exhibits strong absorption peaks in the blue-violet (around 430 nm) and red (around 662 nm) regions of the spectrum. Chlorophyll b complements this by absorbing light in the blue (around

453 nm) and red-orange (around 642 nm) regions, thus broadening the spectrum of light that plants can utilise for photosynthesis (Croft & Chen, 2018). The reflectance profiles of carotenoids and chlorophyll overlap, leading to high covariation, which makes carotenoids hard to distinguish spectrally (Gitelson et al., 2002; Croft & Chen, 2018; Gitelson, 2020; Sonobe et al., 2020). Carotenoids absorb strongly around 450 nm and reflect highly in green to red wavelengths. Anthocyanins most strongly absorb wavelengths around 530 nm, and reflect blue and strongly reflect red wavelengths (Croft & Chen, 2018).

1.4.2 Vegetation Indices (VI)

In the research chapters presented throughout this thesis, Vegetation Indices (VI) are routinely used to make inferences about the health status of Sitka spruce (For full names, formula and references for the VI used within this thesis see Tables 2.1 (p.43) and 2.2 (p.58)). VI are mathematical combinations of wavelengths (generally 2 or 3 bands) associated with specific plant biophysical properties (Xue & Su, 2017; Zeng et al., 2022). VI are simple, robust and diverse. They provide a measurable link between plant reflectance and a myriad of biophysical processes. VI make use of the spectral signatures of pigments, other compounds (e.g. water, nitrogen) and plant morphology (e.g. Leaf Area Index (LAI), Leaf Angle Distribution (LAD) and clumping index (CI)) to infer plant statues (Holzwarth et al., 2020; Zeng et al., 2022). The specific choice of wavelengths (these can be narrow or broadband) is selected to maximise a biophysical property, while minimising unwanted effects of spectral contaminants, e.g. the atmosphere or soil (Didan et al., 2015; Zeng et al., 2022). VI are simple to obtain and robust at different spatial scales, from hand held, leaf level devices to global satellite coverages (Zeng et al., 2022). Therefore, the use of VI in ecological research and earth science has been vast since inception in the 1970s (Huete, 2012; Zeng et al., 2022).

The first developed, and still most commonly used group of VI, e.g. Simple Ratio (SR)) and Normalised Difference Vegetation Index (NDVI), are based on the theory that chlorophyll pigments strongly absorb red light, and strongly reflect Near-infrared (NIR) light (Didan et al., 2015). The difference between the two spectral regions gives information about the presence of chlorophyll. There is more chlorophyll in healthy vegetation which reflects more green light, therefore these VI effectively measure the 'greenness' of a vegetated surface to determine plant statues. NDVI is perhaps the most extensively used VI for a variety of purposes including assessing drought stress status in vegetation (Anyamba & Tucker, 2012; AghaKouchak et al., 2015) and as a plant productivity proxy (Hashimoto et al., 2012; Gamon et al., 2016; Huang et al., 2019). However, NDVI suffers from atmospheric contami-

nation, soil effects and saturates over dense vegetation. Other VI were developed to negate these effects, most notably the Enhanced Vegetation Index (EVI) (Liu & Huete, 1995; Didan et al., 2015). It has a greater vegetation density saturation point so performs better at high LAIs such as conifer forests (Hufkens et al., 2012; Huang et al., 2019; Zeng et al., 2022). EVI minimises atmospheric effects by using the difference between blue and red reflectance. High cross scattering in the blue wavelengths means that, with higher aerosol concentration, the differences between the two bands becomes larger (Didan et al., 2015).

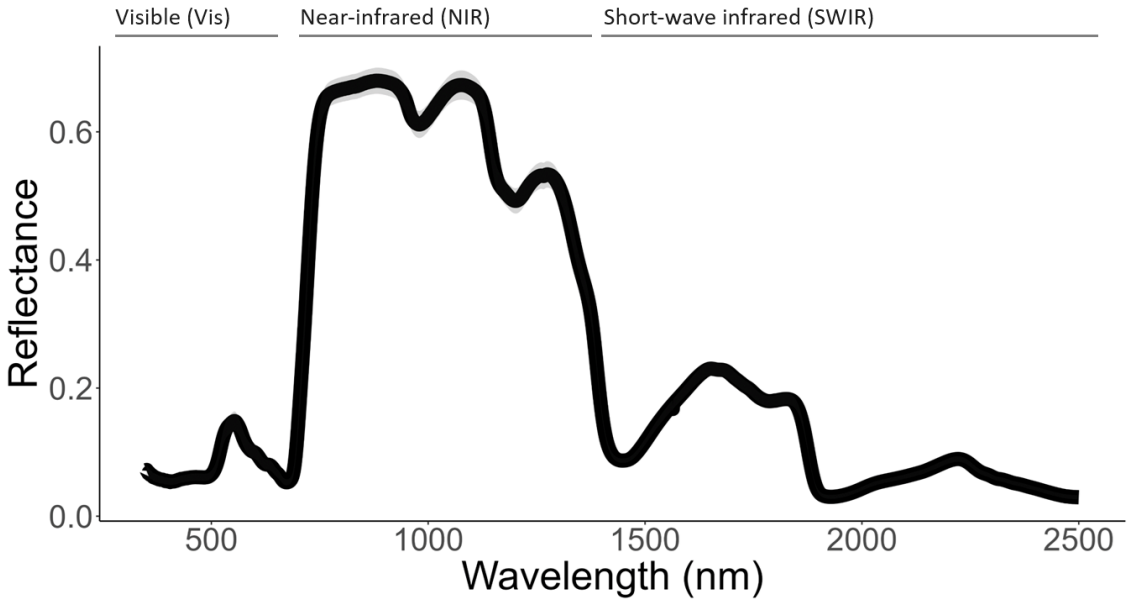

Figure 1.2: A typical Sitka spruce needle reflectance profile measured with a field spectroradiometer (ASD FieldSpec 4 standard Res, Analytik Ltd, Cambridge) during a polytunnel experiment as part of the present reseach. An average of five repeated measures of 25 rapidly collected spectra is displayed. Reflectance is unitless. The spectral resolution is 3 nm to 10 nm. Roughly, (visible wavelengths (VIS) are 400 - 700 nm, Near infrared (NIR) are 700 - 1300 nm and short-wave infrared (SWIR) are 1300 - 2500 nm. Low reflectance in the visible region is due to high absorption by pigments, especially in non-green portions (Note: the spike in reflectance around 495–570 nm is due to higher reflectance by chlorophyll in the green region, giving plants their characteristic green colour). The NIR profile is largely affected by structural factors and the high reflectance of spongy mesophyll. Strong absorption in SWIR is due to water, especially water absorption features at 1450 nm, 1940 nm, and 2500 nm.

A plethora of narrow band VI have also been developed which can detect more specific biophysical properties. For example, VI have been developed for pigment, water content, plant residues and nitrogen assessments (Gao, 1996; Gitelson et al., 2001; Zarco-Tejada et al., 2001; Gitelson et al., 2002, 2005; Zeng et al., 2022). Narrow band VI are applicable using hyperspectral spectroradiometers in the lab

or field, whereby relative to satellite mounted sensors, the limitations of spatial and spectral resolution and atmospheric interference are negated.

An important group of VI for the present thesis are those based on reflectance at 531 nm, namely the Photochemical Reactance Index (PRI) and the Chlorophyll/Carotenoid Index (CCI) (Gamon et al., 1992, 1997; Gamon et al., 2016). Reflectance at this specific region is sensitive to the xanthophyll cycle, the energy dissipation mechanism used for stress amelioration and seasonal photosynthetic acclimation (Jiang et al., 2006; Filella et al., 2009; Takahashi & Badger, 2011; Wong & Gamon, 2015a; Gamon et al., 2016). As xanthophylls undergo de-epoxidation and the reverse reaction, reflectance at 531 is altered. Under drought stress, PRI has routinely been used to track photosynthetic efficiency in conifers (Peguero-Pina et al., 2007; Filella et al., 2009; Hernández-Clemente et al., 2011; Wong & Gamon, 2015a; Mõttus et al., 2017, 2019). Some limitations with PRI retrieval have been highlighted. The difference in absolute reflectance between the two PRI bands is small, relative to visible and NIR contrasting indices (e.g. NDVI), the PRI signal therefore can be susceptible to other influences, including the soil background at low LAI. PRI suffers particularly high variation with view angle and is sensitive to LAD at high view angles (Gamon et al., 1992; Barton & North, 2001).

The characteristic absorption pattern of water, which heavily influences reflectance in the Shortwave Infrared (SWIR) region of the spectrum (Figure 1.2) means VI based on water content have been developed and widely used (Hunt & Rock, 1989; Penuelas et al., 1993; Gao, 1996; Peñuelas et al., 1997; Zarco-Tejada et al., 2001; Chen et al., 2005; Cai et al., 2021). As SWIR radiation penetrates beyond the surface, these VI can give representation of water content within a leaf, which can give insights into drought stress when desiccation or reduced water content occurs during a stress event (Ceccato et al., 2002; Chen et al., 2005; Stimson et al., 2005; Xue & Su, 2017; Cai et al., 2021). Drought stress can also be inferred from remote sensing by measuring temperature changes from evapotranspiration reductions (García-Tejero et al., 2018) or measuring solar-induced chlorophyll fluorescence (SIF) (Govender et al., 2009).

1.5 Gross Primary Productivity (GPP)

Plant productivity can be considered a 'global sensor of environmental stress' as plants regulate photosynthesis to maintain photostasis (Biswal et al., 2011). As discussed above, staged photosynthetic down regulation occurs as drought stress intensifies (Ensminger et al., 2015). A great deal about a plant's stress status can be inferred from productivity. Gross Primary Productivity (GPP) is the total amount

of carbon that is assimilated by plants through photosynthesis over a given period (Hashimoto et al., 2012). GPP is one of the most crucial and uncertain parameters for forest monitoring and global carbon models (Zhou et al., 2016; Joiner et al., 2018; Joiner & Yoshida, 2020). The possibilities of Sitka spruce GPP retrieval via SRS are explored in the current thesis due to the link between GPP and plant stress status.

GPP cannot be measured directly with SRS, therefore modelling techniques exist with various levels of complexity (Joiner et al., 2018; Joiner & Yoshida, 2020), see Xiao et al. (2019) for an in depth review. Most simply, GPP can be inferred directly from VI (Section 1.5.1).

1.5.1 VI and the Light Use Efficiency (LUE) model

A number of VI have been used for relatively accurate GPP retrieval (Nagai et al., 2010; Gamon et al., 2016; Joiner & Yoshida, 2020), including those based on 'greenness' VI (Hashimoto et al., 2012; Hmimina et al., 2013; Gamon et al., 2016; Huang et al., 2019), NIR reflectance (Badgley et al., 2019; Huang et al., 2019) and carotenoid dynamics (Gamon et al., 2016; Wong et al., 2022). The analyses in Chapter 5 assess how well a number of satellite-retrieved VI relate to Sitka spruce stand GPP using theory from the Light Use Efficiency (LUE) model. This section will introduce the VI used in Chapter 5 and how they related to LUE.

The Light Use Efficiency model (Equations 1.1 and 1.2), is a simplification of GPP which, since its first inception by Monteith (1977), has been at the core of plant productivity research (Wu et al., 2012; Joiner & Yoshida, 2020; Wang, Gamon, et al., 2020; Wong et al., 2022). The parametrisation of the LUE model can take on many forms but the basic formula is,

$$\mathrm{GPP} = \mathrm{APAR} \times \varepsilon \tag{1.1}$$

$$\mathrm{APAR} = \mathrm{FPAR} \times \mathrm{PAR} \tag{1.2}$$

where, GPP is equal to the fraction of total photosynthetically active radiation absorbed by plants (APAR) and the light use efficiency of plants in converting this radiation into biomass (ε). PAR is the total photosynthetically active radiation incident on a leaf and FPAR is the fraction absorbed. FPAR is closely related to NDVI (and other greenness VI such as EVI) and is often used as the proxy for its retrieval (Running et al., 2004; Wong et al., 2020). Whilst PAR may be estimated from meteorological data or ground sensors, the parametrisation of ε is difficult and is a major limitation of LUE model accuracy (Turner et al., 2005; Wong et al.,

2022). It is often indirectly estimated from a biome specific Look-Up Table (LUT) or meteorological data such as temperature or VPD (Running et al., 2004; Yuan et al., 2007). ε has also been linked to remotely sensed measures of SIF (Li, Zhang, et al., 2020) or, as discussed below, VI (Rahman et al., 2004; Middleton et al., 2009; Goerner et al., 2011).

As discussed above NDVI and EVI are measures of 'greenness' and have successfully been used to estimate GPP across a wide range biomes and vegetation types (Goward et al., 1985; Xiao et al., 2004; Rahman et al., 2005; Huete et al., 2008; Sims et al., 2008; Hashimoto et al., 2012; Huang et al., 2019) as well as proxies for FPAR (Running et al., 2004; Verma et al., 2015; Noumonvi & Ferlan, 2020; Wong et al., 2020; Junttila et al., 2023).

CCI, based on broadband reflectance centred at 531 nm, was developed to track seasonal changes in pigment ratios in conifers from satellites (Wong & Gamon, 2015a; Gamon et al., 2016) and is a derivative of the widely used Photochemical Reflectance Index (PRI). Conifers undergo large changes in carotenoid pigment pools, associated with temperature changes, which seasonally regulate photosynthetic activity (Gamon et al., 2016). Increases in relative carotenoid pool size leads to decreased photosynthetic capacity detectable with CCI (Ensminger et al., 2004; Wong et al., 2022), meaning CCI can track photosynthetic dynamics better than traditional indices in conifers (Gamon et al., 2016; Yin et al., 2022). Although in its research infancy, CCI has potential as a direct proxy for GPP (Rahman et al., 2004; Wong et al., 2020) and has also performed well in tracking end of season phenological changes in deciduous forests (Zeng et al., 2022). Carotenoid dynamics are also altered at finer temporal scales for regulating photosynthesis during stress, potentially enabling CCI to detect acute stress responses as well as seasonal cycles. The ability of CCI to track seasonal photosynthetic activity means that theoretically it can be used as a proxy for ε in the LUE model (Rahman et al., 2004; Middleton et al., 2009; Goerner et al., 2011).

Near-Infrared Radiation from vegetation (NIRv) proposed by Badgley et al. (2017) is another VI which can be used to estimate GPP by multiplying total NIR reflectance, a measure of vegetation photosynthetic capacity, with NDVI, a measure of vegetation cover (Baldocchi et al., 2020). NIRv has been shown to be a good proxy for GPP estimation, at monthly and annual scales (Badgley et al., 2019; Wang et al., 2021), for species including eastern white pine (*Pinus strobus L.*) (Wong et al., 2020). However, NIRv may just represent seasonal greening-up and photosynthetic potential rather than actual GPP (Wang, Gamon, et al., 2020; Wong et al., 2022). NIRv effectively captures the fraction of incoming solar radiation that is absorbed by the plant canopy so it acts as a proxy for APAR (FPAR $\times$ PAR) in the LUE model

(Wong et al., 2022). Due to these relationships, Wong et al. (2022) formulated the LUE using only VI as:

$$\text{GPP} = \text{NIRv} \times \text{CCI} \tag{1.3}$$

This formulation removes the need for other data inputs; however, its use in the literature outside Wong et al. (2022) is thus far non-existent. The authors termed this: MODIS NIRv x CCI, however, for simplicity, here it is referred to as GPP_{VI}.

Temporal scale is an important determinant of the VI/ GPP relationship (Dechant et al., 2020; De Pue et al., 2023) and as such is included in Chapter 5 analysis. The comprehensive analysis of remote sensing VI models, meteorological process-based models and hybrid models by De Pue et al. (2023) demonstrated how the major determinant of GPP variability changes from meteorological variables at subseasonal temporal scales to biophysical variables at annual to interannual scales. Therefore it is expected that meteorological inputs of the LUE are more crucial as time intervals shorten. Exactly how this dynamic reveals itself in Sitka spruce may have important consequences for UK forestry applications.

The five outlined VI (NDVI, EVI, CCI, NIRv, GPP_{VI}) will be compared to evaluate their usefulness for stress and drought monitoring. Their formulae, full names and original publications are presented in Table 2.2 (p.58).

Increased accuracy and complexity in GPP retrieval is possible with process-based models (Chapter 6). These are built on the understanding of the fundamental mechanisms and interactions that drive ecological or meteorological processes, e.g. photosynthesis. Process-based models incorporate equations that represent physiological processes and environmental interactions. For GPP representation, the most commonly used is the Farquhar–von Caemmerer–Berry photosynthetic model (Farquhar et al., 1980; Collatz et al., 1991), which is routinely used in isolation or integrated into larger models for GPP estimation (Alton, Ellis, et al., 2007; Powell et al., 2013; Alton, 2016; Zhou et al., 2019; Chou et al., 2020; Liang & Wang, 2020; Qian et al., 2021).

1.5.2 Eddy Covariance (EC)

Eddy Covariance (EC) CO_2 flux measurements are used to test accuracy of GPP retrieval to validate techniques (Baldocchi, 2003). The EC technique directly measures the exchange of gases, energy, and momentum between the Earth's surface and the atmosphere and is considered the 'gold standard' for GPP estimation (Joiner et al., 2018). By capturing rapid fluctuations in vertical wind velocity and gas concen-

trations, this method calculates the covariance between these variables to determine fluxes of CO_2, water vapour (H_2O), and other trace gases. EC has proved popular for validation of satellite based GPP estimates because it produces ecosystem level measurements, on temporal scales ranging from seconds to years, which can be related directly to canopy GPP (Baldocchi, 2003; Joiner et al., 2018). EC is sampled over a specific area (flux footprint), which determines the probability of where a specific flux originates. This provides a spatial area, ranging from less than a hundred metres to several kilometres, that can directly relate to satellite images (Schmid, 1994). EC instrumentation is mounted on tall (depending on forest canopy height) towers. Installation and maintenance are expensive, however global networks (e.g. FLUXNET (Baldocchi et al., 2001)) link EC data sets, facilitating global scale validation across multiple biomes and plant functional types (PFT) (Reichstein et al., 2007; Chen et al., 2009; Hashimoto et al., 2012; D'Odorico et al., 2015; Tang et al., 2021; Zhang et al., 2023).

1.6 Thesis outline

The environmental threats to UK forests due to the changing climate are unprecedented. However, the potential for remote sensing to assess, model and monitor these threats, at previously unattainable scales (spatial, temporal), has never been greater. The present thesis aims to explore potential ways in which UK forestry could adopt remote sensing to transition towards a more drought resilient sector. The major avenues explore, (i) the potential for ground based hyperspectral measurements to characterise detailed drought stress responses in Sitka spruce, and (ii) evaluate the possibility for high throughput drought screening, for future breeding programmes, and (iii) evaluate satellite based GPP retrieval, for opportunities for a country wide forest monitoring programme. This would facilitate pioneering insights into the state of forests and their responses to drought and other stressors. The thesis includes a materials and methods chapter (Chapter 2) including site description, an experimental set up, satellite data processing and data source descriptions. This is followed by four primary research chapters (Chapters 3 - 6) and a general discussion (Chapter 7) to link themes together and draw conclusions on the thesis as a whole. The research chapters are as follows.

Chapter 3 - Evaluating the drought responses of Sitka spruce (*Picea sitchensis*) clones using Vegetation Indices (VI). Are genetic differences detectable through VI?

Sitka Spruce is susceptible to drought stress. Characterising the dynamic effects of

early drought stress, and screening or selecting for more drought resistance in Sitka spruce genotypes, could prove crucial in moving towards a more drought resilient UK forestry sector. By exposing six Sitka spruce clonal groups, from the Forest Research clonal archive, to a progressively intensifying experimental drought, Chapter 3 investigates the effects of drought on needle reflectance over eight weeks to determine; (i) the best VI to monitor drought stress; and (ii) if genotypic differences occurred and were detectable using VI.

Chapter 4 - The effect of canopy position on Vegetation Indices (VI) for Sitka Spruce (*Picea sitchensis*) needles during an experimental drought.

Localised variation in environment, both in space and time, and plant life cycles mean biophysical properties vary across a forest canopy. This variation is often not accounted for by satellite based remote sensing which indiscriminately captures and homogenises different leaf classes. In Chapter 4, using an artificial drought experiment, spectral differences in canopy positions are evaluated in Sitka spruce clonal groups. To determine (i) if biophysical differences throughout the canopy are detectable with VI, and if needle canopy position and needle age effect VI and (ii) if the VI drought response varies across the canopy.

Chapter 5 - Evaluating five MODIS Vegetation Indices (VI) for tracking GPP seasonal dynamics in a UK mature Sitka spruce (*Picea sitchensis*) plantation. Are effects of the 2018 drought detectable from space?

Satellite-based remote sensing facilities the study of forests at stand to global scales. Deriving Gross Primary Productivity (GPP) from satellites allows assessments of forest heath, seasonal cycles, phenological events and stress status. GPP is routinely modelled via the LUE model using satellite inputs or in some instances GPP can be inferred directly from VI. Chapter 5 evaluates the accuracy of VI based GPP retrieval, using MODIS satellite imagery and LUE theory, for a mature even-aged Sitka spruce plantation in the UK. Five VI are evaluated within 10 model formulations, at three temporal scales, to identify (i) how well these VI relate to GPP and if newer VI (CCI, NIRv GPP_{VI}), are better correlated to Sitka GPP than traditional greenness VI (NDVI, EVI). Chapter 5 also assesses if (ii) drought induced GPP reductions can be detected with satellite models at multiple temporal scales and (iii) temporal aggregation or interpolation can overcome low data availability at a high latitude site and whether (iv) drivers of GPP change between time intervals, effecting model choice.

Chapter 6 - Testing the Simple Biosphere Model (SiB) for GPP retrieval in a UK mature Sitka spruce (*Picea sitchensis*) plantation. Can new VI improve the model and are effects of the 2018 drought detectable with SiB?

Correct parameterisation of process based eco physical models can facilitate high accuracy Gross Primary Productivity (GPP) retrieval by simplifying the mechanistic responses of plants into a series of formulae and sub models. The Simple Biosphere model (SiB) had proved successful for good quality forest trait retrieval at satellite scales. SiB however, like all models, is non-ideal. Chapter 6 uses different SiB parameterisations for GPP retrieval of a mature, even aged Sitka spruce plantation in the UK. These are analysed and model improvements tested to evaluate if (i) introducing a more biologically realistic Vcmax improves SiB-GPP predictions, and if VI (CCI and GPP_{VI}) can act as Vcmax proxies; (ii) if other VI (EVI, CCI, NIRv GPP_{VI}), relative to NDVI, improve SiB GPP estimation; (iii) and whether the model performs differently across seasons, and (iv) if the introduction of a water stress term, based on VPD, improves SiB sensitivity to drought stress.

1.7 Thesis aims

The chapters outlined will be used together to test the following questions:

— Can VI can detect drought responses in Sitka spruce (at the needle scale and canopy scale)?

— Can VI detect clone and canopy difference in drought responses in Sitka spruce?

— Do new generation VI based on xanthophyll dynamics outperform traditional 'greenness' ones?

— Can new generation VI improve process based modelling?

A general discussion is present in Chapter 7 where results from all chapters are evaluated in relation to the thesis aims and conclusions of the research as a whole are made.

Chapter 2

Data and Methods

2.1 Overview

Methods and data used for the proceeding research are outlined in this Chapter. Chapters 3 and 4 are analyses of data collected in an artificial drought experiment, designed to test a wide range of Vegetation Indices (VI), collected using hyperspectral field spectroradiometry. Chapters 5 and 6 then evaluate VI at coarser spectral and spatial resolution using satellite based remotely sensed reflectance. In Chapter 6 the VI are ingested into a process-based biophysical land surface model.

This Chapter details the methods and data that provide the basis for, and are common to, the subsequent research. The outline for this Chapter is as follows,

— **2.1 - The design and outline for a drought experiment on Sitka spruce** (analysed in Chapters 3 and 4). Including development of a novel methodology for non destructive, *in-situ*, hyperspectral reflectance retrieval for conifer needles.

— **2.2 - Description of the flux tower field site at Harwood forest, UK.** This site is a commercial even aged Sitka spruce plantation. For Chapters 5 and 6, satellite observations were validated against Harwood forest flux data. The 'truth' data used for validation was initially collected and published by Xenakis et al. (2021).

— **2.3 - Long term (20+ years) VI datasets ($\mathbf{VI_{day}}$, $\mathbf{VI_{16}}$, $\mathbf{VI_{month}}$),** were developed for this thesis, for use in Chapters 5 and 6. These are produced at three temporal resolutions and are based on MODIS reflectance data.

— **2.4 - Description of the process-based biophysical land surface model (the Simple Biosphere Model (SiBx)).** This is based upon the formu-

lation of the model presented by Sellers, Randall, et al.; Sellers, Tucker, et al. (1996, 1996), which includes the photosynthesis model from Collatz et al. (1991) and canopy integration by Los et al. (2000) but includes additional components developed for this thesis.

— **2.5 - Development of maximum carboxylation rate (Vcmax) time series.** The static parameterisation of Vcmax is a potential limitation of SiBx so a series of novel seasonally dynamic Vcmax time series are outlined which are tested in Chapter 6.

— **2.6 - Two datasets are described and validated in this Chapter before use in later analysis.** Specifically, the ERA5 climate reanalysis dataset is compared to corresponding flux tower meteorological variables, and the newly developed VI_{16} is compared to the already established MODIS VI (MOD13) dataset.

In general, throughout the thesis, statistical analysis is described within the corresponding research chapter.

2.2 Experimental design for Chapters 3 and 4

2.2.1 Introduction

Remote sensing provides opportunities to monitor forest health at landscape scales, by use of satellite mounted spectral sensors, informing foresters of early stress detection and stress monitoring (Grulke et al., 2020). It also provides potential to identify more drought tolerant individuals or genotypes by linking remotely sensed variables with stress response phenotypes (Plesa et al., 2019). Satellite imagery is limited in its spectral, spatial and temporal resolution and continuity. To better understand the mechanistic processes linking reflectance and plant biophysical processes, studying plant stress relationships at the leaf level is crucial. Therefore, for the purposes of this PhD, a polytunnel drought experiment was set up to gain an understanding of how the response of Sitka spruce subjected to drought is reflected in VI, at a level of detail unachievable by satellite imagery. These findings will both provide novel insights into Sitka spruce drought stress responses as well as inform later chapters.

The specific aims of the experiment were to

— Measure the spectral response of Sitka spruce clones to progressively increasing levels of drought at the leaf level.

— Identify VI that are sensitive to drought for further research and spatial scaling.

— Assess whether genetic differences in Sitka spruce result in differing stress responses that are detectable with remotely sensed VI.

— understand how these VI responses differ due to needle age and needle canopy position.

This section outlines the experimental design and procedure. The results and discussion of the outlined experiment are presented in Chapters 3 and 4.

2.2.2 Spectra collection and processing

The experiment was carried out in a polytunnel located at the Forest Research Northern Research Station in Roslin, Midlothian during the Summer 2022. The polytunnel allowed for total control of plant water inputs as it excluded external precipitation. Temperature and humidity exceeded that of the outside norms however, to ameliorate these effects, the polytunnel doors were left open and a temperature operated fan increased air flow and cooled the environment.

2.2.2.1 Technical design considerations

The experimental procedure required repeat measures of Sitka spruce needles. To ensure accurate and reliable spectra collection, technical considerations were overcome. This section outlines the practical challenges of needle spectral retrieval to justify the chosen methodology.

Needle reflectance spectra were collected weekly for the duration of the experiment using a field spectroradiometer (ASD FieldSpec 4 standard Res, Analytik Ltd, Cambridge) which records wavelengths in the range of 350 nm to 2500 nm (3 nm to 10 nm resolution). This instrument is widely used for hyperspectral field or laboratory campaigns for leaf reflectance measurements (Mõttus et al., 2012; Serbin et al., 2014; Hovi, Forsström, et al., 2017; Hovi, Raitio, & Rautiainen, 2017; Lange et al., 2017; Vanino et al., 2018). The instrument measures with a contact probe which contains a light source perpendicular to the measuring surface on the end of a fibre optic bundle. The standard leaf clip contact and probe available with the FieldSpec 4 is designed for broadleaf leaves therefore, measuring conifer needles poses specific technical challenges (Lukeš et al., 2013).

Broadleaf plants often have an, assumed to be, flat and relatively large adaxial surface area. Whereas coniferous plants, with needle-like leaves, have a rhomboid cross-sectional shape and small adaxial surface area. The cross-sectional shape (cylindrical geometry) changes the incident angle, reducing the effective absorbing surface

(Gates et al., 1965). Multiple scattering is high in coniferous plants due to mutual shading in needle clumps, this traps incoming photons, increasing the likelihood of absorption, and thus reduces reflectance detected at the instrument (Yanez-Rausell et al., 2014). High multiple scattering poses significant challenges in radiative transfer modelling and biophysical trait retrieval (Rautiainen & Stenberg, 2005), as the spectral signals from different leaves are mixed non-linearly, making complex structural effects (Mõttus et al., 2017). Multiple scattering in conifers is thought to be the main driver of NIR darkness relative to broadleaf plants (Rautiainen & Stenberg, 2005; Rautiainen et al., 2012).

Despite these limitations, needle spectra are routinely analysed. However, they are usually destructively sampled and the needles are placed in an integration sphere (Mõttus et al., 2012; Potůčková et al., 2016, Wu et al., 2018), laid flat as a single layer of tightly packed needles (O'Neill et al., 2002; Zuzana et al., 2013), loosely packed as a random bundle of needles (Serbin et al., 2014) or imaged using a small contact probe (∼0.5 mm diameter) (Richardson et al., 2001).

For the experimental set up here, repeated spectral measurements on small plants with relatively sparse canopies were desired to monitor drought over time. Therefore plants needed to be non-destructively sampled, to maintain full canopies, and avoid stress associated with high levels of defoliation. Non-destructive repeat sampling of conifer reflectance is rare. Mõttus et al. (2017) measured *in-situ* Scots pine needles, by inserting single needles into a grooved leaf clip, with a visor to limit stray light. However, for the present analysis, no leaf clip capable of holding an individual needle was available. Concerns about signal-to-noise ratio of measuring individual needles (Sitka spruce needles are smaller than Scots pine so would decrease the signal-to-noise ratio) required a new *in situ*, non-destructive, repeat sampling procedure to be developed.

2.2.2.2 Spectra measurement procedure

Using a standard contact probe and low reflectance gloves, needles were arranged to form a flat continuous surface over the probe's field of view, this used the contact probe's full field of view to maximise signal. The low reflectance gloves allowed external light to be blocked where gaps between the probe lens and sample were present (Figure 2.1, see also Appendix A, Figure A.1(p.176)). The correct amount of pressure could be applied to the sample by the user ensuring a good contact with the probe without damaging the needles (Serbin et al., 2014).

The glove was highly absorbent across all wavelengths so performed a similar function to a black reference panel. The black reference panel available with the spectro-

radiometer and the glove were compared spectrally, and both produced almost no reflectance in any band. However, the thick layer of needles ensured minimal light would penetrate fully through the sample. The method outlined by Mõttus et al. (2017) requires two people for sampling, one for inserting the sample and the other to operate a computer. The use of a glove and a laptop holder, allowed samples to be taken efficiently by one operator, who could position and hold the sample with one hand, and record measurements with the other (Figure 2.2).

Figure 2.1: Measuring Sitka spruce spectra *in situ* on a branch. Left image: Using the leaf clip without a glove creates gaps between the contact probe and the sample (seen by the light escaping above the sample, also see Appendix A, Figure A.1 (p.176)). Right image: with the introduction of a low reflectance glove the user is able to apply pressure to the sample which facilitates a greater contact between the sample and probe.

To reduce measurement noise one measurement consisted of an average of 25 rapidly collected spectra. To account for the systematic bias that could arise from a specific orientation of the plant material or probe characteristics (Serbin et al., 2014), the probe was removed from the sample after each measurement, then brought back to the same location on the branch. Due to the regular arrangement of needles surfaces facing vertically upwards, the same surface of needles was predominantly sampled (Figure 2.3). Five measurements (25 rapidly collected spectra) were averaged to produce a single spectrum which constituted one observation.

Needles from a number of positions in the canopy were taken. Current year nee-

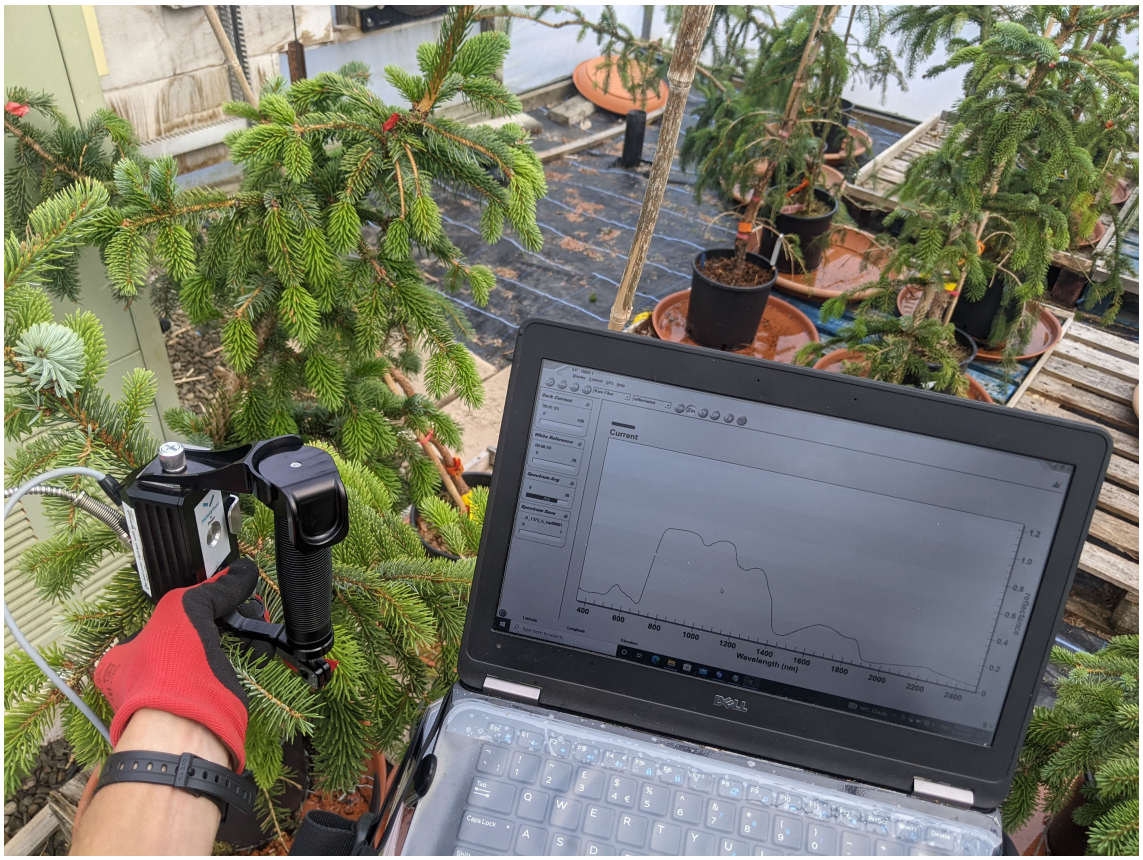

Figure 2.2: Reflectance measurements are recorded by a single operator. Samples are held still with one hand while the computer is operated with the other. The computer is held by an ASD laptop carrier (Analytik Ltd, Cambridge).

dles were ignored as their spectral properties vary greatly during the first year of expansion (Wu et al., 2018; M. Perks, personal communications, 2022), confounding the drought response. Measurements consisted of top of canopy needles (N^{upper}), bottom of canopy needles (N^{lower}) and previous year needles (N^{old}).

N^{upper} and N^{lower} were overwintered needles from the previous year's growth (2021), taken in the top or bottom 25% of the vertical canopy profile. N^{old} were sampled from the top 25% of the canopy where possible or the highest available whorl. These were needles grown in 2020. Sitka spruce needles are regularly arranged as branches, branchlets and needles, so needle age is easily determined by counting internodes backwards, from the current year (O'Neill et al., 2002) (Figure 2.3). One observation per position on every tree was taken. A white reference was taken between each tree using a 99% Spectralon white reference panel. Every tree was sampled on a weekly basis to construct the spectral time series. The contact probe and low reflectance glove were routinely assessed for plant material or dust and wiped with cleaning alcohol wipes.

Figure 2.3: Regular arrangement of Sitka spruce needles. Each internode represents the boundary for a different year's growth. The above sample is four years of growth.

2.2.2.3 Spectra processing

Spectra were interpolated to 1 nm. The spectroradiometer consists of three individual sensors (350 - 1000 nm, 1000 - 1800 nm and 800 - 2500 nm), which take independent spectra that are joined together by the instrument's hardware. Noise occurs where these spectra are joined so spectra are smoothed with a Savitsky-Golay filter (Savitzky and Golay, 1964). Field collected spectra were converted from relative (R_{sample}) to absolute reflectance (R_{abs}) by,

$$R_{abs} = \frac{DN_{sample}}{DN_{WR}} \times R_{WR} \tag{2.1}$$

Where DN_{sample} is the collected spectra, DN_{WR} is the white reference taken in the field and R_{WR} is a lab calibrated reflectance value calculated by the NERC spectroscopy facility (Edinburgh, UK).

2.2.3 Experimental setup

2.2.3.1 Study plants

Sitka spruce (*Picea sitchensis* (Bong.) Carr) study plants was taken from the Forest Research clonal archive (Roslin, UK). Ten ramets from six clonal groups were used. Each ramet originated from scions, collected from mature grafts of the original breeding population trees from West Scotland and Southwest England. Two of these clonal groups made up part of the general breeding population in the UK. These were grafted to root stock in 2015 and planted in 9.5 L pots in 'nursery stock general' soil (ICL, Suffolk) with slow-release fertiliser (120N, 60P, and 199K mg/l).

The groups of clones were randomly assigned to control or drought treatments and moved to the polytunnel in late May 2022. Drought trees were placed on pallets to stop any uptake of moisture from the ground (Figure 2.4). Plants were arranged, so that there was equal representation of each clone around the edges, and no clone existed more than once in any row or column (Figure 2.5).

Figure 2.4: Study plants before experimental drought initiation. Plants on the left (Drought treatment) were placed on pallets to avoid uptake of moisture from the ground. Pot saucers were used when watering the control plants to ensure high soil moisture content.

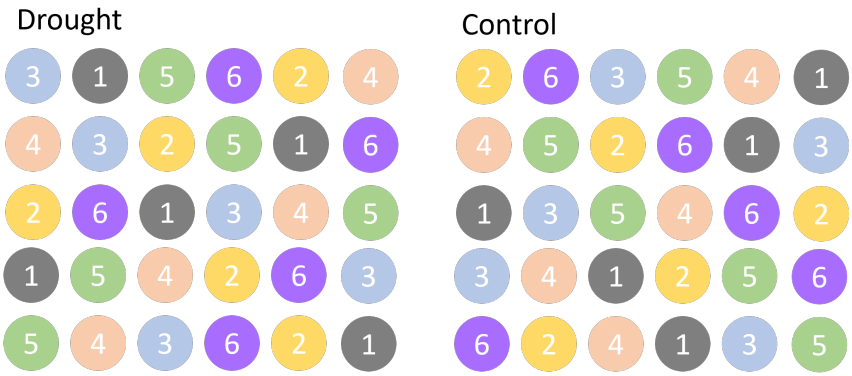

Figure 2.5: Experimental layout of study plants. Plants were arranged so that there was equal representation of each clone around the edges and no clone existed more than once in any row or column. The numbers and colours denote the six different clonal groups. 60 individual plants were used in total. 30 in the drought and control treatments and 10 repeats within each of the six clonal groups.

2.2.3.2 Vegetation Indices (VI)

Vegetation indices (VI) were taken from the literature and are categorised as: Greenness VI (VIg) sensitive to chlorophyll concentration, Pigment VI (VIp) sensitive to stress related pigments (Carotenoids and Anthocyanins) and Water Content VI (VIw) which are sensitive to water content within needles. The VI used and their formula is presented in Table 2.1.

Table 2.1: Vegetation Indices (VI) used in Chapter 3 and 4, the formula used to calculate them and the full and abbreviated names. VIg = greenness indices, VIp = pigment indices, VIw = water content indices. Note: in Chapter 3 CCI is considered a VIg due to the measurement of Chlorophyll; however, in Chapter 4 it is referred to as a VIp due to its relatedness to PRI and Carotenoid stress responses.

VIg	**Greenness Vegetation Indices**		
CCI	Chlorophyll/Carotenoid index	$(R531 - R645)/(R531 + R645)$	Gamon et al., 2016
CIgr	Green Chlorophyll Index	$(R750/R550) - 1$	Gitelson et al., 2005
CIre	Red-edge Chlorophyll Index	$(R750/R710) - 1$	Gitelson et al., 2005
NDVI	Normalised Difference Vegetation Index	$(R800 - R670)/(R800 + R670)$	Hasegawa, 1976; Tucker, 1979
NDVIre	Red edge Normalised Difference Vegetation Index	$(R750 - R710)/(R750 + R710)$	Gitelson and Merzlyak, 1994
SR	Simple Ratio	$R800/R670$	Middleton et al., 1997
VIp	**Stress Pigment Indices**		
ARI	Anthocyanin Reflectance Index	$(1/R550) + (1/R700)$	Gitelson et al., 2001
ARI2	Anthocyanin Reflectance Index 2	$R800[(1/R550) + (1/R700)]$	Gitelson et al., 2001
CRI1	Carotenoid Reflectance Index 1	$(1/R510) + (1/R550)$	Gitelson et al., 2002
CRI2	Carotenoid Reflectance Index 2	$(1/R510) + (1/R700)$	Gitelson et al., 2002
PRI	Photochemical Reflectance Index	$(R531 - R570)/(R531 + R570)$	Gamon et al., 1997
VIw	**Water Indices**		
MSI	Moisture Stress Index	$(R1600/R820)$	Hunt and Rock, 1989
NDWI	Normalised Difference Water Index	$(R970 - R1450)/(R970 + R1450)$	Gao, 1996
NDWI2	Normalised Difference Water Index 1640	$(R858 - R1640)/(R858 + R1640)$	Chen et al., 2005
SRWI	Simple Ratio Water Index	$R860/R1240$	Zarco-Tejada et al., 2001
WI	Water Index	$R900/R970$	Penuelas et al., 1993; Peñuelas et al., 1997
WI/NDVI	Water Index normalised by NDVI	$(R900/R970)$/NDVI	Peñuelas et al., 1997

2.2.3.3 Soil moisture

Soil moisture was recorded using two methods, both using ThetaProbe ML2x soil moisture sensors (Delta-T Devices Ltd, Cambridge, UK). Continuous measurements were automatically taken every 30 minutes by a datalogger (CR1000x, Campbell Scientific, Shepshed, UK) to give diurnal change in soil moisture (see Appendix A, Figure A.2 (p.177)). One individual from each clonal group, in both treatments, received an *in situ* probe for the duration of the experiment. Soil moisture was also measured manually, two to three times a week, using a ML2x sensor wired to a handheld HH2 soil moisture meter (Delta-T Devices Ltd, Cambridge, UK). For these measurements, the sensor was fully inserted into the soil. Three measurements per pot were taken around the tree and an average calculated to give representative soil moisture of the pot.

2.2.3.4 Sensor calibration

To ensure accurate soil moisture readings, a soil-specific calibration was performed. A 2 L sample of soil was removed from a Sitka spruce clone, not used in the experiment, which was potted with the study plants. The soil was weighed and a reading in volts taken with a soil moisture sensor. The sample was then oven dried at 105 °C for 24 hours. Once dry it was reweighed and a new voltage measurement taken. The probe voltage is converted into dielectric constant with a third order polynomial fit using,

$$\sqrt{\varepsilon} = 1.07 + 6.6V^2 - 6.4V^2 + 4.7V^3 \tag{2.2}$$

Where V is measured voltage. A specific soil conversion from V to soil moisture is then calculated using,

$$\theta = \frac{\sqrt{\varepsilon} - a_0}{a_1} \tag{2.3}$$

a_0 and a_1 are soil-specific coefficients, a_0 is the dielectric constant of the dry sample and a_1 is,

$$a_1 = \frac{\sqrt{\varepsilon_w} - \sqrt{\varepsilon_0}}{\theta_w} \tag{2.4}$$

Where $\sqrt{\varepsilon_w}$ and $\sqrt{\varepsilon_0}$ are the wet and dry soil dielectric values and θ_w is,

$$\theta_w = \frac{W_w - W_0}{L} \tag{2.5}$$

In which W_w and W_0 are wet and dry soil weights and L is the soil sample volume in litres.

2.2.3.5 Watering regime

Before the drought treatment began, all pots were watered to saturation then left for two hours for excess water to drain. Soil moisture readings were taken, and this value was used to determine the field capacity (FC) for each pot. Control plants were maintained at around 80-100% FC with regular watering, occasionally dropping to 75%. This ensured that these plants were never limited by water availability.

Drought plants were exposed to gradually decreasing water availability, to avoid rapid soil drying, which is unlikely to occur in natural conditions. In weeks one and two, water content was allowed to drop, and was then maintained at around 20% to 25% FC. For the next two week period, the pots were then watered to 20% FC, once a week, then left unwatered for the remainder of the drought period.
To achieve the desired water content in each pot, a water deficit in L was calculated using,

$$Deficit = SM_{FC} - SM_T \tag{2.6}$$

where,

$$SM_{FC} = \theta_{FC} \times 9.5 \tag{2.7}$$

SM_{FC} is the total water in L at field capacity. θ_{FC} is soil moisture (m^3m^3) at FC and 9.5 is the total pot volume in litres

and,

$$SM_T = SM_{FC} \times \frac{Tg}{100} \tag{2.8}$$

SM_T is target water in L and Tg is the target percentage of FC.

2.2.3.6 Maximal photochemical efficiency (*Fv/Fm*)

Chlorophyll fluorescence is a non-invasive measure of photosystem II activity and can provide direct inferences of plant photosynthetic performance (Murchie & Lawson, 2013). It can provide relatively quick and reliable indications of plant function, so

measurements were taken to complement the hyperspectral analysis. Chlorophyll fluorescence is a phenomenon where chlorophyll molecules emit light (fluoresce), when they return to their ground state, after being excited by light absorption (Baker & Rosenqvist, 2004). When chlorophylls receive light energy it can take one of three pathways, most light is absorbed, some excess energy is dissipated as heat (NPQ) and a small portion is emitted as longer wavelength light, in the red (around 680 nm) and far-red (around 730 nm) regions. Measuring this re-emitted light is the basis of chlorophyll fluorescence. Because these three processes occur in competition with each other, chlorophyll fluorescence provides information about the quantum efficiency of photochemistry and heat dissipation (Murchie & Lawson, 2013).
Multiple metrics can be inferred from chlorophyll fluorescence, here the maximal photochemical efficiency of photosystem II (*Fv/Fm*) is used, as an indicator of plant photosynthetic activity, and a good proxy for drought stress (Mena-Petite et al., 2000; Fang-yuan & Guy, 2004; Bigras, 2005; Cifre et al., 2005; Zhuang et al., 2020; Baldi & La Porta, 2022). *Fv/Fm* represents the potential efficiency of the photochemical reactions occurring in photosystem II (PSII) when all reaction centres are open.

Fv/Fm was measured with a Pulse-Amplitude-Modulation (PAM) chlorophyll fluorometer (MINI-PAM-II, H. Walz, Effeltrich, Germany). *Fv/Fm* is calculated as,

$$\frac{Fv}{Fm} = \frac{(Fm - Fo)}{Fm} \tag{2.9}$$

Where Fo is the minimum fluorescence and Fm is the maximum fluorescence in the dark-adapted state. Needles are arranged to form a flat continuous surface and dark acclimated for 30 minutes using a dark leaf clip (DLC-8, H. Walz, Effeltrich, Germany). Fo is taken using a low intensity measuring light. Fm is taken immediately after a 0.8 s saturating pulse.

2.2.3.7 Polytunnel conditions

The experiment ran from 27$^{\text{th}}$ June 2022 when the drought treatment initiated, and continued until 24$^{\text{th}}$ August 2022 when the drought plants were watered. Temperature and humidity were recorded as 10 minute averages at 2 m above the trees within the polytunnel, however, data are only available from 11th July 2022 due to low accuracy of initial measurements.

2.2.3.8 Needle measurements

Dimensions for needles of all study trees were taken at the start of the experiment. Three needles from N^{upper}, N^{lower} and N^{old} were removed and the length and width recorded with a pair of callipers to 0.1 mm accuracy. An average of the three samples from each tree and canopy position were calculated.

2.3 Study location for Chapters 5 and 6

Following on from the polytunnel drought experiment, Sitka spruce was then studied in natural environmental conditions, at a larger spatial scale. This was done via satellite based VI retrieval at a mature plantation field site. The field site is outlined in this section.

2.3.1 Introduction

The standardised global spatial coverage and long term temporal continuity of satellite based plant biophysical trait retrieval, facilitates forest monitoring with limited cost. The primary focus of Chapters 5 and 6 is the retrieval of Sitka spruce Gross Primary Productivity (GPP) from satellite based reflectance and meteorological variables. GPP cannot be directly observed with remote sensing so various modelling approaches are used to link biophysical traits to productivity (Canadell et al., 2000; Zhang et al., 2015). This PhD relates Moderate Resolution Imaging Spectroradiometer (MODIS) reflectance data to Sitka spruce GPP, using either VI as direct GPP proxies, LUE term proxies (Chapter 5), or GPP retrieval via process-based ecophysical land-surface modelling (Chapter 6). Modeling approaches require validation, and the use of the eddy covariance (EC) technique is the primary method for high quality GPP measurements, and therefore model validation (Norman et al., 1997; Baldocchi, 2003; Gonsamo et al., 2013; Wang, Gamon, et al., 2020; Wang, Chen, & Ju, 2020a). For the aims of this PhD, GPP validation comes from the EC flux and microclimate monitoring site in Harwood forest, England (Xenakis et al., 2021). This section outlines the study site and data availability.

2.3.2 The Harwood forest

Harwood Forest is a commercial upland conifer forest in Northumberland, NE England (55°13'00"N, 2°01'32"W) (Figure 2.6). It is an even aged, second rotation, mature Sitka spruce plantation covering 40 ha, planted in 1973. The site leaf area index is 5.7, mean tree density is 1348 trees ha^{-1} and top height is 26 m. The site is situated at 290 m elevation with a 2 °slope. Mean annual temperature is 7.6 °C and

total precipitation is 1300 mm. The soil is peaty-gley. Sitka spruce is extensively planted across the UK (Figure 2.6) and covers around half the planted conifer area. The Harwood Forest site is climatically representative of typical forestry in Scotland and much of northern upland UK (Locatelli et al., 2021).

Data from the site are collected via instrumentation on a tower installed in 2014 to a top height of 32 m. Carbon fluxes are recorded with a modified semi enclosed IRGA (LI7500, Li-Cor Inc., Lincoln NE, USA Clement et al., 2009). Air was sampled along a vertical profile to determine CO_2 and H_2O fluxes at a frequency of 10 measurements per second. Meteorological variables such as air temperature, humidity, incoming radiation and photosynthetically active radiation were also recorded at 5 s intervals. For a more detailed description of flux calculation and instrumentation see Xenakis et al. (2021). A site footprint was determined using the Kormann and Meixner (2001) model. This was used to determine a four-year average cumulative footprint, to determine the sample location, within satellite images (Figure 2.8). CO_2 flux data from 2015 to 2018 were used. Soil water content was recorded with 107 probes (CS605, Campbell Scientific Ltd) at four soil depths (0.02, 0.1, 0.3, and 0.6 m). An average of these depths was taken to give soil water content at a depth of 0.3 m.

2.3.2.1 GPP calculation

The storage flux (Fs, µmol CO_2 m^2 s^{-1}) was determined by Xenakis et al. (2021), by calculating the differences in CO_2 mixing ratio, multiplied by the depth of each canopy layer, every 30 minutes, using the method described by Yang et al. (2007). See section 2.2.2 in Xenakis et al. (2021) for more detail. These 30 minute Fs values were filtered to exclude any period where incoming global shortwave radiation < 20 W m^2. These were considered as day-light observations and were then aggregated to give daily values (Fs, µmol CO_2 m^2 s^{-1}). This was converted to GPP gC d^{-1} by,

$$\text{GPP} = Fs \times ds \times \frac{0.85}{10^6 \times 12} \tag{2.10}$$

Where ds is the number of seconds of daylight at the specific latitude. This was multiplied by 0.85 to account for low light intensities at sunrise and sunset. This value is converted to g C by converting CO_2 to mols then multiplying by the total molecular weight of C within CO_2 (12).

2.3.2.2 Meteorological variables

Other meteorological variables recorded at the flux tower were made available. These are used in Section 2.7 to validate the European Centre for Medium-Range Weather Forecasts (ECMWF) Reanalysis v5 (ERA5) data set, used for parametrisation of

Figure 2.6: The location of the Harwood flux tower site in north East England. The red point represents the position of the flux tower. The scale bar represents 100km The green area is the distribution of conifers from the National Forest Inventory 2020 (Forestry Commission. © Crown copyright and database right (2020), Ordnance Survey [100021242]). Forest cover data is not available for Ireland and Northern Ireland.

the Simple Biosphere Model (SiBx) (Chapter 6). The available variables were air temperature (°C), Photosynthetically Active Radiation (PAR) (mW m^2), relative humidity (%), atmospheric pressure (KPa), soil water content (%) and precipitation (mm day^{-1}).

2.4 Satellite data sources and data processing

2.4.1 Introduction

For the analysis in Chapters 5 and 6, a number of satellite based data sources were used. A description of these data and processing steps are outlined in the following section. Section 2.4.5 gives a detailed description of the processing steps undertaken to develop a series of continuous VI time series, at three temporal time scales, from MAIAC processed MODIS data.

2.4.2 ERA5

Meteorological variables used to drive the LUE model (Chapter 5) and SiBx model (Section 2.5 and Chapter 6) were taken from the European Centre for Medium-Range Weather Forecasts (ECMWF) Reanalysis v5 (ERA5) dataset (Hersbach et al., 2020; Muñoz Sabater, 2021). ERA5 combines observation with model data to produce a globally consistent and temporally continuous climate dataset containing a detailed record of the evolution of 50 variables. It has global coverage at 0.1° x 0.1° and hourly temporal resolution. Temporal coverage dates from January 1950 to the present. ERA5 and its previous versions have been widely used, including among other uses, in the Intergovernmental Panel on Climate Change (IPCC) State of the Climate Assessments, atmospheric sciences and plant process modelling (Chen et al., 2020; Hersbach et al., 2020; Intergovernmental Panel on Climate Change (IPCC), 2021). ERA5 is routinely used, and selected for this thesis, due to its assessed reliability (IPCC, 2021).

ERA5 data is available directly from https://cds.climate.copernicus.eu/. However, for the present work, data were acquired through the Google Earth Engine GUI (Gorelick et al., 2017). Whereby, for the ERA5 pixel overlapping the Harwood flux tower footprint (55°13'00"N, 2°01'32"W), hourly values for the desired variables were averaged, to obtain daily observations for all days from 2015 to 2018. The ERA5 variables are presented and discussed in Section 2.7.

2.4.3 MODIS

The focus of this PhD is evaluating the applicability of various VI for Sitka spruce health monitoring. Chapters 5 and 6 use satellite based spectroscopy to evaluate VI performance at the landscape scale. A variety of long term, globally expansive, open source satellite mission data sets exist. For the present thesis, data acquired from the Moderate Resolution Image Spectroradiometer (MODIS) were selected. This was due to:

— **The availability of specific wavelength bands** - most notably MODIS band 11 is centred at around 531 nm (the band width is 526 - 536 nm), which is not present in higher spatial resolution sensors e.g. Sentinel-2. This makes the retrieval of CCI possible (Gamon et al., 2016).

— **Daily overpasses** - the high frequency of cloud cover at the study site means data availability is low. High temporal resolution is therefore favoured to ensure the best chance of cloud free observations.

— **Long (+20 years) data availability** - this ensures the data is available over the study period (2015 - 2018), but also provides a good sample for historical averages required for time series construction.

MODIS was launched on the 'Terra' satellite in 1999 and the 'Aqua' satellite three years later, and has provided continuous reflectance measurements ever since (Salomonson et al., 2006). The sensors collect reflectance across 36 bands at 250 - 1000 m spatial resolution (bands 1-2 @ 250 m, bands 3-7 @ 500 m and bands 8 - 36 @ 1000 m). Since its launch, a large suite of MODIS products have been made available including raw radiances, atmospheric products, cryosphere products, ocean products and land products. Including, but not limited to, ready processed LAI, FPAR, GPP, NDVI and EVI as well as various preprocessed surface reflectance products. The literature and use of these products is extensive and active (García-Mora et al., 2012; Yan et al., 2021).

To achieve the desired objectives for forest monitoring, data availability, due to frequent cloud cover, was the major limitation. To overcome this, a series of temporally continuous datasets were developed using various compositing and interpolation techniques. The requirements of the developed datasets were to be

— Temporally continuous

— Contain multiple VI (NDVI, EVI, CCI, NIRv and GPP_{VI})

— Be repeatable over any MODIS pixel

To achieve these aims, two existing MODIS products were used which are outlined below. (i) The MODIS VI product (MOD13) is an established VI product, which here provides a reference data set that has been justified within the literature. And (ii) the MAIAC reflectance product, which provides high quality processed reflectance data, from which the new time series are developed.

2.4.3.1 MODIS VI (MOD13)

MOD13 is an established data product produced globally, which is a temporally continuous time series of two 'greenness' VI (NDVI, EVI), at regular 16 day intervals (23 observations per year) (Didan et al., 2015). The images are corrected for molecular scattering, ozone absorption and aerosols. MOD13 overcomes discontinuous observations, by implementing a Constrained View Maximum Value composite (CV-MVC) algorithm, which selects the 'best' observation, for each 16-day window, based on view angle and high NDVI (see Section 2.4.5.2 below). Compositing like this strongly reduces the effects of clouds and noise (Testa et al., 2018), while maintaining high precision for phenological cycles (Zhang et al., 2009). The product is well established and has been widely used in the literature (Testa et al., 2014), including for phenological start and end of seasons estimations (Testa et al., 2018), canopy dynamics (Ahl et al., 2006), tree mortality levels (Spruce et al., 2019) and forest defoliation (Spruce et al., 2011). It is however, limited to NDVI and EVI, two indices which, although useful, are sub-optimal for some biophysical trait retrieval (Huete et al., 2002), especially in evergreen conifers (Gamon et al., 2016). Therefore, the new datasets proposed in this thesis (Section 2.4.5), expand on the CV-MYC framework, to include newer VI.

MOD13 processing (VI_{MODIS})

MOD13 products from both satellites (Terra (MOD13A2) and Aqua (MYD13A2)) were selected to ensure the best chance of good quality observations. These products are at 1 km resolution making them comparable with the full range of MODIS reflectance bands (bands 8 to 36 are only available at 1 km resolution). All data from the pixel corresponding to the location of the flux tower (55°13'00"N, 2°01'32"W) (see section 2.4.6), were cropped and downloaded for the years 2000 to 2022, using Google Earth Engine (GEE) (Gorelick et al., 2017). Due to extreme values, from non-ideal quality observations, the data were then further filtered. The filtering used the inbuilt quality flags, to remove snow and cloud influenced pixels (QA = 0, 1). Observations which had view angles greater than 35° and extreme EVI values (< 0.3) were also removed. This left a final dataset of NDVI and EVI consisting of 506 observations across the 22 year period (Figure 2.7). Filtering was conducted in R and RStudio (RStudio Team, 2020). This filtered MOD13 dataset is henceforth referred to as VI_{MODIS}.

2.4.3.2 MAIAC

For high quality MODIS reflectance the Multiangle Implementation of Atmospheric Correction (MAIAC) algorithm (Lyapustin et al., 2018) was used. The MAIAC

algorithm grids MODIS L1B measurements to fixed 1 km cells, and with a number of pixel and image-based processing steps detects clouds, snow and aerosols and performs a number of image atmospheric corrections, using short sliding window time series, known LUT inputs and a bidirectional reflectance distribution function (BDRF) model (Laypustin et al., 2008, 2011, 2012, 2018).

MAIAC pre-processing (*Filtered_ MAIAC*)

The MAIAC corrected MODIS data were downloaded from NASA Earthdata https://search.earthdata.nasa.gov and processed in R and RStudio (RStudio Team, 2020). Every 1 km pixel corresponding to the location of the flux tower was downloaded for the period 2000 - 2022 (see Section 2.4.6). Multiple daily overpasses results in four to five daily observations. Only the clear sky data were selected based on the MAIAC quality assurance (QA) band. Data with a view angle of more than 45 °were removed to avoid anisotropic reflectance effects (Gamon et al., 2016; Middleton et al., 2016; Yin et al., 2022). Observations with extremely high blue reflectance values (> 0.01) were removed to minimise aerosols and other contaminates (Didan et al., 2015). When there were multiple observations per day the observation with the highest NDVI was selected. This filtered dataset (*Filtered_ MAIAC*) was then used to construct the continuous VI datasets at different spatial resolutions (section 2.4.5). The *Filtered_ MAIAC* was highly discontinuous and consisted of 400 high quality observations over 23 years (Appendix A, Table A.1 (p.179)), the distribution of these is discussed in Section 2.4.4.

2.4.4 Cloud contamination and quality data

The discontinuous nature of satellite reflectance retrieval poses a major limitation for studying seasonal patterns and stress anomalies. To achieve continuous data sets, differing interpolation and gap filling techniques can be employed.

Temperate regions such as the UK suffer from high frequency of cloud cover. The average probability of a cloud free satellite image for the UK is 21.3% over a year (Armitage et al., 2013). This figure drops significantly across much of Scotland and upland areas. Zhang et al. (2017) finds the likelihood of a good quality MODIS pixel decreases with latitude. These high cloud cover areas are generally where Sitka is planted (Armitage et al., 2013)

Temporal gaps in the *Filtered_ MAIAC* timeseries, between clear sky observations, were frequent and large due to cloud contamination (Figure 2.7). On 20 occasions, between 2000 and 2023, the gaps between observations were two or more months. Three data gaps of at least five months occurred over the same period. On average

17 cloud free pixels were available per year although this varied considerably between years. There were 33 cloud free observations in 2003 compared to less than 10 in four other years (2000, 2002, 2015, 2016). Spring is the most imaged season, and on average 6.3 observations a year were available, compared to 4.3 in Autumn, 3.5 in Summer and 3.3 in Winter. For six years (2000, 2002, 2010, 2015, 2016, 2018), no observations were available for winter. The Aqua satellite mission was launched in August 2002 meaning that only seven to ten observations are available for the first three years. The full number of observations are presented in Appendix A, Table A.1 (p.179). The VI_{MODIS} contains data gaps due to quality filters applied after the MVC-CV meaning it is not a complete, continuous dataset (Figure 2.7).

2.4.5 Developing new VI time series

The below sections outline the processing steps for the newly developed VI time-series; they are all based on the full *Filtered_ MAIAC* dataset (section 2.4.3.2) (2000 - 2023). Three datasets are outlined which all contain five VI (NDVI, EVI, CCI, NIRv, GPP_{VI}) and are produced at regular and continuous but differing time intervals. These are,

— VI_{day} - Interpolated to daily observations

— VI_{16} - Aggregated to 16 day intervals using CV-MVC

— VI_{month} - Aggregated to monthly observations

2.4.5.1 VI_{day}

The variable quality of observations and subsequent removal of low-quality data resulted in discontinuous time series, indicative of satellite observations in geographical regions with high cloud cover. To account for this, Decomposition and Analysis of Time Series software (DATimeS) (Belda et al., 2020) was used for interpolation, to reconstruct continuous seasonal cycles of *Filtered_ MAIAC* VI. DATimeS is a stand-alone image processing GUI toolbox containing many mathematical fitting algorithms, including conventional methods like Fourier transform and Whittiker smoothing, as well as a suite of Machine Learning (ML) algorithms.

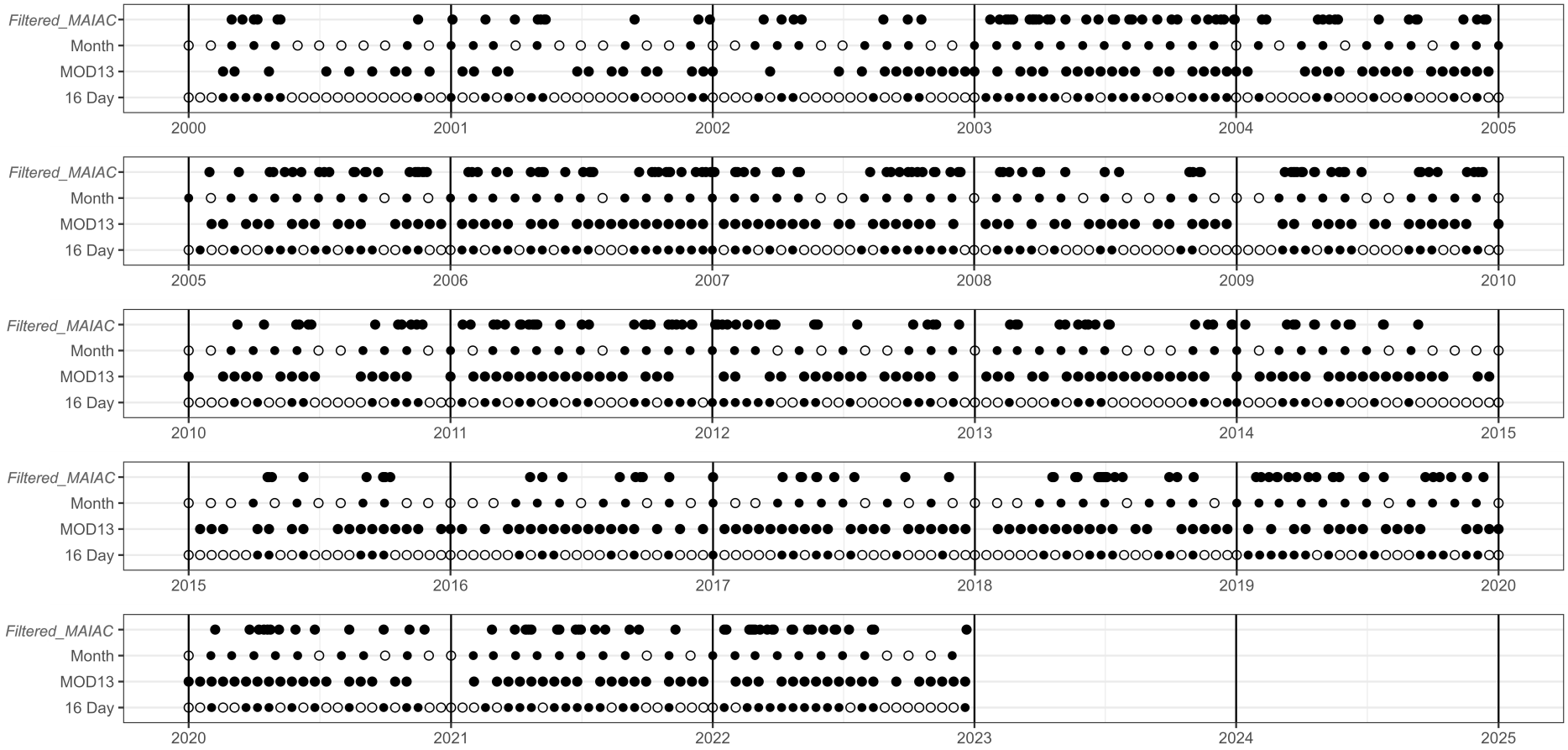

Figure 2.7: Observation dates for the reconstructed time series 2000 - 2022. *Filtered_MAIAC* is the high quality MODIS pixels used for the construction of the other time series. Month and 16 Day are time series processed from MODIS reflectance data using CV-MVC. MOD13 is the MODIS vegetation index global product. Filled points represent where observations are present. Unfilled points are historical averages that have been used to gap fill data. The daily time series is excluded as a modelled observation exists for every day. The MOD13 contains data gaps due to quality filters applied after the MVC-CV meaning it is not a complete, continuous dataset.

When gaps in *Filtered_ MAIAC* were greater than one month, an average value was inserted. This value was the average monthly value over the full dataset (2000 - 2023). This time series was then processed in DATimeS. To determine the most appropriate gap filling method, the discontinuous *Filtered_ MAIAC* was fitted using multiple ML and conventional algorithms (Gaussian Process Regression (GPR), Kernel Ridge Regression; Fourier Transform, Sigmoid, Whittiker and linear fit) to daily observation within DATimeS.

These data were then compared to flux tower GPP (ftGPP) using regression analysis to determine the most appropriate interpolation method (see Appendix A, Table A.2 (p.182) for regression analysis results). Gaussian process regression (GPR) consistently performed well relative to other tested algorithms (high R^2 when correlated with ftGPP). GPR has been outlined as an optimum fitting algorithm, for vegetation reconstruction over multiple seasons (Verrelst et al., 2019; Belda et al., 2020), due to accuracy and the uncertainty estimates that can be produced. Other algorithms also performed well, although GPR uses a Bayesian framework to calculate probabilistic outputs, meaning that confidence intervals are possible, which facilitates robustness assessments (Verrelst et al., 2011, 2019). GPR was therefore used for all interpolation.

2.4.5.2 VI_{16}

Innovative to this research, the CV-MVC method implemented in the MOD13 is adopted here, but expanded to a wider range of VI (NDVI, EVI, CCI, NIRv, GPP_{VI}), to create a comparable 16 day dataset. The *Filtered_ MAIAC* dataset is split into 16 day windows. For each 16 day window, the two pixels with the highest NDVI are selected (Didan et al., 2015). NDVI is reduced by the presence of clouds and atmospheric contamination in most cases (Los et al., 2000; Didan et al., 2015). Therefore, over a short time frame, where NDVI will be relatively stable, the highest NDVI value for a given point will be the least contaminated pixel. From these two pixels, the one with the smallest view angle, to reduce BRDF effects, is used. If, for a given 16 day window, no high-quality observations are available then a historic average, calculated on all available data for that 16 day period, is used to fill the gap (see Appendix A, Figure A.5 for high quality observation dates). Applying these methods to the *Filtered_ MAIAC* produced the product (for a time series of the full VI_{16} data set see Appendix A, Figure A.6 (p.181)).

2.4.5.3 VI_{month}

Monthly averages of *Filtered_ MAIAC* were calculated for the full time series (2000 - 2022). When no observations for a specific month were available a historical

average value was inserted (Figure 2.7). The historical averages were calculated as the average monthly value for the full *Filtered_MAIAC* dataset.

2.4.6 Pixel selection

Two MODIS pixels overlapped the flux tower footprint (Section 2.3.2 and Figure 2.8). The footprint was calculated as the average area over the study period (2015 - 2018) in which 70% of all fluxes originated. The position of the flux tower (55°13'00"N, 2°01'32"W) was on the boundary of the two footprint overlapping MODIS pixels (Figure 2.8). The more southerly of these two pixels overlapped only the Harwood forest, whereas the northerly pixel encompassed felled forest, and some surrounding agricultural land. Therefore, the southerly pixel was used in analysis. Harwood is an even age monoculture, so despite the relatively coarse resolution of the desired MODIS bands (1 km), the response of the vegetation within the pixel will likely be relatively homogenous, reducing mixed pixel related error.

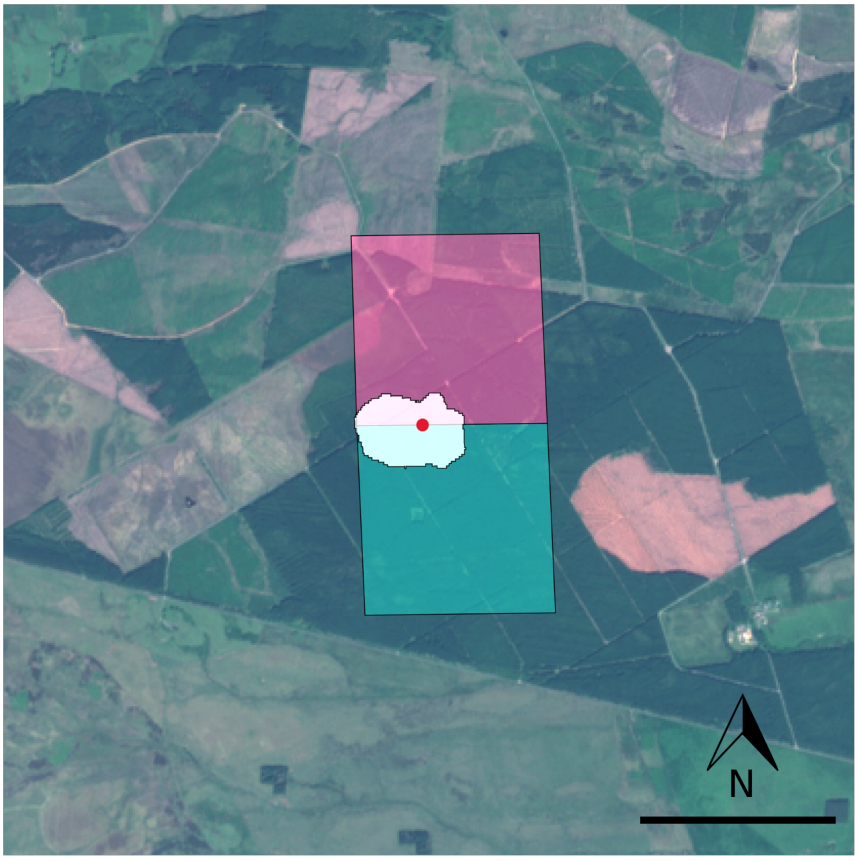

Figure 2.8: The Harwood field site. The red point is the tower location. The grey shape is the flux tower footprint, representing where on average, over the four study years, 70% of the recorded fluxes originated from. The two coloured boxes represent the MODIS pixels (1000 m x 1000 m) which overlap the flux footprint. Scale bar is 1000 m. The background image is a Sentinel-2 scene imaged on 24th June 2018.

2.4.7 Satellite Vegetation Indices (VI)

Five VI were calculated from MODIS MAIAC reflectance for the VI_{day}, and VI_{month} time series. Each VI is related to plant productivity and has been previously correlated to GPP, and used as a proxy for specific terms in the LUE model, in the literature (Gamon et al., 2016; Badgley et al., 2019; Liu et al., 2021; Wang et al., 2021). They consist of traditional 'greenness' VI (NDVI, EVI) and newer generation VI (CCI, NIRv, GPP_{VI}) (a brief history and explanation of these is discussed in Section 1.4.2 (p.25)). The selected VI and their formulae are presented in Table 2.2.

Table 2.2: Vegetation Indices used in VI_{day}, VI_{16} and VI_{month}. All VI are taken from the literature and have been related to Gross Primary Productivity (GPP). B followed by a number is the MODIS band it represents in the formula presented. The central wavelength and band range for each band used are: $B1$ (Red) = 659 nm (620 - 670 nm), $B2$ (NIR) = 865 nm (841 - 876 nm), $B3$ (Blue) = 470 nm (495 - 476 nm), $B11$ = 531 nm (526 = 536 nm). The additional constants in EVI are; $g = 2.5$, $C1 = 6$, $C2 = 7.5$ and $L = 1$. GPP_{VI} appears in Wong et al. (2020) as MODIS NIRv x CCI however for simplicity, it is referred to throughout this thesis as GPP_{VI}, as it is a version of the Light Use Efficiency model (LUE) using VI alone as inputs.

Abbrev.	Vegetation Index	Formula	Reference
NDVI	Normalised Difference Vegetation Index	$(B2 - B1)/(B2 + B1)$	Hasegawa, 1976
EVI	Enhanced Vegetation Index	$g \times (B2 - B1)/(B2 + C1 \times B1 - C2 \times B3 + L)$	Liu and Huete, 1995
CCI	Chlorophyll/carotenoid index	$(B11 - B1)/(B11 + B1)$	Gamon et al., 2016
NIRv	Near-infrared radiation from vegetation	$(NDVI - 0.08) \times B2$	Badgley et al., 2017
GPP_{VI}	Gross Primary Productivity Vegetation Index	$NIRv \times CCI$	Wong et al., 2020

2.5 The Simple Biosphere Model (SiB)

2.5.1 Introduction to SiB

The analysis in Chapter 6 uses process-based modelling to simulate Sitka Spruce GPP at the leaf and canopy scale, and evaluates this in relation to spatially overlapping EC flux tower canopy GPP (ftGPP) calculated by Xenakis et al. (2021).

The modelling techniques used, are based on the Simple Biosphere model (SiB), a process-based ecophysical land-surface model, originally proposed by Sellers et al. (1989). SiB calculates the transfer of energy, mass and momentum between the atmosphere, land surface and soil, including both biological and physical processes. The work presented here is based on the formulation of SiB2 (Sellers, Randall, et al., 1996; Sellers, Tucker, et al., 1996). Which, unless stated otherwise, is the origin of the outlined equations within this section.

The use of SiB in the literature since its first inception has been extensive. It has been used at global and regional scales and in global circulation models, hydrological modelling and vegetation/ atmosphere flux modelling. The success of SiB is due to relative simplicity and realistic performance at diurnal to seasonal time scales (Sun & Xue, 2001; Baker et al., 2003; Oyama & Nobre, 2004; Baker et al., 2008; Lokupitiya et al., 2009; Wang et al., 2009; Haynes et al., 2020).

The parameters of interest for this thesis are canopy and leaf GPP. Therefore the relevant submodels of SiB are described and used; however, these are not the extent of the full operational model, recently outlined by Haynes et al. (2020). SiB determines carbon assimilation at the leaf level (gross assimilation (A), net assimilation (An)), using a photosynthesis model based on the Collatz et al. (1991) integration of Farquhar et al. (1980) enzymes kinetics and the Ball et al. (1988) stomatal model, to connect stomatal conductance with photosynthesis.

Leaf photosynthesis (A, An) and stomatal conductance (g_s) are scaled to the canopy, using the theory that max photosynthesis exponentially decreases though the canopy, following the Fraction of Photosynthetically Active Radiation (FPAR) gradient (Sellers et al., 1992). Parameters for canopy integration are derived from remotely sensed NDVI using relationships outlined in Sellers, Randall, et al. (1996) and built upon by Los et al. (2000). NDVI is closely linked to FPAR which in turn is related to maximum photosynthetic capacity. Since its initial inception, SiB has been developed and adjusted. For a brief history of its development up to and including SiB4 see Haynes et al. (2020).

The research aims of Chapter 6 are to,

— Evaluate incorporating VI, other than NDVI, into the existing SiB model (Equations 2.33 to 2.40 (p.65-67)).

— Test more biologically realistic dynamic Vcmax time series within the model (Section 2.6.2).

— Introduce a drought stress term (S_d) to improve drought stress monitoring (Equations 2.25 to 2.29 (p.63).

The model presented is therefore relevant to these stated aims. The model outlined here falls within the SiB formulation however, does not include all model components. The corresponding analysis is exploratory rather than final so is hereby referred to as SiBx.

2.5.2 Model formulation

The Collatz et al. (1991) photosynthesis model estimates leaf-level photosynthesis (A) (µmol m^2 s^{-1}) as the minimum value of three separate photosynthetic rate functions, minus respiration for net leaf-level photosynthesis (An),

$$A \approx min\{J_E, J_C, J_S\} \tag{2.11}$$

or

$$An \approx min\{J_E, J_C, J_S\} - R_d \tag{2.12}$$

J_C is photosynthesis limited by Rubsico, the enzyme responsible for carbon fixation. J_S is photosynthesis limited by sucrose synthesis and J_E is the light-limited rate of photosynthesis. In nature, co-limitation means transition from one limiting factor is not instant, so a smoothing function based on finding the solution to two quadratic equations is used. The two equations are solved for their smaller roots.
The smoothing functions are,

$$\theta J_p^2 - J_P(J_E + J_C) + J_E J_C = 0 \tag{2.13}$$

and,

$$\beta A^2 - A(J_P + J_S) + J_P J_S = 0 \tag{2.14}$$

Where A is the assimilation rate (µmol m^2 s^{-1}). θ and β are coupling coefficients (0.98, 0.95) and J_P is the smoothed minimum of J_E and J_C.

The three photosynthetic functions are.
The Light limited rate of assimilation (J_E, µmol m^2 s^{-1}),

$$J_E = (\frac{G(\mu)}{\mu})\epsilon_3(1-\omega_\pi)PAR[\frac{c_i-\Gamma^*}{c_i+2\Gamma^*}] \tag{2.15}$$

where, $G(\mu)$ is the relative projected area of leaves in direction $\cos^{-1}\mu$ and μ is the cosine of solar zenith angle, specific to latitude and time of year. ϵ_3 is the intrinsic quantum efficiency for CO_2 uptake (mol mol^{-1}). ω_π is the leaf scattering coefficient for PAR; PAR is flux of PAR incident on the leaf (Wm^2); c_i is the CO_2 concentration within the leaf (Pa) and Γ^* is the CO_2 compensation point (Pa).

The Rubisco-limited rate of assimilation (Jc, µmol m^2 s^{-1}) for C3 plants (C_3V_m) is,

$$J_C = V_m[\frac{c_i-\Gamma^*}{c_i+K_c(1+PO_2/K_0}] \tag{2.16}$$

V_m is the maximum catalytic capacity of Rubisco (µmol m^2 s^{-1}); PO_2 is the O_2 partial pressure in the leaf interior (Pa); K_c is the Michaelis-Menten constant of CO_2 (Pa); $K_c = 30f_T(T_c)$ (Equation 2.20); K_0 is the inhibition constant of O_2; $K_0 = 30,000f_T(T_c)$ (Equation 2.20). Γ^* is the CO_2 compensation point (Pa) which is, Rubisco's specificity for CO_2 relative to O_2,

$$\Gamma^* = \frac{PO_2}{S} = 0.5 \tag{2.17}$$

when $S = 2600f_T(T_c)$.

V_m is maximum leaf catalytic capacity, (Vcmax µmol m^2 s^{-1}) (see section 2.6.2, for Vcmax parameterisation), at T_c (temperature),

$$V_m = \text{Vcmax}2^{Q_t} \tag{2.18}$$

Where the temperature coefficient (Q_t) is,

$$Q_t = Q_{10}coefficient = \frac{T_c-298}{10} \tag{2.19}$$

And the specific temperature function is,

$$f_T(T_c) = \frac{2Q_t}{1 + exp[s_1(T_c - s_2]} \tag{2.20}$$

For respiration (R_dV_m) s_1 and s_2 in Equation 2.20 are replaced by s_5 and s_6 (s_1 and s_5 are temperature inhibition parameters (K^{-1}) and s_2, and s_6 are half inhibition temperature parameters ($K/2$)). $2Q_t$ is replaced for K_c, K_0 and S by $2.1Q_t$, $1.2Q_t$ and $0.57Q_t$ respectively.

The sucrose limited rate (J_S, µmol m^2 s^{-1}) is,

$$J_S = \frac{V_m}{2} \tag{2.21}$$

Respiration is derived from,

$$R_d = f_d V_m \tag{2.22}$$

where $f_d = 0.015$.

The model balances carbon assimilation and transpiration through stomatal regulation and is based on the theory that, due to natural selection acting on plant growth efficiency, regulation of stomatal conductance (g_s) will be to achieve minimum water loss for maximum carbon gain (Cowen & Farquhar, 1977). Using Equations 2.12 and 2.23, a unique solution for An, g_s and C_i (internal CO_2 concentration) can be obtained by initially estimating C_i then iterating to the unique solution, as in Sellers et al. (1992, Figure 4). C_i is initially determined by,

$$C_i = C_a - 1.4AnP/g_b \tag{2.23}$$

where, C_a is CO_2 concentration in the canopy air space, P is surface pressure (Pa) and g_b is the leaf boundary conductance. Determined from plant functional type (PFT) LUT values and canopy dimensions. Here, canopy dimensions (inflection point and canopy width) are determined from the canopy top height at the study site (Xenakis et al., 2021), and allometric relationships determined by using an existing database of Sitka spruce measurements from Aberfoyle, UK (Suárez, personal communications, 2022).

The Stomatal sub model is,

$$g_s = mAnC_s^{-1}h_sP + b \tag{2.24}$$

Stomatal conductance for water vapour (gs) (mol m^2 s^{-1}); m is the coefficient from observations ($m = 6$ for Evergreen Needleleaf Forests (ENF))) and is a function of CO_2 uptake (An), relative humidity (h_s) and CO_2 pressure at the leaf boundary (C_s); b is the minimal canopy stomatal conductance ($b = 0.01L_G$) where L_G is green leaf area index calculated from NDVI (Equation 2.36). 0.01 is an observation coefficient, derived from gas exchange studies see Collatz et al. (1991, sub model section) for details.

2.5.2.1 Drought stress term (S_d)

The formulation of the model presented here does not include soil moisture, which in other formulations, drives water stress by assuming soil water below field capacity imposes stress on photosynthesis. Water is removed from the soil by transpiration processes (Baker et al., 2008). Atmospheric water deficits (VPD), rather than soil water deficits, are the primary driver of drought stress in the present study system (Chapter 5; Xenakis et al., 2021). Therefore, for this work a novel additional drought stress term was developed (S_d), based on VPD, to improve sensitivity to water stress. This was added after initial model runs failed to detect reduced photosynthesis during a drought in summer 2018. This new term limits A by a drought stress factor (S_d) to give drought stressed assimilation (Asd) by,

$$Asd = A \times S_d \tag{2.25}$$

Where S_d is accumulated VPD normalised to 0 to 1,

$$S_d = \frac{(S_a\vartheta) - S_{max}}{S_{min} - S_{max}} \tag{2.26}$$

Where S_a is the accumulated VPD for the last 5 days for any VPD over the VPD threshold. S_{min} and S_{max} are the minimum and maximum of the accumulated vapour pressure deficit and ϑ is a multiplier to limit the reductions in An caused by S_a. The ϑ value (0.8) was derived from comparing the modelled response to ftGPP, and a known drought response (Xenakis et al., 2021), and adjusting the value. A threshold for stressful VPD was selected to be 0.0045 (mol $\times$ mol^{-1}) based

on analysis of flux tower data and iterative runs of the model. VPD is mole fraction vapour deficit (mol × mol^{-1}).

$$VPD = (\frac{h_s}{100})(\frac{VP_{sat}}{P_A}) \tag{2.27}$$

Where,

$$VP_{sat} = 0.61121exp((18.678 - T_A 234.5^{-1})(T_A 257.14 + T_A)) \tag{2.28}$$

and T_A = air temperature (°C).

2.5.2.2 Canopy scaling

The value of A, An or Asd, calculated from equations 2.11, 2.12 and 2.25 (p.60 and 63) are scaled to the canopy to give gross canopy assimilation (CAg), net canopy assimilation (CAn) or water stressed gross/ net canopy assimilation (CAg_{sd}, CAn_{sd}). This is done by

$$CAg, CAn = A\Pi\delta, An\Pi\delta \tag{2.29}$$

Equation 2.29 can also include the drought stressed productivity terms. CAg is equivalent to GPP and CAn to Net Primary Productivity (NPP).

The canopy integration is based on the theory that photosynthetic performance throughout the canopy will be distributed according to the amount of light over a given amount of time.

A useful relationship between FPAR and NIR reflectance is that they are proportional to one another because NIR is proportional to double the pathlength of FPAR radiation in the canopy (Sellers et al., 1992). This is because radiation must enter and leave the canopy whereas FPAR radiation must only penetrate the canopy.

Π is the canopy PAR use scaling parameter and is derived from satellite imagery estimation of FPAR by,

$$\Pi = \frac{\text{FPAR}}{\overline{k}} \tag{2.30}$$

Where $\overline{k}$ is the PAR extinction parameter within the canopy. This varies between 0.4 and 1. So Π is not just dependent on FPAR but also how the PAR is absorbed

through the canopy ($\overline{k}$).

$$\overline{k} = (\frac{G(\mu)}{\mu})(1 - \omega_{vi})^{0.5} \tag{2.31}$$

ω_{vi}, is the leaf scattering coefficient calculated from the green leaf as

$$\omega_{vi} = L_g(t_v + r_v) + L_g(t_n + r_n) \tag{2.32}$$

Where L_g is the green leaf fraction (Equation 2.36) and t_v, t_n, r_v and r_n are the leaf transmissivity and reflectance for the visible and near infrared regions. $G(\mu)$ is the relative projected area of leaves in direction $\cos^{-1}\ \mu$ and μ is the cosine of solar zenith angle (SZA) specific to latitude and time of year.

2.5.2.3 Biophysical parameters derived from satellite VI

Land surface parameters are estimated from satellite retrieved spectral properties of vegetation. Visible light is strongly absorbed by plants for photosynthesis and infrared is strongly reflected. This provides a basis for estimations of variables associated with photosynthesis. NDVI exploits this response by incorporating visible and NIR light and is therefore closely related to the fraction of absorbed radiation FPAR.

The present model requires estimations of FPAR and the green fraction of LAI (L_g). Work by Sellers, Tucker, et al. (1996) and built upon by Los et al. (2000) use satellite retrieval of NDVI to estimate these biophysical parameters (Equations 2.34 to 2.40, p.66-67).

For the current analysis, other VI (EVI, CCI, NIRv, $\mathrm{GPP_{VI}}$, Section 2.4.7) are incorporated into the model to test their applicability. This was conducted by applying the relationships found between NDVI and biophysical parameters to other indices. Although not based on the exact same physical relationship as NDVI, the VI analysed are all inherently linked by the function of photosynthesis and all better track Sitka spruce photosynthesis compared to NDVI (Chapter 5). They are all related strongly to NDVI, so here, they are effectively used as NDVI proxies and therefore converted to the same scale as NDVI.

In order for the relationships between VI and biophysical parameters to be consistent, with those presented by Los et al. (2000), other VI were transformed to the same scale as NDVI ($\mathrm{VI_{NDVI}}$). By,

$$\mathrm{VI_{NDVI}} = a + bVI \tag{2.33}$$

where a and b are coefficients determined by a simple linear regression between NDVI and the chosen VI (Table 2.3).

Table 2.3: Regression coefficients (Slope and Intercept) for simple linear models for the relationship between NDVI and various Vegetation Indices (VI). These coefficients were used to transform the VI to the same scale as NDVI for use as NDVI proxies.

VI	Slope (b)	Intercept (a)
EVI	0.3284	0.9081
CCI	0.7343	0.9511
NIRv	0.4328	1.546
GPP_{VI}	0.7225	4.8656

Then VI_{NDVI} is used in equations 2.34 to 2.40 taken from Los et al. (2000) to determine biophysical parameters.

$$\text{FPAR} = \frac{(\text{VI}_{\text{NDVI}} - \text{VI}_{\text{min}})(\text{FPAR}_{\text{max}} - \text{FPAR}_{\text{min}})}{\text{VI}_{\text{max}} - \text{VI}_{\text{min}}} + \text{FPAR}_{\text{min}} \tag{2.34}$$

VI_{max} and VI_{min} are related to maximum and minimum FPAR (Los et al., 2000). VI_{max} and VI_{min} are values associated with the 2^{nd} and 98^{th} percentiles in the VI distributions to reduce the influence of outliers caused by noisy data. FPAR_{max} and FPAR_{min} values were set, as in Los et al. (2000), to 0.95 and 0.01.

FPAR is then related to Leaf Area Index (LAI). In Sellers, Tucker, et al. (1996) a linear relationship was derived, however this was found to be invalid at the canopy level for conifers (Los et al., 2000). A logarithmic function is therefore applied using,

$$f_v = \frac{max(\text{FPAR}_y)}{0.95} \tag{2.35}$$

Where f_v is the vegetation cover fraction and $max(\text{FPAR}_y)$ is the maximum FPAR for a given year, this f_v value is then used to adjust FPAR for the vegetation cover fraction ($\text{FPAR}_{fv} = \text{FPAR}/f_v$). Green LAI ($L_G$) is calculated from,

$$L_G = \frac{ln(1 - \text{FPAR})L_{G,max}}{log(0.05)} f_v \tag{2.36}$$

Where $L_{G,max}$ is a biome specific max LAI (0.8 for ENF) (Los et al., 2000). Two dead leaf area indices are also calculated, depending on if LAI is increasing, or decreasing.

$$L_D = 0.0001 + L_s \tag{2.37}$$

or,

$$L_D = 0.5(L_{G-1} - L_G)f_v \tag{2.38}$$

Then the total LAI is,

$$L_T = L_G f_V + L_D \tag{2.39}$$

And the greenness fraction of LAI is,

$$f_G = \frac{L_G}{L_t} \tag{2.40}$$

2.6 Dynamic Vcmax processing

2.6.1 Background

Within the SiBx model outlined in Section 2.5, and other process based photosynthesis models, maximum carboxylation rate, or Rubisco-limited photosynthetic capacity (referred to as Vmax or Vcmax), is one of the most crucial variables for parameterisation, due to its sensitivity and influence on photosynthetic processes (Farquhar et al., 1980; Collatz et al., 1991; Kattge et al., 2009; Alton, 2017; Yan et al., 2021).

Vcmax denotes the catalytic capacity of Rubisco within a leaf at 25°C and is intricately linked to Jc in the co-limiting sub-model in SiB (Section 2.5, Equation 2.16 (p.61)). However, Vcmax exhibits substantial variability across biomes, species, seasonal cycles, and within the canopy (Wilson et al., 2000; Meir et al., 2002; Grassi et al., 2005; Kattge et al., 2009). Such variability presents a significant challenge in accurately parameterising Vcmax (Collatz et al., 1991; Alton, 2017; Pacheco-Labrador et al., 2019; Yan et al., 2021).

Common approaches to Vcmax parameterisation often involve selecting biome or PFT - specific LUT values, and using land cover classifications, which assume constant Vcmax across seasons. However, known dynamic seasonal cycles of Vcmax mean this simplification may lead to substantial errors. Despite this, temporal variation of Vcmax is rarely included in process based modelling (Alton, 2017). Vcmax can be inferred at the leaf level by gas exchange measurements and CO_2 response curves; however, this is time consuming and not practical over spatially large and heterogeneous areas (Long & Bernacchi, 2003; Deng et al., 2024).

To address the seasonality and spatial variability of Vcmax, various methods have been proposed. These include hyperspectral remote sensing techniques, which relate

satellite imagery to nitrogen (N) or chlorophyll content (Dillen et al., 2012; Jin et al., 2012; Alton, 2017; Deng et al., 2024). N content is strongly linked to Vcmax due to the high proportion of plant N existing in Rubisco (Smith et al., 2002; Ollinger et al., 2013). Additionally, assimilating space-borne chlorophyll fluorescence (SIF) into canopy radiative transfer models has been explored (McCallum et al., 2009; Zhang et al., 2014). Alton (2017) developed seasonal Vcmax retrieval using MODIS LAI and hyperspectral canopy chlorophyll estimation. However, this failed to capture season peak Vcmax. The authors highlight the need for Vcmax retrieval that varies across a season and throughout PFTs.

In evergreen conifers, reflectance at 531 nm, and VI associated with it (PRI, CCI, GPP_{VI}), correlate with the conversions of light to canopy photosynthesis, and can therefore track seasonal dynamics (Chapter 5; Gamon et al., 2016). VI based around reflectance at 531 nm may therefore act as good, easy to acquire, proxies for Vcmax, which can be retrieved simultaneously alongside the satellite VI already needed for SiB GPP.

Here, the aims are to develop seasonally dynamic Vcmax to compare with static values traditionally used in SiBx to improve model realism.

Three Vcmax time series are developed. **vmDy** - built from fitting seasonal curves over daily optimised Vcmax values. This timeseries simulates seasonality but includes no interannual variation. **vmCCI** and **vmGPP** are derived from the daily VI datasets for the two MODIS band 11 based indices (531 nm wavelength) (CCI and GPP_{VI}). These VI are transformed to µmol m^2 s^{-1} by min/ max normalisation, where minimum and maximum values are determined by iterative model runs, to minimise the differences between ftGPP and SiB modelled GPP (mGPP).

2.6.2 Vcmax development

Here, the development of the three Vcmax time series is outlined. The applicability of these for SiBx GPP retrieval is tested and discussed in Chapter 6.

2.6.2.1 Dynamic Vcmax (vmDy)

An 'ideal' Vcmax time series was produced using global optimisation (Mullen et al., 2011). This was created by running the SiBx model in its original formulation and for every day running a global optimisation routine using the R package DEoptim (Mullen et al., 2011). The optimisation implements a differential evolution algorithm to minimise a user defined function output. For the Vcmax optimisation here, the absolute difference between SiBx modelled GPP (mGPP) and flux tower (ftGPP)

was selected as the output variable to minimise. So that, for every day of the study period (2015 - 2018), the best value of Vcmax was found to achieve minimal difference between ftGPP and mGPP. The 'ideal' Vcmax is presented in Figure 2.9 (open circles).

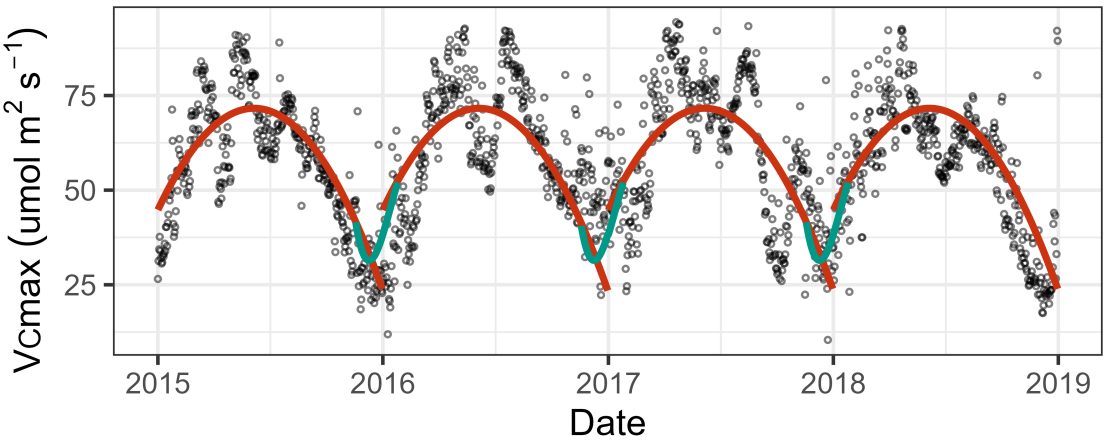

Figure 2.9: Development of Dynamic Vcmax (vmDy) time series. Circles are the initial daily optimised values (the 'ideal' Vcmax). The red line is a quadratic function through the yearly average and the green line is a polynomial fit between years. The final dataset is the red line except between 17th November and 25th January where the between years polynomial is used. For a more detailed description of the process see Section 2.6.2.1.

To decrease the specificity and increase the applicability of the 'ideal' Vcmax time series, for a more general application, it was averaged and smoothed. The four year 'ideal' Vcmax time series was was averaged to give 365 observations. Initial smoothing was conducted by fitting a quadratic function though the yearly average time series (red line in Figure 2.9). Then, to create a smooth transition between individual years, a 3rd order polynomial regression was fitted and inserted between the 17th November and 25th January (Figure 2.9, green lines).

2.6.2.2 VI-based Vcmax (vmCCI, vmGPP)

Determining a robust relationship between satellite based VI and Vcmax would allow spatially and temporally extensive Vcmax parameterisation using direct observations. This could reduce the reliance on static PFT values. These would vary seasonally and temporally with vegetation condition.

CCI and GPP_{VI} are based on MODIS band 11, centred at 531 nm (Chapter 5), which track conifer seasonal photosynthetic patterns. Daily time series of these (see section 2.4.5.1) were selected to build Vcmax VI time series (vmCCI and vmGPP). The VI time series were converted into µmol m^2 s^{-1} by min/ max normalisation using,

$$\text{vmCCI, vmGPP} = \frac{\text{vmMax} - \text{vmMin}}{\text{VI}_{\text{max}} - \text{VI}_{\text{min}}}(\text{VI} - \text{VI}_{\text{max}}) + \text{vmMax} \tag{2.41}$$

where VI_{min} and VI_{max} are the smallest and largest values of the VI 2015 -2018 time series and vmMin and vmMax are high and low Vcmax values; selected by varying them in iterative runs of SiBx (Figures 2.10 and 2.11).

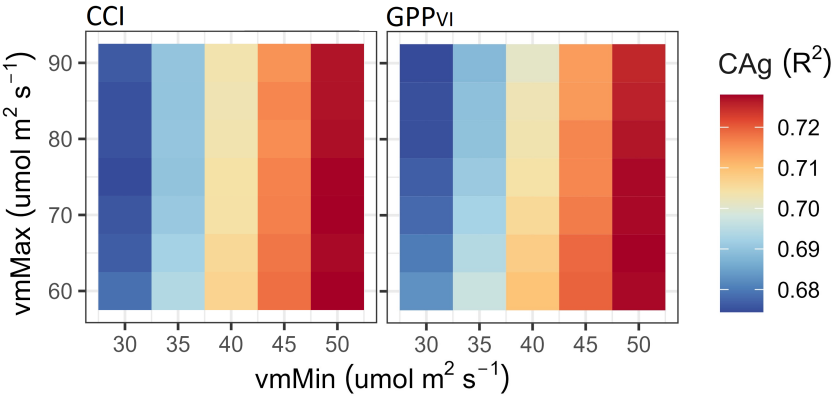

Figure 2.10: Performance results of varying vmMin and vmMax for VI transformation for CCI and GPP_{VI}. *CAg* (R^2) is the coefficient of determination (R^2) for the simple linear relationship between ftGPP and mGPP at the canopy scale. The SiBx model was run iteratively, with different values for minimum and maximum Vcmax (vmMin, vmMax), which were used to transform the VI time series to µmol $\text{m}^2\,\text{s}^{-1}$. For each combination of vmMin and vmMax, the SiBx model was run and mGPP was compared to ftGPP.

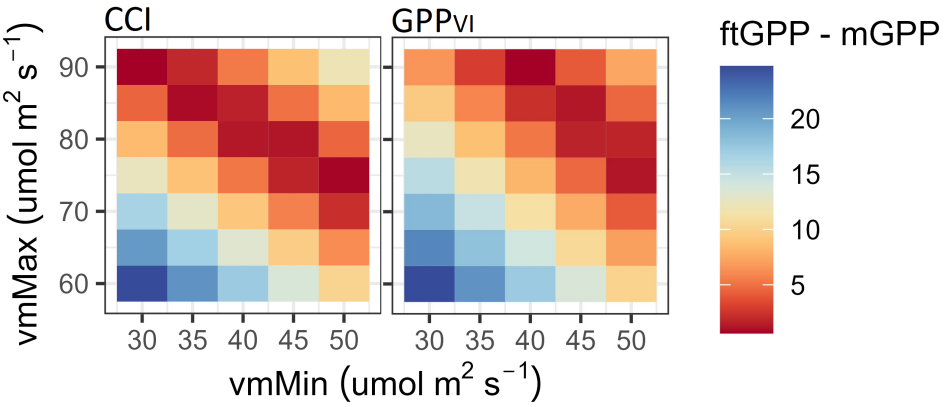

Figure 2.11: Performance results of varying vmMin and vmMax for VI transformation for CCI and GPP_{VI}. ftGPP - mGPP is the difference in estimated canopy GPP (tC ha^{-1} yr^{-1}) between ftGPP and mGPP (absolute values are used). The SiBx model was run iteratively, with different values for minimum and maximum Vcmax (vmMin, vmMax), which were used to transform the VI time series to µmol m^2 s^{-1}. For each combination of vmMin and vmMax, the SiBx model was run and mGPP was compared to ftGPP.

For both VI-based Vcmax time series, *CAg* R^2 increases with increasing vmMin

(Figure 2.10). Within each vmMin value, CAg R^2 is relatively consistent but tends to decrease with increasing vmMax (Figure 2.11). In terms of GPP estimation (ftGPP - mGPP) over the study period (2015 - 2018), for every vmMin there is a 'best' vmMax. This 'best' vmMax is higher for vmGPP compared to vmCCI. Based on these results therefore, the parameters selected differ for the vmCCI and vmGPP. They are presented in Table 2.4.

2.6.3 Summary

The three Vcmax presented here are developed to act as more biologically representative proxies than the traditional fixed value. The aim is to improve the parametrisation of SiB, and other processed-based models, by allowing Vcmax to vary in time (seasonally), and in the case of the VI-Vcmax, spatially within a PFT or biome. The developed VI are incorporated into SiBx in Chapter 6. VmDy is purely statistical, constructed from the smoothing and averaging of an optimised 'ideal' Vcmax time series which was created from optimising Vcmax for every day of the study period (see Section 2.6.2.1). vmCCI and VmGPP are derived from VI associated with reflectance at 531 nm, which has previously been linked to photosynthetic capacity. Due to the strong association with these VI and seasonal photosynthetic dynamics, developments in this field could improve satellite based canopy modelling.

Table 2.4: vmMin and vmMax values for use in equation 2.41 to transform VI to vmCCI and vmGPP (µmol m^2 s^{-1}). vmMin = 50 (µmol m^2 s^{-1}) produced the highest CAg R^2 for both VI whereas a slightly higher vmMax value produced a more accurate total GPP estimate in vmGPP.

VI Vcmax	vmMin (µmol m^2 s^{-1})	vmMax (µmol m^2 s^{-1})
vmCCI	50	75
vmGPP	50	80

2.7 Data validation

Prior to further analysis, where possible, some of the datasets outlined within this Chapter were validated against robust or established existing datasets. The ERA5 reanalysis datasets are evaluated against corresponding meteorological variables, recorded at the Harwood flux site by (Xenakis et al., 2021), and the newly developed VI_{16} time series are compared to the established MOD13 VI time series (VI_{MODIS}).

2.7.1 ERA5 validation

2.7.1.1 Rational

The ERA5 data source is considered an accurate, reliable source of a wide range of meteorological variables (IPCC, 2021)). However, the coarse spatial resolution (0.1 ° x 0.1°) means it may not capture local-scale phenomena. The accuracy of ERA5 is reliant on the quality and quantity of local observations so biases within the model can occur. Here, the specific ERA5 variables used in Chapters 5 and 6 are evaluated against flux tower (*ft*) data to evaluate the biases that may occur in the reanalysis data at the Harwood field site. ERA5 does not produce a relative humidity variable so this was calculated from dew point temperature and temperature at 2m (Zhang et al., 2021) using,

$$RH = 100 \times [\frac{e^{\frac{c_1 D_p}{c_2 D_p}}}{e^{\frac{c_1 T}{c_2 T}}}] \tag{2.42}$$

Where D_P is dewpoint temperature, T is temperature and c_1 and c_2 are constants (c_1: 17.625, c_2: 243.04) calculated by Alduchov and Eskridge (1996).

2.7.1.2 Results

Linear regressions were performed between the *ft* site data and ERA5 dataset for the six meteorological variables. The ERA5 data for air temperature, leaf temperature, atmospheric pressure and PAR all have high correlation ($R^2 > 0.88$) with the corresponding *ft* variable (Figure 2.13, Table 2.5). The two sources of PAR were proportional to each other (Figure 2.13). The ERA5 derived temperature data are on average higher than *ft* temperature, by 1.7℃ for air temperature and 2.2℃ for leaf temperature. ERA5 atmospheric pressure consistently overestimates relative to *ft* (on average 1.7% overestimation) (Figures 2.12 and 2.13). ERA5 soil moisture content correlates and tracks the seasonal dynamics of *ft* soil moisture content moderately well (Figure 2.12, Table 2.5). However, values are on average 8.6% higher, reaching a maximum difference of 14.1 %. The two relative humidity variables are moderately well correlated (Table 2.5). The relative humidity variable calculated from ERA5 systematically underestimates relative to the *ft* by 1% on average (Figure 2.12).

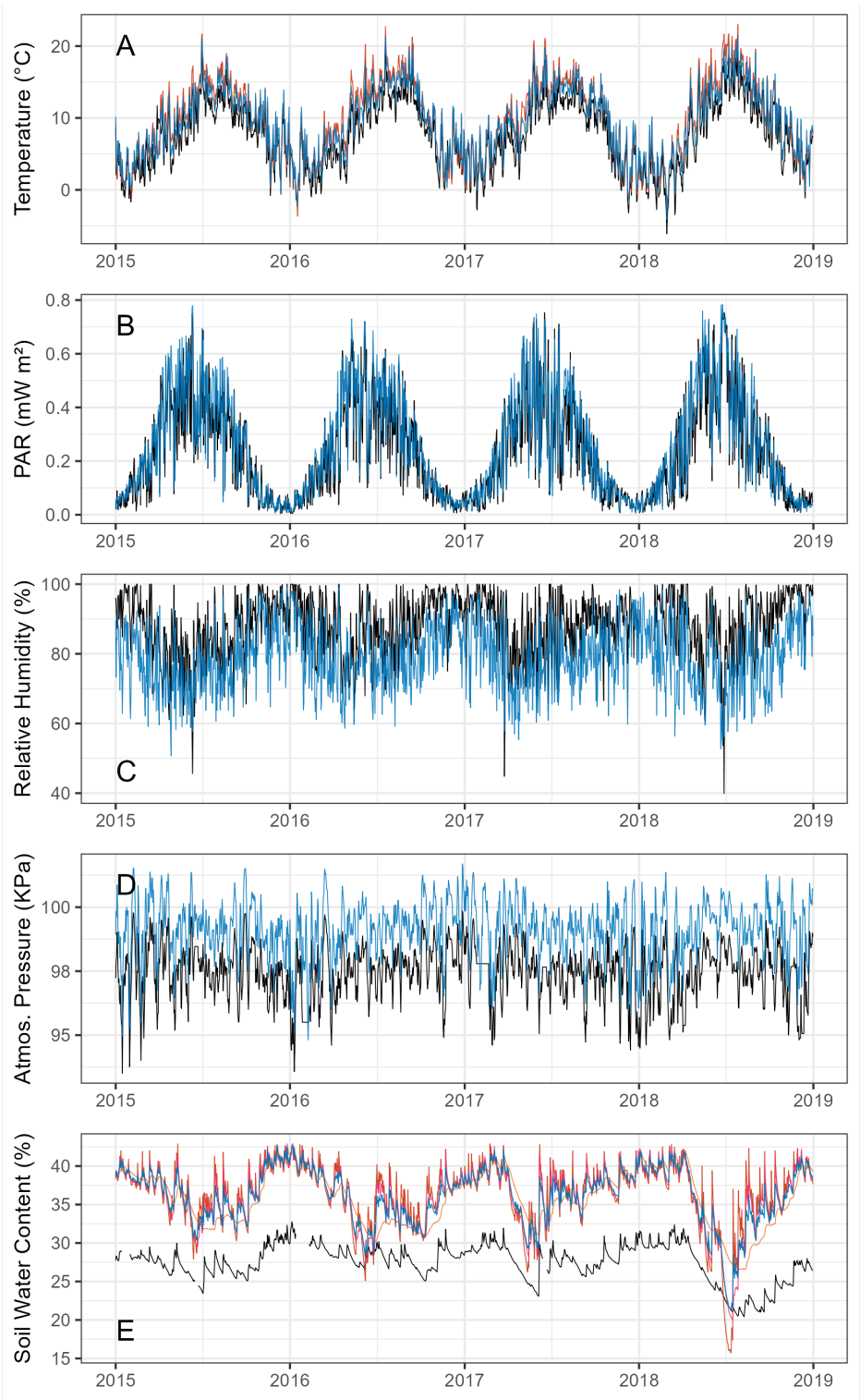

Figure 2.12: Meteorological variables for the Harwood study site from 2015 to 2018. Across all panels the black lines are daily average values of field measurements made at the Harwood field site by Xenakis et al. (2021) and coloured lines are ERA5 variables for the area overlapping the Harwood flux tower footprint. *Caption continued on the following page.*

Figure 2.12: *Continued caption from previous page.* (A) Mean daily temperature (°C). The red line is leaf temperature derived from ERA5: Temperature of the surface of the Earth (°C)(referred to as Leaf Temperature for use in the SiBx model). The blue line is air temperature derived from ERA5: Temperature of air at 2m above the surface of land (referred to as Air Temperature in the SiBx model). (B) Mean daily Photosynthetically Active Radiation (PAR, mW m^2). The blue line is derived from ERA5: Solar radiation reaching the surface of the Earth. (C) Mean daily relative humidity (%) (observations for January 2018 are removed due to anomalous values). The blue line is derived from ERA5: Dew point temperature and ERA5: Temperature of air at 2 m above the surface of land. (D) Mean daily atmospheric pressure (KPa). The blue line is derived from ERA5: Pressure of the atmosphere on the surface of land. (E) Mean daily soil water content (%). The black line is soil water at an average of 30 cm depth, see Xenakis et al. (2021). The red, pink and orange lines are ERA5: Volume of water in soil layer 1 (0 - 7 cm), 2 (7 -28 cm), and 3 (28-100 cm) respectively, and the blue line is the average of the three.

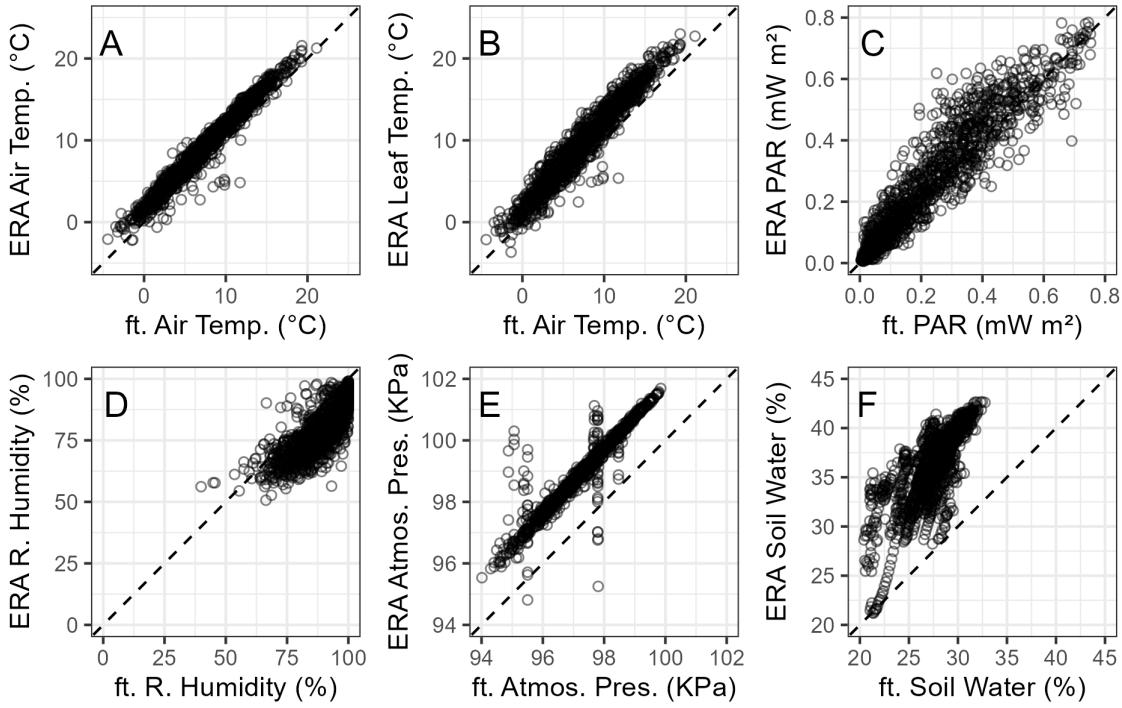

Figure 2.13: Comparison of meteorological variables measured at the Harwood flux tower site (ft, x axis) and derived from ERA5 datasets (ERA, y axis). All points are daily average values across 2015 to 2018. See Figure 2.12 for a detailed description of the variables. Note: For the temperature plots (A and B) two ERA5 variables (Air Temperature and Leaf Temperature) are compared to the same flux tower (ft) variable as this is the only available temperature record.

2.7.1.3 Summary

Relative to the *ft* data, the ERA5 variables varied in the strength of correlation. Both sources of PAR estimation correlated well. The temperature variables had a very tight relationship although ERA5 consistently produced marginally higher

Table 2.5: Regression analysis for ERA5 and Harwood flux tower meteorological variables. Met.Var are the meteorological variables, see Figure 2.12 for details.

Met.Var	F value	*df*	*p* value	R^2
Air Temp.	41187	1, 1459	<0.001	0.97
Leaf Temp.	23401	1, 1459	<0.001	0.94
PAR	11034	1, 1459	<0.001	0.88
R. Humidity	2160	1, 1459	<0.001	0.60
Atmos. Pres.	12713	1, 1459	<0.001	0.90
Soil Water	2077	1, 1459	<0.001	0.60

estimates than the *ft* recorded temperatures (Figure 2.12). Similarly, both pressure data sources correlated well but the ERA5 estimates were slightly higher. The ERA5 soil moisture tracks the overall seasonal patterns and anomalies reasonably well. Soil moisture reanalysis data is complex to measure and a lack of observations hampers the data reliability. However, recent developments in renalyses processing increases this reliability (Li et al., 2020).

The retrieval of relative humidity was similar in accuracy to the soil moisture. Relative humidity is not directly produced in the ERA5 product and involves a secondary calculation (Equation 2.42). Although relative humidity is routinely retrieved from the ERA5 datasets (Zhang et al., 2021), the secondary processing steps outside the overall ERA5 model likely reduces robustness, relative to the other retrieved variables presented here. In contrast to Zhang et al. (2021), who found that ERA5 overestimates relative humidity over China, in this analysis, ERA5 underestimated *ft* relative humidity.

In this section, the accuracy and biases of the ERA5 dataset are evaluated. In general the ERA5 data are reliable and fairly accurately replicate the *ft* meteorological data. However, by understanding where the error and biases lie, appropriate care can be taken and interpretations and analysis of data are better informed.

2.7.2 VI_{16} Validation

2.7.2.1 Rational

Section 2.4.5.2 outlines the methodology for development of a continuous (observation every 16 day) dataset (VI_{16}) consisting of five VI. The dataset used a CV-MYV method, described by Didan et al. (2015), and implemented for the established MOD13 VI product (referred to here as VI_{MODIS} (section 2.4.3.1)). VI_{16} was developed in this thesis to include a wider range of VI compared to VI_{MODIS} however, the two datasets both include NDVI and EVI. Therefore, it is possible to directly

compare the established (VI_{MODIS}) and new datasets (VI_{16}) against each other, and against the flux tower GPP (ftGPP) to understand any biases or anomalies within the data. To ensure a consistent sample size, for any given 16 day window, VI_{16} observations were removed if no VI_{MODIS} observation was available. This resulted in 379 observations. The ftGPP correlations were performed over 2015 - 2018 (flux tower data availability) leaving 72 observations per dataset.

2.7.2.2 Results

Regression analysis was conducted on VI_{MODIS} ($NDVI_{MODIS}$, EVI_{MODIS}), VI_{16} ($NDVI_{16}$, EVI_{16}) and ftGPP to assess how the new datasets relate to the established MODIS product and site productivity. A highly significant correlation between the VI_{MODIS} and the VI_{16} were found for both NDVI and EVI (NDVI: $y = 0.5437 + 0.00002x$, F = 22.94, $d.f$ = 1,377, p = <0.001, EVI: $y = 0.1002 + 0.83999x$, F = 222, $d.f$ = 1, 377, $p = < 0.001$). The $NDVI_{MODIS}$ values were consistently higher than $NDVI_{16}$ but had a similar regression slope with ftGPP(Figure 2.14). EVI_{MODIS} and EVI_{16} had a tighter relationship although EVI_{16} values are generally lower than the MODIS data (Figure 2.14). Regression analysis between ftGPP observations and VI values revealed a larger coefficient of determination (R^2) for both the VI_{16} compared to VI_{MODIS} (Table 2.6). The R^2 for $NDVI_{16}$ was 0.28 compared to 0.13 for $NDVI_{MODIS}$. The EVI datasets had higher R^2 values than NDVI and the EVI_{16} R^2 was 0.41 and EVI_{MODIS} was 0.24 (Table 2.6).

Table 2.6: Regression analysis for VI_{MODIS} (NDVI, EVI) and VI_{16} (NDVI, EVI) with flux tower GPP (ftGPP). Simple linear recessions were performed between each time series and ftGPP.

VI	Time Series	F value	*df*	*p* value	R^2
NDVI	VI_{16}	28.34	1 70	0.000	0.28
NDVI	VI_{MODIS}	11.70	1 70	0.001	0.13
EVI	VI_{16}	50.48	1 70	0.000	0.41
EVI	VI_{MODIS}	23.65	1 70	0.000	0.24

2.7.2.3 Summary

The new dataset (VI_{16}) produces consistently lower NDVI and higher EVI values relative to the MODIS product. This likely predominantly arises from differences in the processing of the reflectance data, prior to the CV-MVC. Both datasets originate from the MODIS Level-1B calibrated radiances (Didan et al., 2015; Vermote et al., 2015; Lyapustin et al., 2018). However, VI_{16} undergoes the MAIAC algorithm (Section 2.4.3.2), which instead of swath-based processing used in VI_{MODIS}, uses

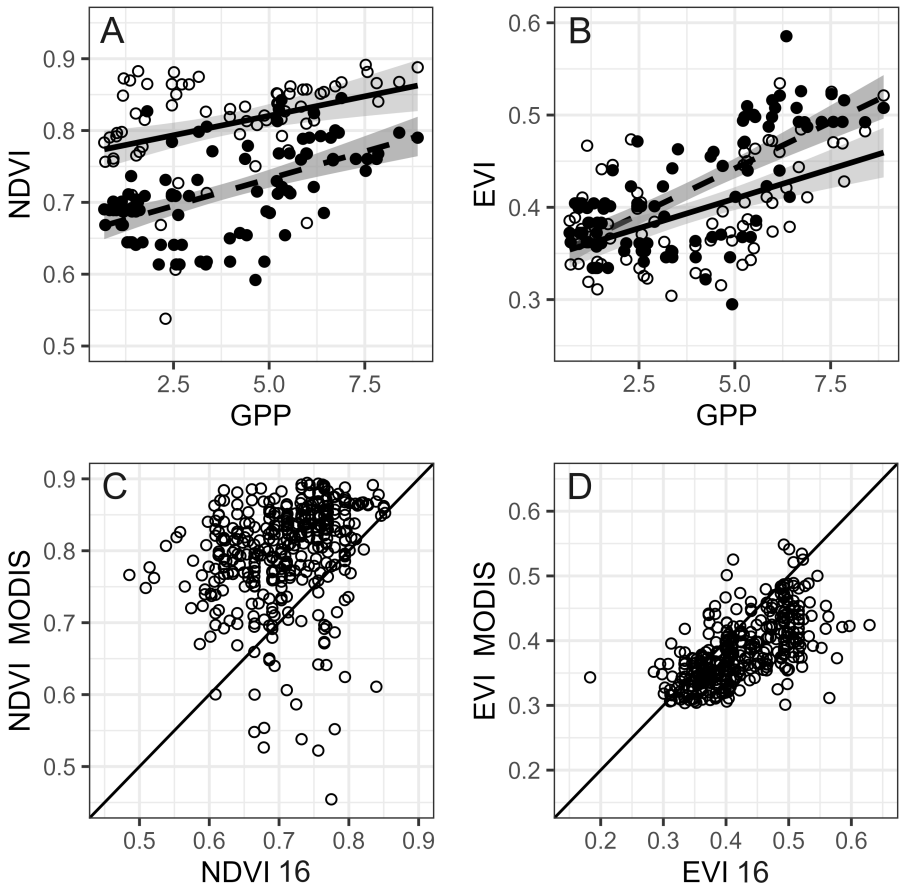

Figure 2.14: Regression analysis for VI_{MODIS} and VI_{16}. A: $NDVI_{16}$ (Dashed line solid circles) and $NDVI_{MODIS}$ (solid line open circles) correlations with ftGPP. B: EVI_{16} (Dashed line solid circles) and EVI_{MODIS} (solid line open circles) correlations with ftGPP. Bottom row - VI_{MODIS} and VI_{16} correlations. C: $NDVI_{MODIS}$ and $NDVI_{16}$. D: EVI_{MODIS} and EVI_{16}. The solid line in the bottom row is the 1:1 line.

a 16 day sliding window technique, combined with a physical-atmosphere-surface model. This aids in the separation of atmospheric and surface effects (Lyapustin et al., 2018). This procedure allows MAIAC data to reveal more realistic greenness reflectances (Wu, Kobayashi, et al., 2018; Smith et al., 2019; Zeng et al., 2022). The VI_{16} time series are better correlated to ftGPP, suggesting the methodological procedure to develop the VI_{16} produces a data set of a quality similar to, or better than, the established MODIS product. Although comparisons are only possible for NDVI and EVI, it is likely that the quality of observations is similar for the other three VI (CCI, NIRv, GPP_{VI}) due to acquisition of all spectral bands occurring simultaneously by the satellite.

2.8 Chapter summary

Chapter 2 has outlined the data, methodologies, study locations, developed and evaluated new analysis techniques and validated some data sources that are used the proceeding research chapters. Statistics and some specific methods are outlined within the corresponding chapter.

Chapter 3

Evaluating the drought responses of Sitka spruce (*Picea sitchensis*) clones using Vegetation Indices (VI). Are genetic differences detectable with VI?

The work in this chapter aims to use Vegetation Indices (VI) to evaluate the drought responses of Sitka spruce (*Picea sitchensis* (Bong.) (Carr.). This is done via an artificial drought experiment. The materials and methods of this experiment are outlined in detail in Section 2.2.

3.1 Introduction

Sitka spruce can be susceptible to drought stress and during two major drought events in the UK this century (in 2003 and 2018) increased damage, mortality, and decreased productivity have been recorded (Green et al., 2008; Green & Ray, 2009; Xenakis et al., 2021). However, due to its current prominence and high productivity, it is likely to be favoured for forestry across much of the UK in the near future (Davies et al., 2020). Its appropriateness across the UK therefore may decrease as drought risk increases.

Drought response within species is important in understanding their suitability to a changing climate. The Sitka spruce breeding programme, established in 1963 has successfully bred and proliferated trees with high timber quality (Lee, 1999). Screening or selecting for more drought resistance strains, could be another useful

tool, in moving towards a more drought resilient UK forestry sector (Schiop et al., 2017).

Remote sensing provides potential to identify more drought tolerant individuals or genotypes by linking remotely sensed variables with stress response phenotypes (Plesa et al., 2019). This study aims to characterise drought stress response in Sitka spruce, using remotely sensed hyperspectral reflectance measurements, and to identify intraspecific reflectance differences, between clonal groups.

VI are mathematical combinations of wavelengths associated with specific plant biophysical properties. Here, they are characterised into greenness indices (VIg), which are historically the most widely used indices, and are based on the assumption that healthy plants are greener, due to the reflectance properties of chlorophyll; pigment indices (VIp) sensitive to other pigments, such as xanthophylls, anthocyanins and carotenoids which are often expressed in stress responses to dissipate excess light energy (Peguero-Pina et al., 2008); and finally, water content indices (VIw) which use water absorption peaks in spectra to measure water within a needle.

This study exposed clonal bank Sitka spruce scions to increasing levels of drought over eight weeks (from 27th June 2022 until 24th August 2022) and measured the spectral response of needles. VI that are sensitive to drought in Sitka spruce are evaluated for further research. Different clonal groups were used to evaluate if genetic differences in Sitka spruce result in differing stress responses and if these are detectable with remotely sensed VI.

3.2 Research aims

Using an experimental drought set up, outlined in Section 2.2, the specific aims were to

- Measure the physiological changes from the onset of drought, compared to control
- Determine the best VIs to monitor this process
- Determine genotype differences
- Early detect clear differences between stressed and control individuals

3.3 Chapter methods

3.3.1 Soil Moisture

After 10 days, water content had dropped to 25% Field Capacity (FC) in the droughted plants (Figure 3.1). Due to this fast decline, drought plants were partially watered at specific times during the experiment, to prolong the early stages of drought stress, and avoid rapid drying of soil, which is unlikely to occur in trees in the UK. Watering pots to the desired FC based on a pot-specific water deficit (Section 2.2.3.3 Equation 2.6 to 2.8 (p.45)), allowed re-watering to be accurate and maintain a similar water content in all pots under the same watering regime, throughout the experiment. Pots in the control group twice reached soil moisture below 75% FC due to no watering over weekends. However, this remains sufficiently high to avoid any significant water limitation.

3.3.2 Polytunnel conditions

Plants were kept in a polytunnel to avoid rainfall. Doors were left open and automatic fans operated to increase airflow however, temperature and humidity levels within the polytunnel were still different to the outside environment. In general, the polytunnel was hotter and more humid than outside. This resulted in temperatures reaching 35°C during two heatwaves potentially causing heat stress to plants (Figure 3.2). However, conditions largely remained within a range likely to be experienced across much of the UK.

3.3.3 Statistical analysis

3.3.3.1 Maximal photochemical efficiency (*Fv/Fm*)

To analyse the effects of drought on Fv/Fm, a Wilcoxon rank sum test was used to identify differences in the means of droughted and well-watered plants. Fluorescence measurements rarely have Guassian distribution so nonparametric tests are used (Lazár et al., 2006). A test was performed for each clonal group on each measurement day.

3.3.3.2 VI model building

To analyse the change in VI over time, mixed effect models were formulated. Models were built for each VI using the lmer package in R (Bates et al., 2015). Each individual plant was treated as a random effect. Time in days after drought treatment initiation (Time), watering regime (Treatment) and clonal group (Clone) were

treated as main effects. Interactive effects of these main variables, including a three-way interaction, were also tested. Where interactions did not show a significant effect ($p > 0.05$, p values calculated by Satterthwaite's method (package lmerTest, Kuznetsova et al., 2017)), and the removal of them improved the model (evaluated by AIC to avoid overfitting), they were excluded from analysis. To account for non-linearity in biophysical response, polynomial regressions ($df = 3$) were fitted when this improved the AIC score relative to a linear trend. Model residuals were tested for normality and autocorrelation.

3.3.3.3 Estimated Marginal means (EMM)

To analyse the effect of drought compared to the control group over time, estimated marginal means (EMM) were calculated. EMM can control for seasonal effects and other variability in the model by adjusting the means of other effects to 0. The EMM could also be used to compare different VI. Where a significant effect of drought over time (Time x Treatment or Time x Treatment x Clone) was found for a specific VI, EMM were performed on each day of the experiment. The t.ratio of EMM gave a statistical measure of difference between control and drought groups, on a relative scale, which was comparable between VI. All analysis was performed in R and R studio (RStudio Team, 2020).

3.4 Results

3.4.1 *Fv/Fm*

In all clonal groups, no differences between drought and control Fv/Fm were detected in the first two weeks (Figure 3.3). By day 56, droughted plants all had significantly lower Fv/Fm than the control plants. The well-watered clones had consistently high Fv/Fm values, only dropping below 0.79 twice and never below 0.77 in any of the groups. In clones C1, C2 and C3, no decreases in Fv/Fm were detected until the final weeks (days 56, 49 and 43 respectively), where Fv/Fm continued to decrease until the end of the experiment. In the clones C4, C5 and C6 which were exposed to drought, low values of Fv/Fm were recorded at day 30, but had all recovered to the control level by the following week (day 38). Clone C6 had low drought values from the third measurement week but recovered during days 38 and 43. Fv/Fm then dropped to below control levels until the end of the experiment. Clones C2 and C4 had very steep decreases in some individual plants, seen by low average values, whereas C1 has the smallest decrease among clones.

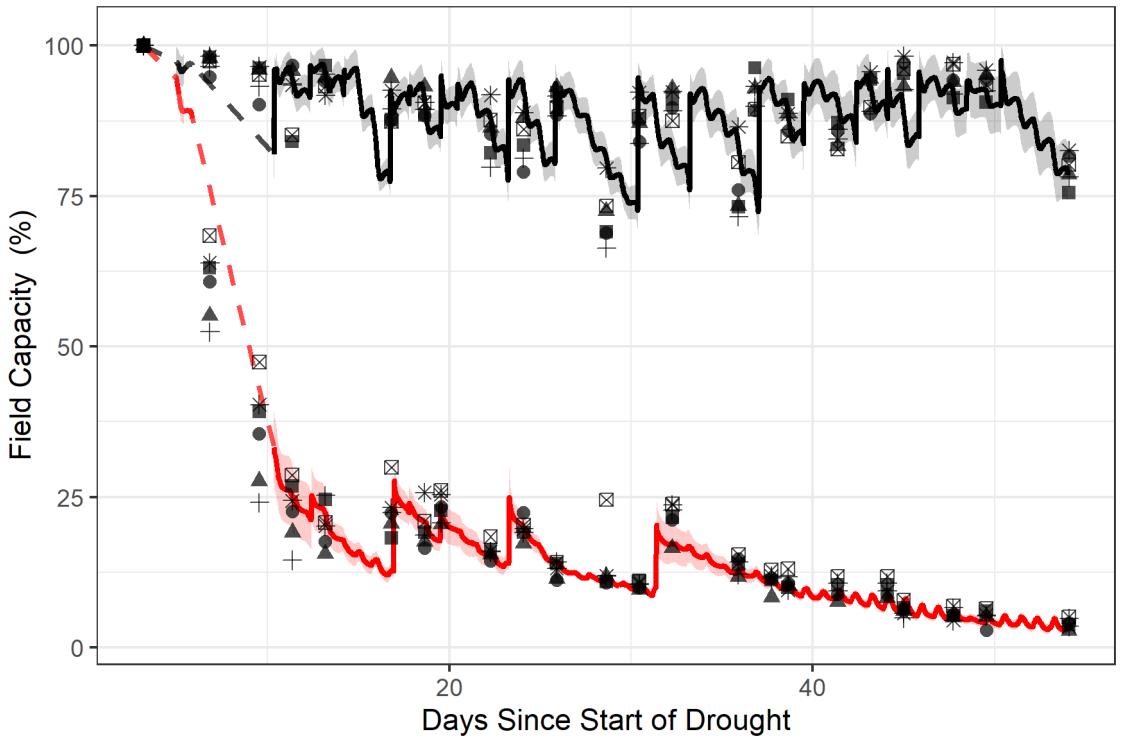

Figure 3.1: Soil moisture as a percentage of Field Capacity (FC). Lines are continuous (30-minute intervals) measurements taken with a data logger. Continuous measurements are averaged (n = 6) by watering regime (± SE). Points are averages (n = 5), for each clonal group for both watering regimes, taken manually with a handheld soil moisture probe. Note: missing continuous data due to file corruption before 29th June and from 30th June to 5th July represented by dashed line. No watering occurred during these missing periods.

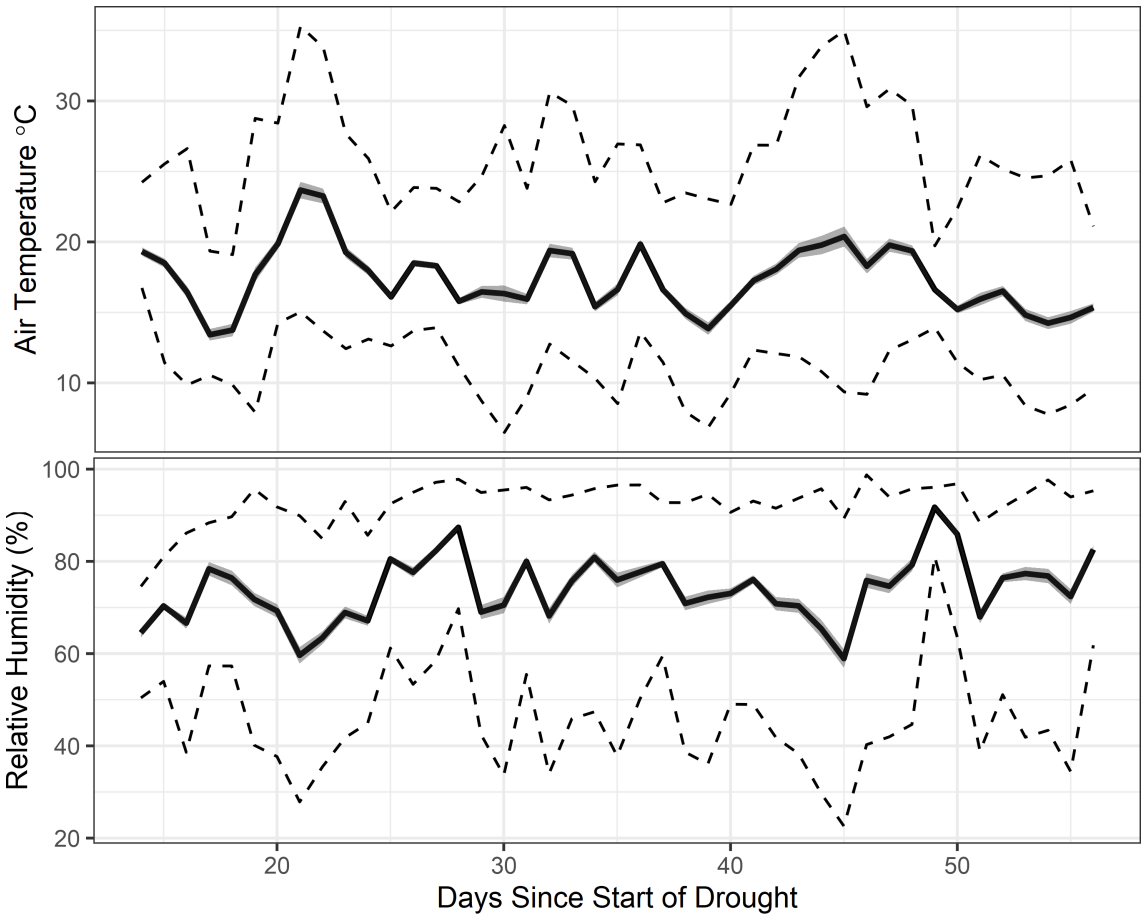

Figure 3.2: Polytunnel conditions at 2 m above canopy. Solid lines are daily averages (± SE) and dashed lines are high and low extreme daily values. Top panel: Air temperature (°C), Bottom panel: Relative humidity (%). No data is available before 11th July (day 14 of experiment) due to low accuracy of initial measurements.

Table 3.1: Results from the mixed effects models built for each Vegetation Index (VI). Results presented are p values (in bold, *ns*: > 0.05, *: $p < 0.05$, **: $p < 0.01$ and ***: $p < 0.001$) when lower than 0.1 and associated F values. Where interactions did not show a significant effect ($p > 0.05$ and the removal of them improved the model, they were excluded from analysis

	Time	Treat.	Clone	Time: Treat.	Time: Clone	3-way	R^2 Cond.	R^2 Marg.
VIg								
CCI	**<0.001*** **	**0.022***	**<0.001*** **	**<0.001*** **	-	-	**0.533**	**0.336**
	48.353	5.5674	7.7253	9.6566				
CIgr	**0.01***	*ns*	**<0.001*** **	**<0.001*** **	-	-	**0.838**	**0.329**
	3.7363	0.1337	7.1152	6.3271				
CIre	**<0.001*** **	**0.091**	**<0.001*** **	**<0.001*** **	-	-	**0.860**	**0.318**
	36.5481	2.9621	5.4200	1.0866				
NDVI	**<0.001*** **	*ns*	**<0.001*** **	-	-	-	**0.444**	**0.290**
	18.7147	1.4017	12.4925					
NRre	**<0.001*** **	*ns*	**<0.001*** **	**<0.001*** **	-	-	**0.875**	**0.319**
	38.3138	2.8286	5.0732	15.2615				
SR	**<0.001*** **	**0.082**	**<0.001*** **	-	-	-	**0.371**	**0.253**
	17.4382	3.1459	11.5687					
VIp								
ARI	**<0.001*** **	*ns*	*ns*	**0.007****	*ns*	**0.006****	**0.622**	**0.446**
	85.8942	0.8679	0.4446	7.2431	0.7437	3.3048		
ARI2	**<0.001*** **	*ns*	*ns*	**0.005****	*ns*	**0.004****	**0.638**	**0.471**
	93.2767	0.7914	0.4548	7.9001	0.9086	3.6006		
CRI1	**0.001****	**<0.001*** **	**<0.001*** **	**0.0267***	-	-	**0.382**	**0.297**
	5.4867	15.7597	17.4781	3.0884				
CRI2	**0.001****	**<0.001*** **	**<0.001*** **	**0.064**	-	-	**0.391**	**0.303**
	5.4695	16.4968	17.7988	2.4410				
PRI	**0.003****	*ns*	**0.061**	**0.036***	*ns*	**0.012***	**0.704**	**0.401**
	8.8385	0.1971	2.2167	4.4166	0.2659	2.9744		
VIw								
MSI	**<0.001*** **	*ns*	**<0.001*** **	**0.026***	*ns*	**<0.001*** **	**0.634**	**0.426**
	5.8121	1.4719	12.0397	3.1288	0.5891	3.4200		
NDWI	*ns*	*ns*	**<0.001*** **	**0.006****	*ns*	**<0.001*** **	**0.593**	**0.426**
	1.7193	1.7703	10.7734	4.2621	0.7005	2.9441		
NDWI2	**0.004****	*ns*	**<0.001*** **	**0.016***	*ns*	**<0.001*** **	**0.641**	**0.496**
	4.5845	0.8937	14.8006	3.4919	0.5987	3.2297		
SRWI	*ns*	*ns*	**<0.001*** **	**0.006****	*ns*	**<0.001*** **	**0.590**	**0.421**
	1.7359	1.5678	10.8518	4.2664	0.7134	2.8821		
WI	*ns*	**0.084**	**<0.001*** **	**0.087**	*ns*	**0.002****	**0.544**	**0.411**
	1.0869	3.0871	16.6311	2.2045	0.7338	2.4364		
WI/NDVI	**<0.001*** **	*ns*	**<0.001*** **	**<0.001*** **	-	-	**0.505**	**0.321**
	16.8131	0.7920	12.7523	5.8726				

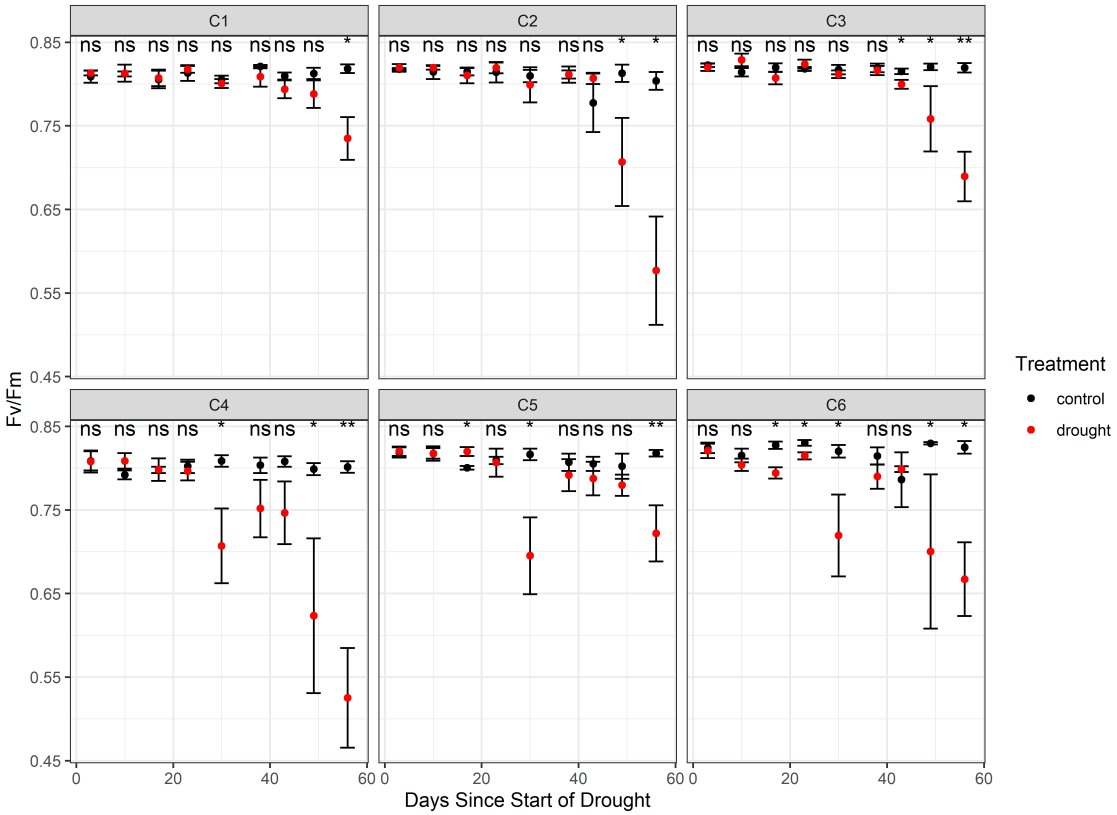

Figure 3.3: Maximum photochemical quantum yield of photosystem II (Fv/Fm) over time in six clones with different watering regimes (black: Control, no water limitation, red: Drought, progressively increasing drought stress). Points are median values (± SE). Difference between Fv/Fv for the watering treatments for each clone and each time point was analysed using Wilcoxon rank sum test (ns: not significant, *: $p < 0.05$, and ** $p < 0.01$).

3.4.2 Greenness Indices (VIg)

All VIg changed over time during the experimental period without the influence of drought (Table 3.1), this effect was weakest in CIgr but was characterised by a slight downwards trend (Figure 3.4). There were strong clonal effects for all VIg irrespective of drought, where VI values were consistently higher or lower, depending on the clone (Figure 3.4). The drought duration (Time x Treatment) had a strong effect on CCI, CIgr, CIre and NDVIre and no effect on NDVI and SR. Despite the strong influence of drought duration on CIgr, which caused an increase towards the middle of the drought period, and subsequent fall as the drought progressed, the modelled t.ratio values never crossed the p value thresholds (Figure 3.5). This is in contrast to other VIg, where the difference progressively became larger as the drought continued (Figure 3.5). The difference in CCI slightly decreased towards the end of the experiment. CCI was the first VIg to cross the $p = 0.01$ line just before day 30 while CIre and NDVIre crossed the $p = 0.01$ line just before day 50.

The models for CIgr, CIre and NDVIre all had a R^2 (cond.) of more than 0.8. The models for NDVI and SR had low R^2 (cond.) (0.44 and 0.37). There was no differing drought response between clones (Time x Treatment x Clone) for any of the VIg.

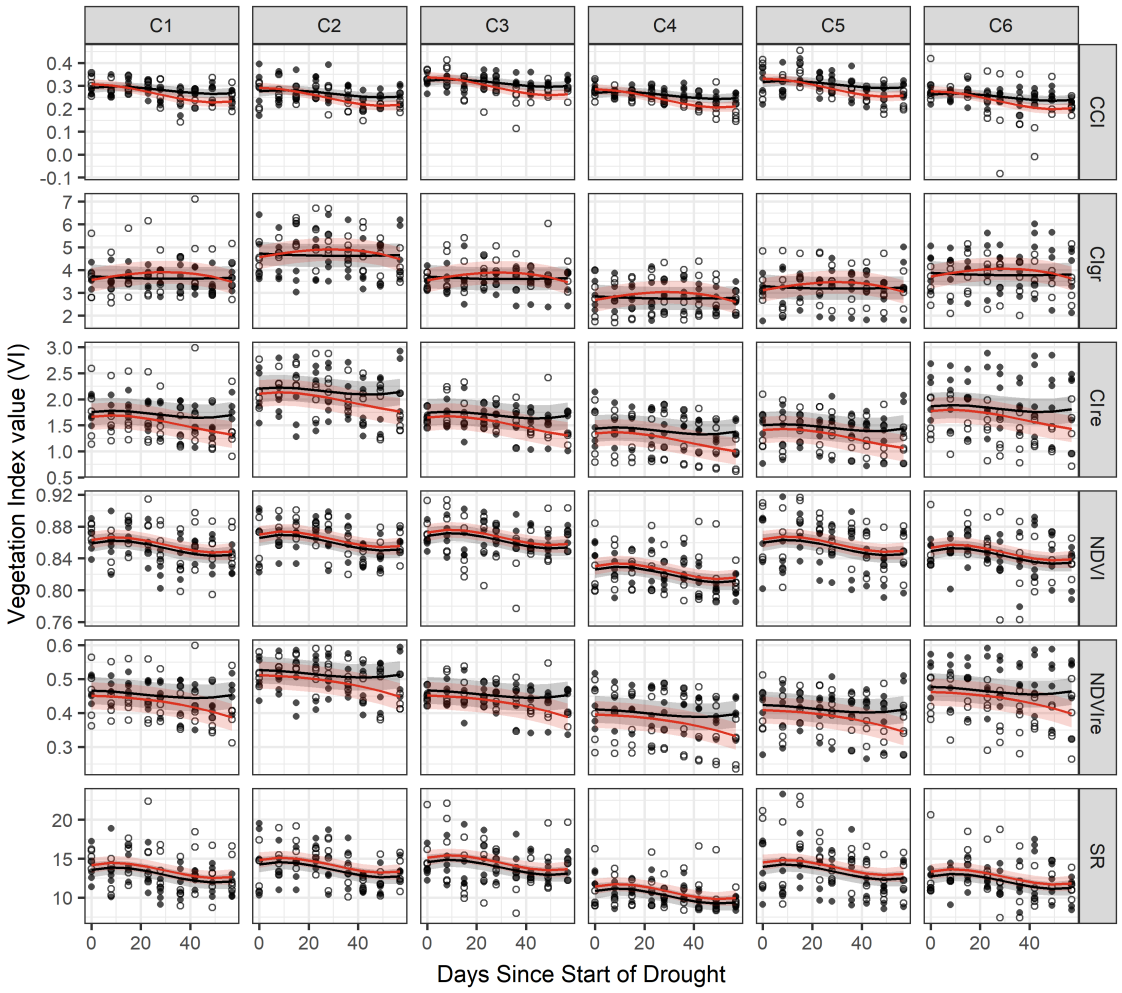

Figure 3.4: Greenness indices (VIg) for six Sitka spruce clones under drought or control conditions. Points are VI values and lines (± SE) are modelled trends. Black lines and filled points are the control treatment plants. Red lines and unfilled points are drought treatment plants. For full VI names, formula and references see Table 2.1 (p.43).

.

3.4.3 Pigment Indices (VIp)

An effect over time was detected for all VIp (Table 3.1) although the slope of the response varied. The two carotenoid-based indices (CRI1 and CRI2), exhibited a shallow non-linear downwards trend, which accelerated towards the end of the experiment (Figure 3.6). A main effect for treatment was found in these carotenoid indices, suggesting differences in the treatment groups, regardless of watering regime. A t-test between drought and control groups was conducted, for measurements made

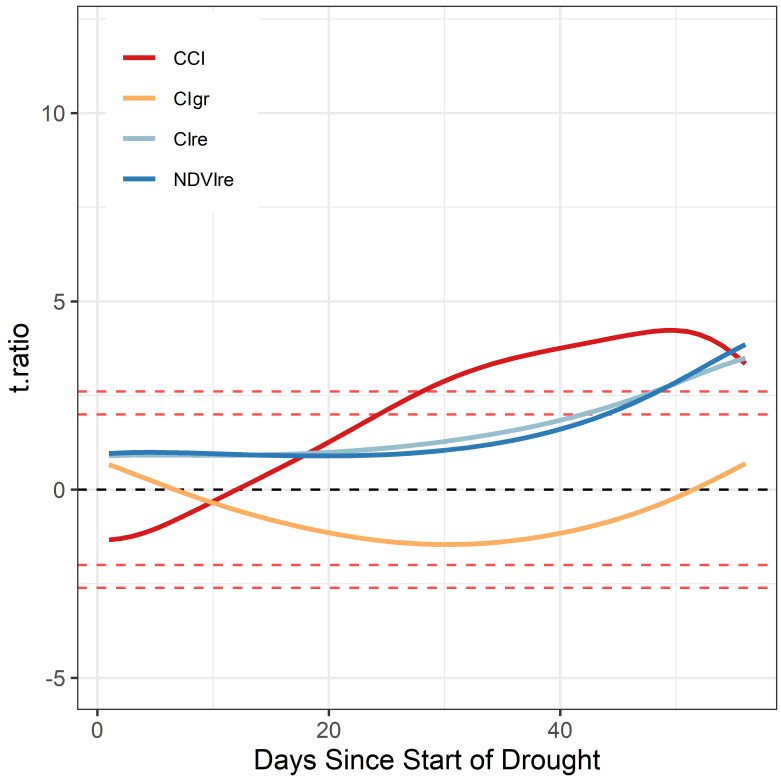

Figure 3.5: t.ratio of estimated marginal means (EMM) for drought effect of greenness indices (VIg). These EMM were calculated when the two way interaction of Time x Treatment was detected. Black dashed line is 0 where the drought and control group are equal. VI are normalised so t.ratio > 0 is the expected stress response. Red dashed lines are estimated p value levels ($p = 0.05$ and 0.01), calculated from the robust relationship between p values and t.ratio produced by EMM. For full VI names, formula and references see Table 2.1 (p.43). For full results for the EMM contrasts see Appendix B, Table B.1 (p.184).

at the start of the experiment, for each clone group and the combined clonal groups, to evaluate pre-treatment differences. However, no significant relationships were found. The strength of Time x Treatment was weak in carotenoid-based indices (CRI1 and CRI2). The p values for the two indices fell either side of $p = 0.05$ (CRI1: $p = 0.027$, CRI2: $p = 0.064$). The Time x Treatment term was included in the CRI2 model as it improved model fit and was only marginally above the significance ($p < 0.05$) threshold however, the VI was not included in the EMM analysis due to the relatively weak relationship. With the exception of SR, these two VI also had the lowest R^2 (cond.) of all other VI tested. The t.ratio of CRI1 gradually increased through the drought and crossed the $p = 0.01$ threshold around day 48 (Figure 3.7). The VIp ARI, ARI2 and PRI had similar responses and were the only VI tested where a linear model was the best fit. This linear trend resulted in progressively greater difference between the control and drought treatment as the drought continued (Figure 3.7). By day 20, all VIp except CRI1 had crossed the

$p = 0.01$ line where ARI, ARI2 and PRI remained above for the duration of the experiment. CRI1 dropped below the line around day 40. The drought effect was different between clones in ARI, ARI2 and PRI, indicated by a significant three-way interaction. The R^2 (cond.) values for these VI was above 0.6 and within a 0.1 range.

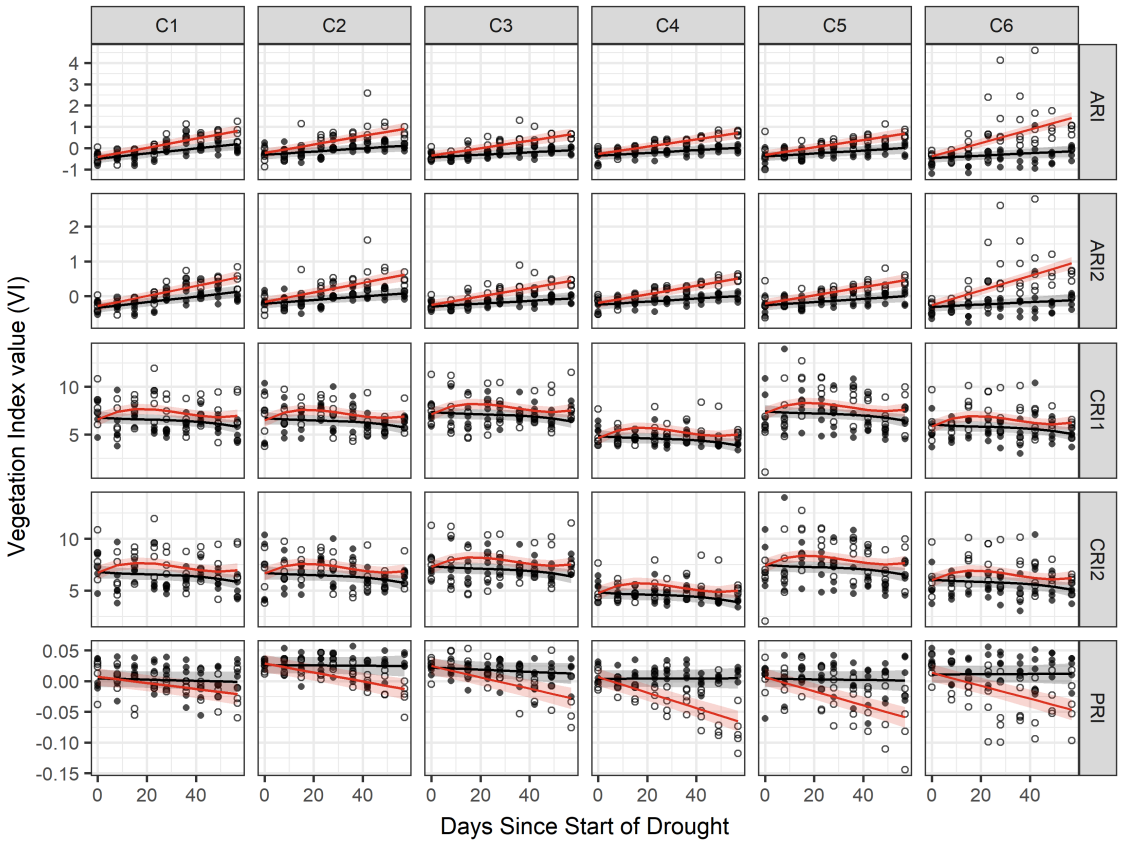

Figure 3.6: Pigment indices (VIp) for six Sitka spruce clones under drought or control conditions. Points are VI values and lines (± SE) are modelled trends. Black lines and filled points are the control treatment plants. Red lines and unfilled points are drought treatment plants. For full VI names, formula and references see Table 2.1 (p.43).

3.4.4 Water Indices (VIw)

NDWI, SRWI and WI were the only VI not influenced by the Time main effect (Table 3.1). All the VIw had significant clone main effects and, with the exception of WI, all had a significant effect of Time x Treatment. The three-way interaction, with the exception of WI/NDVI, was significant across all VIw. Clone C2 had the most drastic change in VIw towards the end of the drought (Figure 3.8). The shape of the curve (although in the opposite direction for MSI), varied between clones, but was conserved across the VIw. All VIw crossed the $p = 0.01$ line within 10 days of

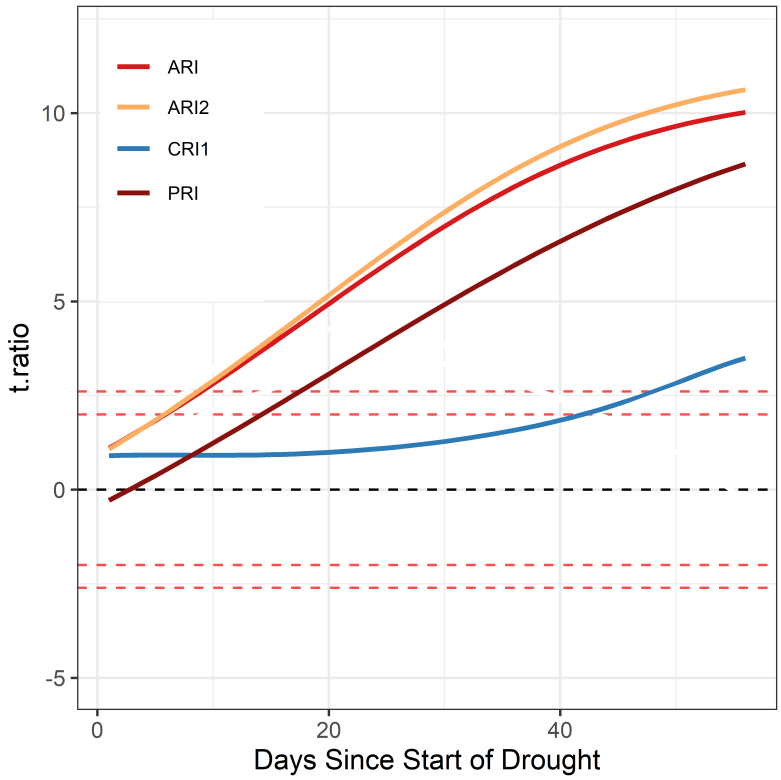

Figure 3.7: t.ratio of estimated marginal means (EMM) for drought effect of pigment indices (VIp). These EMM were calculated when the two way interaction of Time and Treatment was detected. Black line is 0 line where drought and control group are equal. VI are normalised so that t.ratio > 0 is the expected stress response. Red lines are estimated p value levels ($p = 0.05$ and 0.01), calculated from the robust relationship between p values and t.ratio produced by EMM. For full VI names, formula and references see Table 2.1 (p.43). For full results for the EMM contrasts see Appendix B, Table B.1 (p.184).

each other between days 45 to 55 (Figure 3.9). The initial decrease in t.ratio varied in intensity between VIw. This was most pronounced in SRWI where it dropped below the $p = 0.01$ line and least pronounced in WI. NDWI2 had the largest R^2 (cond.) (0.64) and all VIw had a R^2 (cond.) of at least 0.5.

3.4.5 Differing drought responses between clones

When three-way interactions were modelled, estimated marginal means (EMM) plots were used to evaluate differing responses between clones (Figure 3.10). Clone C6 exhibited the strongest anthocyanin response under drought, where ARI and ARI2 crossed the $p = 0.01$ line around day 5, and remained much higher than the other clones for the remainder of the drought. Anthocyanin responses for the other clones were similar, all crossing the $p = 0.01$ line between days 10 and 20 and peaking around t.ratio = 3. PRI in C1 never crossed either of the p value lines. PRI crossed

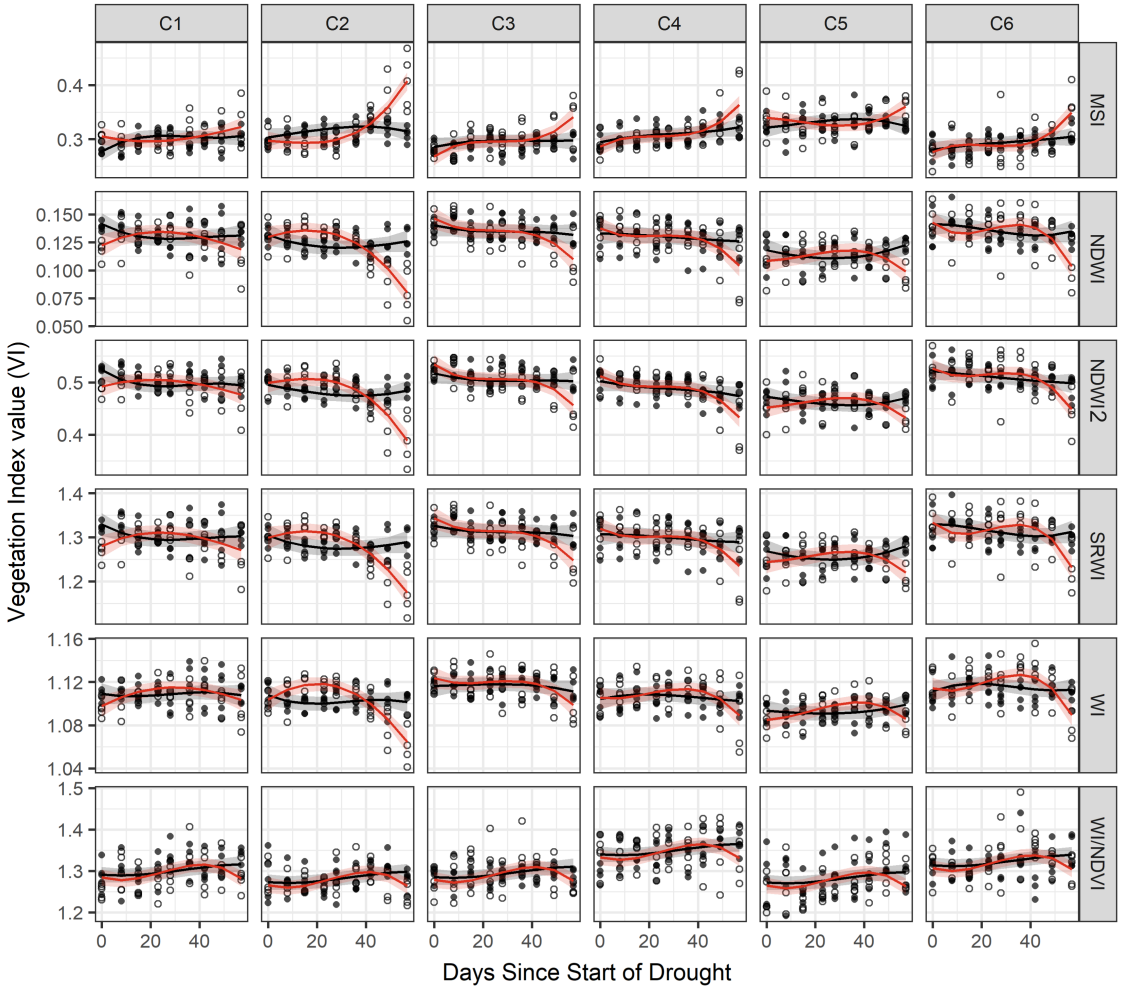

Figure 3.8: Water indices (VIw) for six Sitka spruce clones under drought or control conditions. Points are VI values and lines (± SE) are modelled trends. Black lines and filled points are the control treatment plants. Red lines and unfilled points are drought treatment plants. For full VI names, formula and references see Table 2.1 (p.43).

$p = 0.01$ around day 30 for C2 and C3 and between day 10 and 20 for clones C4, C5 and C6. The response in the VIw was characterised by an initial drop or shallow increase, then slight drop, followed by a rapid rise as the drought progressed. The differences between drought and control were most extreme in C2 and least in C1. In C1, except for around day 0 the VIw never crossed the $p = 0.01$ line. The $p = 0.01$ was crossed for all other VIw; around day 45 in C2 and day 50 in C3, C4, C5 and C6. The drop in VIw during the final few days of the drought, most pronounced in C2, is likely due to a decrease in statistical power, rather than a treatment effect as the variance of data becomes larger.

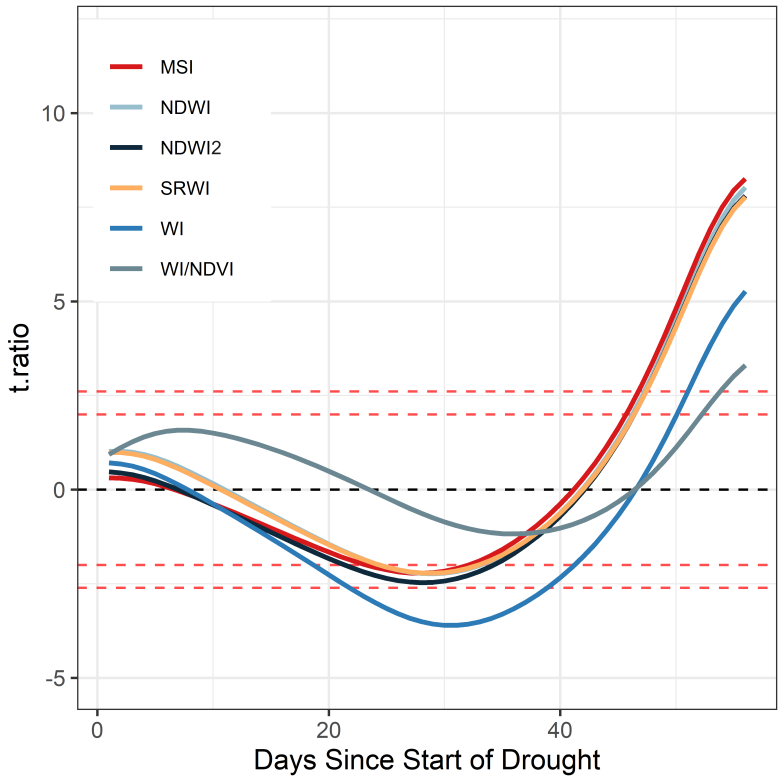

Figure 3.9: t.ratio of estimated marginal means (EMM) for drought effect of water indices (VIw). These EMM were calculated when the two way interaction of Time and Treatment was detected. Black dashed line is 0 line where drought and control group are equal. VI are normalised so t.ratio > 0 is the expected stress response. Red dashed lines are estimated p value levels ($p = 0.05$ and 0.01), calculated from the robust relationship between p values and t.ratio produced by EMM. For full VI names, formula and references see Table 2.1 (p.43). For full results for the EMM contrasts see Appendix B, Table B.1 (p.184).

3.5 Discussion

The combination of multiple VI calculated from hyperspectral reflectance data, gives a picture of drought response in Sitka spruce, over an eight week progressively intensifying drought. By using EMM to statistically account for seasonality, control and drought groups were compared. Due to their major influence on both reflectance and biophysical processes, foliar pigments are the bases for the majority of physically based VI. The characteristic absorption signature of water also links VIw to plant water dynamics. The results presented here show how drought alters pigment concentrations and water content, which affect needle reflectance (Zhang & Zhou, 2019). In general, VI associated with chlorophyll (VIg) decrease or are unchanged under drought, and VIp suggests higher expression of carotenoids and anthocyanins. However, these changes are influenced by multiple factors and are not always linear over time.

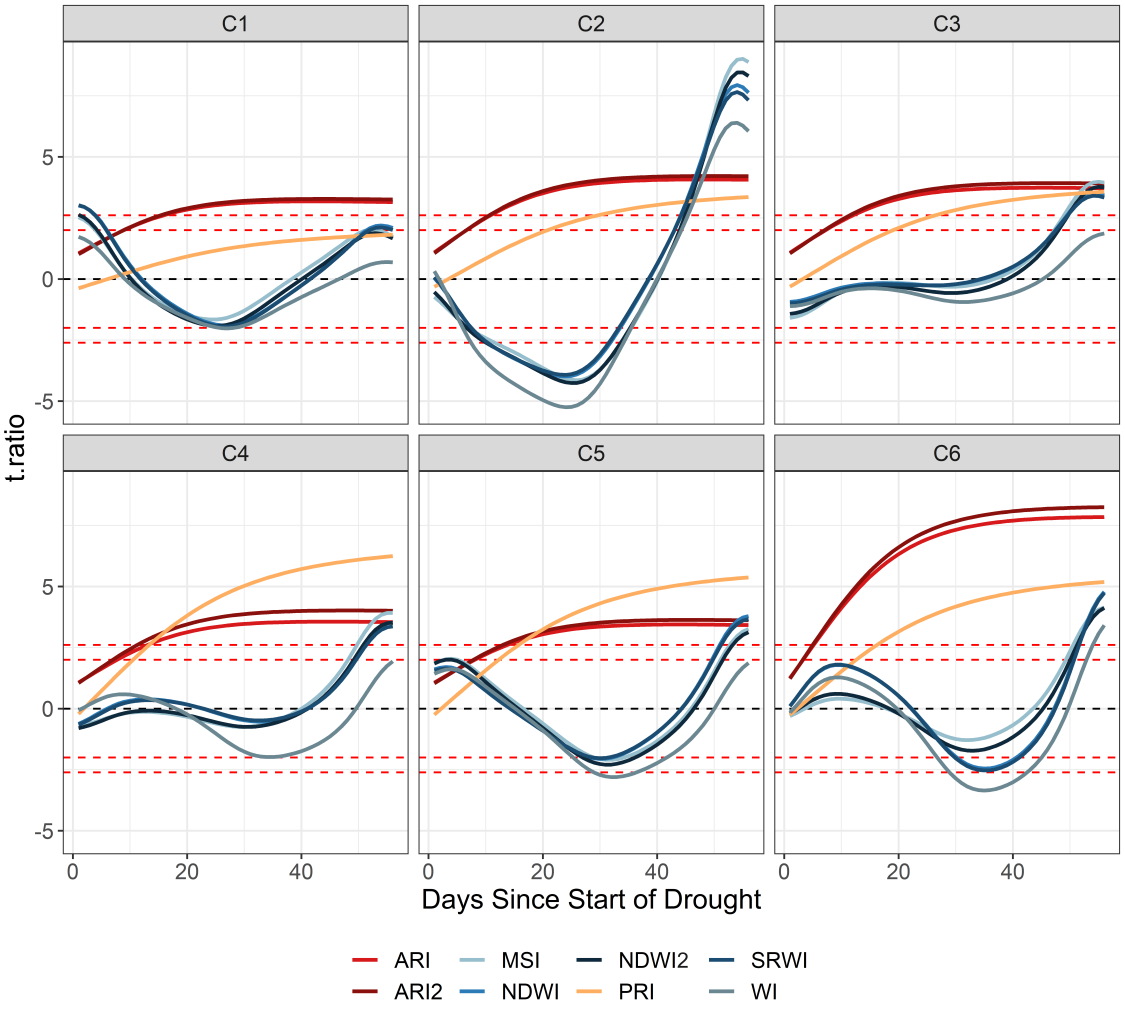

Figure 3.10: t.ratio of estimated marginal means (EMM) for drought effect of VI for each clone group. These EMM were calculated when a significant three way interaction was detected (Time x Treatment x Clone). Black dashed line is 0 line where drought and control group are equal. VI are normalised so that above the black line is the expected stress response. Red dashed lines are estimated p value levels ($p = 0.05$ and 0.01), calculated from the robust relationship between p values and t.ratio produced by EMM. For full VI names, formula and references see Table 2.1 (p.43). For full results for the EMM contrasts see Appendix B, Table B.2 (p.188).

3.5.1 Chlorophyll and greenness VI (VIg)

Chlorophylls are the main light harvesting pigments and are established biomarkers of biotic stress (Chaves et al., 2003; Govender et al., 2009; Plesa et al., 2019). Under drought stress, photoinhibition occurs when the quantity of light energy plants receive outweighs the capacity of photochemistry to use it (Long et al., 1994). During photoinhibition, reactive oxygen species (ROS) accumulate, which are damaging to photosynthetic machinery, including chloroplasts (Rasheed et al., 2021). Decreases in chlorophyll concentration, arising from photoinhibition related chlorosis and re-

duced chlorophyll biosynthesis, can be detected in VIg (Plesa et al., 2019; Grulke et al., 2020). Here, reductions in chlorophyll under drought stress were detected in some, but not all VIg.

NDVI, the most widely used VI, is sensitive to green leaf area but can perform poorly when evaluating evergreen needles (Gamon et al., 2016). NDVI was not affected by drought stress in this study. NDVI and SR use bands with wavelengths in the red portion of the spectrum (625 – 750 nm). In this region, chlorophyll has very high absorption, so the signal is readily saturated. The red-edge region (680 – 750 nm), is an area of the spectrum where absorption by plant pigments rapidly shifts from high to low. The red-edge shifts to shorter wavelengths when chlorophyll decreases. This region is more sensitive to chlorophyll than the red, as lower absorption leads to a weaker saturation effect (Horler et al., 1983; Gitelson & Merzlyak, 1994; Clevers & Gitelson, 2013). This is in line with the findings here, where drought steadily decreased the two red-edge based VIg (CIre, NDVIre), suggesting these may be more applicable for needle level chlorophyll estimation. The CCI model fit the data less well than the red-edge VIg, although CCI crossed the $p = 0.01$ earlier than any other VIg in the EMM analysis. CCI was designed to measure chlorophyll/ carotenoid ratios in evergreen needles for broadband satellite based sensors (Gamon et al., 2016). A possible hypothesis is that CCI responded quicker to stress due to chlorophyll/ carotenoid ratios whereas the red-edge indices may be more applicable for chlorophyll estimation.

Relative to the control group, the response of CIgr (which takes green light infomation) to drought was less pronounced than the red-edge VI. This could be due to the relationship between chloroplasts and green light. Green light is absorbed less readily than other visible light by plant leaves, therefore it passes deeper into the tissue (Brodersen & Vogelmann, 2010). Chloroplasts in the top few layers of cells receive the most excess light during stress causing the greatest photoinhibition. The chloroplasts reflecting green light, which CIgr detects, receive less excess energy so remain less stressed (Liu & van Iersel, 2021).

NDVI and other VIg have a relationship with canopy properties such as Leaf Area Index (LAI). Under drought stress, defoliation is an emergency response in conifers which reduces LAI (Schuldt et al., 2020; Nadal-Sala et al., 2021). Some defoliation was observed in this study, especially in older needles in the drought treatment (see Appendix A, Figure A.4 (p.178)). However, the spectral needle measurements do not detect such canopy parameters so are not reflected in NDVI. This highlights a limitation of scaling VI from needle to canopy level.

3.5.2 Stress Pigment VI (VIp)

Plants have evolved many mechanisms to cope with drought stress. Foliar pigments have a crucial role in photoprotection from oxidative stress caused by ROS. Carotenoids are considered the second major pigment group, after chlorophylls (Blackburn, 2007; Huang et al., 2018). They have many functions including light capture, photoprotection, energy dissipation and antioxidation, when photosynthesis is compromised (Gamon et al., 2016).

There are uncertainties surrounding the exact role of anthocyanins under drought stress (Steyn et al., 2002; Landi et al., 2015; Cirillo et al., 2021). There is a body of evidence to suggest light screening properties of anthocyanins, whereby the severity of photoinhibition is reduced by anthocyanins receiving high energy photons, and directing them away from light saturated photosynthetic machinery (Gould, 2004; Kyparissis et al., 2007; Landi et al., 2015). Anthocyanins may also have an antioxidant role, although this is under debate (Hernández et al., 2009; Cirillo et al., 2021).

The quantities and ratios, relative to chlorophyll, of these two pigment groups increase under drought stress (Lichtenthaler et al., 2007; Cirillo et al., 2021; Wong et al., 2022). In the present study, PRI, ARI and ARI2 were linearly affected by drought. Decreasing ARI and ARI2 indicates increasing anthocyanins, which alter reflectance, as the plants upregulate photoprotection and try to acclimate to stressful conditions. The anthocyanin drought response was quick and increased throughout the drought, suggesting the regulation of these pigments is crucial in Sitka spruce, from mild to severe drought stress.

PRI is becoming an ever increasingly used VI to infer plant stress and photosynthetic function. Here, PRI decreases linearly under drought stress. PRI is based on a specific group of carotenoid pigments called xanthophylls, which change the distribution of absorbed light at a specific region (Demmig-Adams & Adams, 1996; Gamon et al., 2016). The xanthophyll cycle dissipates excess light and heat energy, via the de-epoxidation of violaxanthin to zeaxanthin, and the reverse reaction (Jiang et al., 2006; Takahashi & Badger, 2011). Under drought stress, PRI decreases due to the de-epoxidation of xanthophylls, seen across differing conifer species (Peguero-Pina et al., 2007; Filella et al., 2009; Wong & Gamon, 2015a; Mõttus et al., 2017; Hernández-Clemente et al., 2019; Mõttus et al., 2019).

The carotenoid based VI (CRI1 and CRI2) responded weakly to the drought over time. The CRI1 drought response was very similar to the chlorophyll VI responses. The spectral overlap between carotenoids and chlorophylls make it hard to extract carotenoid-only information (Blackburn, 1998; Gitelson et al., 2002; Sonobe et al.,

2020). A study monitoring carotenoid concentration in crops, using carotenoid VI included here, to estimate pigment concentration concluded that the accuracy and robustness of these indices needs to be improved for accurate carotenoid estimation (Huang et al., 2018). The results suggest that focusing on reflectance at 531 nm (as used in CCI and PRI), which acts as a proxy for the xanthophyll cycle, provides the most drought sensitive information on carotenoids in Sitka spruce.

3.5.3 Water VI (VIw)

VIw all exhibited a similar pattern during the drought. Initially, VIw decreased relative to the control, then sharply increased from days 30 - 40 (except MSI which is inverted relative to other VIw). VIw are correlated with foliar water content and water potential in conifers (Stimson et al., 2005). The rapid change in VIw towards the end of the experiment, strongly suggests a rapid loss of water in needles as the plants become increasingly stressed, and were unable to maintain foliar water. The initial increase in water content relative to control plants was unexpected. Water content in conifer needles can take a long time to decline (Dao et al., 2021). It is hypothesised that in the early stages of drought, while stomata are closed, high water potential is maintained in the needles, due to lack of transpiration. This is similar to pre-dawn needles maintaining high water potential due to stomata closure overnight (Andrews et al., 2012). Past a certain drought stress threshold (Irvine et al., 1998), the spruce cannot maintain water content and needles begin to desiccate rapidly. This effect should be studied further in Sitka spruce by combining VIw with direct water content and water potential measurements over time.

3.5.4 *Fv/Fm*

Fv/Fm is a relatively quick to measure indicator of plant photosynthetic activity and a good proxy for drought stress (Mena-Petite et al., 2000; Fang-yuan & Guy, 2004; Bigras, 2005; Cifre et al., 2005; Zhuang et al., 2020; Baldi & La Porta, 2022). Healthy plants have a Fv/Fm of over 0.8, which the control plants in this study maintained. As the drought progressed, Fv/Fm decreased in water limited plants. Around day 30, just before the final watering in the drought group, many plants exhibited a decline in Fv/Fm, indicating signs of stress. This recovered post watering. Declines of Fv/Fm due to drought and rapid recovery post watering has been measured in Sitka spruce (Black et al., 2005) and Norway spruce (*Picea abies*) under differing irrigation treatments (Matisons et al., 2021). This highlights the dynamism of Fv/Fm as a stress marker. Grant and O'Reilly (2017) exposed Sitka spruce to a gradual, less intense drought, potentially more indicative of most natural droughts, and found no change in Fv/Fm. The sensitivity of Fv/Fm in Sitka spruce should

be further evaluated in contrasting drought intensities or under field conditions.

3.5.5 Clonal differences

Selection of appropriate species or genotypes will be crucial in ensuring a drought resilient UK forestry sector (Locatelli et al., 2021). Linking species genetic information to remotely sensed VI, or fluorescence data, highlights the potential for rapid non-destructive, and cost effective drought tolerance assessment and high throughput phenotyping (Plesa et al., 2019; Liming & Huichun, 2020; Baldi & La Porta, 2022). This could be incorporated into existing breeding programmes, to select for drought resilient progeny for future forest management.

By using six clones from the breeding population, initial evaluation of spectral phenotypic variability in Sitka spruce, using existing VI, is performed here. Conifer spectral heritability research is in its infancy, but a few recent studies are beginning to identify important regions of the spectrum, to identify intraspecific genetic differences. In Scots pine (*Pinus sylvestris*), heritable spectral variation was largest in the red-edge portion of the spectrum (found also in rice (Feng et al., 2017)). Significant variation was also present in near infrared (NIR) and shortwave infrared (SWIR) (Čepl et al., 2018). Spectral measurements on three different Norway spruce ecotypes, were taken across two months, by Hejtmánek et al. (2022). For differing ecotypes, previous year needles measured in May had significant variation around the red-edge and visible part of the spectrum. Whereas, when mostly current year needles were measured in August, differences were found between medium and low elevation trees in the NIR and SWIR region. Differences between medium and high elevation trees were found in the blue and red regions (Hejtmánek et al., 2022). These studies have highlighted the red-edge as a high potential area to differentiate genetically distinct conifers from their spectral reflectance, although factors such as needle age, environmental stress and time of year add complexity.

Differences between clones were detected in all chlorophyll-based indices (VIg). The red-edge VI were among the best fitting models, adding to existing evidence that chlorophyll reflectance, especially in the red-edge, could be a useful marker for genetic variation in conifers (Čepl et al., 2018). The chlorophyll stress response, however, was conserved across clones. These findings suggest VIg alone may be of limited use for identifying drought tolerant clones.

Intraspecific drought responses are widespread in the plant kingdom and have been reported in conifers (López et al., 2009; Sánchez-Gómez et al., 2011; Taïbi et al., 2017; Balekoglu et al., 2023), including Sitka spruce (Grant et al., 2018). However, evaluating these differences through remote sensing is rare (Čepl et al., 2018).

Chlorophyll fluorescence has been the most widely explored remotely sensed intraspecific drought tolerance marker in conifers (Lüttge et al., 2011; de Miguel et al., 2014; Čepl et al., 2016; Grant & O'Reilly, 2017; Taïbi et al., 2017). Identifying drought tolerant varieties of agricultural crops using VI is possible (Barakat et al., 2016; El-Hendawy et al., 2019). However, no analysis of intraspecific drought tolerance using remotely sensed VI on conifers exists.

This study provides new insights of differing clonal stress responses, by tracking VI over the course of an experimental, progressively increasing drought. The two anthocyanin VI, PRI, VIw and Fv/Fm drought responses differed between clones. Assessing multiple VI and Fv/Fm simultaneously using repeated measures gives a more complete overview of stress response. For example, Clone C1 had the smallest change in PRI and Fv/Fm, a relatively weak ARI response and maintained control level water content for most of the drought. The VI response for Clone C6 however, was much more pronounced, and was one of the first clones to show a significant drop in Fv/Fm, suggesting a much greater susceptibility to drought than C1. Clones C2 and C3 are part of the UK Sitka spruce general breeding population. C3 appears to be relatively drought tolerant. C2 however, has an extreme drop off in water content and Fv/Fm. This preliminary work suggests that currently, breeding population trees could be different in their drought tolerance, and some may be potentially vulnerable.

Conifer drought responses are complex, involving multiple physiological processes and mechanisms, which vary through time and stress severity (Baldi & La Porta, 2022). The results here highlight this complexity, and the value in combining VI and analysing stress at regular time points. Clone C2 was the second last clone to show a decrease in Fv/Fm (seen in week 8), and had a relatively small change in PRI. However, by the end of the drought, it appeared to be the most severely stressed group (based on Fv/Fm and rapid loss of water content). Using only one VI or time point could lead to incorrect conclusions about drought tolerance.

3.5.6 Seasonality

The biophysical properties of plants are not static in time. Healthy vegetation undergoes cycles at multiple time scales (Wong & Gamon, 2015b). This results in a constantly dynamic reflectance signal from leaves, where different processes have contrasting influences. One of the most dramatic changes trees undergo is across seasons. As temperatures and available light change, leaves make adjustments to ensure optimum photosynthesis, or to protect organs from climatic extremes, which involve long term changes in metabolism (Ensminger et al., 2004; Wong & Gamon, 2015a). The eight-week period of this study was from mid to late summer, where

trees may start to downregulate physiological processes, prior to the winter months.

All pigment indices showed some level of change over the study period, irrespective of irrigation treatment. Pigment pools vary substantially in seasonal cycles in conifers, where photosynthetic capacity is regulated primarily through pigments, rather than senescence (Gamon et al., 2016). Chlorophyll/ carotenoid ratios track evergreen conifers seasonal photosynthetic patterns, this increases reflectance in the visible region from summer to winter (Gamon et al., 2016). This increase was observed here, affecting all VI with bands in the visible region. This is largely driven by a down regulation of chlorophyll and increase in xanthophylls and the overall carotenoid pools (Miller et al., 1991; Ensminger et al., 2004; Gamon et al., 2016). Chlorophyll is down regulated to reduce light absorption while lower temperatures reduce the efficiency of photosynthesis. Xanthophyll pools increase to aid in photoprotection (Ensminger et al., 2004).

The needles measured in this study were overwintered needles and reflectance in the NIR region increased over the experimental period. A study looking at boreal forest trees compared needle spectra from June and September (Hovi, Raitio, & Rautiainen, 2017). The authors found increased NIR in current year needles. However, Hovi, Forsström, et al. (2017) found that NIR reflectance of previous years was dynamic and likely caused by changes in pigment composition, although the authors found this hard to explain. These are likely to be biochemical changes rather than structural as morphology is conserved in older needles. Minimal data for overwintered needles is available (Rautiainen et al., 2018). It has also been suggested that a decrease in NIR in overwintering needles could be due to accumulation of starch (Middleton et al., 1997) so the increase here may be caused by non-structural carbohydrate processes.

Water content can also change seasonally in conifer needles, although in over wintered needles, this change is limited. In lodgepole pine (*Pinus contorta*), for current year needles, water associated reflectance increased substantially in the NIR and SWIR regions, compared to a much smaller increase in the SWIR, and negligible change in the NIR in old needles (Qi et al., 2014). The slight increase over the season in the SWIR recorded by Qi et al. (2014) is comparable to the spectra collected here. And, excluding WI/NDVI which is influenced by chlorophyll content, the VIw that used SWIR bands (NDWI2 and MSI) showed a significant difference over time without drought influence. This suggests that in older needles the SWIR region is the most sensitive region to seasonal water change.

3.6 Conclusions

The study here used several different VI, broadly characterised into three groups (VIg is associated with chlorophyll, VIp is associated with stress pigments, and VIw is associated with water content). Many of these VI capture the same biophysical processes however, due to spectral interspecific plant variation, sensor sensitivity and collection methods, the most appropriate VI for a given use changes. The study here was concerned with highlighting appropriate VI, for drought stress detection in Sitka spruce, and the potential to differentiate stress responses between clones. For chlorophyll detection, a useful biomarker of stress, at the needle level, found that indices based on the red-edge were most sensitive, despite NDVI often being favoured in the literature. VIw provided good indicators of severe water stress once a critical threshold has been crossed. The initial increase in water content suggests that care should be taken using these indices, when using single time point measurements, or measuring mildly stressed trees. The VIw indices NDWI and SRWI would be recommended when evaluating drought stress due to a weaker seasonal effect. The detection of stress associated pigments can inform a great deal about a plant's current state. Here ARI, ARI2 and PRI were the best performing models in the current study. The linear nature of the response provides the most robust measure of stress. The stress response is also different between clones, suggesting that these VI could be important in identifying intraspecific drought tolerance for use in future breeding programmes.

Chapter 4

The effect of canopy position on Vegetation Indices (VI) for Sitka spruce (*Picea sitchensis*) needles during an experimental drought

4.1 Introduction

In Chapter 3, the spectral response of Sitka spruce to an experimental drought was assessed using pigment and water content Vegetation Indices (VI). The study measured upper canopy needles of the same age (from the 2021 growing season). Satellite or airborne sensors function at the canopy scale, rather than needle or individual branch. This means that the spectral signal will encompass needles of different ages and canopy depths. In order to produce reliable estimates of spectral response, it is therefore important to assess the variability across the canopy, to establish potential inconsistencies in spectral responses which may contribute to the canopy signal. This chapter follows on from Chapter 3 and uses the same experimental set up as outlined in Section 2.2 however, uses spectra collected throughout the canopy for analysis.

Across a plant canopy, biophysical traits are regulated for efficient light assimilation. As Kattenborn and Schmidtlein (2019) state for optical properties, 'reflectance follows function'; environmental conditions and plant phenology can cause leaf biophysical properties to vary, which alters reflectance (Kierzkowski et al., 2007; Mõttus et al., 2014; De Tomás Marín et al., 2016; Vinod et al., 2022). Needles in the upper canopy are likely to be exposed to higher levels of radiation, which can be explained by Beer's Law (also known as the Beer–Lambert law, or Beer–Lambert–Bouguer

law) ('C/F', Monsi et al., 2005). This describes decreasing probability of light attenuation with increasing leaf area throughout a plant canopy (Foroutan-pour et al., 2001; León & Bailey, 2019). Pigment levels in leaves therefore tend to follow irradiance gradients, as absorbing excess light energy is potentially disadvantageous due to photoinhibition or oxidative damage (Niinemets et al., 2003; Gamon & Berry, 2012). A body of evidence highlights how spectral differences occur throughout the canopy, due to age, structure and environmental conditions (O'Neill et al., 2002; Niinemets et al., 2003; Lukeš et al., 2013; Olascoaga et al., 2014; De Tomás Marín et al., 2016; Rautiainen et al., 2018; Kattenborn & Schmidtlein, 2019; Lhotáková et al., 2021). However, the effects are often overlooked in canopy level analysis (Wu et al., 2018; Bi et al., 2022).

The influence of drought on these differences is less well studied. Previous work has shown that drought responses can vary throughout a canopy in tropical forests (Smith et al., 2019), and that different age or height classes of tree can have different drought responses (Cavender-Bares & Bazzaz, 2000; Vinod et al., 2022). Needle life history influences biophysical function, as long-lived needles may incur legacy effects of drought damage given needles are not rapidly replaced (Song et al., 2022). It is therefore highly possible that the drought responses found in Chapter 3 may differ with age or vertical canopy position. If differences in drought response exist within a Sitka spruce canopy, and can be detected by VI, then this should inform interpretation of remote sensing work at larger spatial scales (canopy, regional or global). For example, Smith et al. (2019) suggest refining whole-canopy reflectance interpretations by accounting for distinct canopy layers. Without this, in situations where different portions of the canopy have contrasting phenologies or life histories, measuring the reflectance of the canopy as a whole could fail to detect important stress responses.

4.2 Research aims

The aims of these analyses are to build upon the findings in Chapter 3 to determine whether:

— Biophysical differences throughout the canopy are detectable with Vegetation Indices (VI), and if canopy position and age affect VI.

— The VI drought response varies across the canopy.

4.3 Chapter methods

Using the experimental set up and data collection methods set out in Section 2.2, the processed VI for the experimental drought period (27th June 2022 to 24th August 2022) for all canopy positions (top of canopy needles (N^{upper}), bottom of canopy needles (N^{lower}) and previous pear needles (N^{old})), were analysed. Due to inconsistent N^{lower} and N^{old} measurements in Clone 6, these data were removed from this analysis. These inconsistencies arose from the small vertical stature of some trees making the N^{upper} and N^{lower} canopy distinction vague. Clone 6 genotypes were also exposed to high rates of defoliation, especially in N^{upper} and N^{old} in the drought treatment (see Appendix A, Figures A.3 and A.4 (p.177, 178)).

4.3.1 Statistical Analysis

4.3.1.1 Mixed effects models

To determine how the position in the canopy affected VI dynamics over the drought, mixed effects models that treated each individual plant as a random effect were built for each VI. The main effects modelled were: time in days after drought treatment initiation (Time); watering regime (Treatment); position of needles in the canopy (Position); and clonal group (Clone). Additional interaction effects for the main effects over Time (Treatment:Time, Position:Time and Clone:Time), and three way interactions between Time:Treatment:Position and Time:Treatment:Clone, were included in the model where this improved model fit (determined using AIC to avoid overfitting). To account for non-linearity in biophysical response, polynomial regressions ($df = 3$) were fitted where this improved the AIC score relative to a linear trend. Model residuals were tested for normality and autocorrelation.

4.3.1.2 Estimated Marginal Means (EMM)

Using these models, estimated marginal means (EMM) were used to evaluate specific questions. If a significant ($p < 0.05$) main effect of Position was detected in the model, EMM contrasts were made between the three canopy positions. To evaluate how this relationship varied across time (when a significant Time:Position interaction was detected), canopy position contrasts were performed every seven days over the study period. Contrasts for the Time:Treatment:Position interaction were also evaluated to determine if the drought effect differed throughout the canopy. The N^{old} and N^{upper} needles are measured at a similar canopy height. The contrasts between canopy positions therefore evaluated; the effect of age on VI (N^{upper}:N^{old}), effect of vertical position in the canopy on VI (N^{upper}:N^{lower}) and the effect of vertical position and age on VI (N^{old}:N^{lower}).

4.3.1.3 Treatment main effect

For some VI, a main effect of Treatment was detected. To establish if differences between drought and control groups existed before the drought treatment had initiated, EMM contrasts between the control and drought groups for each VI and clonal group at day 0 (t0) were conducted.

4.3.1.4 Needle measurements

Needle measurements (length and width) were taken prior to the drought initiation (Section 2.2.3.8). These data were analysed using a two-way-anova to determine differences between canopy positions and clonal groups. All statistical analysis was conducted in R and RStudio (RStudio Team, 2020).

4.4 Results

Time series of measured VI and model estimates are presented in Figures 4.2 - 4.4. Results from the mixed-effect models are summarized in Figure 4.1, and presented in full in Appendix C, Table C.1 (p.198).

4.4.1 Position main effect

Position as a main effect was highly significant ($p < 0.001$) for all VI (Figure 4.1), highlighting clear differences in reflectance between canopy positions, resulting in differences between VI. EMM contrasts where therefore conducted between canopy positions for all VI (Figure 4.5; full contrast results are presented in Appendix C, Table C.2 (p.202)).

VI values were greater in N^{upper}, for the carotenoid based VI (CCI, CRI1 and CRI2) and all water based VI (excluding MSI which is on the reverse scale), than in N^{old}. VI values were lower in N^{upper} compared to N^{old} in most other VI (with the exception of NDVI, SR and WI/NDVI, where no differences were detected).

There was consistency in the N^{upper}:N^{lower} contrasts across VI (Figure 4.5). N^{upper} values were lower than N^{lower} across all pigment VI (greenness and pigment) (Figures 4.2, 4.3 and 4.1). This difference was most pronounced in CIgr (estimated difference 1.08 $\pm$ 0.07) and PRI (estimated difference: 0.02 $\pm$ 0.005) and weakest in CCI (estimated difference: 0.03 $\pm$ 0.005). Conversely, N^{upper} was larger than N^{lower} in all water VI (with the exception of MSI, where the scale is reversed) (Figures 4.4 and 4.5). The statistical strength of this was similar across VI, with the exception of WI/NDVI (Figure 4.5).

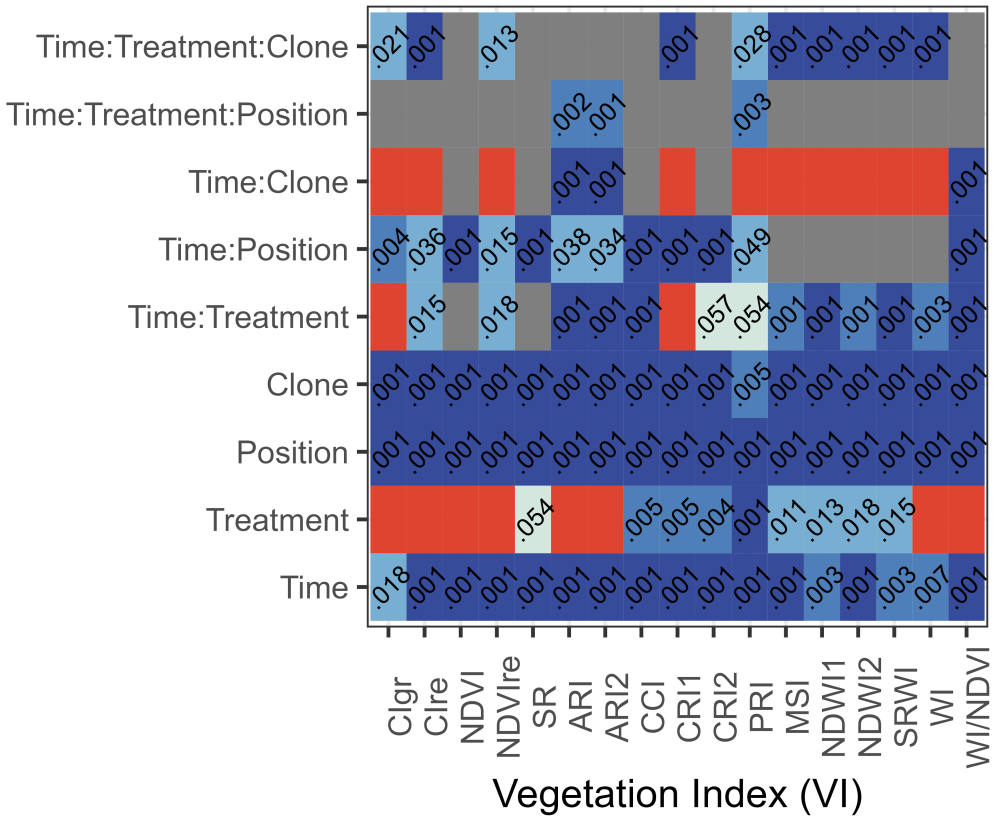

Figure 4.1: Summary of mixed effects models for all Vegatetion Indcies (VI) showing main and interaction effects. Model terms are on the y-axis. Colours denote the statistical significance (p values), where dark blue is $p < 0.001$ (highly significant), light blue is $p < 0.01$ and white is $p < 0.1$. Red indicates $p > 0.1$ and grey indicates the term is not included in the model. For $p < 0.1$, p values are displayed. Note: .001 represents any p value equal to or less than than 0.001. Full results are presented in Appendix C, Table C.1 (p.198). For full VI names, formula and references see Table 2.1 (p.43).

For NDVI, SR, CCI, CRI1, CRI2 and MSI, N^{lower} VI values were greater than N^{old} (Figure 4.5). For CIre, NDVIre, NDWI1, NDWI2, SRWI, WI and WI/NDVI, N^{lower}, VI values were smaller than N^{old} VI values. And for CIgr, ARI, ARI2 and PRI, there was no difference between N^{lower} and N^{old} (Figure 4.5).

4.4.2 Canopy position over time

A significant Time:Position interaction was detected in 12 out of 17 VI (Figure 4.1). These included all pigment and greenness VI. WI/NDVI was the only water based VI where a Time:Position interaction was present. The results of the EMM contrasts for these VI, are summarised in Figure 4.6 and presented in full in Appendix C, Table C.3 (p.204).

For ARI and ARI2, no differences were detected in the N^{old}:N^{lower} contrast. For

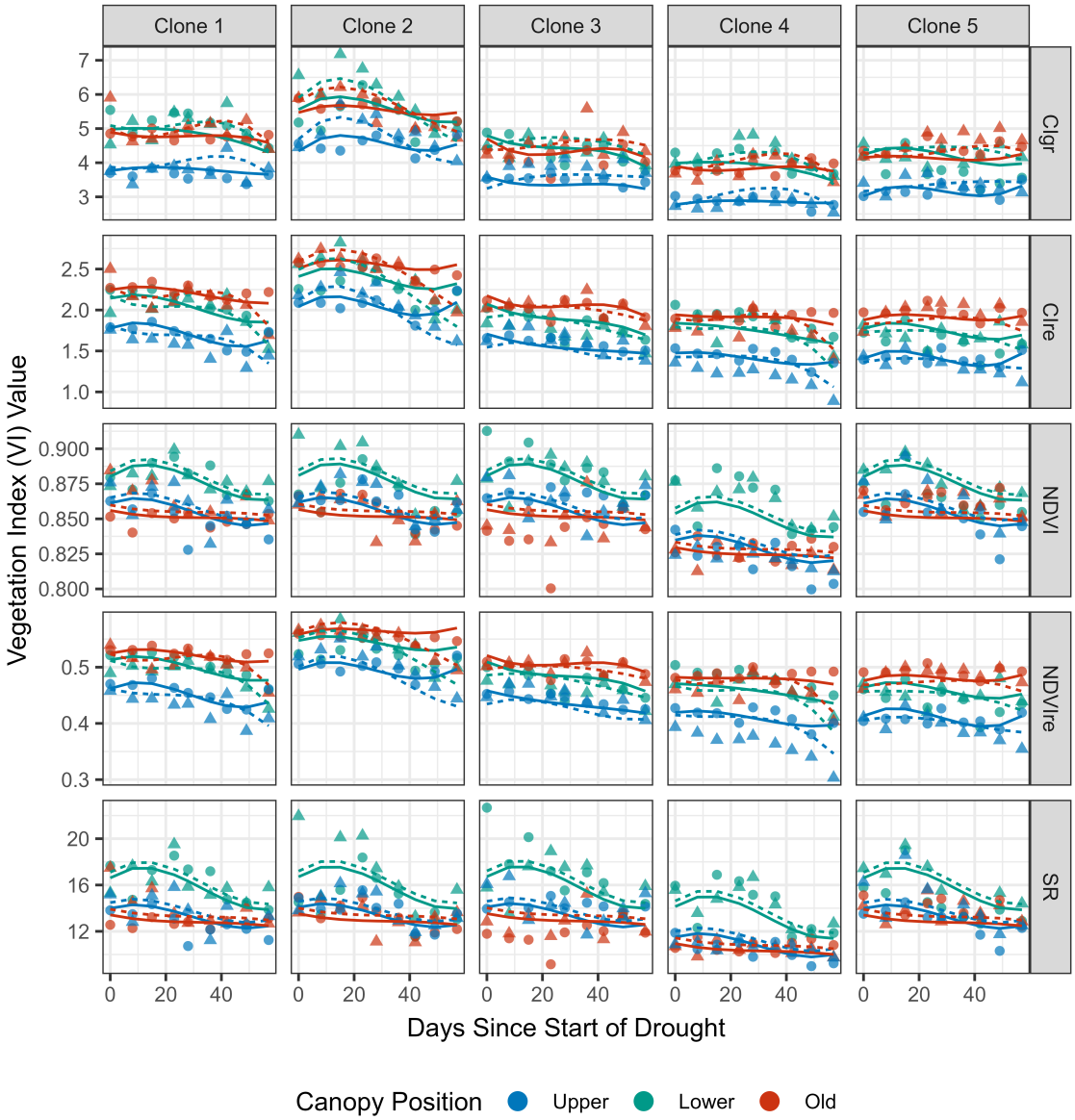

Figure 4.2: Time series of greenness/chlorophyll VI over the drought period. The points denote the average value for repeats of each clone group. Circles signify control groups and triangles signify droughted plants. Lines are plotted using estimates from mixed effects models, where solid lines are the control group and dashed lines are droughted plants. The full results for the mixed effects models are presented in Appendix C, Table C.1 (p.198). For full VI names, formula and references see Table 2.1 (p.43).

N^{upper}:N^{old} and N^{upper}:N^{lower}, the VI differences between canopy positions were most pronounced at the start of the experiment, then gradually converged, until by day 49 they were not significantly different.

For the carotenoid based VI (CCI, CRI1, CRI2), N^{upper} VI values were generally

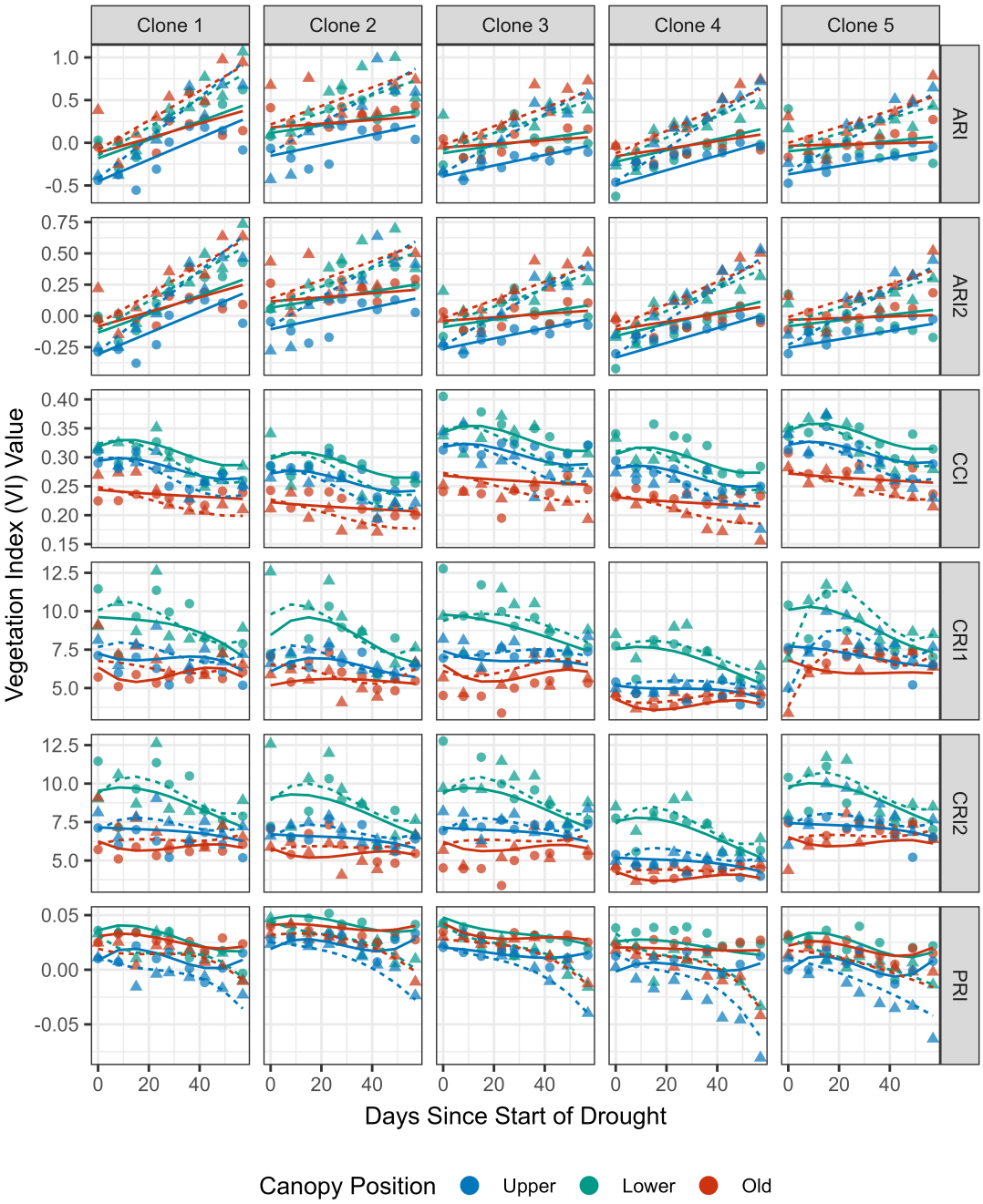

Figure 4.3: Time series of pigment VI over the drought period. Point and line notation matches that detailed in 4.2.The full results for the mixed effects models are presented in Appendix C, Table C.1 (p.198). For full VI names, formula and references see Table 2.1 (p.43).

higher than N^{old} (Figures 4.3 and 4.6). This difference is most pronounced near the start of the experiment around day 7, and then is gradually reduced. For CRI1 and CRI2, by day 49 there is no significant difference (Figure 4.6). The other two contrasts (N^{upper}:N^{lower} and N^{lower}:N^{old}) for the carotenoid based VI followed the same pattern. N^{lower} had constantly higher VI values than N^{upper} and N^{old}. These

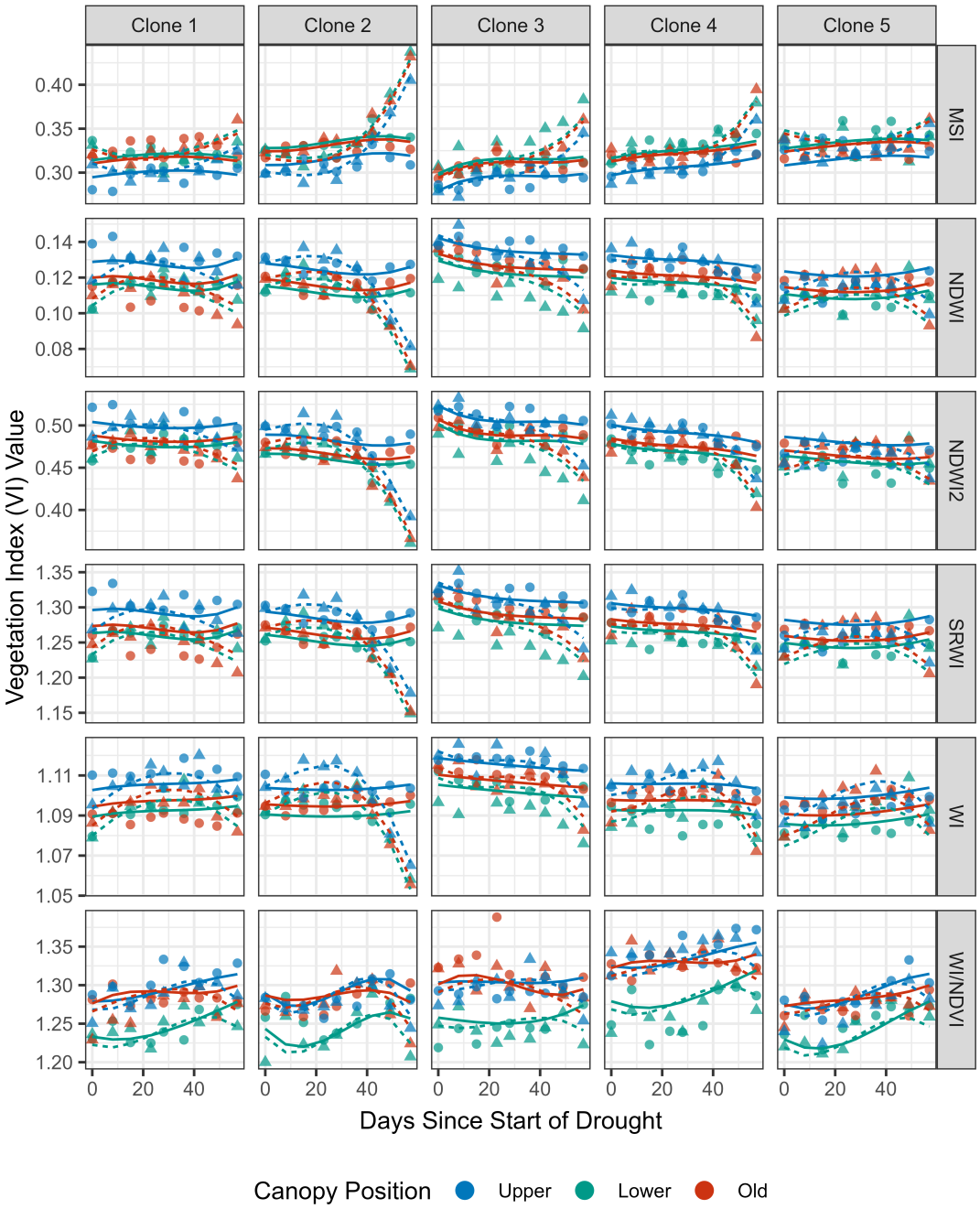

Figure 4.4: Time series of water based VI over the drought period. Point and line notation matches that detailed in 4.2.The full results for the mixed effects models are presented in Appendix C, Table C.1 (p.198). For full VI names, formula and references see Table 2.1 (p.43).

values began to converge as the experiment continued. The difference was weakest for CCI N^{upper}:N^{lower}.

NDVI and SR followed the same pattern as the carotenoid VI across all the contrasts (Figure 4.6). However, the difference between N^{upper}:N^{old} was smaller and no difference was detected up until day 7 and after day 21. For the red edge VI (CIre

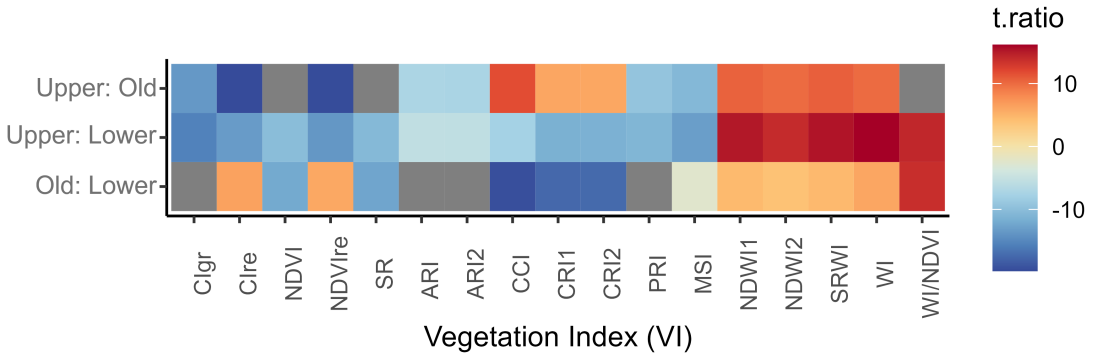

Figure 4.5: Estimated marginal means (EMM) contrasts between canopy positions for VI. For each contrast, colours denote the t.ratio. Grey squares indicate non-significance ($p < 0.05$). Note that MSI is on a reversed scale relative to other water VI. A positive t.ratio (red) indicates the first contrast term (e.g. 'Upper' in 'Upper:Old') has a higher VI value, and a negative t.ratio (blue) indicates the first contrast term has a lower VI value. The full results are presented in Appendix C, Table C.2 (p.202). For full VI names, formula and references see Table 2.1 (p.43).

and NRre), N^{upper} and N^{old} diverged from N^{lower} over the experimental period. The difference between N^{upper} and N^{lower} remained relatively stable throughout (Figure 4.6).

For CIgr and PRI, the difference in VI values between N^{upper} and N^{old} was lower during the first half of the experiment and then began to increase from around day 14 (Figure 4.6). N^{lower} and N^{old} were similar or the same for CIgr and PRI. No difference between N^{upper} and N^{old} was observed for NDVI/WI until day 42. The differences between N^{lower} and the other positions for WI/NDVI were greatest at day 14, and they gradually converged and then diverged before and after this point.

4.4.3 Differing drought effects across the canopy

For three VI (ARI, ARI2 and PRI) a significant Time:Treatment:Position interaction was detected (Figure 4.1). The pattern in all EMM contrasts between the control and drought treatments for these VI is broadly conserved in all three VI at all canopy positions (Figure 4.7, full EMM contrast results are presented in Appendix C, Table C.4 (p.212)). Up until day 7, for N^{upper} and N^{old}, and day 14, for N^{lower}, no differences between the control and drought groups are detected. After this point, the difference gradually increased. Between canopy positions, the extent of the divergence between control and drought groups over time differed. This was strongest in N^{upper} and weakest in N^{lower}. For ARI and ARI2, where differences were detected, the VI values for the control treatment were consistently higher than in the drought group. For PRI, the VI values for the drought treatment were consistently lower (Figure 4.3).

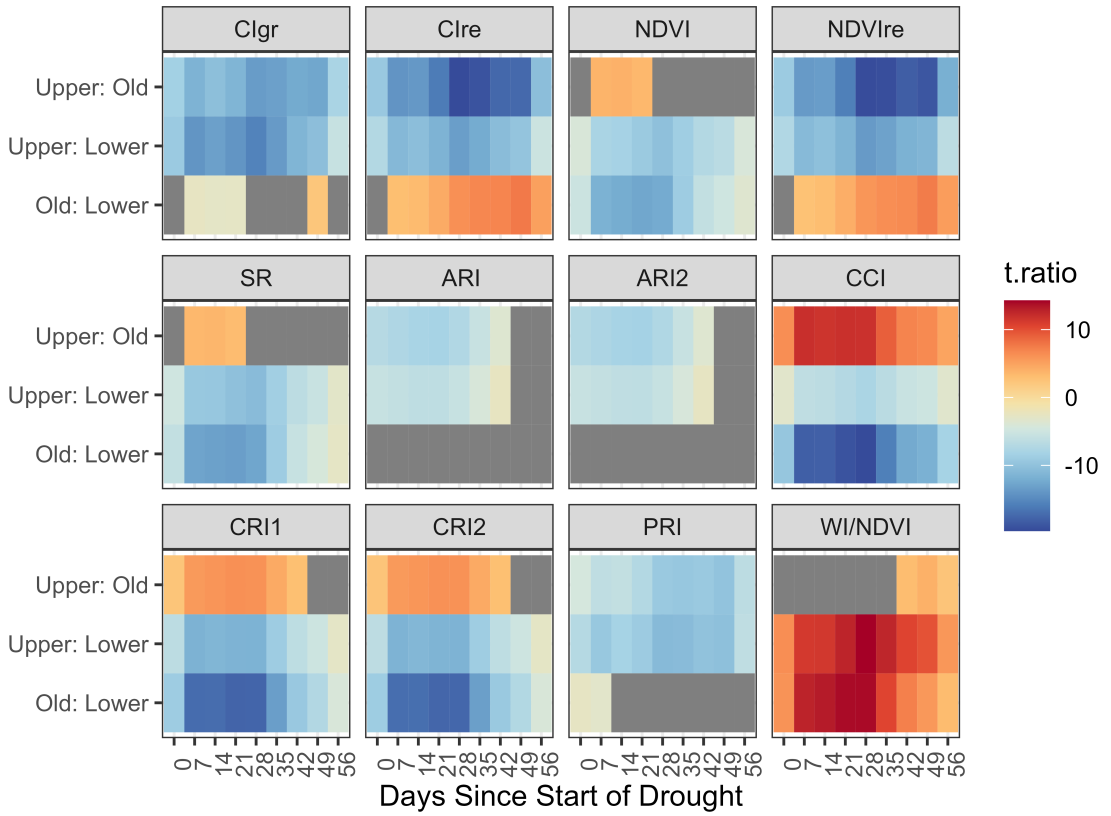

Figure 4.6: Estimated marginal mean (EMM) contrasts between canopy positions for VI over time. A EMM contrast is conducted on each VI model at regular time intervals every 7 days. Colour and notation matches those detailed in Figure 4.5. The full results are presented in Appendix C, Table C.3 (p.204). For full VI names, formula and references see Table 2.1 (p.43).

4.4.4 Needle measurements

Needle width and lengths differed significantly between canopy positions (ANOVA: Width: F = 41.659, df = 1,2, $p < 0.001$, Length: F = 158.213, df = 1,2, $p < 0.001$) and clones (ANOVA: Width: F = 4.016, df = 1,2, $p = 0.04696$, Length: F = 46.022, df = 1,2, $p < 0.001$) (Figure 4.8). Needles were clumped by position. In general N^{upper} needles were the longest and widest, whilst N^{lower} needles were longer than N^{old} but existed over a similar range of widths.

4.4.5 Treatment main effects

Where significant treatment main effects were detected, EMM contrasts revealed some differences between control and drought groups at t0 which are presented in Appendix C, Figure C.1 and Table C.5 (p.215 and 215). Differences at t0 occurred in Clone 1 and 5 for the water VI (MSI, NDWI NDWI2, SRWI). This was consistent

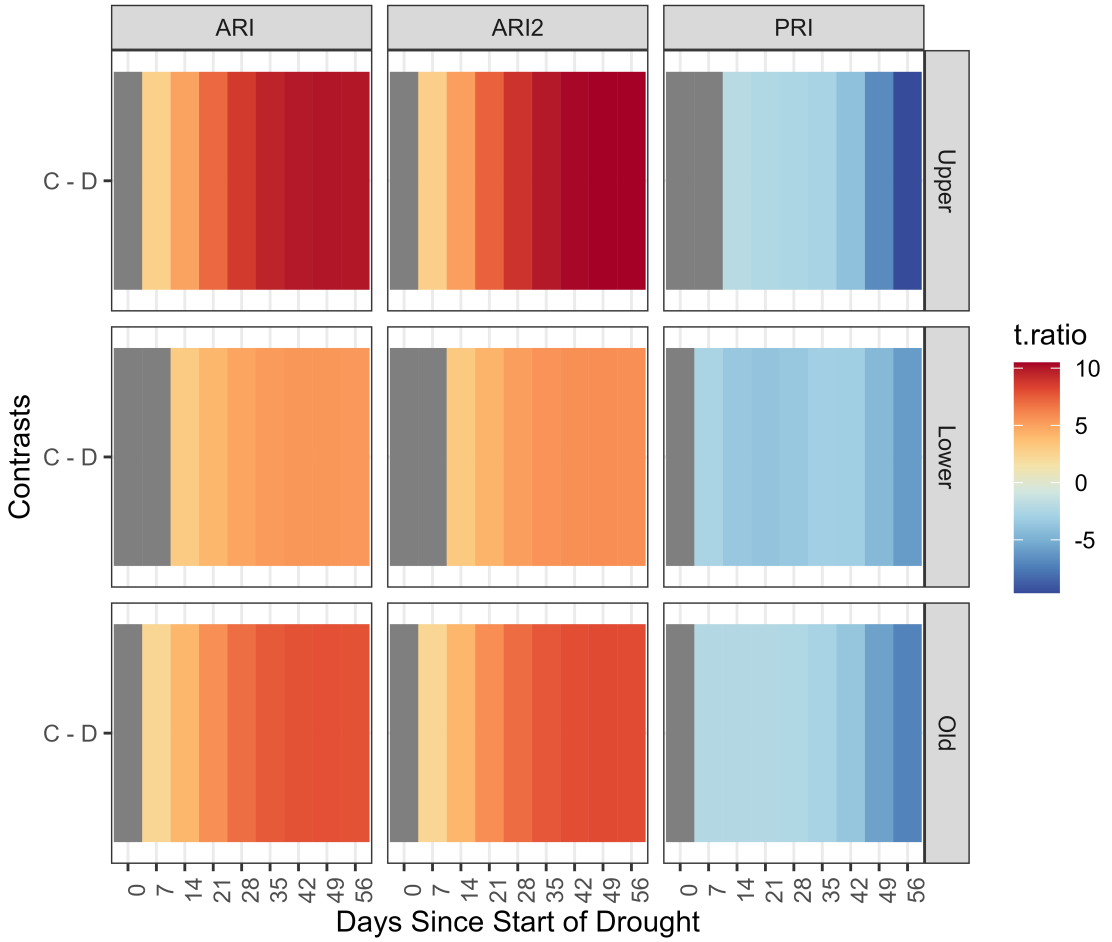

Figure 4.7: Estimated marginal mean (EMM) contrasts for drought effects over time for different canopy positions. A EMM contrast is conducted between the control (C) and drought (D) treatments for each position at regular 7 day intervals. The full results are presented in Appendix C, Table C.4 (p.212). For full VI names, formula and references see Table 2.1 (p.43).

across VI but not across clones. Differences between groups also occur in CRI1 in Clone 2 and 5.

4.5 Discussion

Differences in microclimate and physiology lead to variation in needle optical properties within a single plant canopy. Chapter 3 focuses on needles from a specific age class and vertical canopy position. Scaling leaf-level properties to the canopy is important for SRS vegetation monitoring (Lhotáková et al., 2021). Therefore, understanding variation in VI within the canopy provides crucial information relating leaf-level processes to canopy-level information. The analysis here aimed to evaluate if variations in vertical position and age are detectable with a range of VI during an artificial drought experiment on Sitka spruce. This work demonstrates

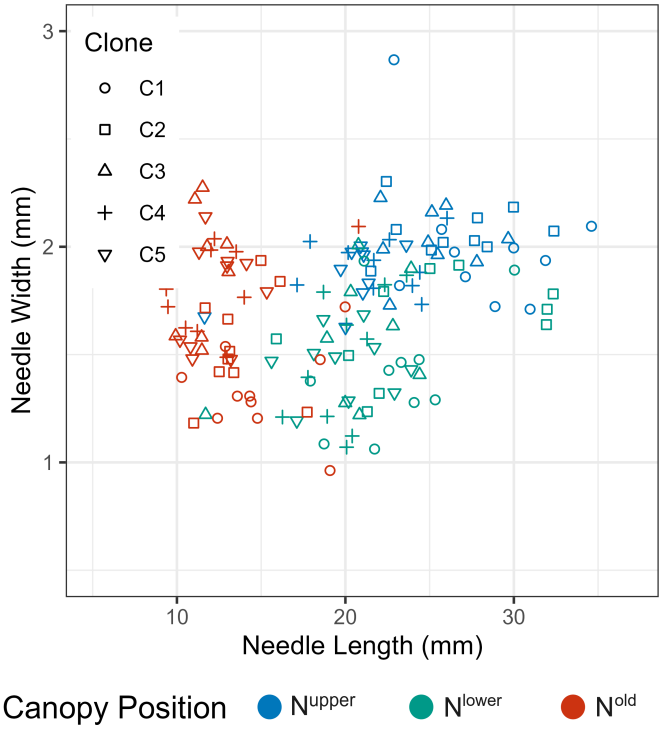

Figure 4.8: Needle dimensions of study plants. Colours denote the position in the canopy the needles were removed from (N^{upper} and N^{lower} were overwintered needles from the previous year's growth (2021), taken in the top or bottom 25% of the vertical canopy profile. N^{old} were sampled from the top 25% of the canopy where possible or the highest available whorl.) Shapes indicate the clones (C1 = Clone 1 etc.).

significant variation in VI values between canopy positions, providing evidence for within canopy pigment differences and stress response in Sitka spruce.

Light gradients are a strong driver of canopy biophysical variation across needles of the same age (Lukeš et al., 2013; Chin & Sillett, 2017; Kramer et al., 2018; Lhotáková et al., 2021) and within-canopy needle differences can be larger than interspecific age differences (Tegischer et al., 2002). Top of canopy needles receive the most incident light, whilst shading in the lower canopy reduces the quantity of light available. The small stature and relatively sparse canopies, of the study plants used for this work, might suggest relatively little differences in light levels throughout the canopy. However, the plants are from a clone bank, stored in high density, and close proximity, creating a high contrast in light levels between the upper and lower canopies. The needle measurements clearly show morphological differences between all three needle classes (Figure 4.8), which for N^{upper}:N^{lower} contrasts is attributed predominantly to microclimatic differences (Lewandowska & Jarvis, 1977). Needles in the N^{upper} are the widest on average, which is an adaption to high light environments reported previously in Sitka spruce (Chin & Sillett, 2017).

4.5.1 Pigments throughout the canopy

Canopy position affected all VI studied. Differences in vertical canopy position were the most consistent. Sitka spruce needle morphology has been found to be the primary ecological driver of needle anatomical variation in Sitka spruce (Chin & Sillett, 2017). Across all pigment based VI, values were higher in N^{lower} compared to N^{upper} suggesting higher concentrations of chlorophylls, carotenoids and anthocyanins lower in the canopy. In the lower canopy, light availability will be reduced due to increased shading. Under lower light conditions, plants can increase light absorption efficiency by investing in pigments in shaded or lower areas of the canopy (Demarez et al., 1999; O'Neill et al., 2002; Robakowski & Bielinis, 2017). Regulating chlorophyll according to available light increases total canopy photosynthesis due to improved distribution of light harvesting throughout the canopy (Simkin et al., 2022). This is consistent with an extensive canopy depth review by Vinod et al. (2022), who found denser chloroplast layers in shaded leaves. In Sitka spruce, chlorophyll concentration has been demonstrated to be greater in the lower canopy (O'Neill et al., 2002), in shaded canopy needles (Lewandowska & Jarvis, 1977). Homolová et al. (2007) present the same response in Norway spruce (*Picea abies*), while (O'Neill et al., 2002) found that chlorophyll correlated with reflectance more than any other measured biophysical property.

For three of the four carotenoid VI (CCI, CRI1, CRI1), higher values suggest higher quantities of carotenoids in the lower canopy. This adds to evidence that, under shaded conditions, conifers invest more in photosynthetic apparatus when light intensities are lower. Carotenoids have a diverse set of functions including light capture, and are crucial in absorbing light in the blue-green region or spectrum, where absorption by chlorophyll is low. Carotenoids pigments transfer energy to chlorophyll, thus expanding the available spectrum of light available to a plant, and making efficient use of the available energy (Ida, 1981; Hashimoto et al., 2016; Simkin et al., 2022). Ida (1981) found that carotenoids increased almost linearly with chlorophylls with shading in four Taxodiaceous conifers. Homolová et al. (2017) found slightly increased carotenoids and chlorophyll in sunlit Norway spruce needles, but the ratio between the two remained consistent.

PRI is also associated with carotenoids. However the PRI value suggests higher concentrations of carotenoids in the upper canopy. This contradictory finding may be explained by the diversity of carotenoid groups, and their functions, which act on different temporal scales (Wong & Gamon, 2015b). PRI uses the specific reflectance band at 531 nm, which is sensitive to the interconversion of pigments within the xanthophyll cycle (Wong & Gamon, 2015a). The xanthophyll cycle is crucial in energy dissipation, acting on short term scales with reversible adjustments. This is

considered a *facultative* response (Gamon & Berry, 2012). Over longer time scales carotenoid concentration changes can alter photosynthetic capacity over seasonal time scales to track changing light and temperature levels. This is considered a *constitutive* response (Gamon & Berry, 2012). In-depth analysis of PRI on three conifer species (Gamon & Berry, 2012), in accordance with this study, found higher investment in xanthophyll pigments (violaxanthin, antheraxanthin and zeaxanthin), in sun exposed needles. This highlights investment into photoprotection mechanisms in higher light microclimates, which has also been demonstrated elsewhere (Demmig-Adams, 1998; Niinemets et al., 2003; Porcar-Castell et al., 2009).

The contrasting responses in this study between PRI and other carotenoid VI could be explained by different sources of carotenoid variation. PRI is likely detecting *facultative* (short term) responses to increased light levels in the upper canopy, which ameliorate detrimental photoinhibition. By contrast, the other three indices (CCI, CRI1 and CRI1) are sensitive to *constitutive* pigment pools, and other carotenoid pigments (e.g. α-carotene and β-carotene), which act to maximise photosynthetic capacity in the shaded lower canopy. These results demonstrate the complexity of sources of variation within the carotenoid pigment group, and highlight the need to understand mechanistic responses behind reflectance based VI.

Analysis from Rautiainen et al. (2018) and Hovi, Raitio, and Rautiainen (2017) suggests that age is more important than canopy position for reflectance in conifers. As a basic principle, conifers accumulate photosynthetic pigments over time (O'Neill et al., 2002; Homolová et al., 2013, 2017; Lhotáková et al., 2021). However, younger needles are the most photosynthetically active (Warren, 2006; Merilo et al., 2009; Lhotáková et al., 2021; Wu et al., 2021). Here, depending on the VI, the relationship between the two needle age classes differed. For CIgr, CIre and NDVIre, N^{old} values were higher than N^{upper}, suggesting increased chlorophyll concentrations. This is in agreement with general consensus in the literature (Tegischer et al., 2002; Homolová et al., 2013, 2017; Lhotáková et al., 2021). Likewise, O'Neill et al. (2002) found a small increase in chlorophyll with age in Sitka spruce needles. NDVI and SR are also related to chlorophyll concentration, however no difference between N^{old} and N^{upper} needles was found. As discussed in Chapter 3, NDVI and SR use red light, rather than red edge or green light (as in CIgr, CIre and NDVIre) to detect chlorophyll. Red light is readily saturated by chlorophyll and so is less sensitive to change (Horler et al., 1983; Gitelson & Merzlyak, 1994; Clevers & Gitelson, 2013), meaning relatively subtle chlorophyll age differences could be missed. Needle spectral analysis by Dengel et al. (2013) also concluded that NDVI was not sensitive enough to detect age related differences in Scots Pine (*Pinus sylvestris*).

The opposite trend is found in carotenoid VI, where values are lower in N^{old} rel-

ative to N^{upper}. The discrepancy between this and previous findings in Norway spruce that chlorophyll and carotenoid concentrations increased with needle age (Homolová et al., 2017; Lhotáková et al., 2021), may make sense in the context of carotenoid:chlorophyll ratios. A detailed pigment analysis by Tegischer et al. (2002) compared Norway spruce needles from the current and previous year, and found that while chlorophyll concentrations increased in the old needles, neoxanthin, lutein, α-carotene and β-carotene decreased relative to chlorophyll. Total chlorophyll is more abundant in leaves than total carotenoids (Homolová et al., 2017; Lhotáková et al., 2021), and the spectral influence of chlorophyll and carotenoids overlaps, leading to strong covariation between the two (Gitelson et al., 2002; Gitelson, 2020; Sonobe et al., 2020). Because of this, VI relating to carotenoids can be heavily influenced by chlorophyll concentrations and therefore carotenoid:chlorophyll ratios. CCI and PRI are related closely to carotenoid:chlorophyll ratios in conifers (Wong & Gamon, 2015a; Gamon et al., 2016). Gitelson et al. (2002) tried to overcome the influence of chlorophyll to directly estimate carotenoids by introducing bands at 550 and 700 nm for CRI1 and CRI2 respectively. These wavelengths were found to be linearly proportional to chlorophyll in some deciduous species. However, the relationship between carotenoids and chlorophyll varies between species, growth stages and environmental stresses (Gamon et al., 2016; Gitelson, 2020; Sonobe et al., 2020). It is therefore plausible that CRI1 and CRI2 are influenced by carotenoid:chlorophyll dynamics. Future work should look to establish a robust carotenoid estimation VI applicable to conifers or specific conifer species. These results further highlight the complexity of pigment dynamics (Tegischer et al., 2002), and the care which should be taken in VI analysis when accompanying metabolomics are not possible.

Studies examining anthocyanin relationships throughout the canopy are sparse for conifers although their roles are important and diverse (Gould, 2004; Simkin et al., 2022; Shi et al., 2023). Like carotenoids, anthocyanins absorb light in the blue region of the spectrum (Chalker-Scott, 1999; Feild et al., 2001; Simkin et al., 2022), and so may aid efficient light absorption. The results presented here suggest that, like chlorophyll and carotenoids, Anthocyanins accumulate over time in needles and in the lower canopy. Possibly to improve canopy light uptake distribution (Robakowski & Bielinis, 2017; Lhotáková et al., 2021; Simkin et al., 2022). Anthocyanins are also important in stress responses, as seen in Chapter 3, and can act as photo protectants in times of extreme stress (Chalker-Scott, 1999; Steyn et al., 2002; Kyparissis et al., 2007; Zhu et al., 2016; Simkin et al., 2022). However, no evidence of increased photoprotection by anthocyanins in the upper canopy is found here.

4.5.2 Water content throughout the canopy

The water based VI were consistent in suggesting that water content is less in N^{lower} and N^{old} compared with N^{upper}. Water content has also been shown to decrease with needle age in silver fir (*Abies alba*) (Robakowski & Bielinis, 2017), maritime pine (*Pinus pinaster*) (Eimil-Fraga et al., 2015), Scots Pine, Norway Spruce, Western hemlock (*Tsuga heterophylla*), Lawson cypress (*Chamaecyparis lawsonian*) and Western redcedar (*Thuja plicata*) (Hatcher, 1990). However, evidence for variation in water content throughout conifer canopies due to vertical position or sun/ shading is limited. In the Sitka spruce specific analysis by O'Neill et al. (2002), the highest water content was found in the lower canopy, and lowest in the upper canopy; however, these effects were small and conducted on mature (mean height 6.5 m) trees. Using spectral data and direct water content measurements, Homolová et al. (2017) found slightly lower water content in shaded needles for Norway spruce in immature (∼40 years) and mature trees (∼80 years). Neither of these studies however, posit an explanation for why these differences in needle water content distribution exist.

In contrast, Zhu et al. (2017) found no significant differences in water content between canopy levels in multiple species of non-conifers. Although they recorded a slight trend towards higher water content lower in the canopy for weeping fig (*Ficus benjamina*). The authors attributed this partly due to the small vertical stature of the study plants.

One possible explanation for the detection of lower quantities of water in lower, more shaded needles is that higher photosynthetic rates and stomatal conductance occurs in upper canopy leaves (Sellin & Kupper, 2004). The 'leaf economic spectrum' hypothesis states that maintaining higher levels of metabolic function requires increased resource allocation (Prieto et al., 2018). It is feasible therefore, that the study plants could be moving increased water to needles with higher photosynthetic demands higher in the canopy. Another possibility is that morphological differences between the needles in N^{upper} and the other canopy layers may have led to more biomass being measured in the N^{upper} samples (Lillesaeter, 1982; Gao, 1996; Sims & Gamon, 2003; Berard et al., 2017). A fuller investigation of this relationship could consider determining water content on a per weight basis, which was beyond the scope of the non-destructive methods used here.

4.5.3 VI temporal dynamics

Chapter 3 discusses the seasonality of VI within Sitka Spruce needles and highlights the great complexity of varying pigment and water dynamics within a growing season. This is attributed to pigment pool regulation, which acts to maximise pho-

tosynthetic capacity while minimising photoinhibition at multiple temporal scales (sub-hourly, daily and seasonally) (Miller et al., 1991; Ensminger et al., 2004; Gamon & Berry, 2012; Wong & Gamon, 2015b; Hovi, Raitio, & Rautiainen, 2017). Water content shifts were also detected in Chapter 3, especially in the SWIR region (Qi et al., 2014), likely reflecting plant acclimation strategies.

The aims here were to understand if VI temporal dynamics varied between needles in different canopy positions across the experimental period. If large differences or contrasting seasonal responses are present, then this should affect how canopy measurements (i.e. satellite based) are interpreted. For the water based VI, (except WI/NDVI, which is influenced by changes in NDVI), the temporal effects did not differ between canopy positions. However, differences occurred for all pigment-based (chlorophyll, carotenoid and anthocyanin) VI. These results paint a complex picture of potentially multiple dynamic processes competing over time, whilst also demonstrating reasonably consistent relationships between different canopy positions. In general, the contrasts between canopy positions remain either positive or negative (Figure 4.6). It is only the strength of the relationship which changes over time. The differences between canopy positions are greatest in the middle of the experimental period and estimates converge more towards the start and end.

Despite the established differences found within canopies for needle age classes and positional/ light levels (Demarez et al., 1999; O'Neill et al., 2002; Hovi, Raitio, & Rautiainen, 2017; Robakowski & Bielinis, 2017; Rautiainen et al., 2018), and the knowledge that at a needle level, reflectance properties over time are dynamic (Gamon et al., 2016; Hovi, Forsström, et al., 2017), studies which simultaneously monitor reflectance throughout the canopy over time are rare (Wu, Song, Song, Wang, Chen, & Yu, 2018; Wu et al., 2020), but see Wu, Kobayashi, et al.; Wu, Song, Song, Wang, Chen, and Yu (2018, 2018). Wu, Song, Song, Wang, Chen, and Yu (2018) took reflectance measurements of Chinese fir (*Cunninghamia lanceolata*) needles, of varying ages, across a growing season. They found that phenological spectral differences in visible and NIR reflectance were found between current year and mature (at least one year old) needles. The current year needles showed increased absorbance in the visible and NIR bands, while mature needles decreased NIR absorbance over the same period. In Wu, Kobayashi, et al. (2018), for Amazonian tropical canopies, incorporating leaf demography in radiative transfer modelling (RTM) greatly increased explained model variability.

Explaining the precise mechanism for how pigments in different canopy positions vary across the experimental period, and how this influences VI, is challenging without more detailed metabolomic analysis. It is hypothesised that during times of high productivity in mid/late summer, pigment differences throughout the canopy are at

their most pronounced and dynamic (as suggested by Dengel et al. (2013)). The growing season peak is when plants are both capable of maximin rates of photosynthesis, but also at high risk of photoinhibition from high radiation levels and temperatures. By combining gas exchange measurements and photosynthesis modelling, Wu et al. (2021) found that in Chinese fir, maximum rate of photosynthesis (Vcmax) was highest in younger and sunlit needles and lowest in mature shaded needles. In Wu et al. (2021), the seasonal cycles of Vcmax followed the same pattern over the growing season, peaking in the middle of summer, at which point the differences in Vcmax between needle classes were largest. Similarly to the results from Wu et al. (2021), the results here show the general seasonal VI pattern across positions was conserved, but the difference between them changed.

4.5.4 Drought effects throughout the canopy

The experimental setup for this study was predominantly focused on using VI to detect drought responses, which is covered in Chapter 3. However, how these drought effects differ throughout the canopy is of interest and importance in its own right, as well as a relevant factor in remote sensing of forest canopies. Across the majority of VI, drought effects were consistent between age classes and vertical positions. In three VI (ARI, ARI2 and PRI) however, drought effects differed. In the upper canopy, drought effects were most pronounced, followed by the N^{old} needles then N^{lower}. Anthocyanins and the xanthophyll cycle (PRI) are associated more with stress responses than light capture (Chalker-Scott, 1999; Steyn et al., 2002; Chou et al., 2017; Wang, Chen, & Ju, 2020a; Simkin et al., 2022), and ARI, ARI2 and PRI were identified as the best performing VI for drought stress monitoring in Chapter 3. It is perhaps unsurprising that these indices are sensitive to within-canopy stress response variation. For all three of these VI, the stress response is greatest in N^{upper}, followed by N^{old} then N^{lower} (Figure 4.7). During drought stress, stomata close to avoid water loss, which reduces photosynthesis and therefore the quantity of energy which can be dissipated. Under these conditions, plants are more susceptible to photoinhibition as they have an excess of energy (Filella et al., 2009; Wong & Gamon, 2015a; Mõttus et al., 2019). This is counteracted by expression of non photochemical quenching mechanisms such as the xanthophyll cycle and anthocyanin expression. Gonzalez-Dugo et al. (2012) finds heterogeneity in drought stress response (closed stomata) throughout an Almond (*Prunus dulcis*) canopy. Taller trees are inherently more vulnerable to drought stress due to higher evaporative demand, non-linear increase in xylem-wall resistance with height and higher radiation (Bennett et al., 2015; McDowell & Allen, 2015; Stovall et al., 2019). Top-dying has been observed as a response to drought in Norway spruce (Green & Ray, 2009). It is likely that in

the upper canopy (N^{upper} and N^{old}), higher light intensities are intensifying photo inhibitory effects leading to a more pronounced drought stress response because these needles are effectively in a higher stress environment.

4.6 Conclusions

Repeat measurements and calculation of VI provide possibilities to efficiently evaluate a range of plant biophysical properties over time and throughout a plant canopy. The results here highlight clear differences in needle reflectance properties between needle positioning in the canopy and needle age. In support of existing evidence, higher quantities of all pigments were detected in the lower canopy, despite the trees in this experiment being relatively small in stature (all trees were < 3 m). General pigment patterns were less clear across needle age cohorts. Pigments in needles accumulate over time in many conifer species, however, this effect was not detectable in carotenoid VI. It is suggested here that the overlapping spectral range of chlorophyll and carotenoids makes retrieval of carotenoid concentrations difficult and that chlorophyll:carotenoid ratios are better represented. Future work could aim to develop conifer specific carotenoid estimation with remote sensing, possibly by using a wider range of hyperspectral bands to disentangle the effects of the two pigment groups. Anthocyanins are routinely understudied in the literature despite their important and diverse roles in plant regulatory mechanisms. Directly measuring anthocyanin content in needles across canopies could further understanding of their distribution and allocation.

An explanation for the distribution of water content through the canopy using the leaf economic spectrum hypothesis is presented, with the caveat that measurements using longer wavelength (NIR, SWIR) reflectance should be interpreted with caution. The cruciality of water distribution during drought stress suggests this merits further research.

The work here highlights the potential to build on reflectance-based trait retrieval methods using complementary metabolomic or water content measurements. Including repeat pigment sampling across various canopy positions, over an experimental stress, in combination with hyperspectral analysis, would further provide potentially crucial insight into Sitka canopy dynamics.

Chapter 5

Evaluating five MODIS Vegetation Indices (VI) for tracking GPP seasonal dynamics in a UK mature Sitka spruce (*Picea sitchensis*) plantation. Are effects of the 2018 drought detectable from space?

5.1 Introduction

Monitoring plant drought stress through Satellite-based Remote Sensing (SRS) can contribute to effective forestry management (Le et al., 2023) and reduce drought risk (Altemus Cullen, 2023) at the regional scale (Vicente-Serrano, 2007; Brown et al., 2008; Song et al., 2013). The potential to evaluate and monitor UK forestry species could greatly improve future drought resilience, by informing their silviculture and identifying drought resistant or vulnerable populations. Despite increasing recognition of drought stress as a critical issue for forest health and future forest resilience, research on remote-sensed methods to assess water stress in forests is relatively limited (Le et al., 2023), with the majority of work being conducted on agricultural systems. Most UK commercial forestry species are conifers, which are one of the most at risk groups of drought induced mortality (McDowell, 2011; McDowell & Allen, 2015; Klein et al., 2019; Balekoglu et al., 2023). Mortality could be detrimental to the long term investments required for forestry and reduce the important carbon sink forests provide (Berry & Brown, 2021; Locatelli et al., 2021).

The drought experiment analysed in Chapters 3 and 4 highlighted the usefulness of VI for detecting drought responses in Sitka spruce and the plethora of information that can be acquired with hyperspectral imaging. Scaling this to the satellite level must overcome a number of practical constraints such as decreased spectral, temporal and spatial resolution. To overcome these limitations, the scope of trait retrieval is narrowed compared to previous chapters and the focus here is on linking VI to Gross Primary Productivity (GPP).

GPP is the total carbon assimilated through photosynthesis (Hashimoto et al., 2012). It is related directly to photosynthetic function and growth (Landsberg et al., 2020) and is therefore an important component of global forest monitoring and carbon models (Beer et al., 2010). GPP is generally downregulated under both abiotic and biotic stressors and can be considered a 'global sensor of environmental stress' (Biswal et al., 2011; Liu & van Iersel, 2021). Correct parameterisation of GPP is difficult but essential, with accurate detection of GPP phenology and dynamics giving insights into forest health including drought stress detection and monitoring. Using SRS to retrieve GPP is therefore a critical research aim.

A reliable and robust time series of GPP derived from satellite VI would be a vital tool for the UK forestry sector. It could help detect and monitor drought and other stressors to mitigate risks as well as evaluate carbon stocks to aid in carbon budgeting at regional and global scales. The study here will focus on Sitka spruce, the UK's most abundant conifer which is planted across uplands in northern England, Wales and Scotland (Armitage et al., 2013).

Evergreen conifers are notoriously difficult to assess using traditional VI as they stay green all year round with very subtle foliage changes (Wong et al., 2020). This means that canopy structure and pigment compositional alterations are more subtle than deciduous trees which seasonally undergo full canopy senescence.

5.1.1 Vegetation Indices (VI) selection

Many VI are available which are sensitive to a range of biophysical processes. This study uses five VI which are measures of processes related to GPP and the LUE model (Section 1.5.1 (p.28)). The selected VI have been previously correlated to GPP in the literature (Badgley et al., 2019; Huang et al., 2019; Liu et al., 2021; Wang et al., 2021) as well as related to components of the LUE model (Running et al., 2004; Middleton et al., 2009; Goerner et al., 2011; Verma et al., 2015; Noumonvi & Ferlan, 2020; Wong et al., 2020; Junttila et al., 2023). They consist of traditional 'greenness' VI (NDVI, EVI) and newer generation VI (CCI, NIRv GPP_{VI}). For a background and the theoretical bases for these VI see Sections 1.4.2 and 1.5.1 (p.25

and 28). The formula for these VI is presented in Section 2.4.7, Table 2.2 (p.58).

5.1.2 Contamination and discontinuity

Temperate regions such as the UK suffer from high frequency of cloud cover (see Section 2.4.4 (p.53)). Various gap filling and composite creating methods exist to deal with the discontinuity of satellite time series. However, these suffer from potential bias (Testa et al., 2018), can miss rapid vegetation transitions and cannot account for prolonged periods with no usable observations. The analysis here uses the MODIS VI time series developed in Section 2.4.5 (p.54) which aims to overcome this limitation with various compositing and interpolation techniques. These include time series of the VI outlined above at three temporal resolutions which differ in their signal-to-noise trade offs (Verbesselt et al., 2010; Yan et al., 2020). This study will evaluate the VI and associated models at these time intervals and discuss the recommendations of each for future work at high cloud probability sites.

5.1.3 Research aims

— Evaluate five VI for uses in modelling Sitka spruce GPP phenology. How do different formulations of the LUE model affect GPP prediction and is combining meteorological variables (PAR, air temperature, VPD) crucial for accurate GPP estimation?

— Are newer VI (CCI, NIRv GPP_{VI}) better correlated to GPP than traditional greenness VI (NDVI, EVI) for evergreen needleleaf forests?

— Can drought induced GPP reductions be detected with VI models at multiple temporal scales?

— How well can temporal aggregating or interpolation successfully overcome low data availability at a high latitude site? And what are the cost-benefits of different time interval VI timeseries?

5.2 Chapter methods

5.2.1 Data

The study was conducted at the Harwood field site using data spanning 2015 - 2018 (Section 2.3.2 (p.47)). This period was characterised by a drought in 2018 which reduced site productivity (Xenakis et al., 2021). The analysis used a number of data sources. For detailed description of study site and data sources see Sections 2.3.2 and 2.4 (p.47 and 50). Briefly, time series for five VI (NDVI, EVI, CCI, NIRv

and GPP_{VI}), at three temporal resolutions (VI_{day}, VI_{16}, VI_{month}), were created from the same MODIS MAIAC scenes which spatially overlap the flux tower footprint of the study site (55°13'00.1"N 2°01'31.7"W). VI_{day} uses a Gaussian process regression (GPR) to statistically interpolate available data to daily observations (Belda et al., 2020). The VI_{16} uses a Constrained View-Maximum Value Composite (CV-MVC) (Didan et al., 2015) procedure to select the best available pixel every 16 days. VI_{month} are monthly averages of high quality observations. For VI_{16} and VI_{month} when data are not available for a specific time window, a historical average value is inserted. For construction of LUE models (Section 1.5.1 and 5.2.2), in combination with the VI timeseries, meteorological variables were downloaded from the ERA5 climate reanalysis dataset (Muñoz Sabater, 2021) (see Section 2.4.2), namely Mean daily Photosynthetically Active Radiation (PAR, mW m^2, mean daily temperature (°C) and mean daily mole fraction vapour pressure deficit (VPD, derived from temperature and relative humidity using Equation 2.28, (p.64)).

Eddy covariance flux tower GPP data (ftGPP) were recorded at the study site. This was used to evaluate the relationship between VI model and forest productivity. The ftGPP was treated as ground 'truth' data. To characterise the drought period, ERA5 meteorological variables and the analysis by Xenakis et al. (2021) were used. ftGPP and meteorological variables were averaged to daily values.

5.2.2 Model construction

For the evaluation of different forms of VI-based GPP retrieval, 10 models were constructed, either using VI alone or incorporating LUE theory and including PAR and a light use efficiency term (ε). As discussed in Chapter 1 (Section 1.5.1, (p.28)), NDVI and EVI can act as proxies for FPAR, NIRv as a proxy for APAR (FPAR × PAR), and CCI as a proxy for ε (ε_{CCI}). As such, the models used in the analysis are as follows.

5.2.2.1 VI only models

Simple linear correlations between VI and GPP are used where,

$$GPP = VI \tag{5.1}$$

and VI is replaced by one of the five selected VI (NDVI, EVI, CCI, NIRv, GPP_{VI}).

5.2.2.2 Light use efficiency term (ε)

For the formulation of LUE models, a measure of ε is needed. And for the purpose of this analysis that comes from either CCI (ε_{CCI}) or from meteorological scalars

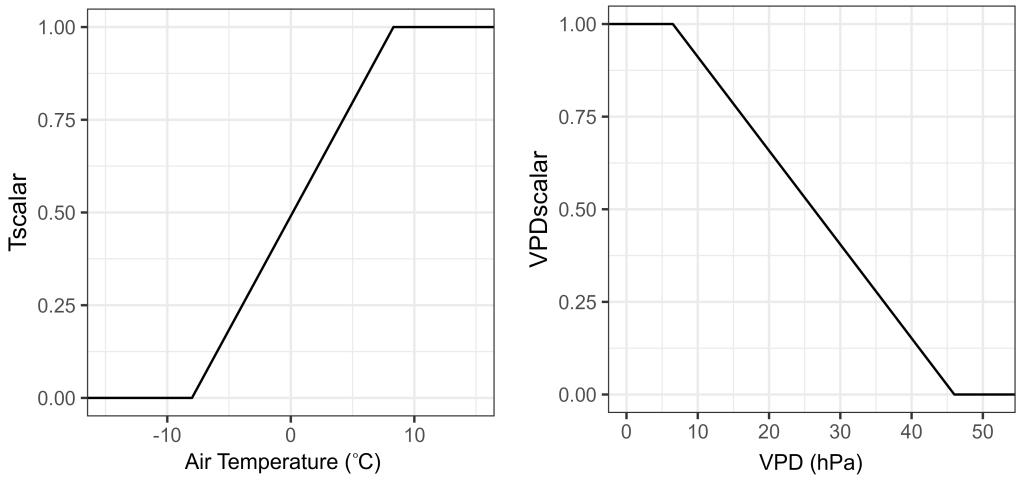

Figure 5.1: Meteorological scalar functions used to reduce ε max in Equation 5.2. Minimum and maximum temperature and Vapour Pressure Defict (VPD) are taken from the MOD17 Biome Parameter Lookup Table (BPLUT) which determine the biome specific meteorological limits to photosynthesis (Running & Zhao, 2015).

($\varepsilon_{\text{MODIS}}$). $\varepsilon_{\text{MODIS}}$ is equal to ε from the MODIS daily GPP product (MOD17) (Running & Zhao, 2015; Junttila et al., 2023) and is calculated as,

$$\varepsilon_{\text{MODIS}} = \varepsilon_{\text{max}} \times \text{T}_{\text{scalar}} \times \text{VPD}_{\text{scalar}} \tag{5.2}$$

Where ε_{max} is a biome specific (Evergreen Needleleaf Forest (ENF)) value of 0.000962. T_{scalar} and $\text{VPD}_{\text{scalar}}$ are temperature and VPD restrictions calculated from linear ramp functions of daily air temperature and VPD (Figure 5.1). The temperature and VPD limits range from 0 which strongly constrains photosynthesis to 1 where no limits on photosynthesis occur. The ε_{max}, temperature limits and VPD limits are taken from the MOD17 Biome Parameter Lookup Table (BPLUT) (Running & Zhao, 2015).

For determination of ε_{CCI}, CCI is scaled to obtain only positive values using the transformation,

$$\varepsilon_{\text{CCI}} = \frac{\text{CCI} + 1}{2} \tag{5.3}$$

as in Drolet et al. (2005) and Rahman et al. (2004) to convert CCI into an 'efficiency' term.

5.2.2.3 LUE models

Four traditional LUE models using a measure of PAR and ε (see Equation 1.1 (p.28)) and one using the equation,

$$\text{GPP} = \text{NIRv} \times \varepsilon_{\text{MODIS}} \tag{5.4}$$

are included in analysis.

Therefore the models used were NDVI, EVI, CCI, NIRv, GPP_{VI}, NDVI $\times$ PAR $\times \varepsilon_{\text{MODIS}}$, NDVI $\times$ PAR $\times \varepsilon_{\text{CCI}}$, EVI $\times$ PAR $\times \varepsilon_{\text{MODIS}}$, EVI $\times$ PAR $\times \varepsilon_{\text{CCI}}$ and NIRv $\times \varepsilon_{\text{MODIS}}$. For conciseness, the nomenclature of models will state the model terms followed by the time interval for example NDVI $\times$ PAR $\times \varepsilon^{\text{CCI}}_{\text{day}}$ and NDVI $\times$ PAR $\times \varepsilon^{\text{CCI}}_{16}$ represents the same model run at the day and 16 day time interval.

5.2.2.4 Model validation

To establish the model coefficients for GPP predictions and perform model validation, a leave-one year-out procedure was used. Using the 16 day timeseries, one year of data was removed (Test data) and models built using the Equations 5.1 to 5.2 using the remaining three years' data (Training data). The coefficients from the training models were then used to predict GPP using the removed Test data. Model performance evaluations were carried out for each of the four study years (2015 - 2018) and averaged. For every model formulation, the coefficients from each of the four training models (one for each year) were averaged. These averaged coefficients were then used to construct models for further analysis at all three time intervals.

5.2.3 The 2018 drought

2018 was considered a drought year. Very little rain fell between late June and early August (Appendix D, Figure D.1 (p.229)). Soil moisture dropped from field capacity (around 32% water content) in mid April, to around 20% by August, as discussed by Xenakis et al. (2021). The total yearly ftGPP dropped 5% in 2018 relative to the previous three year average due to drought.

5.2.4 Statistical analysis

To evaluate how closely the models are related to ftGPP, regression analyses were performed for each model at each time interval (day, 16 day and month). A simple linear least squares regression was used to determine the relationship between the modelled GPP (mGPP) and ftGPP. From this, the coefficient of determination (R^2) and Root Mean Square Error (RMSE) were calculated to compare model perfor-

mance. Annual GPP estimates were calculated by totalling the cumulative mGPP for each year, these totals were used to estimate 2018 anomalies by calculating the percentage differences between the average annual total of 2015-2017 and the 2018 annual total. Data processing and statistical analysis were conducted in R and R studio (RStudio Team, 2020) unless otherwise stated.

5.3 Results

5.3.1 Model creation and validation

A leave-one year-out procedure was conducted using the 16 day time series data to validate the models and generate average coefficients used for further analysis. Performance (R^2 and RMSE) varied between years for all models (Figure 5.2). Results were generally clumped across years for each model. The PAR models (NDVI × PAR × $\varepsilon_{\text{MODIS}}$, NDVI × PAR × ε_{CCI}, EVI × PAR × $\varepsilon_{\text{MODIS}}$ and EVI× PAR× ε_{CCI}) had the highest R^2 and lowest RMSE. NDVI was the worst performing model (low R^2 and high RMSE), followed by EVI and NIRv. For CCI, EVI, NIRv and GPP_{VI}, performance was greatest in 2015 and R^2 was at least 0.1 higher than the across years mean. This corresponds with below average RMSE. For all models except EVI and NIRv correlation was lowest in 2018. This was especially true for the PAR models (except NDVI × PAR × $\varepsilon_{\text{MODIS}}$) and GPP_{VI}, where R^2 was at least 0.08 lower than the across year average. In the case of the EVI×PAR models, 2018 was more than 0.1 lower than the across years mean. The NDVI R^2 in 2016 was 0.11 higher than the across years mean. In general, all other results are within 0.05 (R^2) of the across years mean.

5.3.2 ftGPP/mGPP correlations

The best performing model was NDVI × PAR × $\varepsilon^{\text{CCI}}_{\text{month}}$ (R^2 0.90 and RMSE 1.12 gC $\text{m}^2\,\text{d}^{-1}$) and worst was NDVI_{day} (R^2 0.22 and RMSE 3.53 gC $\text{m}^2\,\text{d}^{-1}$) (Figure 5.3). The PAR models outperform non-PAR models where R^2 and RMSE ranges from 0.74 and 2.04 gC $\text{m}^2\,\text{d}^{-1}$ (NDVI × PAR × $\varepsilon^{\text{MODIS}}_{\text{day}}$) to 0.90 and 1.12 gC $\text{m}^2\,\text{d}^{-1}$ (NDVI × PAR × $\varepsilon^{\text{CCI}}_{\text{month}}$). PAR models run at the month time interval were always best performing, followed by 16 day. For other models, 16 day was the best performing time interval, except NIRv × $\varepsilon_{\text{MODIS}}$ where NIRv × $\varepsilon^{\text{MODIS}}_{16}$ and NIRv × $\varepsilon^{\text{MODIS}}_{\text{month}}$ have the same R^2 (0.6) and similar RMSE (16 day = 2.35 gC $\text{m}^2\,\text{d}^{-1}$, month = 2.26 gC $\text{m}^2\,\text{d}^{-1}$). For VI only models, CCI and GPP_{VI} were the best performing at all time intervals (Figure 5.3). This was most pronounced at 16 day intervals. NDVI poorly tracks GPP at all time intervals. The choice of ε term ($\varepsilon_{\text{MODIS}}$ or ε_{CCI}) had little effect on PAR models when the VI (representing FPAR) remained the same.

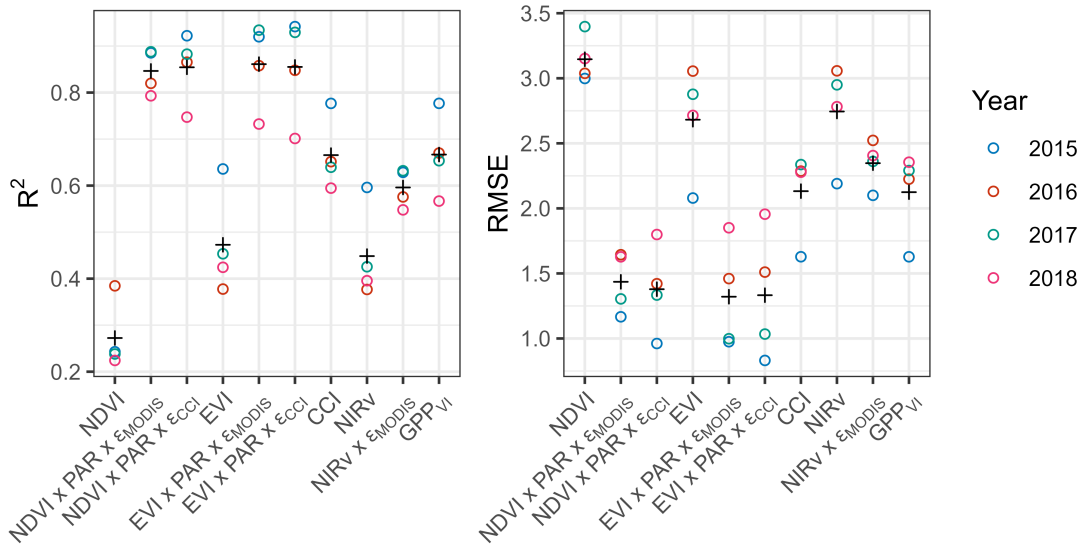

Figure 5.2: Summary statistics (Coefficient of determination (R^2) and Root Mean Square Error (RMSE)) for leave-one year-out GPP predictions. Circles indicate the year of analysis and a black cross indicates the average of all years. RMSE is in gC $m^2\,d^{-1}$. Model construction is outlined in Section 5.2.2 (p.123 - 125). VI abbreviations are; NDVI = Normalised Difference Vegetation Index, EVI = Enhanced Vegetation Index, CCI = Chlorophyll/Carotenoid Index, NIRv = Near-infrared radiation from vegetation and GPP_{VI} = Gross Primary Productivity Vegetation Index. For full VI formula and references see Table 2.2 (p.58)). For full results see Appendix D, Table D.1 (p.219)

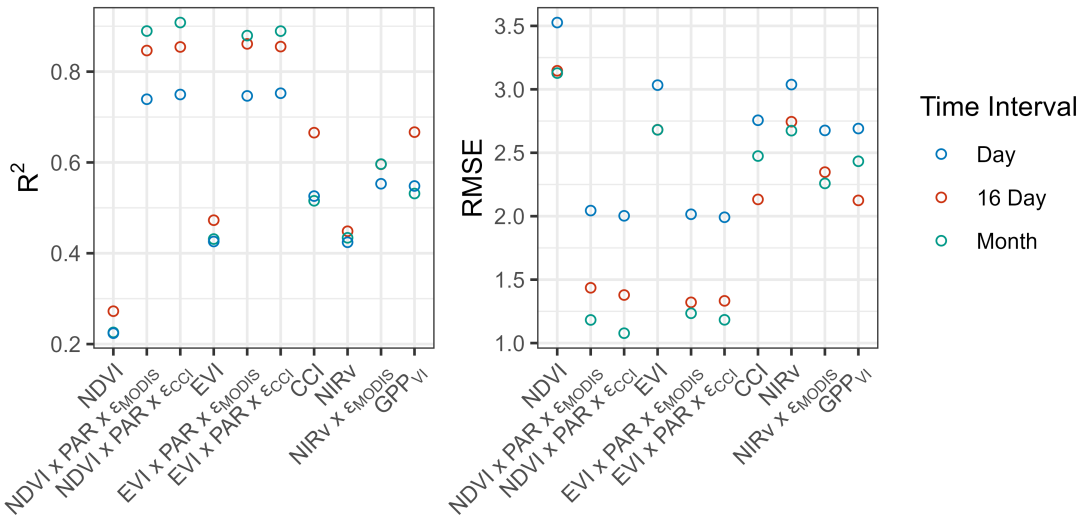

Figure 5.3: Summary statistics (Coefficient of determination (R^2) and Root Mean Square Error (RMSE)) for 10 Gross Primary Productivity (GPP) linear models at three temporal resolutions (Time interval). Model construction is outlined in Section 5.2.2 (p.123 - 125). VI abbreviations are outlined in Figure 5.2. For full VI formula and references see Table 2.2 (p.58). For full results see Appendix D, Table D.2 (p.221).

In these cases R^2 was never more than 0.01 different and RMSE was never more than 0.04 gC m^2 d^{-1} different. However, R^2 was never lower and RMSE never higher in ε_{CCI} models relative to ε_{MODIS} models with the same VI. For NIRv models, adding a ε term increased R^2 (by at least 0.1) and lowered RMSE (by at least 0.2 gC m^2 d^{-1}).

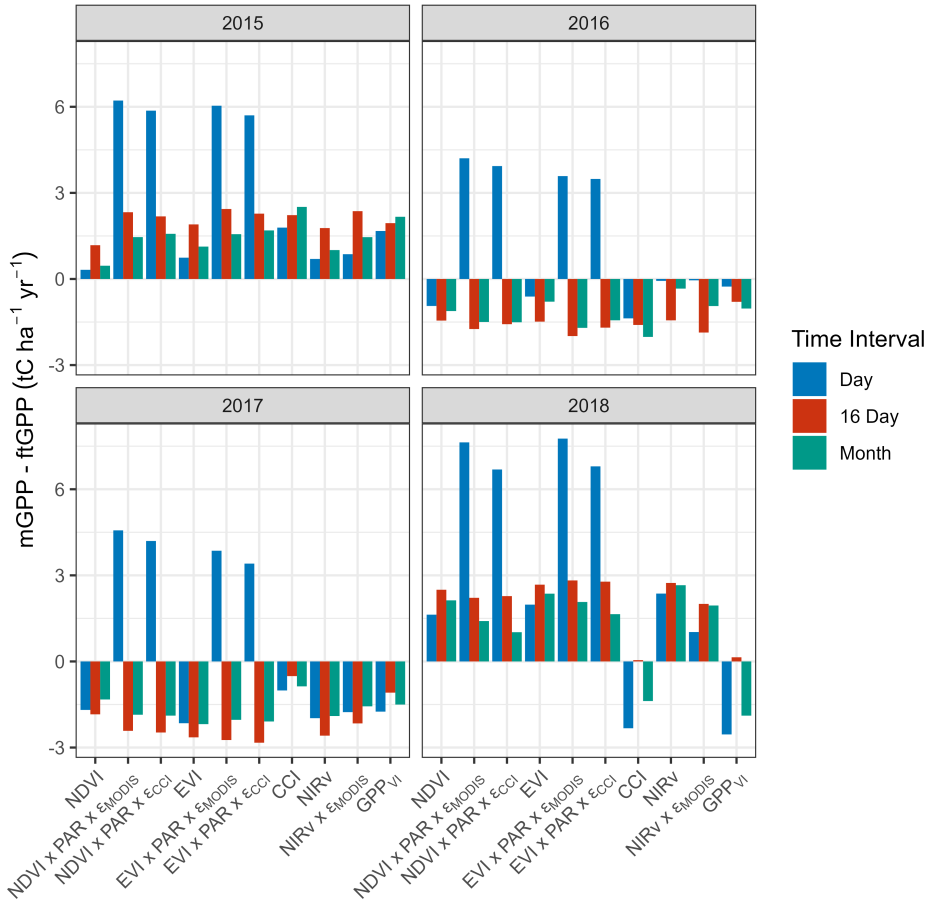

Figure 5.4: The difference between annual totals of modelled Gross Primary Productivity (mGPP) and annual totals of flux tower GPP (ftGPP) for 10 different models at three temporal resolutions (Time Interval) acorss the study period (2015 - 2018). Model construction is outlined in Section 5.2.2 (p.123 - 125). VI abbreviations are outlined in Figure 5.2. For full VI formula and references see Table 2.2 (p.58 - p.125). For full results see Appendix D, Table D.3 (p.222).

5.3.3 Annual GPP totals

The difference between cumulative yearly totals of mGPP and ftGPP were calculated to test each model's ability to predict annual GPP totals (Figure 5.4). Consistently across years, PAR models at the daily scale overestimated annual GPP by at least 3 tC ha^{-1} yr^{-1} (Figure 5.4). All models in 2015 overestimated annual GPP. $NDVI_{day}$, $NDVI_{month}$, $NIRv_{day}$ and $NIRv_{month}$ produced the closest estimates; all falling within 1.8 tC ha^{-1} yr^{-1}. With the exception of the daily PAR models, all other models underestimated annual GPP in 2016 and 2017 but GPP was generally better predicted

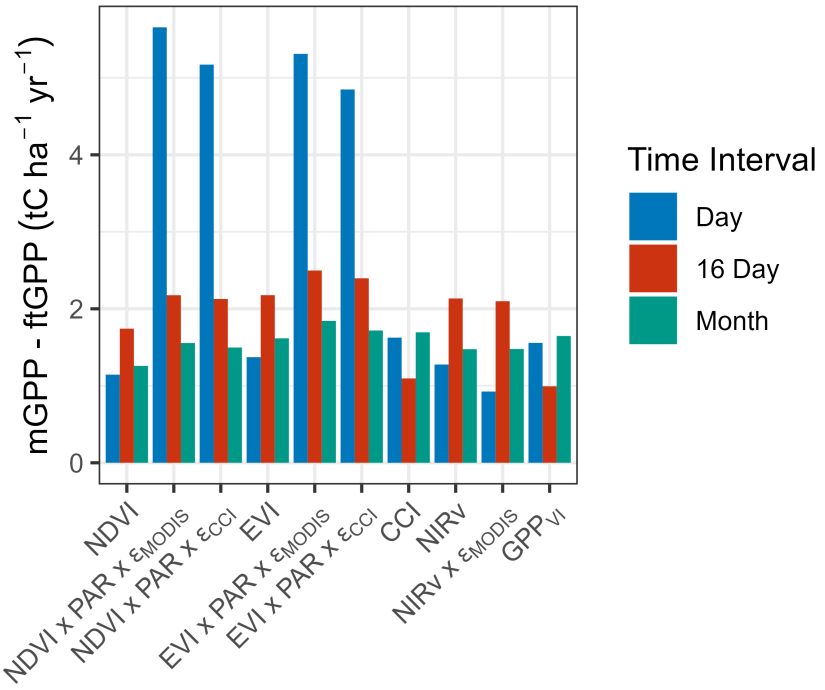

Figure 5.5: The difference between the average annual total of modelled Gross Primary Productivity (mGPP) and average annual total of flux tower GPP (ftGPP) for 10 different models at three temporal resolutions (Time Interval) across the study period (2015 - 2018). Model construction is outlined in Section 5.2.2 (p.123 - 125). VI abbreviations are outlined in Figure 5.2. For full VI formula and references see Table 2.2 (p.58 - p.125). For full results see Appendix D, Table D.4 (p.226).

in 2016. In 2016, at the daily time scale, the three NIRv models (NIRv, GPP_{VI} and NIRv $\times$ ε_{MODIS}) estimated annual GPP to within 0.27 tC ha^{-1} yr^{-1} of ftGPP. In 2018, CCI_{day}, CCI_{month}, GPP^{VI}_{day} and NIRv $\times$ $\varepsilon^{CCI}_{month}$ underestimated annual GPP while all other models overestimated it. CCI_{16} and GPP^{VI}_{16} estimated annual mGPP to within 0.05 tC ha^{-1} yr^{-1} and 0.15 tC ha^{-1} yr^{-1} ftGPP respectively.

On average, non-PAR models better estimated annual ftGPP (Figure 5.5). Average mGPP - ftGPP was 3.9 tC ha^{-1} yr^{-1}, 0.59 tC ha^{-1} yr^{-1} and 0.12 tC ha^{-1} yr^{-1} lower for daily, 16 day and monthly non-PAR models compared to PAR models. On average, day models were the most variable (the worst and best) predictors of annual ftGPP (Figure 5.5). The average estimates for NIRv $\times$ $\varepsilon^{MODIS}_{day}$ and NDVI $\times$ PAR $\times$ $\varepsilon^{MODIS}_{day}$ were 0.93 tC ha^{-1} yr^{-1} and 5.66 tC ha^{-1} yr^{-1} different from ftGPP. Month models had the least variation and all average estimates were within 0.6 tC ha^{-1} yr^{-1} of each other, whereas 16 day models were within a 1.5 tC ha^{-1} yr^{-1} range. On average the best performing 16 day and month models were GPP^{VI}_{16} (0.99 tC ha^{-1} yr^{-1} of ftGPP) and $NDVI_{month}$ (1.26 tC ha^{-1} yr^{-1} of ftGPP) respectively.

5.3.4 Time series

Time series of the cumulative difference in ftGPP and mGPP were plotted to track model performance temporally (Figure 5.6). Relative to ftGPP, the non-PAR models followed a consistent annual pattern however, the intensity of the difference between ftGPP and mGPP varied between years and time intervals (Figure 5.6). Generally, non-PAR models overestimated GPP (positive values of cumulative GPP difference) up to about day 50. After this (values becoming increasingly negative) mGPP underestimates ftGPP up to about day 200-250 and then overestimates for the remainder of the year. This results in annual totals within 3 tC ha^{-1} yr^{-1} of ftGPP. For the PAR models, greater deviation between years and time intervals is seen. All PAR models trace ftGPP well (cumulative GPP difference close to 0) up to ∼day 100 at which point in 2016 and 2017 the 16 day and month models underestimate GPP for the remainder of the year. The 2015 and 2018 16 day and month PAR models overestimate GPP for about 100 days. They then remain stable for the rest of the year. As discussed, the daily PAR models greatly overestimate annual GPP (Figure 5.4 and 5.6), this is due an accelerated rate of overestimation between days 100 to 200. Overestimation then continues (at a slightly reduced rate) for the rest of the year. This effect is most prominent in 2015 and 2018.

All models showed similar seasonal oscillations consisting of summer highs and winter lows (Figure 5.7). Due to the interpolation function, predicted GPP from daily time series are smooth lines, which fail to capture the short term variation that is evident in the ftGPP. The daily PAR model time series show a more pronounced summer high than other models (Figure 5.7), which is especially true in 2018, facilitating the anomalously high annual totals (Figure 5.4). PAR models track winter lows accurately, while VI-only models have a delayed winter low, relative to ftGPP. This is especially true for EVI, NDVI and NIRv. In general, especially in the case of PAR models, little difference between $\varepsilon_{\mathrm{MODIS}}$ and $\varepsilon_{\mathrm{CCI}}$ time series is visually apparent, however, differences between $\mathrm{GPP_{VI}}$ and NIRv $\times\, \varepsilon_{\mathrm{MODIS}}$ can be observed (Figure 5.7, for example in 2017 a summer drop in mGPP occurs in NIRv $\times\, \varepsilon^{\mathrm{MODIS}}_{\mathrm{month}}$ and is not present in $\mathrm{GPP^{VI}_{month}}$ while in 2018 a summer drop occurs in $\mathrm{GPP^{VI}_{month}}$ but not in NIRv $\times\, \varepsilon^{\mathrm{MODIS}}_{\mathrm{month}}$.

5.3.5 Drought anomaly

Xenakis et al. (2021) highlighted a reduction of 5% ftGPP in 2018 compared to the previous three year average due to the effects of a drought. 2018 anomalies were calculated for each model at every time step to identify the model's ability to detect the annual productivity decline of the 2018 drought. CCI and $\mathrm{GPP_{VI}}$ at all time intervals were the only models to detect reductions, relative to the previous three

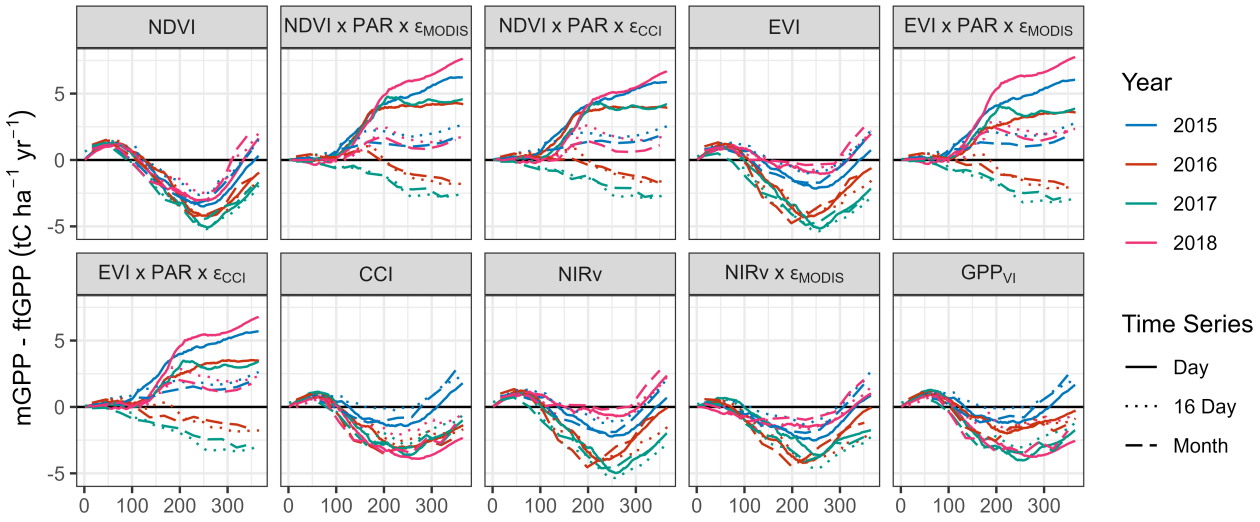

Figure 5.6: Cumulative modelled GPP (mGPP) across 2015 - 2018 for 10 models at three temporal resolutions. mGPP - ftGPP (tC ha^{-1} yr^{-1}) is mGPP minus cumulative flux tower GPP (ftGPP) (tC ha^{-1} yr^{-1}). The black line represents ftGPP (tC ha^{-1} yr^{-1}). Model construction is outlined in Section 5.2.2 (p.123 - 125). VI abbreviations are outlined in Figure 5.2. For full VI formula and references see Table 2.2 (p.58).

year average, in GPP in 2018 (Figure D.5). The strength of these reductions varied greatly between the time intervals. At the 16 day time scale the two models predicted a drought anomaly of -5.10% and -4.62% respectively, within 0.5% of the ftGPP. At the month scale the two models were over 5% lower (10.4% and 12.5%) and over 9% (14.1% and 15.2%) at the day scale. NIRv $\times$ $\varepsilon_{\text{MODIS}}$ at the day scale predicted +0.05% mGPP relative to the previous three year avearge, whereas all other models produced at least a 2.7% increase in 2018 annual GPP compared to the other years. For all models the 16 day time interval predicted the highest percentage difference and this was up to 15% more than ftGPP in the case of EVI $\times$ PAR $\times$ ε_{CCI}.

5.4 Discussion

5.4.1 mGPP / ftGPP correlations

Accurately monitoring and predicting GPP, using only satellite acquired data, has great appeal for forestry research and commercial forestry applications (Donoghue et al., 2004; Hashimoto et al., 2012; Walshe et al., 2020). Satellite data provide consistent and repetitive global observations, facilitating the near continuous GPP tracking of any forested surface (Hashimoto et al., 2012). Due to this appeal, satellite-based GPP retrieval research is widespread, active, and ongoing (Nagai et al., 2010; Gamon et al., 2016; Joiner & Yoshida, 2020; De Pue et al., 2023;

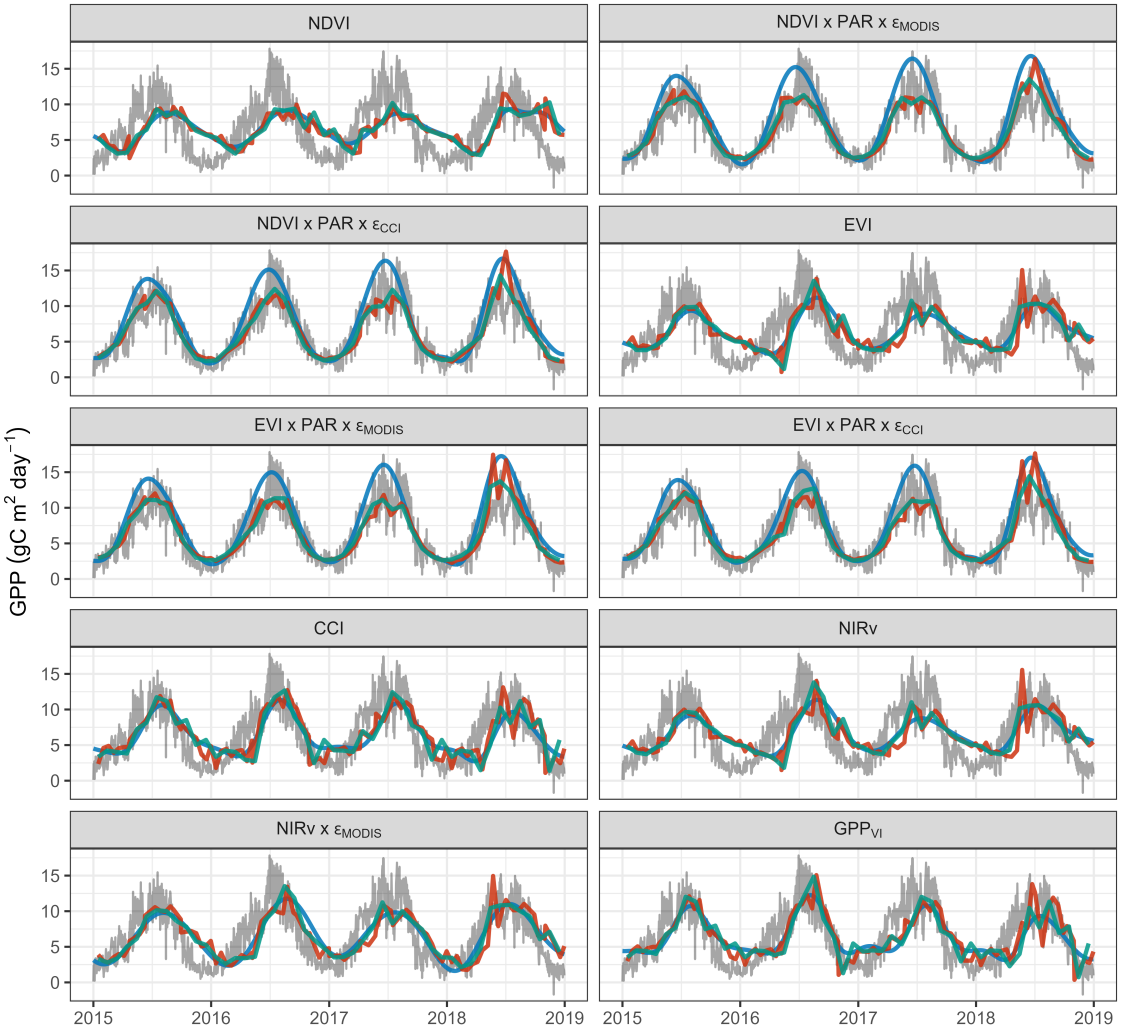

Figure 5.7: Time series (2015 - 2018) of Gross Primary Productivity (GPP) predicted from 10 GPP models and flux tower GPP (ftGPP) at three temporal resolutions. Each box is a seperate model run where colours denote the temporal resolution (Blue = daily, Red = every 16 days, Green = monthly). The grey line in all boxes is ftGPP. Note: estimates at the daily time interval peak in summer due to the interpolation technique fitting a line through peak summer values whereas, at coarser temporal resolutions these more extreme values are averaged across a given temporal window which reduces the summer peak. Model construction is outlined in Section 5.2.2 (p.123 - 125). VI abbreviations are outlined in Figure 5.2. For full VI formula and references see Table 2.2 (p.58).

Junttila et al., 2023). Conifers are inherently difficult to monitor with SRS and are therefore understudied. Research within this field is often focused on traditional 'greenness' VI such as NDVI or EVI (Hmimina et al., 2013). Here, the relationship between several VI and GPP are tested in a mature commercial Sitka spruce forestry plantation, representative of large areas of UK forest (Locatelli et al., 2021). Sitka spruce is the most widespread UK species and arguably the UK forestry sector's most important species (Samuel et al., 2007). Satellite remote sensing work on

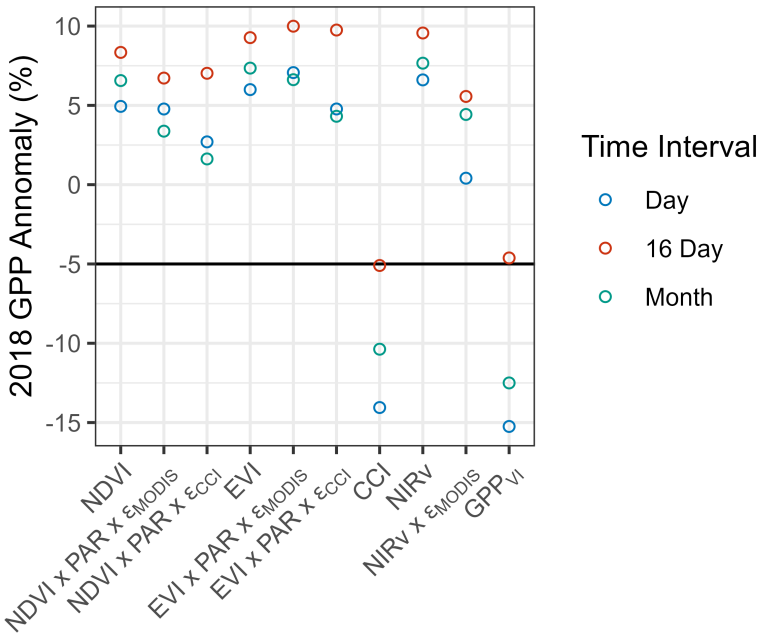

Figure 5.8: Percentage difference of annual GPP in 2018 relative to the previous three year average for 10 Gross Primary Productivity (GPP) models and three temporal resolutions. Each 2018 GPP anomaly is calculated as the difference (%) between the average total annual GPP of 2015 - 2017 and the total annual GPP in 2018. The black line represents the 2018 GPP anomaly for flux tower GPP (ftGPP), as reported by Xenakis et al. (2021). Model construction is outlined in Section 5.2.2 (p.123 - 125). VI abbreviations are outlined in Figure 5.2. For full VI formula and references see Table 2.2 (p.58). For full results see Appendix D, Table D.5 (p.227).

Sitka spruce, has previously been used to link structural and stand parameters to multispectral reflectance or Lidar data (Donoghue et al., 2004; Donoghue & Watt, 2006; Hauglin & Ørka, 2016), distinguish Sitka from other conifer species (Hauglin & Ørka, 2016; Ørka & Hauglin, 2016), assess nutrient deficiency in Irish commercial Sitka stands (Walshe et al., 2020) and track boreal growing seasons (Kimball et al., 2004). However, no previous work on satellite-based GPP retrieval for Sitka spruce exists.

In this study, the strength of the relationship between GPP and VI varied considerably between the choice of model and temporal resolution. Across the literature, relationships between many VI and GPP have been tested (Nagai et al., 2010; Gamon et al., 2016; Joiner & Yoshida, 2020). Simple linear VI/GPP relationships can be robust, are easy to use, and simplify the exploration of vegetation GPP response (Hashimoto et al., 2012). Likewise, introducing meteorological variables (PAR, temperature, and VPD scalars) within the framework of the LUE model enables a simplified representation of photosynthesis at reduced modelling complexity, relative to process-based models (discussed in Chapter 6) (Running et al., 2004;

Middleton et al., 2009; Goerner et al., 2011; Verma et al., 2015; Noumonvi & Ferlan, 2020; Wong et al., 2020; Junttila et al., 2023).

Here, models that included PAR had the strongest linear correlation with ftGPP, adding to existing evidence the usefulness of the LUE equation for GPP estimation. This highlights the advantage of using meteorological data, in conjunction with satellite reflectance, to capture photosynthetic variation (Running et al., 1989; Hashimoto et al., 2012; De Pue et al., 2023).

At the 16 day and month timescales PAR models explained over 80% of ftGPP variation (Figure 5.3). This is similar to the 76% found by Junttila et al. (2023) for eight ENF sites (27 site years of predominantly Scots pine or Norway spruce forests) across Northern Europe. Junttila et al. (2023) achieved this correlation using an EVI $\times$ PAR $\times$ $\varepsilon_{\mathrm{MODIS}}$ model using Sentinel-2 10 m resolution images.

The NDVI $\times$ PAR $\times$ $\varepsilon_{\mathrm{MODIS}}$ model used here is based on the formulation of the MODIS MOD17 product (Running & Zhao, 2015). Here the model explained 85% of ftGPP variation at 16 day resolution, which is higher than 69% achieved for Canadian Eastern white pine (*Pinus strobus L.*) (Wong et al., 2022) or 67% for 16 ENF sites (Hashimoto et al., 2012) using the MOD17 product directly. In the analysis by Wong et al. (2022) a LUE model including CCI as a proxy for ε (NDVI $\times$ PAR $\times$ $\varepsilon_{\mathrm{CCI}}$) only achieved 40% explained ftGPP variation, compared to 85% presented here. In Wong et al. (2022) the authors used CCI directly rather than scaled CCI (Equation 5.3) used in the present analysis. This suggests transforming CCI for ε estimation (as in Rahman et al. (2004) and Drolet et al. (2005)) may be a better approach.

Non-PAR and VI only models were also evaluated. $\mathrm{GPP_{VI}}$ explained up to 66% of ftGPP variation. Higher than the 63% found for Canadian Eastern white pine (Wong et al., 2022). The analysis by Wong et al. (2022) ($\mathrm{GPP_{VI}}$ is referred to as MODIS NIRv x CCI in (Wong et al., 2022)) did not implement any gap filling after cloud screening. The satellite data therefore, were direct observations and not historical averages, aggregated or interpolated values. Wong et al. (2022) used eight years of flux tower data averaging 58.5 observations per year. In the present study however, the cloud contamination and quality filters resulted in only 17.4 observations per year. This highlights the discrepancies in data availability at different global localities, making gap filling necessary at some sites, such as the Harwood site used here. The comparable results between Wong et al. (2022) and this study highlight the effectiveness of the CV-MVC methodology in creating a continuous time series when data availability is low.

The linear CCI/GPP relationship in the present study could also explain up to 66%

of ftGPP variation over the study period. Gamon et al. (2016) tested GPP/CCI over a range of sites which averaged 55% explained ftGPP variation. However, depending on the composition of species, the strength of this relationship varied greatly. At sites with a mixture of deciduous and evergreen cover, R^2 was 0.78 and 0.77. At a site containing predominantly evergreen vegetation, consisting of Douglus fir (*Pseudotsuga menziesii*) and western hemlock (*Tsuga heterophylla*), R^2 was only 0.32. In the context of this analysis by Gamon et al., (2016), the purely evergreen Sitka spruce site analysed in the present study performs well, even without the seasonal optical influence of deciduous vegetation. Using 105 FLUXNET sites across 526 site years, NIRv could explain 56% of GPP variation at monthly scales (Badgley et al., 2019); better than the 44% presented here. However, with the addition of the $\varepsilon_{\text{MODIS}}$ term results were between 55-59%, depending on the time interval, highlighting the improvements that hybrid models (those including SRS reflectance and meteorological inputs) can have over reflectance-only based models, even without the inclusion of PAR.

The 16 day and month correlations between ftGPP and EVI for Sitka spruce presented in this study were 47% and 43% respectively, which is similar to the 16 day and 32 days composite found by Hashimoto et al. (2012) (47% and 46%), who averaged the GPP/EVI response over a range of needleleaf FLUXNET sites. The NDVI relationships found here (27% and 23%) however, were around 10% worse than 38% and 32% presented by Hashimoto et al. (2012). In the present study, NDVI was the model with the weakest linear correlation with GPP and explained 23-28% of GPP variation depending on the temporal resolution. NDVI is well documented to perform poorly in tracking evergreen seasonal cycles, due to saturation, and subtle changes in 'greenness' in evergreen forests (Huete et al., 2002; De Pue et al., 2023). Other authors have found NDVI to perform marginally worse (Hashimoto et al., 2012) or better than EVI (Huang et al., 2019), worse than NIRv (Huang et al., 2019), and substantially worse than CCI (Gamon et al., 2016) for evergreen needleleaf forests.

5.4.2 Light use efficiency (ε) term

Despite different approaches, the choice of ε had little effect on model performance (Figure 5.3). Both ε terms selected for this analysis have previously been used to estimate GPP using satellite data (Rahman et al., 2004; Running & Zhao, 2015; Junttila et al., 2023; Prentice et al., 2024). The widely used MOD17 data set (which includes $\varepsilon_{\text{MODIS}}$) limits photosynthetic capacity (ε_{max}) by VPD and temperature scalars and is based on biome-specific values (Running & Zhao, 2015; Junttila et al., 2023). A significant assumption of the MOD17 LUE model (and therefore $\varepsilon_{\text{MODIS}}$)

is that no variation of ε within biomes is accounted for, which fails to capture temporal and spatial dynamics and limits potential model accuracy (Rahman et al., 2004; Huang et al., 2024; Prentice et al., 2024). In the present system, the $\varepsilon_{\text{MODIS}}$ provided almost no constraints to mGPP throughout summer in any year (Appendix D, Figure D.2 (p.230)), despite known VPD photosynthetic limitations in 2018 (Xenakis et al., 2021), suggesting poor parametrisation of VPD scalars. The poor simulation of VPD limits on growth could be due to a non-optimal choice of VPD threshold for Sitka spruce, highlighting issues that may arise from biome specific values. $\varepsilon_{\text{MODIS}}$ did limit photosynthesis due to low temperature constraints during winter and the transitions to peak growing season.

The relationship between ε and PRI (of which CCI is a derivative) was initially demonstrated by Gamon et al. (1992), modelling this theoretical relationship through SRS models is challenging (Coops et al., 2010). In 2018, drought-induced reductions in GPP were detected annually by CCI models (discussed in Section 5.4.4); however, declines in mGPP were not detected in 2018 by models including the ε_{CCI} term. Very minor summer mGPP differences are detected between $\varepsilon_{\text{MODIS}}$ and ε_{CCI} models, and both predict high 2018 annual GPP. This suggests ε_{CCI}, like $\varepsilon_{\text{MODIS}}$, fails to sufficiently limit photosynthesis during a drought year. 531 nm based VI (e.g. CCI, GPP_{VI} and PRI) offer the potential for spatially and temporally dynamic ε retrieval that can reduce the reliance on LUT $\varepsilon_{\text{MODIS}}$–type terms, potentially facilitating more model realism (Rahman et al., 2004; Huang et al., 2024; Prentice et al., 2024). A number of successes in the literature have been achieved, generally with MODIS band 11 (centered at 531 nm) reflectance (Rahman et al., 2004; Drolet et al., 2005; Drolet et al., 2008; Guarini et al., 2014; Middleton et al., 2016). Using VI-satellite based retrieval of ε, Rahman et al. (2004) found that PRI could track mid-season reductions in LUE from drought stress. As discussed in Section 1.4.2 the PRI (and so CCI) signal is influenced by solar and view angles (Gamon et al., 1992; Barton & North, 2001) and, although satellite images with $> 45°$view angle were not included here, non-ε variation could be distorting the CCI signal. When only forward scatter views were taken into account, Middleton et al. (2016) achieved more accurate ε retrieval than MOD17. Therefore, future work should specifically account for all sources of CCI variation when deriving ε_{CCI}. Another avenue of research focuses on the combination of PRI measurements with SIF to provide complementary information for ε retrieval (Schickling et al., 2016; Wang, Chen, & Ju, 2020b), however, the most suitable approach has not been established (Prentice et al., 2024).

5.4.3 Temporal resolution

Retrieving time series and phenological metrics, from satellite remote reflectance data, often relies on creating a smooth VI time series from noisy discontinuous data or aggregating observations to a coarser temporal scale (Atkinson et al., 2012). Choosing the temporal scale to retrieve time series involves a trade-off between the signal-to-noise ratio (Verbesselt et al., 2010; Yan et al., 2020). High frequency observations can potentially give the truest representation of vegetation function, but suffer noise from cloud clover, BDRF effects or other signal interferences (Wang et al., 2004; Wang, Chen, & Ju, 2020a). Interpolation techniques increase temporal resolution but can introduce large bias (Wang et al., 2004; Verbesselt et al., 2010). Compositing or temporal averaging gives a more aggregated and smoothed representation of vegetation dynamics, minimising the impact of short-term noise; however, temporal resolution is lost (Testa et al., 2014; Wang, Chen, & Ju, 2020a) and simple metrics such as annual totals capture the interannual variability of an ecosystem and are useful tools for monitoring forest function. These can reveal long term dynamics (Fu et al., 2017; Wang et al., 2021), and contribute to calculating global carbon budgets (Gilabert et al., 2017; Tang et al., 2021).

The drivers of GPP vary at different temporal scales which needs to be accounted for in modelling (De Pue et al., 2023). Despite the strongest correlations at daily, 16 day and monthly scales, the PAR models produced the worst estimates of annual GPP. Similarly to the present study, analysis by De Pue et al. (2023) looked at the performance of models with or without meteorological components and found that at sub seasonal timescales meteorological factors are the most important driver of GPP variation. However, this relationship does not hold true at annual timescales.

The NDVI models correlated poorly to ftGPP at daily, 16 day and monthly scales however, link relatively well to annual productivity. NDVI has previously been highlighted as an annual predictor of GPP (Goward et al., 1985; Hashimoto et al., 2012; Gilabert et al., 2017; Fernández-Martínez et al., 2019; Wang, Chen, & Ju, 2020a; Liu et al., 2021), as has EVI (Hashimoto et al., 2012; Gilabert et al., 2017; Fernández-Martínez et al., 2019; Liu et al., 2021; Sri Rahayu Romadhoni et al., 2022) and CCI (Fernández-Martínez et al., 2019; Wang, Chen, & Ju, 2020a). Here, on average NIRv based models produced the best annual estimations over the study period, which supports recent findings that NIRv is strongly related to annual GPP (Fernández-Martínez et al., 2019; Liu et al., 2021). Due to this relationship Wang et al. (2021) recently used NIRv to capture global interannual GPP.

At sub-annual timescales PAR models perform better than VI-only models (Figure 5.3). This is likely due to the changing drivers of photosynthesis (De Pue et al.,

2023). At shorter timescales, photosynthesis is predominantly driven by changes in microclimatic variables (Stoy et al., 2009), e.g. PAR. These short term variations minimally change structural or pigment composition so are not detectable optically. Over longer time periods, plants acclimate to larger seasonal patterns which involves structural and physical regulation of, for example, chlorophyll concentration or LAI. These longer term changes are optically visible using VI and therefore correlate to GPP. Within the VI only models, those including the MODIS ocean band 11 (CCI and GPP_{VI}) were best correlated to ftGPP at the sub-annual scales. This is likely due to these capturing xanthophyll cycle dynamics which act on multiple temporal scales, to regulate energy dissipation (Lichtenthaler et al., 2007; Govender et al., 2009; Gamon et al., 2016; Wang, Gamon, et al., 2020; Wang, Chen, & Ju, 2020a; Wong et al., 2020, 2022).

A limitation of PAR models is that the estimation of GPP depends on the quality of meteorological forcing (De Pue et al., 2023). For annual estimations, VI alone may be sufficient. This may simplify modelling procedure and reduce bias associated with sometimes highly variable meteorological inputs (De Pue et al., 2023).

mGPP/ftGPP correlations were generally weaker for models interpolated to the daily time interval compared to the 16 day and month composites (Figure 5.3). Daily interpolations of VI time series are rare in the SRS literature (Verbesselt et al., 2010) but can produce less variability in phenological indicators than 16 day products (Hmimina et al., 2013). Here, a Gaussian Process Regression (GPR) was used to interpolate observed data to the daily time-step (Verrelst et al., 2019; Belda et al., 2020). Daily models captured general seasonal cycles however, when used to predict annual totals, resulted in high variability between models (Figure 5.4). Annual mGPP totals were especially poor at estimating annual ftGPP in PAR models. These models greatly overestimated annual ftGPP owing to very high summer GPP rates (Figure 5.7). The poor performance of daily PAR models could be due to a sampling bias which the daily interpolation exaggerates. The un-interpolated reflectance values used to construct the time series are acquired when clear satellite observations are present. These will be when cloud cover is low so PAR is disproportionately high. This means the interpolation is based only on high PAR observations and therefore summer values are exaggerated. In future aggregated PAR should be taken to reduce error, as in Junttila et al. (2023) who aggregated flux tower PAR to 7 day rolling averages.

In agreement with the findings by Hashimoto et al. (2012) the two aggregation methods used here (16 day and month) performed similarly to each other, and better than the daily interpolation, for capturing variations in ftGPP (Figure 5.3). Therefore, the 16 day models provided the best trade-off between robustness and temporal

resolution. 16 day composites are widely used for SRS phenological analysis (Huete et al., 2002; Kross et al., 2011; Guindin-Garcia et al., 2012; Yan et al., 2019; Zhao et al., 2022) however, limitations exist. Compositing methods can lead to large errors, as the exact date of acquisition is lost. For a 16 day composite, the acquisition date of two contiguous data points could be up to 32 days apart, if the best quality observation is at the beginning of one 16 day window and the end of the next (Testa et al., 2014; Wang, Chen, & Ju, 2020a). This artefact can greatly affect phenological interpretation. Compositing to a higher frequency, e.g. 8 days composites are commonly used, would introduce more missing data so is not advisable for this location which already relies heavily on historical average values to fill gaps.

5.4.4 Drought effects

Drought stress in natural forested environments is difficult to study (Clark et al., 2016; Locatelli et al., 2021). The present study system provides a serendipitous opportunity to evaluate VI models' ability to track a known GPP drought effect (Xenakis et al., 2021). By using energy balance and gas flux data, Xenakis et al. (2021) precisely quantified carbon fluxes of the Harwood study site and attributed a 5% decline in GPP to a natural drought event in 2018.

Annual anomalies were calculated to evaluate how well models detected the drought induced GPP reductions (Figure 5.8) reported by Xenakis et al. (2021). Only CCI and GPP_{VI} (the two VI that include reflectance at 531 nm) estimated a decline in annual GPP in 2018 relative to the previous three year average (Figure 5.8). The intensity of this decline was most accurate at the 16 day time interval. At the month and day scale however, the estimates were too low. CCI and GPP_{VI} track the ratio of carotenoids relative to chlorophyll. During drought, photosynthesis is arrested, therefore plants must dissipate excess light energy, which otherwise would be damaging. Carotenoids act as photo-protectants and antioxidants, and dissipate this excess light energy (Lichtenthaler et al., 2007; Govender et al., 2009; Gamon et al., 2016; Wang, Gamon, et al., 2020; Wang, Chen, & Ju, 2020a; Wong et al., 2020, 2022). This provides a mechanism for xanthophyll associated VI to track relatively subtle drought effects that 'greenness' VI may miss, as discussed in Chapter 3. NIRv performed well for annual GPP estimation here and in the literature (Wang et al., 2021) however, it performs poorly in the drought year suggesting its performance may be vulnerable to drought stress anomalies.

The poor parametrisation of the ε terms in the LUE models, as discussed, explains why the drought anomaly was not detected and annual totals were higher in 2018 relative to the three year average (Figure 5.8). High PAR levels occurred during drought (Appendix D, Figure D.1 (p.229)) which causes the model to predict high

photosynthetic rates while poor ε parametrisation fails to arrest this effect.

Summers like 2018 are likely to become the norm in the UK by 2050 (Betts & Brown, 2021) so detecting drought induced GPP dynamics will become ever more crucial. A model that is coupled closely enough to GPP to detect relatively subtle drought, or other stress-related reductions in Sitka spruce GPP is a vital tool for forestry research and management. This could facilitate UK wide early stress detection and stress monitoring (Song et al., 2013; Davies et al., 2020; Yang et al., 2020). Here the CCI and GPP_{VI} based models provided the best drought detection at the annual scale however, at finer temporal scales model performance was weakest at 16 day intervals in 2018 (Figure 5.2).

5.5 Conclusions

Here, 10 models using satellite based VI, meteorological inputs and LUE theory at multiple temporal resolutions were evaluated for their applicability for Sitka spruce GPP retrieval. The main drivers of GPP vary with temporal resolution so that, at sub annual scales models incorporating meteorological components, especially PAR, better capture photosynthetic regulation that is not visible optically. Therefore, PAR models are recommended for tracking GPP time series. For annual estimations this study supports evidence that LUE models cannot predict annual variation better than simple VI models. Traditional VI such as NDVI perform poorly at finer temporal resolutions but better for annual estimations; however, new VI (NIRv, CCI, GPP_{VI}) may have some advantages. NIRv on average was the best predictor of annual GPP, while VI including a band centred at 531 nm, associated with the xanthophyll cycle, captured the drought reduced anomaly in 2018, where no other models did. Despite some links between CCI and stress related GPP reductions, using CCI as proxy for ε in the LUE model failed to sufficiently reduce mGPP. ε_{MODIS} was poorly parametrised for the present system highlighting a limitation of biome specific LUT values in ecological modelling.

Chapter 6

Testing the Simple Biosphere Model (SiB) for GPP retrieval in a UK mature Sitka spruce (*Picea sitchensis*) plantation. Can new VI improve the model and are effects of the 2018 drought detectable with SiB?

6.1 Introduction

Gross primary productivity (GPP) is one of the most crucial parameters of forest health, global carbon monitoring and effective forest management (Cai & Prentice, 2020, see Section 1.5 and Chapter 5). Modelling it accurately is therefore of the utmost importance. Satellite data provide the means for GPP estimation at near continuous spatial (globally, at metre to kilometre resolution) and temporal scales (up to daily observations for the current century). Chapter 5 evaluated the relationship between five satellite-based Vegetation Indices (VI) and eddy covariance flux tower canopy GPP (ftGPP), using the LUE model, for a mature even-aged Sitka spruce plantation. Chapter 5 highlighted that the ability of simple SRS-based models to track seasonal canopy GPP is useful but limited.

In this chapter, process-based biophysical modelling, in the form of the Simple

Biosphere Model (SiB) (Section 2.5 (p.59)), is introduced. This is to assess if the increased complexity of this model, compared to simple LUE model formulations or VI-GPP relationships, provides worthwhile improvements to GPP retrieval to recommend it for monitoring UK conifer plantations. This analysis looks not only to evaluate the suitability of SiB for Sitka spruce GPP retrieval, but also to develop and test improvements to the ever evolving SiB model group (as documented in Haynes et al. (2020)). Current manifestations of SiB use satellite-based NDVI inputs to determine the biophysical parameters leaf area index (LAI), fraction of absorbed radiation (FPAR), and greenness fraction. This is largely for the integration of modelled leaf level photosynthesis (A) to the canopy scale (Sellers, Tucker, et al., 1996; Los et al., 2000, Section 2.5, Equations 2.34 to 2.40 (p.66 - 67)). However, as demonstrated in Chapter 5, NDVI poorly tracks evergreen conifer phenology and seasonal photosynthetic cycles. Other, newer VI, namely those incorporating the MODIS ocean band 11, centred around 531 nm, are better related to conifer GPP (Chapter 5, Gamon et al., 2016).

The novel analysis outlined in this thesis aims to improve the SiB model parameterisation by incorporating other VI, either as direct NDVI proxies, or for the development of Vcmax (maximum carboxylation rate) time series. Vcmax is one of the most important parameters for processed-based photosynthetic modelling due to sensitivity and influence on photosynthetic processes (Farquhar et al., 1980; Collatz et al., 1991; Kattge et al., 2009; Alton, 2017). It is commonly parameterised as a fixed value, which is unrepresentative of true biological systems where Vcmax is dynamic over seasonal cycles, peaking in midsummer in northern latitude climates (Alton, 2017). The analysis here aims to better represent a biologically meaningful Vcmax by introducing seasonal dynamic Vcmax time series (developed and presented in Section 2.6.2 (p.68)). Briefly, the Vcmax time series are; vmDy, built from fitting seasonal curves over daily optimised Vcmax values. This timeseries simulates seasonality and includes no interannual variation. vmCCI and vmGPP are derived from the daily VI datasets for the two MODIS band 11 based indices (CCI, GPP_{VI}).

The study forest used in this thesis suffered reductions in summer GPP due to a prolonged drought in 2018 (Xenakis et al., 2021). This provided an opportunity to test the outlined model for drought stress detection and also to improve understanding of drought induced GPP reductions in Sitka spruce, by introducing a drought stress term driven by the local vapour pressure deficit (VPD). VPD has been highlighted as a major driver for the stress induced photosynthetic reductions at the Harwood forest Sitka spruce study plantation (Xenakis et al., 2021).

6.2 Research aims

This chapter seeks to explore the effects of Vcmax, VI, seasonality and drought on model capacity to accurately predict GPP and seeks to answer the following research questions:

— Does introducing a more biologically realistic Vcmax improve SiB GPP predictions, and how well do VI (CCI andGPP_{VI}) act as Vcmax proxies?

— How do different VI represent vegetation parameters in SiB, and do other VI, relative to NDVI, improve SiB GPP estimation?

— How well does SiB model Sitka spruce GPP and does the model perform differently across seasons?

— Can the introduction of a water stress term (S_d, Section 2.26, p.63), based on VPD, improve SiB sensitivity to drought stress?

6.3 Chapter methods

The SiBx model (outlined in Section 2.5) was iteratively run with varying parameters to investigate the specific research aims and hypothesis of this Chapter. The model inputs were,

— Meteorological variables taken from the ERA5 climate reanalysis dataset (Section 2.4.2 (p.50)).

— MODIS reflectance based VI (NDVI, EVI, CCI, NIRv, GPP_{VI}), interpolated to daily observations using a Gaussian Process Regression (GPR) model (Section 2.4.5.1 (p.54)), and transformed to the same scale as NDVI using a predictive regression (Section 2.5.2.3 (p.65)).

— SiB2 parameters outlined in Sellers and Mintz; Sellers, Randall, et al.; Sellers, Tucker, et al. (1989, 1996, 1996) including Evergreen Needle Leaf (ENL) specific values.

— Dynamic Vcmax time series developed in Section 2.6.2 (p.68).

Iterative runs of SiBx were executed to test the suitability of the original fixed Vcmax proposed by Sellers, Randall, et al. (1996) for GPP modelling at a mature, even-aged Sitka Spruce site. The model was run for a series of Vcmax values, initially ranging from 20 to 200 $\mu mol\, m^2\, s^{-1}$ at 20 $\mu mol\, m^2\, s^{-1}$ intervals, and subsequently ranging from 50 - 70 $\mu mol\, m^2\, s^{-1}$at 2 $\mu mol\, m^2\, s^{-1}$ intervals. These iterative runs were conducted for five VI (NDVI, EVI, CCI, NIRv, GPP_{VI}). SiB is usually run with

NDVI and the other four VI have never previously been integrated into the model. Model runs were also performed with the introduction of the dynamic Vcmax time series presented in Section 2.6.2. Static VI runs were introduced to negate the source of seasonal variation introduced by dynamic VI within the model and quantify the influence of VI. The static VI values were determined by running the model with a range of values and selecting a high (0.76), medium (0.73) and low (0.7) VI value that minimised mGPP - ftGPP across the range of Vcmax inputs.

6.3.1 Statistical analysis

SiBx calculates net photosynthetic rate at two levels; the leaf (A), and the canopy (CAg). To evaluate the accuracy of these photosynthetic rates, they were compared to flux tower GPP (ftGPP). These were treated as 'truth' measurements, due to the accuracy of Eddy Covariance (EC), and their spatial overlap with satellite data used. Simple linear regressions were fitted for ftGPP and SiBx A or SiBx CAg. From these, the coefficient of determination (R^2) was extracted, to evaluate the amount of ftGPP variation explained by the SiBx model. The difference between ftGPP and SiBx modelled canopy GPP (mGPP) was therefore calculated as ftGPP - mGPP. This was conducted over varying spatial scales (total study period (2015-2018), annually or daily)).

Interannual variability was calculated to assess flexibility of annual estimations of mGPP for SiBx model runs and to compare this with the ftGPP. This was calculated as the difference between the lowest annual GPP estimation and highest annual GPP estimation. Seasonal CAg R^2 was derived from linear regressions between ftGPP and mGPP after all data had been separated by seasons (Winter = December, January, February; Spring = March, April, May; Summer = June, July, August. Autumn = September, October, November). SiBx model runs were also executed with and without the introduction of a drought term (S_d, Section 2.26, Equations 2.25 to 2.29 (p.63)) and compared to ftGPP.

6.4 Results

The five daily VI timeseries, normalised to the NDVI range for model ingestion (Section 2.5.2.3 (p.65)), are presented in Figure 6.1.

6.4.1 Static Vcmax

Vcmax values between 50 - 70 $\mu mol\, m^2\, s^{-1}$ produced the most realistic GPP estimates when compared with ftGPP (Figure 6.2). Higher Vcmax values explained

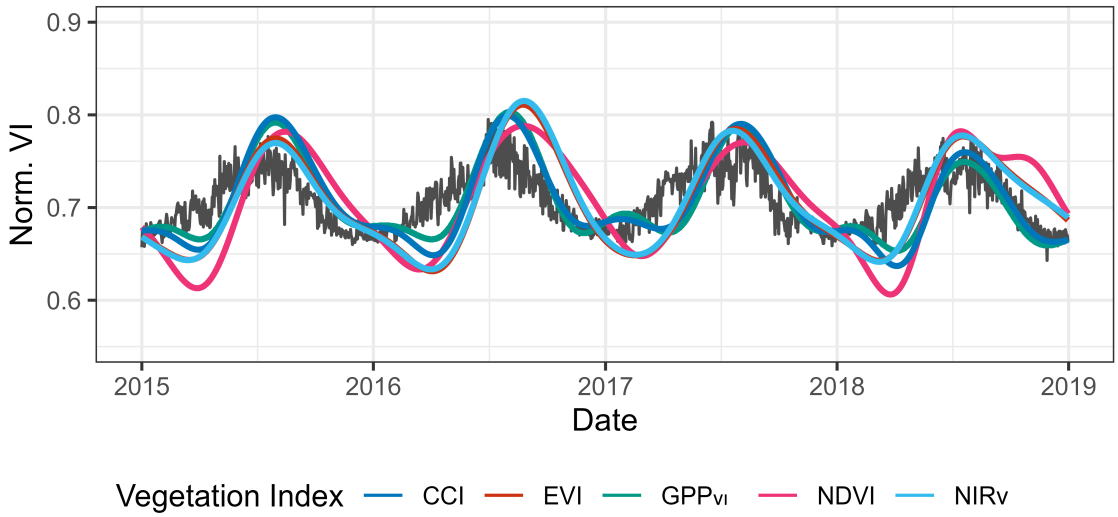

Figure 6.1: Time series of the five Vegetation Indices (VI) (CCI, EVI, GPP_{VI}, NDVI and NIRv) and flux tower GPP (ftGPP, black line). VI time series are smoothed and interpolated to daily time step by a Gaussian Process Regression (GPR) model. All VI and ftGPP are transformed to the NDVI range by a linear regression prediction. VI abbreviations are; CCI = Chlorophyll/Carotenoid index, EVI = Enhanced Vegetation Index, GPP_{VI} = Gross Primary Productivity Vegetation Index, NDVI = Normalised Difference Vegetation Index and NIRv = Near-Infrared Radiation from Vegetation. For full VI names, formula and references see Table 2.2 (p.58).

more GPP variation at the leaf and canopy scale for all five vegetation indices VI (NDVI, CCI, EVI, NIRv, GPP_{VI}), as determined by higher CAg R^2 and A R^2 (Figure 6.2; analysis of the full range of Vcmax values is presented in Appendix E, Table E.1 (p.231)). There was very little difference in A R^2 and ftGPP - mGPP between VI (Figure 6.2). For CAg R^2, modest differences (range of $R^2 \sim 0.023$) were found between VI, and these differences were consistent across the Vcmax range. At Vcmax = 60, NDVI had the lowest CAg R^2 (0.736), and GPP_{VI} the highest (0.762). CCI had the second highest CAg R^2 (0.759) at Vcmax = 60, while EVI and NIRv had the same value (0.749). Higher Vcmax increased mGPP and reached ftGPP - mGPP = 0 at between 62.5 and 62.7 (Vcmax) $\mu mol\, m^2\, s^{-1}$ across VI (Table 6.1).

Table 6.1: Regression parameters for the relationship between ftGPP and mGPP. And the predicted Vcmax, where ftGPP - mGPP = 0 (Optimal Vcmax). VI abbreviations match those detailed in Figure 6.1.

VI	Slope	Intercept	Optimal Vcmax
NDVI	1.246	-78.19	62.7
EVI	1.254	-78.34	62.5
CCI	1.252	-78.40	62.6
NIRv	1.254	-78.34	62.5
GPP_{VI}	1.252	-78.46	62.7

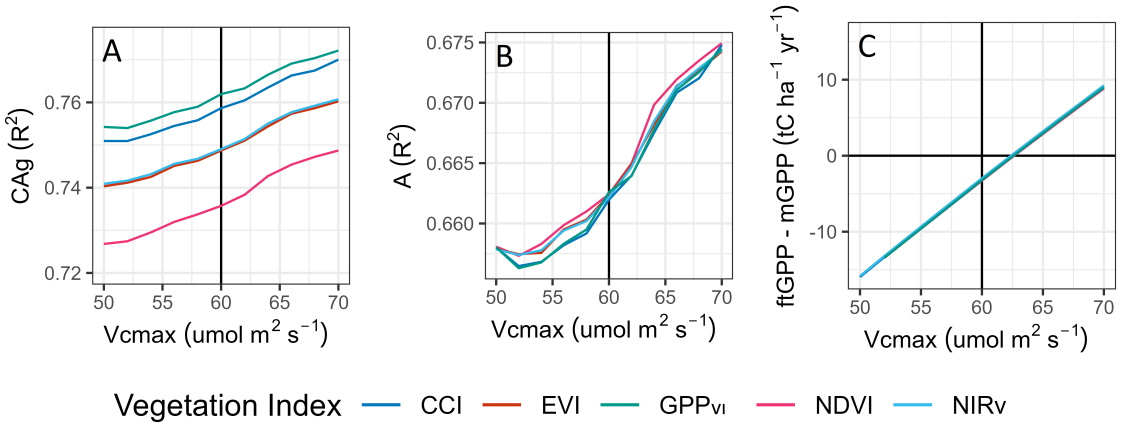

Figure 6.2: Summary statistics for iterative runs of SiBx, for the years 2015 - 2018, where the Vegetation Index (VI) and Vcmax parameters are altered. VI inputs are each of the daily VI datasets and the Vcmax values are between 50 - 70 µmol m^2 s^{-1}. Plot A = the coefficient of determination for the simple linear relationship between ftGPP and mGPP at the canopy scale (CAg (R^2)); Plot B = the coefficient of determination for the simple linear relationship between ftGPP and mGPP at the leaf scale (A (R^2)); Plot C is the difference in estimated canopy GPP (tC ha^{-1} yr^{-1}) between ftGPP and mGPP (ftGPP - mGPP). VI abbreviations match those detailed in Figure 6.1. Full analyses are presented in Appendix E, Table E.1 (p.231).

6.4.2 Dynamic Vcmax

Excluding the static VI, summary statistics from SiBx model runs with varying Vcmax and VI inputs are clumped, according to choice of Vcmax across the study period (Figure 6.3). The use of vm60 underestimates GPP (ftGPP - mGPP < 0) by 2.97 - 3.22 tC ha^{-1} yr^{-1}. The three dynamic Vcmax (vmDy, vmCCI, vmGPP) overestimate GPP (ftGPP - mGPP > 0). The overestimation is smallest in vmDy ranging from 0.77 to 1.3 (tC ha^{-1} yr^{-1}). The range of ftGPP - mGPP is between 1.05 and 2.07 tC ha^{-1} yr^{-1} for vmCCI and vmGPP. vmCCI consistently produces lower estimates than vmGPP across VI. vmDy has the highest CAg R^2 of all Vcmax, ranging from 0.783 for NDVI and 0.791 for GPP_{VI}. On average vm60 has slightly higher CAg R^2 (0.75) than vmCCI (0.738) and vmGPP (0.737). Across the Vcmax models, with the exception of static VI, the VI differences were slight but relatively consistent. NDVI had the lowest CAg R^2 (vm60 =0.736, vmCCI = 0.726, vmGPP = 0.727, vmDy = 0.783) for all Vcmax inputs and GPP_{VI} the highest (vm60 =0.762, vmCCI = 0.746, vmGPP = 0.743, vmDy = 0.791). The difference was most pronounced in vm60 (0.026) and least in vmDy (0.008).

6.4.3 Static VI

Changing the static Vcmax value strongly affected ftGPP - mGPP. Increasing static VI increased mGPP, however it had negligible effect on CAg R^2 (Figure 6.3). Among

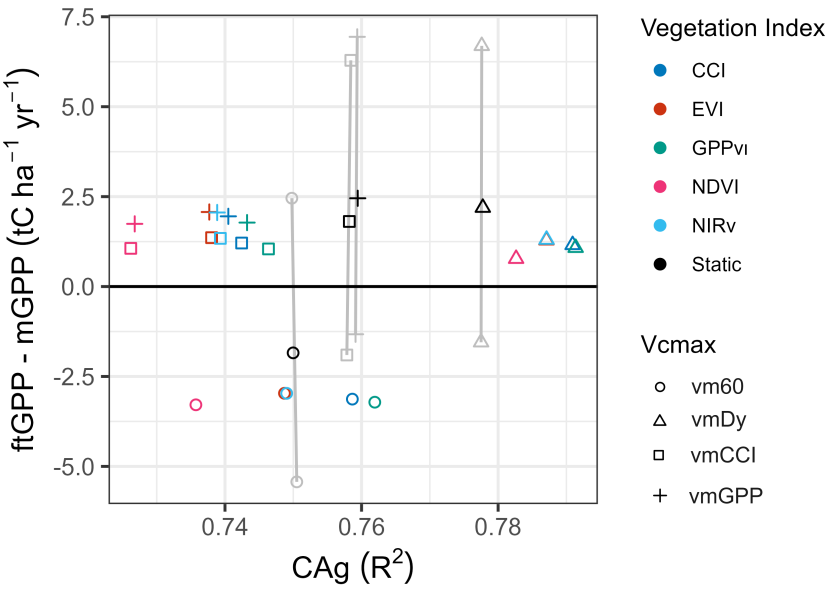

Figure 6.3: Summary statistics for the relationship of SiBx model runs, with different Vegetation Indices (VI) and Vcmax parameters, and ftGPP, for all observations across 2015 - 2018. ftGPP - mGPP is the difference in estimated canopy GPP (tC ha^{-1} yr^{-1}) between ftGPP and mGPP and *CAg* R^2 is the coefficient of determination for the simple linear relationship between ftGPP and mGPP at the canopy scale. Black shapes are static VI = 0.73. This was selected as it gives a reasonable mGPP estimation across all Vcmax. The grey points represent static VI = 0.7 and VI = 0.76 to highlight the effect of changing the static VI value. VI abbreviations match those detailed in Figure 6.1. Full analyses are presented in Appendix E, Table E.2 (p.233).

differing Vcmax models, compared to the dynamic VI average, introducing static VI improved model performance (increased *CAg* R^2) for vmCCI and vmGPP (+0.02). It reduced model fit for vmDy (-0.01), and fell in the centre of the vm60 range.

6.4.4 Individual years

The highest *CAg* R^2 across Vcmax models was generally in 2015 (Figure 6.4). Most models overestimated GPP in 2015 but never by more than 2 tC ha^{-1} yr^{-1}. Models run with vm60 provided the closest yearly estimates of GPP, in 2015, which were all within 0.5 tC ha^{-1} yr^{-1} of ftGPP. In 2016, all models run with vmGPP slightly overestimated GPP, but never by more than 0.51 tC ha^{-1} yr^{-1}, while the rest of the model runs underestimated ftGPP. vmCCI also accurately predicted GPP to within 0.5 tC ha^{-1} yr^{-1}. vm60 models underestimated GPP by around 1.5 tC ha^{-1} yr^{-1}. All models had the lowest *CAg* R^2 in 2017. vmDy models had the highest *CAg* R^2 (0.78). The two VI based Vcmax were characterised by relatively lower R^2 but good GPP estimates in 2017. In 2018 vmDy overestimated GPP by 1.79 tC ha^{-1} yr^{-1} for static VI, 1.71 tC ha^{-1} yr^{-1} for EVI and NIRv and 1.46 tC ha^{-1} yr^{-1} for

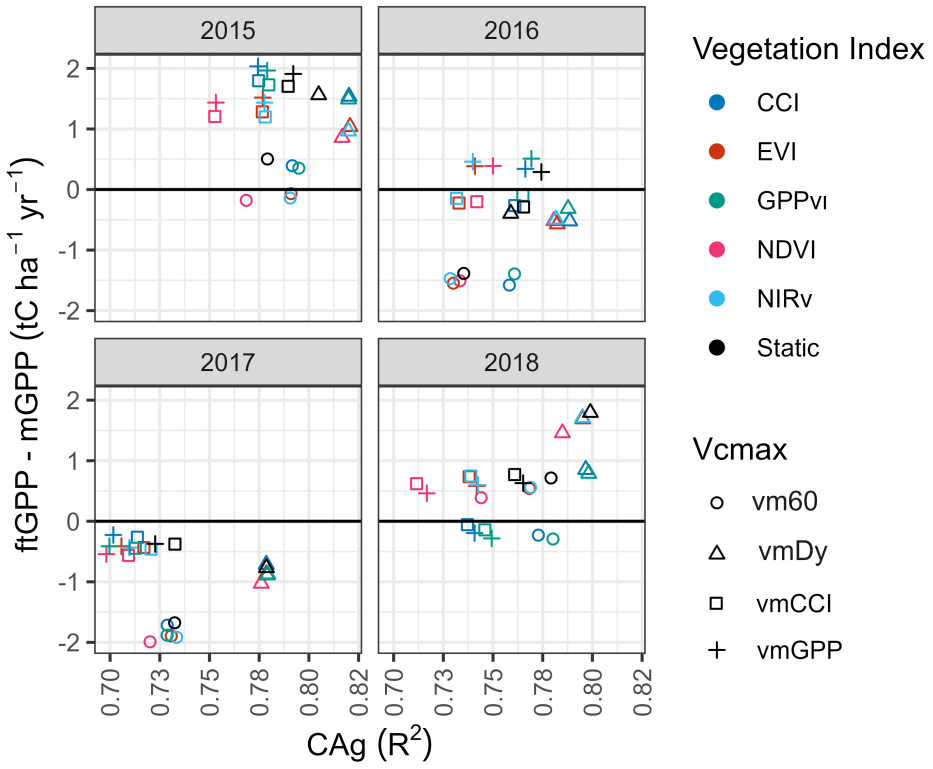

Figure 6.4: Summary statistics for the relationship between ftGPP and mGPP, with different Vegetation Index (VI) and Vcmax parameters, for each of the study years (2015 - 2018). ftGPP - mGPP is the difference in estimated canopy GPP (tC ha^{-1} yr^{-1}) between ftGPP and mGPP, and *CAg* R^2 is the coefficient of determination for the simple linear relationship between ftGPP and mGPP at the canopy scale. The black static VI = 0.73, selected as it gives a reasonable GPP estimation across all Vcmax inputs. VI abbreviations match those detailed in Figure 6.1. Full analyses are presented in Appendix E, Table E.3 (p.235).

NDVI. All other VI and Vcmax combinations, in 2018, estimated GPP within 1 tC ha^{-1} yr^{-1}.

6.4.5 Interannual variability

The ftGPP is characterised by lower GPP in 2015 and 2018 and higher yearly totals in 2016 and 2017. 2017 was the most productive year (25.5 tC ha^{-1} yr^{-1}) and 2015 the least (22.15 tC ha^{-1} yr^{-1}) (Xenakis et al., 2021) (Figure 6.5). The interannual variability of ftGPP was 3.35 tC ha^{-1} yr^{-1}. The vm60 total annual mGPP estimates were relatively accurate for the two least productive years but greatly underestimated GPP in 2016 and 2017 (Figure 6.5). The lowest GPP estimates were in 2015 for all vm60 model runs. For vm60, NDVI, EVI and NIRv had similar mGPP for the other three years (2016 - 2018) while CCI and GPP_{VI} predicted lower yearly GPP in 2018. vmDy displayed a similar pattern of yearly mGPP to vm60 but all mGPP estimates were higher.

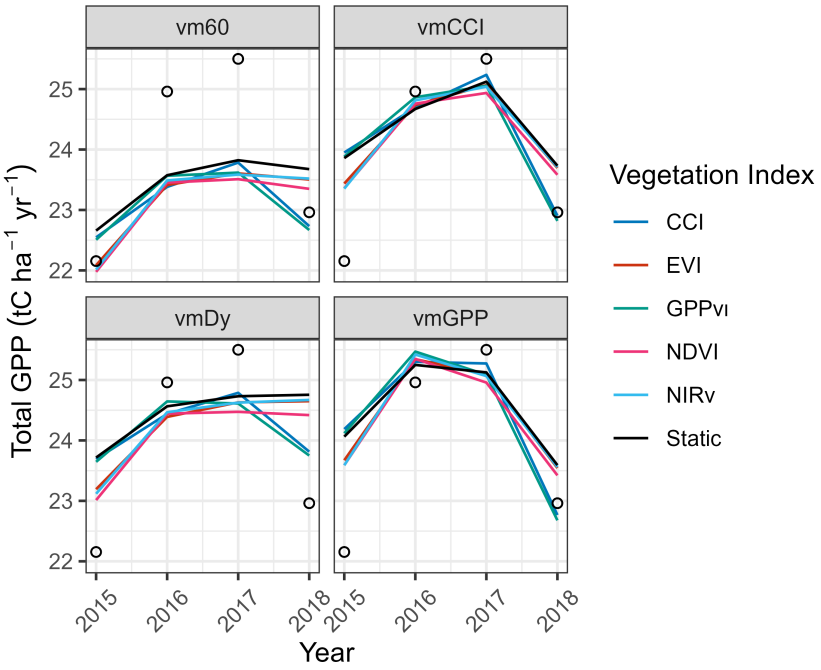

Figure 6.5: Annual mGPP totals (tC ha^{-1} yr^{-1}) for SiBx runs with varying Vegetation Indices (VI) and Vcmax inputs across the study period (2015 - 2018). ftGPP total annual totals (tC ha^{-1} yr^{-1}) are represented by circles. VI abbreviations match those detailed in Figure 6.1.

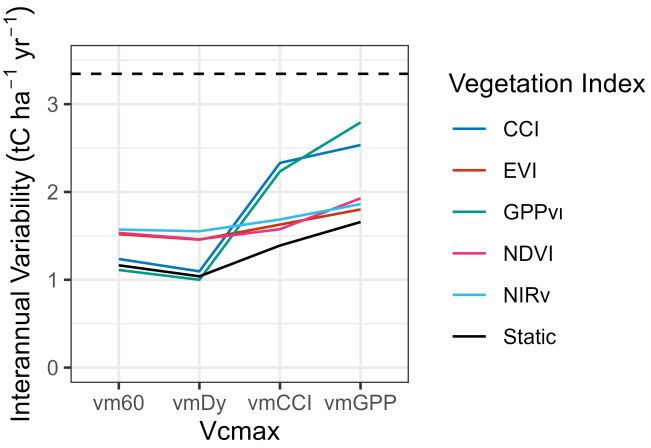

Figure 6.6: Interannual variability in annual totals (tC ha^{-1} yr^{-1}) for SiBx runs with varying VI and Vcmax inputs. The dashed line at 3.35 tC ha^{-1} yr^{-1} represents the ftGPP interannual variability. Interannual variability is the difference between the maximum and minimum annual mGPP or ftGPP (tC ha^{-1} yr^{-1}). VI abbreviations match those detailed in Figure 6.1.

The two VI based Vcmax models (vmCCI and vmGPP) had the greatest interannual variability and closest interannual variability to ftGPP (Figure 6.6). However, interannual variability varied between VI. vmCCI and vmGPP models with CCI or GPP_{VI} VI inputs had the greatest variability exceeding 2.2 tC ha^{-1} yr^{-1} whereas all other models were below 2 tC ha^{-1} yr^{-1}. Across Vcmax, NDVI, EVI and NIRv

had little difference in variability ranging from 1.53 to 1.92 tC ha^{-1} yr^{-1}. Whereas, CCI and GPP$_{VI}$ varied from 1 to 2.79 tC ha^{-1} yr^{-1}. The static VI had similar interannual variability to CCI and GPP$_{VI}$ when run with vm60 or vmDy and the lowest interannual variability when run with vmCCI or vmGPP.

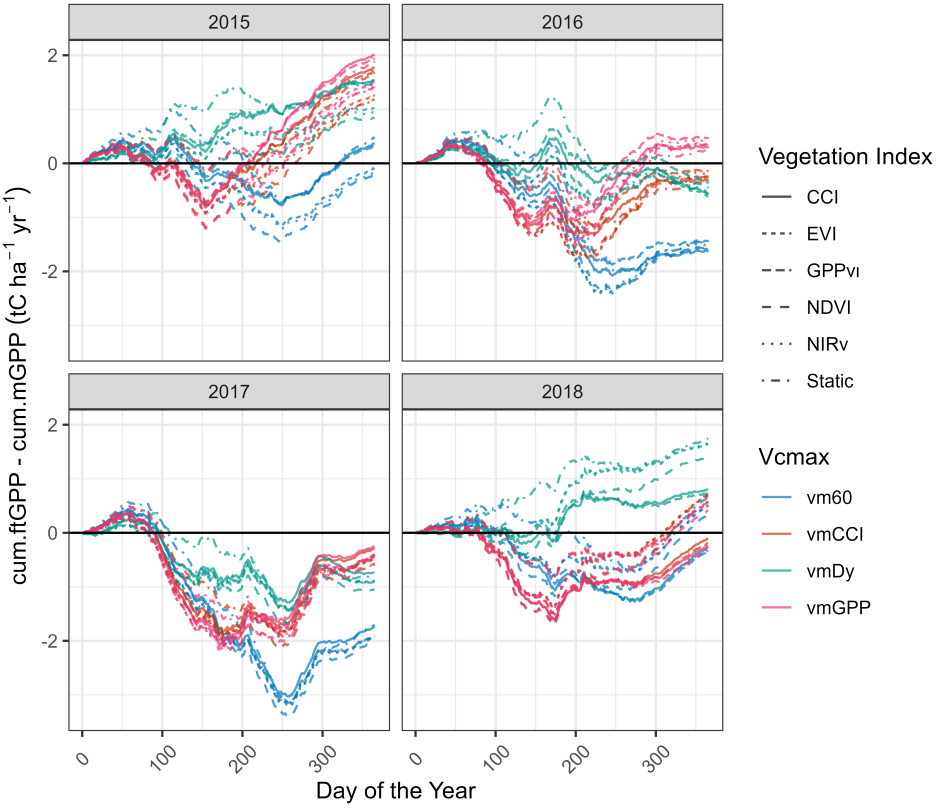

Figure 6.7: Cumulative difference between ftGPP and mGPP (tC ha^{-1} yr^{-1}). Lines represent the cumulative ftGPP - cumulative mGPP for each day of the year across the four study years (2015 - 2018). The black horizontal line is cumulative ftGPP - cumulative mGPP = 0. Vegetation Index (VI) abbreviations match those detailed in Figure 6.1.

6.4.6 Cumulative VI

Across years and Vcmax, the choice of VI does not greatly affect the seasonal mGPP dynamics (Figure 6.7). The choice of Vcmax however, has a much greater effect. vm60, vmCCI and vmGPP are characterised by slight initial overestimation of GPP until around day 100 (Figure 6.7). For vmCCI and vmGPP, mGPP is then underestimated (post day 100) throughout the season. The difference each year between ftGPP and mGPP peaks around day 150 - 200. From this point mGPP estimates are higher than ftGPP, so the cumulative ftGPP - mGPP drops for the remainder of the year. This drop is most extreme in 2015, where vmCCI and vmGPP end

with overestimations of GPP (Figures 6.5 and 6.7). In the remaining three years, the overestimation for the second half of the year is such that the annual estimates are relatively accurate. The cumulative difference between ftGPP and mGPP (tC ha^{-1} yr^{-1}) reveals how mGPP dynamics differ throughout the year depending on the choice of Vcmax. This provides temporal information not present in annual totals.

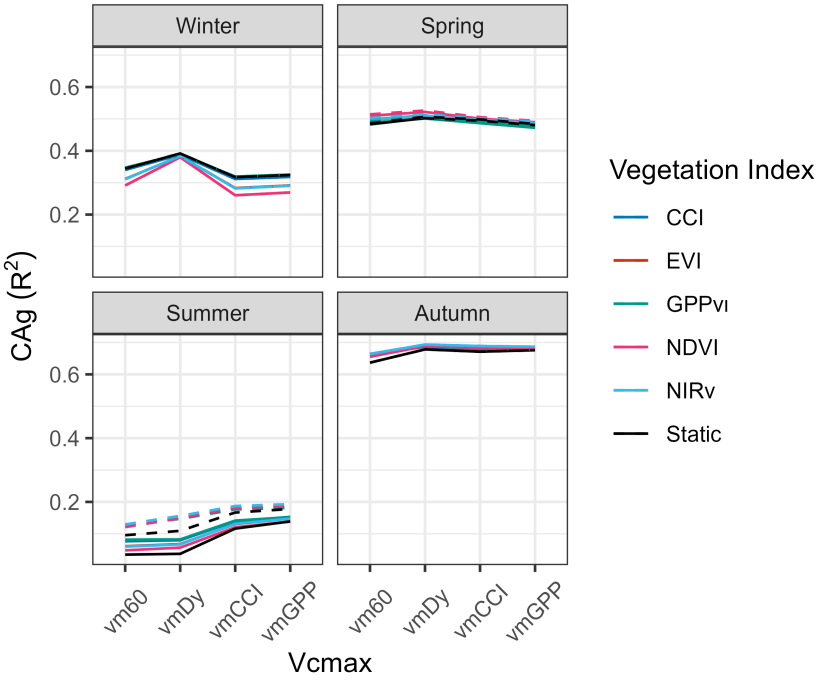

Figure 6.8: Coefficient of determination for the simple linear relationship between ftGPP and mGPP at the canopy scale (CAg R^2) after data has been separated by season. SiBx models are run with varying VI and Vcmax parameters and colours denote the choice of Vegetation Index (VI). The dashed lines are models run with the drought stress term (Sd). VI abbreviations match those detailed in Figure 6.1. For full results see Appendix E, Table E.4 (p.240).

vm60 follows the same basic pattern of summer underestimation post-day 100 as observed in vmCCI and vmGPP. However, ftGPP - mGPP reaches peak underestimation later in the year than vmCCI and vmGPP (around day 250 - 300). This peak is quite extreme in 2016 and 2017, reaching around -2 tC ha^{-1} yr^{-1} and -3 ha^{-1} yr^{-1} respectively. Models run with vmDy generally have a tighter relationship to cumulative ftGPP, but this varies between years. The general trend in 2015 is that of gradual overestimation over the year. In 2016 the model tracks ftGPP well over the summer, whereas 2017 follows the trend of vm60 but with a less intense underestimation peak (about 1.2 - 1.3 tC ha^{-1} yr^{-1}). In 2018, vmDy mGPP tracks ftGPP very closely until around day 165, at which point it over-estimates GPP for the remainder of the year.

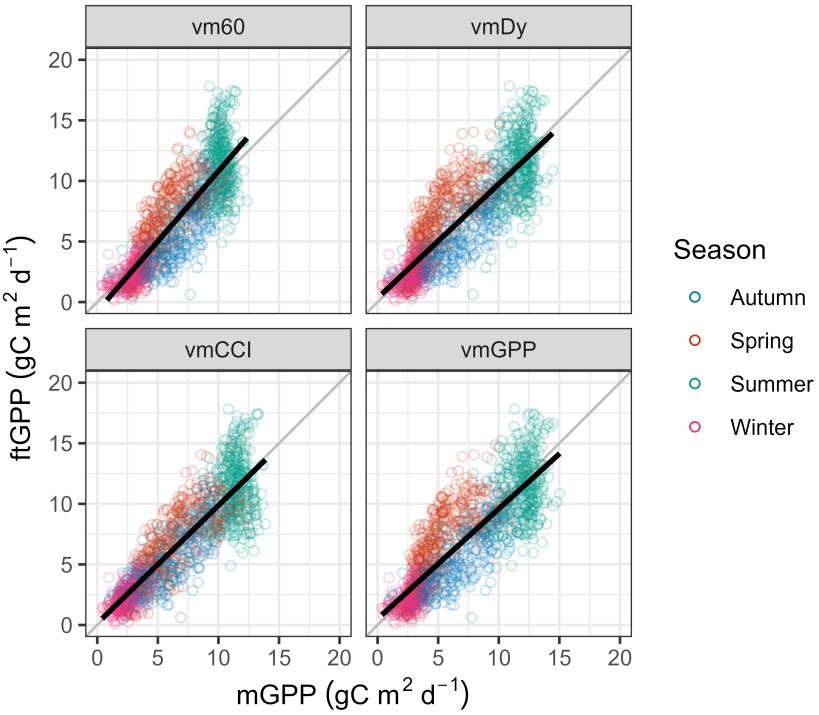

Figure 6.9: Relationship between mGPP and ftGPP (gC m^2 d^{-1}). The black solid line is the regression line between the two variables. Only models run with NDVI are given for conciseness; however, the general patterns seen remain relatively consistent between Vegetation Indices (VI). See Appendix E, Figure E.1 (p.245).

6.4.7 Seasonal relationships

The strength of relationship between ftGPP and mGPP varies between seasons (Figure 6.8; full analyses are presented in Appendix E, Table E.4 (p.240)). Across Vcmax and VI, SiBx models best describe the variation in ftGPP (higher CAg R^2) in Autumn. Autumn CAg R^2 varies between 0.637 and 0.693 (Figure 6.8). vm60 has marginally lower CAg R^2 than the three dynamic Vcmax. Spring CAg R^2 range from 0.472 to 0.521 and are relatively consistent among VI and Vcmax. Winter CAg R^2 values peak when running the vmDy models and are lowest for vmCCI and vmGPP. There is greater variation between VI in Winter than other seasons in vm60, vmCCI and vmGPP. Summer CAg R^2 values are low relative to other months (Figure 6.8). CAg R^2 is around 0.1 higher in vmCCI and vmGPP relative to vm60 and vmDy. The low summer CAg R^2 values are attributed to saturation of mGPP at high ftGPP values (Figure E.1). The values for mGPP saturation are highest for vmGPP (between 12.5 and 15 gC m^2 d^{-1}) and lowest for vm60 ($<$12.5 gC m^2 d^{-1}) (Figure 6.9).

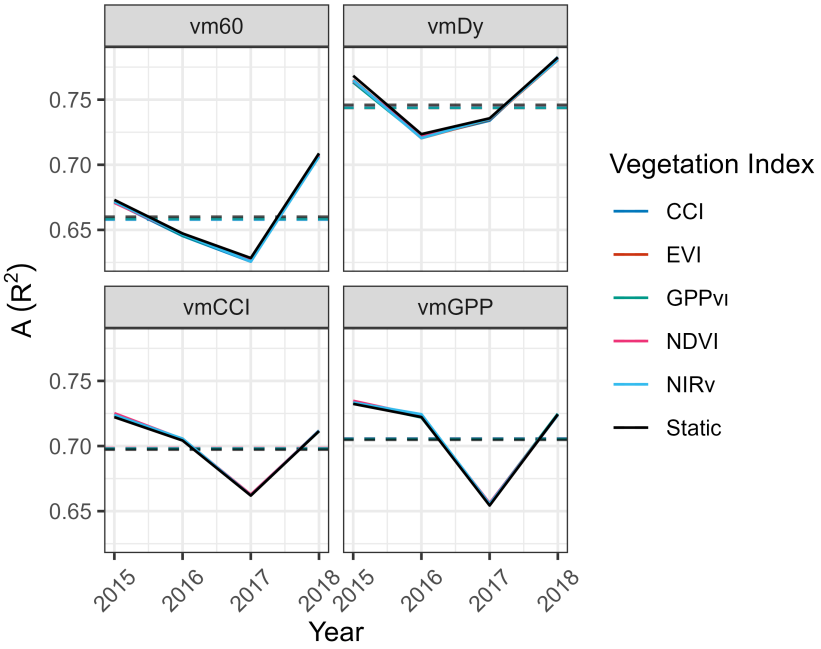

Figure 6.10: Coefficient of determination for the simple linear relationship between ftGPP and mGPP at the leaf scale (A (R^2)) for each of the four study years (2015 - 2018). The dashed horizontal lines represent the average A R^2 for each specific model parameterization. For full results see Appendix E, Table E.3 (p.235). Vegetation Indices (VI) abbreviations match those detailed in Figure 6.1.

6.4.8 Leaf level photosynthesis (A)

At the leaf level (A), R^2 varies between choice of Vcmax and year (Figure 6.10). vm60 has consistently lower A R^2 than other Vcmax models. The average vm60 A R^2 across years ranges from 0.658 to 0.66 depending on VI. vmDy has the highest A R^2 (0.744 to 0.766). vmCCI and cmGPP perform similarity (0.697 to 0.699 and 0.705 to 0.706 respectively). vm60, vmCCI and vmGPP have the highest A R^2 in 2015 and worst in 2017. vmDy performs best in 2015 and 2017 and worst in 2016.

6.4.9 Drought stress term (S_d)

As reported in Xenakis et al. (2021) and Chapter 5, 2018 was characterised by a drought induced reduction in ftGPP (Figure 6.11). The ftGPP drought drop was missed by the original SiBx model formulation. A drought term based on VPD was therefore introduced, leading to reductions in mGPP (Figure 6.11). These reductions were temporally consistent with ftGPP, and these are consistent across Vcmax parameters. However, the mGPP has more exaggerated fluctuations during the drought period: mGPP values reached higher and lower peaks compared to ftGPP in the drought stress models. The introduction of the drought term does marginally improve the summer CAg R^2 of all models, while other seasons are relatively un-

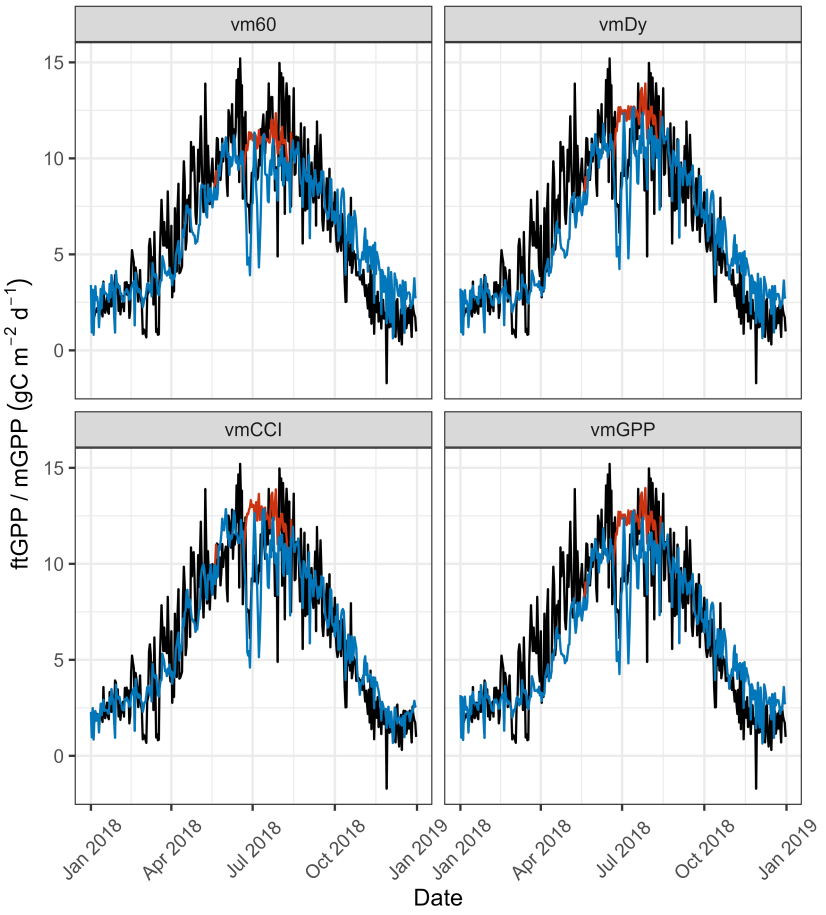

Figure 6.11: Time series of flux tower Gross Primary Productivity (ftGPP, gC $m^2\,d^{-1}$) and the SiBx modelled Gross Primary Productivity (mGPP, gC $m^2\,d^{-1}$) across 2018. The black line is ftGPP. Red and blue lines are mGPP from SiBx model runs using NDVI (other Vegetation Indices (VI) produced similar results, see Appendix E, Figure E.2 (p.246)) separated by choice of Vcmax. Red line is the original model formulation while the blue line includes a drought stress term based on vapour pressure deficit (VPD).

affected (Figure 6.8). When all seasons are combined in 2018, slight increases in CAg R^2 were found for vmDy, vmCCI and vmGPP for all dynamic VI models with the drought stress term; however, CAg R^2 decreased in vm60 (Figure 6.12). For the static VI, CAg R^2 decreases occur in vm60 and vmDy. Marginal increases in vmGPP occurred from the drought stress term while vmCCI are unaffected.

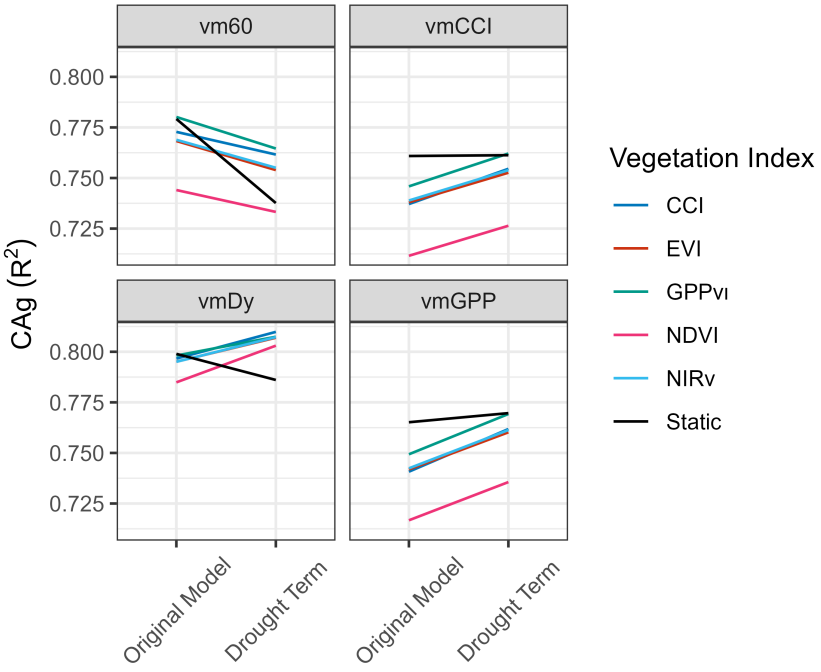

Figure 6.12: Coefficient of determination for the simple linear relationship between ftGPP and mGPP at the canopy scale (CAg R^2) for SiBx models run with differing Vegetation Indices (VI) and Vcmax parameters in 2018. Original Model is the formulation proposed by Sellers, Randall, et al.; Sellers, Tucker, et al. (1996, 1996) and the Drought Term includes a drought stress term (S_d) based on vapour pressure deficit (VPD). VI abbreviations match those detailed in Figure 6.1.

6.5 Discussion

The two major branches of land-surface modelling are predominantly based on either simple formulae, such as the Light Use Efficiency model (LUE) (see Section 1.5 (p.27) and Chapter 5), which requires few parameters; or complex process-based models (Alton, 2016), such as SiB and its derivatives. Relative to LUE models or VI/GPP proxies (Chapter 5), process-based models such as SiB are less reliant on high quality, temporally continuous satellite data. However, this comes with the cost of increased complexity from the introduction of calibrated or empirical parameters (Chuine et al., 2003; Lawrence et al., 2012; Haynes et al., 2019).

In this chapter, the worst performing model presented (SiBx run with NDVI and vmCCI) explained 72% of ftGPP variation across four years. In Chapter 5, at daily time intervals, the best VI/GPP correlation explains around 70% ftGPP variation, however, these poorly represented the 'true' vegetation signal and greatly overestimated annual GPP. The SiBx GPP estimates better represent ftGPP which demonstrates the potential benefits of the added complexity of this modelling procedure for GPP monitoring.

6.5.1 Vcmax

Within runs of SiBx, the static Vcmax value proposed by Sellers, Randall, et al.; Sellers, Tucker, et al. (1996, 1996) performed relatively well against ftGPP (Figure 6.2). Across the four years studied here (2015 - 2018), total GPP estimation accuracy was slightly improved by increasing Vcmax by around 2 $\mu mol\, m^2\, s^{-1}$. Accurate parameterisation of Vcmax is crucial for increasing biological realism in process based models, as GPP is highly sensitive to Vcmax (as discussed in Section 2.6.2; Farquhar et al., 1980; Collatz et al., 1991; Kattge et al., 2009; Alton, 2017). The formulation of SiB uses a fixed value of Vcmax (Sellers, Tucker, et al., 1996). This is derived from a Plant Functional Type (PFT) specific value (Sellers, Randall, et al., 1996; Sellers, Tucker, et al., 1996). Vcmax can vary within PFT (Kattge et al., 2009; Alton, 2017; Wu, Liu, et al., 2018). However, the inherent variability of natural systems, e.g. across years, sites, environmental conditions and age to name a few, suggests the original static value is relatively suitable for GPP retrieval, in a mature Sitka spruce plantation, representative of large areas of UK upland commercial forest. However, the analyses presented here suggest marginal improvements can be made by increasing Vcmax.

Simplifications of biological and physical processes are an inherent part of modelling (Box, 1979; Bonan et al., 2021). They facilitate the study of complex systems, such as plant-atmosphere interactions, by allowing them to be represented with fewer knowns. However, over simplification can lead to error. Vcmax is not static in time (Wilson et al., 2000; Grassi et al., 2005; Alton, 2016), and the misrepresentation of this dynamic process is commonly noted as a cause of error in photosynthesis models (Jin et al., 2012; Alton, 2017; Wu, Liu, et al., 2018; Chou et al., 2020). Incorporating dynamic Vcmax is therefore a promising avenue for potential model improvements (Jin et al., 2012; Alton, 2017). In Section 2.6.2, two methodologies for dynamic Vcmax retrieval are proposed. Firsty, a purely statistical and annually repeating Vcmax time series (vmDy), derived from curve fitting a globally optimised Vcmax dataset. Secondly, two satellite based Vcmax (vmCCI and vmGPP), retrieved from satellite VI derived from MODIS band 11, which is related to conifer seasonal productivity dynamics (Gamon et al., 2016). Therefore, the analysis presented here looked to establish if introducing a more biologically realistic Vcmax improved SiB GPP predictions.

SiBx model runs incorporating vmDy best explained ftGPP daily variation (CAg R^2), this was true for combined and individual years (Figures 6.3 and 6.4). The strong relationship between ftGPP and mGPP is unsurprising as vmDy is derived from model optimisation, however, it suggests a proof of concept and promising avenue for developing seasonally dynamic Vcmax model inputs. Much like the static

values originally proposed, a PFT specific annual Vcmax which includes a measure of seasonality may improve process-based models without requiring additional measured parameters. The vmDy procedure outlined in Section 2.6.2 could be expanded to other EC sites, for example using the FLUXNET network (Baldocchi et al., 2001), and may highlight possible commonalities within PFT. The introduction of the dynamic Vcmax time series improved the relationship between leaf level photosynthesis (A) and ftGPP relative to static Vcmax (Figure 6.10). Although the value of this relationship between these metrics should not be overstated (as they are measured at different scales), they are inherently linked. The Farquharr–von Caemmerer–Berry photosynthetic model (Farquhar et al., 1980; Collatz et al., 1991) which produces A is fundamental, not just for SiB and its derivatives, but for most terrestrial biochemical models (Alton, Ellis, et al., 2007; Powell et al., 2013; Alton, 2016; Zhou et al., 2019; Chou et al., 2020; Liang & Wang, 2020; Qian et al., 2021). The potential benefits of improving the parameterisation with seasonal Vcmax could therefore be widespread.

Spectral data has the potential to derive Vcmax values from vegetation that are biologically relevant, based on physical observations and are dynamic in space and time. This can reduce the reliance on PFT static values (Jin et al., 2012; Deng et al., 2024). It is therefore a promising and active area of research (Barnes et al., 2017; Qian et al., 2021; Deng et al., 2024). The majority of studies find reliable relationships between field based hyperspectral reflectance and direct Vcmax measurements (Dillen et al., 2012; Jin et al., 2012; Serbin et al., 2012; Barnes et al., 2017; Dechant et al., 2017; Silva-Perez et al., 2018; Chou et al., 2020; Wu et al., 2021; Yan et al., 2021; Kumagai et al., 2022; Deng et al., 2024). However, none of these studies investigate ENF, and work using satellite data is sparse. Jin et al. (2012) reported a strong ($R^2 = 0.81$) relationship that scaled well between simulated MODIS NDVI and Vcmax in natural Japanese beech forests (*Fagus crenata*). Qian et al. (2021) successfully derived Vcmax from chlorophyll estimations from crop and grasslands derived from the Medium Resolution Imaging Spectrometer (MERIS), highlighting the feasibility of satellite based Vcmax retrieval. The work here looked to link Vcmax to the group of VI associated with carotenoid dynamics (eg, CCI, GPP_{VI}, PRI). These are related to photosynthetic capacity at different temporal scales (Gamon et al., 1997; Wong & Gamon, 2015b; Gamon et al., 2016; Chou et al., 2020; Wong et al., 2022), and in the current study system are more applicable to photosynthetic dynamics than NDVI, or other 'greenness' indices (Chapter 5).

In the absence of 'true' ground based leaf level Vcmax measurements, exploratory analysis was conducted here via an iterative procedure using transformation and min/ max values determined from SiBx model runs (Section 2.6.2). In terms of

total GPP estimations and R^2, the VI-based Vcmax models (vmGPP and vmCCI) performed similarly to the original static value SiBx formulation (vm60) (Figure 6.3). However, the most promising finding is the ability of these to detect interannual variability, which facilitates increased flexibility within the model (Figure 6.5 and 6.6). An 'ideal', biologically representative Vcmax would be dynamic across years. Although sub-optimal, and limited by the quality of the VI timeseries (Chapter 5), vmCCI and vmGPP go some way to predict the differences in annual GPP totals across years (Figure 6.5). This is most prevalent during 2016-2018 which, due to the stress related mechanisms of carotenoid /chlorophyll dynamics, are able to predict an annual GPP drop in 2018, relative to 2016 and 2017, at a similar magnitude to ftGPP. It is this potential flexibility and dynamism across seasons and years which makes accurate VI based Vcmax parameterisation such a promising research goal and possible modelling improvement.

Although promising, the vmDy tested here fails to improve on vm60 in terms of interannual variation. Due to the homogeneous yearly cycle, vmDy and vm60, provide no mechanism to allow for variation between years if variation is not accounted for in the VI or meteorological inputs.

6.5.2 Vegetation Indices (VI)

SiBx overcomes limitations in temporal continuity from satellite observations by using mechanistic functions and the ERA5 reanalysis dataset to model forest processes on a daily timescale. Historically, NDVI (and previously the simple ratio (SR)), has been used to scale leaf level processes to the canopy within the SiB architecture (Sellers, Randall, et al., 1996; Sellers, Tucker, et al., 1996; Haynes et al., 2019), due to its robust relationships with various useful biophysical properties (Sellers et al., 1992; Los et al., 2000).

In general, model runs incorporating NDVI performed marginally worse than the other VI (Figures 6.3 and 6.4), highlighted by lower CAg R^2 across all Vcmax choices. Within Vcmax parameterisations, NDVI generally produced lower GPP estimations. The analysis conducted throughout this thesis has evidenced that other VI routinely outperform NDVI in their accuracy for studying a range of photosynthetic and drought stress metrics in Sitka spruce. Specifically, VI that are associated with carotenoid dynamics have a closer sub-annual relationship with Sitka spruce canopy GPP (Chapter 5) and Sitka spruce drought stress responses (Chapter 3), relative to traditional 'greenness' indices. Therefore, it was hypothesised that incorporating other VI could improve the performance of SiBx. EVI has been shown to improve satellite LAI retrieval over NDVI in some cases (Chen & Vierling, 2007; Potithep et al., 2013), but not in others (Qiao et al., 2019). LAI-NIRv relationships

have also been tested across deciduous, crop and grassland sites (Qiao et al., 2019), but performed marginally less well than NDVI. However, never before has the integration of non traditional 'greenness' indices into SiB been published, despite the improvements in simple LUE models possible with other VI (Badgley et al., 2019; Wong et al., 2022).

The Gaussian Process Regression (GPR) smoothing procedure (Section 2.4.5.1) increases temporal resolution, but cannot perfectly distinguish noise from signal, and so some information is lost. This results in homogenisation of the VI timeseries (Figure 6.1), and could explain the relatively small differences found between VI and their impact on mGPP. The interpolation techniques were used to compensate for a lack of primary satellite observations caused by cloud contamination at the field site (Section 2.4.4). This is typical of northern temperate upland areas satellite-based reflectance retrieval (Armitage et al., 2013; Zhang et al., 2017; Badgley et al., 2019; Liu et al., 2021) and characterises the major limitation to quality. SiB was developed for global circulation models, and it is likely that higher quality VI time series consisting of larger proportions of direct observations are available at lower latitudes. Satellite retrieval at these latitudes is less heavily reliant on mathematical interpolations or temporal compositing and may produce less homogeneous VI datasets which could separate the effect of different VI within SiB.

Another explanation for the limited improvements of other VI over NDVI could be the relatively small contribution to mGPP that VI plays within the model. This is highlighted most clearly when seasonality is completely removed by introducing a static VI value (Figure 6.3). Unsurprisingly, the choice of value is directly proportional to the absolute value of mGPP, and increasing the VI value increases mGPP. Interestingly however, substituting a seasonally dynamic VI dataset (representing LAI and FPAR within the model) with a static VI has relatively limited effect. For vm60, over the four study years, model performance (CAg R^2) with a static VI is similar to the mean of the five dynamic VI choices. It is marginally (<0.02 R^2) reduced for vmDy, and actually improves model fit in the VI-based Vcmax models. These findings may highlight the importance of high quality meteorological data inputs for detecting canopy seasonality. With static values for both VI and Vcmax (e.g. static VI and Vcmax = 60), the model still performs comparably well to more observationally driven parameterisations (e.g. daily NDVI timeseries and vmDy), and picks up on the seasonal variations in canopy GPP. This is due to the underlying environmental controls on leaf photosynthesis which are driven by the ERA5 data.

In summary, despite the discussed limitations in the underlying VI timeseries, slight improvements in mGPP were detected by replacing NDVI with other VI. These improvements were consistent across Vcmax choices and, akin to findings in Chapter

5; the VI associated with MODIS band 11 (CCI, GPP_{VI}) outperformed others. This was driven in part by the drought induced reductions of CCI and GPP_{VI} in 2018 (Figure 6.6). The improvements were most pronounced in vm60 and least in vmDy.

6.5.3 Seasonal Differences

In these analyses, summer mGPP/ftGPP correlations were found to be much weaker than the other seasons (Figure 6.8), resulting from saturation at high summer values (Figure 6.9; and see Chapter 5). In temperate ecosystems, seasons are characterised by markedly different GPP dynamics. Productivity peaks in summer, is low in winter, and transitions between these states in spring and autumn. In Chapter 5 VI/GPP relationships varied considerably depending on the season: negative VI/GPP reactions were detected in winter, and weakly positive relationships occurred in summer. This was due in part to saturation effects. The SiBx model assumes the 'Big-Leaf' (BL) principle, whereby vegetation is treated as a homogeneous layer of phytomass where physical properties (leaf orientation, sun:shade ratios, leaf age, leaf clumping) do not vary throughout the vertical canopy (Bonan et al., 2021). SiBx assumes that the maximum photosynthetic rate decreases with the light extinction coefficient ($\overline{k}$), which is linearly related to the canopy nitrogen profile. While this may hold true in some instances (Sellers, Randall, et al., 1996), BL models often underestimate GPP (Luo et al., 2018), as radiation gradients are unable to explain rapid changes in photosynthesis. Rapid increases in light, occurring predominantly in summer (due to higher light intensity and less crown shadowing), will increase lower canopy photosynthesis more than the radiation average imposed by the light extinction model (Luo et al., 2018). More accurate representatives of canopy photosynthesis can be achieved by using multilayer models or separating diffuse and direct sunlight within the BL principle (Alton, North, & Los, 2007; Alton & Bodin, 2010; Alton, 2016; Luo et al., 2018; Bonan et al., 2021). Introduction of a multilayer model to SiBx could therefore ameliorate the summer (high value) saturation effect seen.

6.5.4 Drought

Incorporating accurate drought stress responses within biophysical modelling is both necessary and challenging (McDowell et al., 2011; Zhou et al., 2019). One barrier is the lack of empirical and established drought methods to represent drought in process-based models (Zhou et al., 2019). More comprehensive formulations of SiB exist than the procedure outlined here (Sellers, Randall, et al., 1996; Baker et al., 2008; Haynes et al., 2020), such as those containing soil moisture sub-models that contribute to a measure of water stress via various soil moisture pools, which are

depleted via transpiration and replenished by precipitation (Baker et al., 2008). However, this drought response requires 'substantial development' for predicting future drought scenarios (Powell et al., 2013). In these analyses, the drought stress representation within SiBx is simplified by a lack of soil moisture components. The water stress term (S_d) developed here, limits A by VPD (atmospheric drought), rather than soil moisture (soil drought). Atmospheric droughts are an important driver of drought induced reductions in productivity (Allen et al., 2010; Xenakis et al., 2021; Bauman et al., 2022; Schönbeck et al., 2022). The simplicity of VPD driving drought is attractive and greatly reduces model complexity by ameliorating the need for multiple soil layers interacting with multiple sources of transpiration (Haynes et al., 2020), as well as the inherent difficulties in retrieving soil moisture measurements from space via reanalysis datasets (Bauman et al., 2022) which justify the choice of drought stress driver used here.

Slight improvements to SiBx model performance were achieved via the newly proposed drought stress term (S_d). However, these were limited and not universal across model parameterisations (Figure 6.12). Without the drought term, the dramatic reductions in ftGPP, relative to the normal seasonal pattern during the drought in late June and July 2018 would be missed (Figure 6.11). Models run with S_d characterise the initial drought response well, however, mGPP fluctuates greatly during the recovery and remains unseasonably low, while ftGPP recovers to pre-drought levels relatively quickly. The formulation presented here is simple and non-ideal, however, it suggests a proof of concept that directly reducing leaf level photosynthesis by VPD may act as a direct way to simulate drought response without the introduction of multiple soil layers.

Parameterising Vcmax as a single PFT value has been highlighted as a limitation of process-based models to capture sensitivity to drought (Zhou et al., 2019). Here, models run with vm60 performed worse with the drought term included. The static nature of vm60 means that in winter GPP is overestimated, whilst in summer it is underestimated (Figure 6.7). Further reductions in summer mGPP therefore weaken the ftGPP/ mGPP relationship, due to the drought stress term. In 2018, total annual GPP was reduced by 5% relative to the previous three year average, resulting from drought conditions (Xenakis et al., 2021) (Figure 6.5). The utility of linking CCI and GPP_{VI} to drought stress is highlighted in Chapter 5, and continues to generate promising outcomes here. For all Vcmax choices, 2018 annual GPP reductions were better detected while using CCI or GPP_{VI} , relative to other VI (Figure 6.5). And, as discussed above, the interannual variability is detected using vmCCI and vmGPP as a result of stress related mechanisms of carotenoid /chlorophyll dynamics. This adds to the body of evidence that the association of reflectance at 531 nm

and drought stress response makes these indices more suitable than the traditional 'greenness' VI for studying drought stress in evergreen conifers.

6.6 Conclusions

The analysis here builds upon work in Chapter 5 to evaluate the use of a range of MODIS based VI for GPP retrieval in a mature Sitka spruce plantation where VI retrieval is subject to high levels of cloud contamination. The added complexity of SiBx facilitates more realistic daily ftGPP/mGPP correlations, so where possible and feasible, it is recommended for daily satellite based GPP retrieval.

Vcmax is highlighted as a crucial model input in process-based modelling, and the following conclusions are drawn about its parameterisation:

— The model performs well in this study system with a static Vcmax, using the original PFT value (60 µmol m^2 s^{-1}) proposed by Sellers, Randall, et al. (1996). However, best performance is achieved when Vcmax = 62.5 µmol m^2 s^{-1}.

— Dynamic Vcmax provide more biological realism, and can improve model fit (vmDy) and predictions of interannual variation (vmCCI and vmGPP).

— Despite limitations of the methodology presented here, the potential for retrieving spatially and temporally dynamic Vcmax from carotenoid/ chlorophyll dynamics via VI (CCI, GPP_{VI}) is promising.

— SiBx suffers from saturating effects in summer at high GPP values. Multilayer models could overcome this BL associated error.

For the first time, SiB was parameterised with a new set of VI which are better related to conifer seasonal productivity dynamics and stress responses. However, these have surprisingly little overall effect on model performance, which highlights the importance of accurate meteorological and Vcmax inputs to SiB performance. A new 'atmospheric drought' stress term is introduced in the absence of soil moisture pools in SiBx, this greatly simplifies the model and in some cases improves drought stress detection. However it would require tuning using a wider set of study systems (different species, different drought levels) to further evaluate feasibility and potential accuracy.

Chapter 7

General discussion and conclusions

7.1 Overview

Globally, forests are facing unprecedented anthropological threats to their health: indirectly, through climate alterations via major and rapid disruptions to the carbon cycle, and the myriad of consequences that entails, and directly, through deforestation and mismanagement (Nemani et al., 2003; Foley et al., 2005; Somers & Asner, 2012; Gauthier et al., 2015; Lewis et al., 2015; Millar & Stephenson, 2015; Wingfield et al., 2015; Lausch et al., 2016). Arguably, the most overtly damaging of the environmental threats to forests is the increase of drought, in both frequency and severity, that is already responsible for large scale mortality events on every vegetated continent on Earth (Ciais et al., 2005; Phillips et al., 2008; Allen et al., 2010; Zhao & Running, 2010; McDowell et al., 2011; Anderegg et al., 2012; McDowell & Allen, 2015; Anderegg et al., 2019).

Due to advancements in technology, the current decade is also characterised by unprecedented data availability (Ma et al., 2015). Since the 1970s the rapid rise of remote sensing data, facilitating the study of forests at leaf to global scales, provides the tools to monitor and model forests. These tools can improve understanding in order to mitigate against the threats facing future forest health.

Increasing drought and remote sensing data availability are both key to the current state and future of UK forestry (Locatelli et al., 2021). The present thesis evaluates the possibilities of reflectance based remote sensing, in the form of VI, for studying non-fatal drought stress in Sitka spruce, the UK's most important forestry species (Samuel et al., 2007; Krakau et al., 2013). The thesis explores the contribution that hyperspectral and broadband VI could play in transitioning UK forestry into a more drought resilient sector.

A well managed forestry sector will contribute to the sustainable production of timber, which also acts as a carbon sink, sequestering CO_2 to mitigate against the worst effects of climate change; while also revising management of stands to be at low risk from drought now and into the future. Well informed decisions are crucial in forestry, as the time between investment (tree planting) and returns (timber production) is long (Berry & Brown, 2021; Locatelli et al., 2021). Vast quantities of Sitka spruce exist across the UK, meaning that young trees now will mature into climatically different environments, throughout the next 30 to 40 years (Betts & Brown, 2021; Intergovernmental Panel on Climate Change (IPCC), 2021). Accurately monitoring how these trees respond to the increasingly hot and dry summers will provide paramount information to inform future decisions. The planting of new forests, and choice of location, species and genotypes are perhaps the most crucial decisions that foresters now, and in the near future, face as the 'business as usual' model becomes increasingly disparate from the climatic reality (Intergovernmental Panel on Climate Change (IPCC), 2021; Locatelli et al., 2021).

This thesis explores two major avenues of Sitka spruce stress monitoring at two spatial and spectral scales. First, (i) a controlled experimental drought was imposed on genetically distinct Sitka spruce clones, during which needle level hyperspectral measurements were recorded, over eight weeks. Chapters 3 and 4 analysed these data, exploring the stages of increasing drought, at high spectral fidelity, using VI to infer a number of physiological responses, at multiple points within the canopy. Then, (ii) Chapters 5 and 6 utilised the availability of open source satellite based reflectance (the MODIS MAIAC product) to infer GPP, a 'global sensor of environmental stress' (Biswal et al., 2011), via direct VI timeseries, the LUE model or an established process based model (SiB), from a mature Sitka spruce plantation.

The following sections discuss the main findings from each chapter and tie them together to identify themes, important findings, potential limitations and how the present research can inform the forestry sector, and the wider forest ecology community.

7.2 Chapter summaries

Chapter 3 characterised the drought response of six Sitka spruce clones from the Forest Research clonal archive using 17 VI and Fv/Fm measurements. The analysis highlighted an array of drought responses which were detected. VI associated with stress response pigments, most prominently xanthophylls and anthocyanins, clearly demonstrated increased expression of these pigments in early drought. These mechanisms protect vulnerable photosynthetic machinery by dissipating light energy into

heat, via non photochemical quenching, directing high energy photons away from chloroplasts and possible roles in antioxidation (Gould, 2004; Kyparissis et al., 2007; Hernández et al., 2009; Landi et al., 2015; Gamon et al., 2016; Cirillo et al., 2021). An unexpected response was detected in water based VI which are influenced by the characteristic absorption profile of water within needles. In the early stages of drought, water content increased, and this was attributed to reduced stomatal conductance acting to maintain hydraulic connectivity, by reducing the evaporative demand, therefore maintaining water at high concentrations in the needles. A critical threshold is reached as the drought continues and water content in needles rapidly decreases. Identifying thresholds and tipping points like these are important in characterising and understanding plant drought responses in order to predict forest stress and mortality (Huang et al., 2015; Munson et al., 2018; Krishnamurthy et al., 2020).

The analysis in Chapter 3 highlighted the usefulness of measuring multiple VI, or taking information from across the spectrum, to account for the multiple facets of drought stress. These results agree with Verrelst et al. (2019) who suggest moving away from traditional two or three band VI. By using computational power and machine learning techniques, methods exist to build indices based on the full spectrum, utilising the plethora of information in hyperspectral reflectance.

Conifer spectral heritability research is in its infancy, and this study was the first to use VI to assess different conifer drought responses across clones. By demonstrating the possibility of VI to detect intraspecific stress responses non destructively, great possibilities for advances in drought tolerance screening are opened up (Feng et al., 2017; Janni et al., 2019). Sitka spruce is likely to continue to be planted across the UK in the near future (Davies et al., 2020), therefore, introducing drought tolerance into the breeding programme is appropriate. The analysis presented here has demonstrated that variation in stress response exists in the Sitka clonal archive, and that it is detectable, via high throughput phenotyping, using remote sensing. The differences in stress responses between clones also suggests that current planted breeding population Sitka spruce trees may differ in their vulnerability to drought.

Chapter 4 extended the analysis of the drought experiment to look at how VI differ through the canopy. Variation throughout the canopy was detected across all VI tested. The vertical canopy profile, likely driven by variations in microclimate caused by light gradients, resulted in differences in all VI between the top and bottom canopy. Needle age classes affected chlorophylls, carotenoids, anthocyanins and water content. These differences are discussed in detail in Chapter 4. The analysis highlighted knowledge gaps surrounding water content distribution throughout conifer canopy layers.

Evidence from Chapter 4 suggests that the stress response was higher in the upper canopy. Micro climatic variation causing differences in stress responses could inform future forest management (Aussenac, 2000). More exposed trees could be more susceptible to drought which could inform planting density. Smaller Scots pine trees are more drought resilient due to stratification of the canopy leading to microsite climatic conditions, e.g. solar radiation, humidity or temperature (Merlin et al., 2015). The susceptibility of exposed trees, or parts of trees, may present a trade off for planting density, between yield and drought tolerance, which should be considered, alongside competition between water and nutrients (Aussenac, 2000). Sitka spruce could be especially susceptible to these effects due to specific growth traits. High needle morphological variation occurs in Sitka spruce as it is shade tolerant (Taylor, 1990), but will produce much wider needles in high light environments to maximise growth (Chin & Sillett, 2017), as it employs a 'grow-fast-die-young' strategy (Kramer et al., 2018). The ability to maximise growth across microclimates could accentuate the discrepancy in stress response across an individual tree canopy.

The differences in optical properties highlighted here should be considered when scaling remote sensing to canopy level using airborne or SRS. Optical remote sensing predominantly observes the outer canopy surface, which will influence the majority of the measured response. O'Neill et al. (2002) concluded that in Sitka spruce, the differences in biochemical concentrations throughout the canopy were slight enough that top down retrieval could be representative of the canopy as a whole. Here, the upper canopy appeared to have a stronger stress response, which may aid in the earlier detection of stress responses at canopy scales, as an exaggerated representation of the canopy as a whole is one that will be predominantly detected.

Chapter 5 evaluated the ability of five broadband VI to act as proxies for components of the LUE model and GPP for the Harwood Forest Sitka spruce field site and plantation. The EC data collected at Harwood allowed the VI-based models to be evaluated against high quality GPP flux measurements. A drought in 2018, provided a serendipitous opportunity to evaluate the drought response of mature Sitka spruce, in natural environmental conditions. A key component of reducing drought associated risks in UK forestry, involves studying mature forest drought responses, which are extremely difficult and expensive to do artificially (Locatelli et al., 2021). Despite low satellite data availability due to frequent cloud contamination, modelled GPP time series correlated well with ftGPP. When combining PAR with VI in the LUE model, the strength of correlations up to 90% were produced at the monthly time interval and up to 86% at the 16 day time interval. Using VI only models explained ftGPP variation up to 67% (for CCI and GPP_{VI}), which compared sim-

ilarly to studies within the literature (Hashimoto et al., 2012; Gamon et al., 2016; Huang et al., 2019; Wong et al., 2022; Junttila et al., 2023), even compared to sites with higher satellite observation frequency (Gamon et al., 2016; Wong et al., 2022). Daily interpolated models including PAR greatly overestimated annual GPP totals despite good correlation at sub annual time intervals, highlighting the bias that temporal interpolation can produce (Wang et al., 2004). The analysis in Chapter 5 highlighted how drivers of GPP change with different temporal resolutions and that at sub-annual timescales metrological forcings, namely PAR, strongly effect GPP so should be included in VI-based models. At coarser resolutions, meteorological data become less important as VI reflect longer term plant acclimation and therefore GPP (Junttila et al., 2023). The only models that detect annual drought induced GPP reductions, as presented by Xenakis et al. (2021), were VI-only (no meteorological variable inputs) and based on the xanthophyll cycle (CCI and GPP_{VI}). This highlights (i) poor parametrisation of ε terms in LUE models, owing to limitations of biome specific, LUT model inputs and non-established methodologies for retrieving ε from satellite based VI. The result also suggests (ii) some potential for CCI and GPP_{VI} to detect drought induced GPP anomalies where other, more traditional 'greenness' VI cannot. The 16 day VI product (VI_{16}) developed using CV-MYV for this analysis performed well relative to other temporal resolutions. This provides a rationale to expand the MODIS VI product (MOD13, which currently produces NDVI and EVI time series) to an increased number of VI. Without any additional data retrieval, the MOD13 algorithm could be expanded to create a globally extensive and temporally continuous dataset, including NIRv and VI associated with Band 11 which this research has found to be most sensitive to annual drought induced GPP anomalies.

Using the well established SiB model architecture, **Chapter 6** evaluated whether adding modelling complexity, relative to VI-GPP proxies and the LUE made improvements for GPP retrieval, recommended for forestry. The SiB model increases daily correlation between ftGPP and mGPP (up to 79% explained ftGPP variation) and produced more realistic GPP time series and greatly improved annual total estimation. If accurate GPP retrieval, possible at daily time intervals, is the primary concern, and increased modelling complexity can be afforded, the SiB, or other processed based productivity model, could be important tools to foresters. However, there were limitations to this. For drought stress detection, the SiBx model was non-ideal. SiB can model drought via multi-layer soil moisture pools which add increased complexity (Baker et al., 2008; Powell et al., 2013; Haynes et al., 2020). The present thesis proposed a more simplistic VPD driven drought stress term, which may be able to detect earlier drought stress in Sitka spruce, due to atmospheric

drought limiting productivity before soil drought (Chapter 5). However, this requires further development. For drought detection, using satellite data VI, e.g. CCI and GPP_{VI}, may be more appropriate tools for use with Sitka spruce owing to their inherent link to forest stress.

This thesis has presented the first attempt to infer seasonal Vcmax from MODIS band 11 based VI. Due to the strong association with these VI and seasonal photosynthetic dynamics, they could facilitate spatiotemporal Vcmax retrieval, which could improve satellite based canopy modelling reducing the reliance on externally tuned or PFT values, which are often based on poorly defined parameters (Rogers, 2014). Models can be tuned to specific time periods, sites or species. However, the more tuning needed, the less universally applicable a model is. An ideal model will contain inbuilt flexibility, to detect the interannual variability of a system, without model adjustments.

7.3 Pigments and drought stress

Pigments are the primary driver of VIS reflectance. Information about plant condition can be derived via pigment dynamics, and therefore are the bases for the majority of VI. Throughout this thesis, three major groups of plant pigments are discussed, and inferences about their composition are made, based on VI signals. The following section discusses findings in the context of pigment dynamics demonstrated throughout the chapters.

7.3.1 Chlorophyll

As the primary photosynthetic pigments and the bases for the most frequently used group of VI, historically and currently, the importance of chlorophylls in remote sensing is high and the VIg, e.g. NDVI, SR and EVI, set the benchmark for forest reflectance retrieval. Chlorophylls are an established biomarker of drought stress, due to their relationship with photosynthetic activity, and down regulation or damage during stress (Plesa et al., 2019; Grulke et al., 2020; Walshe et al., 2020). The relationship between chlorophyll reflectance and plant condition has proved useful and robust in a multitude of studies and therefore VIg are often the 'go to' for satellite based vegetation health monitoring and assessments (Bounoua et al., 2000; Anyamba & Tucker, 2012; Lange et al., 2017; Vorobiova & Chernov, 2017; Yang et al., 2017; Testa et al., 2018; Spruce et al., 2019; Gao et al., 2021; Huemmrich et al., 2021; Pompa-García et al., 2021). It was important to determine the usefulness of NDVI, and associated VIg, for studying a number of drought and productivity related metrics in Sitka spruce.

In Chapter 3, under increasingly severe water limitation, some VIg were completely insensitive to drought stress (NDVI, SR). In others (CIgr, CIre and NDVIre), differences between the drought and control group were marginal compared to other VI, but did increase as the drought progressed. This analysis highlighted the importance of choice of VI for specific applications. Within the VIg, those based on red-edge reflectance, were most sensitive to changes in chlorophyll. This is due to red light being more readily saturated than NIR light as chlorophyll absorption is higher (Horler et al., 1983; Gitelson & Merzlyak, 1994; Clevers & Gitelson, 2013). Reduced sensitivity in non red-edge VIg, was also documented in Chapter 4, where NDVI and SR, failed to detect differences between needle age classes, while CIre and NDVIre did.

The difference between Sitka spruce clones was detectable across all VIg (Chapters 3 and 4) and chlorophyll reflectance, namely red-edge reflectance, has been highlighted in the literature as a promising region for genotypic variation detection (Feng et al., 2017; Čepl et al., 2018; Hejtmánek et al., 2022). However, VIg all failed to detect varying drought responses between clones (Chapters 3 and 4), suggesting that other spectral regions may be more appropriate for intraspecific drought tolerance detection (e.g. PRI, ARI discussed below).

At the satellite scale, which NDVI and EVI were initially developed for, greenness VI correlated poorly with ftGPP unless multiplied by PAR in a LUE formulation (e.g. NDVI PAR models explained around 60% more ftGPP variation relative to VI-only models), highlighting how these VI are more closely related to FPAR than to GPP directly (Chapter 5). As predictors of annual GPP, NDVI and EVI were less reliant on PAR for GPP retrieval however, failed to capture drought induced productivity reductions, as a result of the 2018 summer drought (Chapter 5). VIg models predicted annual GPP increases of 1.6% to 7% in 2018, despite 5% reductions recorded at the flux tower (Xenakis et al., 2021). The insensitivity to drought stress detected by chlorophyll related VI throughout this thesis, suggests that these should not be the focus for early drought stress detection in Sitka spruce, especially at the satellite level, where the choice of VIg is more limited due to the reduced availability of spectral bands.

7.3.2 Carotenoids and the xanthophyll cycle

Throughout the present thesis, VI representing carotenoid dynamics were important in inferring how Sitka spruce responds to environmental conditions. In Chapters 3 and 4 PRI, in accordance with the literature, was a good marker of conifer health status during drought stress (Peguero-Pina et al., 2007; Filella et al., 2009; Hernández-Clemente et al., 2011; Wong & Gamon, 2015a; Mõttus et al., 2017, 2019),

whereby it tracks the facultative (short term) response to drought stress (see Chapter 4 for discussion of this) (Gamon & Berry, 2012). PRI proved sufficiently sensitive to differentiate variations in stress responses between Sitka spruce clones (Chapter 3) and canopy positions (Chapter 4).

CCI is a derivative of PRI, but designed for broadband MODIS sensors (Gamon et al., 2016). Like PRI, the central wavelength for the detection of the xanthophyll cycle is 531 nm (the central wavelength of MODIS band 11). Using a hyperspectral sensor at the needle level, CCI proved less sensitive to drought stress than PRI (Chapters 3 and 4). However, at the satellite scale, where PRI retrieval is limited due to a lack of bands covering reflectance at 570 nm, CCI detected annual drought induced anomalies in GPP. Alongside GPP_{VI}, CCI was the VI most closely related to the seasonal cycles of GPP, shown by higher R^2 (over 0.5) (Chapter 5). CCI tracks seasonal photosynthesis and stress responses, due to its relationship with chlorophyll/carotenoid dynamics, that track both changing light and temperature levels across a season and the energy dissipation mechanisms that the xanthophyll cycle plays in drought stress mediation (Wong & Gamon, 2015a). This ability for CCI to track both seasonal photosynthetic dynamics and stress responses provided the theoretical bases for exploring its relationship with ε and Vcmax. The accurate parametrisation of which has been identified as a major limitation to the LUE (Rahman et al., 2004; Huang et al., 2024; Prentice et al., 2024) and process based modelling (Long & Bernacchi, 2003; Rogers, 2014; Alton, 2017; Deng et al., 2024). As discussed in Chapter 5 using scaled CCI (ε_{CCI}) as a proxy for ε had limited effect on GPP retrival, despite the theoretical link. Inferring Vcmax directly from VI was a novel approach. The most promising finding outlined in Chapter 6 was the possibility of improved detection of interannual variability, facilitated by VI derived Vcmax, which is dynamic in both space and time.

7.3.3 Anthocyanins

Anthocyanin-related VI were among the best for drought stress detection (Chapters 3 and 4). A linear drought response was detected in ARI and ARI2, which were sensitive enough to detect differences between clones (Chapter 3), and canopy positions (Chapter 4). Increased anthocyanin expression was detected in the upper canopy, especially in younger needles. Anthocyanins however, are understudied relative to other pigments, especially at the satellite scale (Viña & Gitelson, 2011). The satellite work here (Chapters 5 and 6) was focused on GPP, as a combined indicator of stress and seasonal cycles that links to the carbon cycle, as well as a crucial component of the SiB model. Anthocyanins have a minor, if any, role in photosynthesis (Simkin et al., 2022). The choice of VI was selected based on established links to

GPP which excluded anthocyanin based VI.

Although limited in quantity, research in the literature highlights that anthocyanins can be inferred from satellite VI (Viña & Gitelson, 2011; Bayle et al., 2019). Therefore, anthocyanin VI could play a role in stress detection from space. Especially in conifers, which do not undergo full canopy seasonal senescence (which anthocyanins play a promenade role in), which could confound stress detection. As anthocyanins are less related to photosynthesis than other pigments (Simkin et al., 2022), it may be easier to disentangle stress specific responses via anthocyanins relative to carotenoids, which are spectrally confounded by chlorophyll and biophysically confounded by the association with photosynthesis (Gitelson et al., 2002; Wong & Gamon, 2015a; Gitelson, 2020; Sonobe et al., 2020). Therefore, satellite-based anthocyanin detection may be of use for drought monitoring in Sitka spruce.

7.4 Scaling

One of the reasons for the applicability of VI is spatial scalability (Zeng et al., 2022). This means that VI selected for the needle level analysis in Chapters 3 and 4 can be applied at the canopy scale for regional or global analysis. However, some limitations of scaling and differences between scales were identified across this thesis. Defoliation and needle necrosis occurred as a direct response to drought stress in the drought experiment (see Appendix A, Figure A.4 (178)). Needle level analysis, as discussed in Chapter 3, did not detect crown thinning, so failed to capture structural parameters (e.g LAI) associated with NIR radiation (Croft & Chen, 2018). VI such as NDVI, which use NIR reflectance, can capture changes in LAI when whole canopies are imaged (Yang et al., 2017). However, no major drought induced defoliation occurred in 2018 at the Harwood forest, as drought induced senescence is a severe stress response in conifers (Green & Ray, 2009; Choat et al., 2018).

Satellite reflectance retrieval cannot differentiate within individual needle classes and homogenises the response of different portions of the canopy. Chapter 4 demonstrated the variety of VI responses throughout Sitka spruce canopies, due to environmental and age differences (O'Neill et al., 2002). Pigment concentrations were lower in the top canopy and accumulated in older needles. Understanding this is important to fully explain, or model, the two dimensional data that satellite based reflectance measurements retrieve. Saturation in summer GPP retrieval was a limitation in Chapters 5 and 6. As discussed in Chapter 6, multilayer models can overcome these saturation effects (Alton, North, & Los, 2007; Alton & Bodin, 2010; Alton, 2016; Luo et al., 2018; Bonan et al., 2021). Analyses such as in Chapter

4 are key to inform these models which often partition sun and shaded canopy responses to model canopy layers. Pigment differences were most pronounced mid season when GPP is expected to be greatest (Chapter 4). Incorporating dynamic differences between canopy layers, over a growing season, could therefore facilitate higher modelling accuracy and reduce summer saturation effects.

7.5 Best performing VI

VI are relatively simple to acquire, have robust relationships with plant bio-physiology, and are easily interpretable to non experts (important for widespread use in forestry (Locatelli et al., 2021; Zeng et al., 2022)). Therefore, VI could be useful tools to provide forest managers with information on drought vulnerability and stress (Locatelli et al., 2021). Linking VI to forest health metrics, using freely available satellite data, could provide foresters with capabilities to map various stress metrics. A VI that is closely linked to drought stress, or productivity, in Sitka spruce, could be used to rapidly assess the condition of stands countrywide. Therefore assessing and identifying promising VI was a major research aim of this thesis.

NDVI and associated VI performed poorly for drought stress detection across research chapters, however, when modelled with metrological variables were able to track non stressed GPP. VI associated with the xanthophyll cycle (PRI, CCI, GPP_{VI}) are better associated with drought stress (see Section 7.3.2 above), and were the VI most tightly associated with ftGPP seasonal dynamics (Chapter 5). The relationship between MODIS band 11 and conifer productivity has been discussed (see Chapters 5 and 6). Therefore CCI and GPP_{VI} are highlighted here as promising VI for future UK forestry, potentially facilitating simple and rapid assessment of Sitka spruce health at individual tree to stand or country scales.

7.6 Low productivity in 2015 compared to 2018

Chapters 5 and 6 used GPP recorded at the Harwood site to infer plant function. In 2018 a reduction in productivity, which here, and in Xenakis et al. (2021), is attributed to drought stress due to association with a number of measured variables. In spring and summer 2018, a long period of no rainfall occurred as temperatures were high, causing relative humidity to drop. Soil moisture reached substantially lower values in 2018 compared to the other three years and evapotranspiration was exceptionally high in 2018 causing a large reduction in Water Use Efficiency (WUE) (see Figure 2.12 (pp.73) and Xenakis et al. (2021)). These factors contributed to an anomalous year. Total annual GPP was lower in 2015 compared to 2018 however,

was not considered a drought year. Temperature and soil moisture all occur within a range that is similar to 2016 and 2017. VPD appears slightly raised relative to 2016 and 2017 however, this is not accompanied by abnormally high or low evapotranspiration and, unlike 2018, WUE remains normal throughout the year (Xenakis et al., 2021). It is therefore assumed that the low productivity of 2015 is due to a combination of 'non-ideal' growing conditions, creating an overall less productive year, without the plants being actively stressed, or initiating a stress response. Legacy of droughts can impact forests productivity in subsequent years (Peltier & Ogle, 2019; Kannenberg et al., 2020; Locatelli et al., 2021), which may contribute to the low 2015 GPP however, no data from Harwood forests exists pre 2015. This highlights the inherent difficulty of studying natural systems without environmental controls and the difficulty in estimating productivity.

7.7 Future research

The analysis in Chapters 3 and 4 demonstrated that intraspecific clonal differences can be detected among Sitka spruce clones. For the first time, differential drought responses were detected via VI in conifers. This opens avenues for the UK forestry sector for rapid non-destructive, and cost effective drought tolerance assessments, and high throughput phenotyping (Plesa et al., 2019; Liming & Huichun, 2020; Baldi & La Porta, 2022). Future work should build on Chapters 3 and 4, by identifying key reflectance markers, related to drought tolerance, using simple VI, multiple VI, or ML derived VI which can exploit a greater spectral range (Verrelst et al., 2019). If reliable spectral drought tolerance markers can be established, they should be incorporated into the Sitka spruce breeding programme, which currently, only selects for high timber quality and to maintain genetic diversity (Lee, 1999). Introducing more drought resilient progeny into future plantations will go some way to 'drought proofing' future forests in a changing climate.

The non destructive repeat spectral measurements procedure, developed for this thesis, successfully monitored pigment and water content of Sitka spruce scions, across the early to later stages of drought, giving insights into multiple stress responses. A recommendation, where possible, would be to combine this type of experiment with metabolomic and water content measurements of needles, to give a clearer picture of the process inferred from VI. This would be especially interesting in the case of water content, which appeared to increase in Sitka spruce needles in the initial stages of drought. In Chapters 3 and 4 the benefits of measuring drought stress with multiple VI were discussed. Focusing on one drought stress trait, e.g. water content, would miss a pigment response. ML algorithms allow links with biophysical traits and the

whole spectrum to be made (Verrelst et al., 2019). Developing ML indices could potentially capture a fuller drought response than using only one metric. This could be especially useful to build a Sitka spruce drought index which incorporates the many facets of stress response or the genetic differences between clones. Future work should look to characterise the whole spectral profile of plants under drought stress to try to establish drought responses. At the satellite level, the ability of MODIS band 11 VI to detect drought stress from space is promising for UK foresters. UK wide stress monitoring could be developed using VI based in band 11 (e.g. CCI, GPP_{VI}). By expanding VI retrieval to greater spatial area, stress hotspots could be identified, where Sitka spruce are more vulnerable to drought stress, which could inform future forestry planning (Green & Ray, 2009; Locatelli et al., 2021).

Deriving Vcmax from satellite spectral data provides great potential for introducing more biological realism into process-based models. Static Vcmax values have been outlined as a major limitation to processed-based eco physiological modelling. The theoretical link between CCI/ GPP_{VI} and photosynthetic capacity provides a justification to derive Vcmax from them. The preliminary new work here, should be developed by testing the relationship between these types of VI and measured Vcmax, across various species and sites, to establish if a robust link between the two exists. This could potentially facilitate a global and temporally-continuous Vcmax product, akin to MODIS based LAI or FPAR products.

MODIS can be related to the xanthophyll cycle due to reflectance retrieval at 531 nm. The spectral resolution of MODIS is poor compared to newer satellite missions e.g. Sentinel-2. However, Sentinel-2 lacks bands centred at 531 nm. Future satellite missions should incorporate these wavelengths at higher spatial resolution in order to better capture biophysical processes.

7.8 Final Conclusions

The present thesis has evaluated the use of VI for studying drought stress and productivity in Sitka spruce at various spatiotemporal scales, aiming to explore potential ways that the UK forestry sector could adopt remotely sensed VI and transition towards more drought-resilient management. Consistently, VI associated with the xanthophyll cycle and reflectance based at 531 nm (PRI, CCI, GPP_{VI}) were identified as key metrics for monitoring and assessing drought stress and the general health of Sitka spruce. Relative to NDVI, the most frequently used VI, the xanthophyll-related VI (i) better detected early and progressively increasing drought stress at the needle level, where they were able to distinguish differences between clones and canopy positions, (ii) more closely tracked seasonal GPP (when mete-

orological variables were omitted) and (iii) identified stress-mediated annual GPP declines, which were detectable with MODIS satellite imagery. A novel approach to improving process-based model realism is described and tested using the theoretical link between CCI (and its derivative GPP_{VI}) and Vcmax, opening possibilities for spatially and temporally dynamic global Vcmax retrieval. This approach aims to overcome static Vcmax parametrisation, which is currently a major limitation in local and global biophysical modelling. For the first time, the possibility of rapid screening of conifer clones for drought tolerance using reflectance measurements is demonstrated. This opens up possibilities for high-throughput phenotyping to improve drought resistance in the Sitka spruce breeding program. Never before has UK forestry been at such high risk from drought. This risk will continue to increase as anthropogenic activities fail to curb global emissions. Remote sensing provides unprecedented data availability to monitor and model how the existential threats faced will impact forests. By using this data, informed decisions may help mitigate the very worst impacts and, in some way, future-proof commercial and natural forests.

Appendix A

Supplementary material: Chapter 2

Data and methods

A.1 Experimental set up

Figure A.1: The standard leaf clip for spectral measurements using a field spectroradiometer (ASD FieldSpec 4 standard Res, Analytik Ltd, Cambridge). The leaf clip is designed for flat, broadleaf plants. When recording *in situ* conifer needles light escapes, potentially confounding spectral measurements.

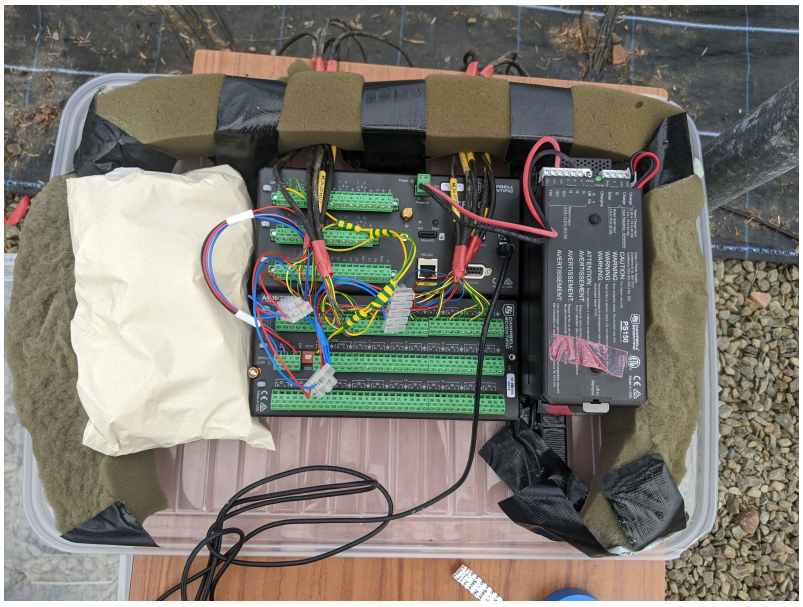

Figure A.2: A Data logger (CR1000x, Campbell Scientific, Shepshed, UK) was used to automatically record soil moisture readings for six droughted and six control Sitka spruce. Readings were taken every 30 minutes for the duration of the study and supplemented by manual hand held soil moisture measurements. A clear plastic box was placed over the data logger alongside a bag of desiccant to protect the equipment from high humidity levels.

Figure A.3: Small vertical stature of Clone 6 individual. Some Clone 6 individuals had smaller vertical structure relative to the other trees. This meant splitting the individual into distinct vertical canopy profiles was not possible. Therefore, Clone 6 individuals were excluded from the analysis in Chapter 4.

Figure A.4: High defoliation rates on two Clone 6 individuals subject to experimental drought. Defoliation was generally higher in older needles. The high defoliation rates of a number of Clone 6 individuals meant reliable measurements on all canopy positions on all individuals was not possible so Clone 6 was excluded from Chapter 4 analysis.

A.2 Cloud free MODIS observations

Table A.1: The number of high quality MODIS observations available for analysis. All data from the pixel corresponding to the location of the flux tower (55°13'00"N, 2°01'32"W) where downloaded then filterd using the MODIS QA band (QA= 0,1). High view angles ($> 35°$) and low EVI values were removed. The numbers in the table are the total number of observation left for analysis after filtering. Observations are separated by year and season where, Winter = December, January, February. Spring = March, April, May. Summer = June, July, August. Autumn = September, October, November.

Year	Winter	Spring	Summer	Autumn	Total
2000	0	6	0	1	7
2001	4	5	0	1	10
2002	0	4	1	2	7
2003	11	8	9	5	33
2004	5	5	2	3	15
2005	1	5	6	10	22
2006	7	6	7	8	28
2007	8	5	1	10	24
2008	3	4	2	5	14
2009	3	14	2	6	25
2010	0	3	3	6	12
2011	4	12	3	8	27
2012	8	10	1	4	23
2013	5	4	5	3	17
2014	1	6	4	1	12
2015	0	3	1	5	9
2016	0	2	2	4	8
2017	1	6	2	2	11
2018	0	4	12	3	19
2019	6	7	3	5	21
2020	1	7	2	3	13
2021	1	9	6	3	19
2022	8	10	7	0	25
Average	3.3	6.3	3.5	4.3	17.4
Total	76	145	80	99	400

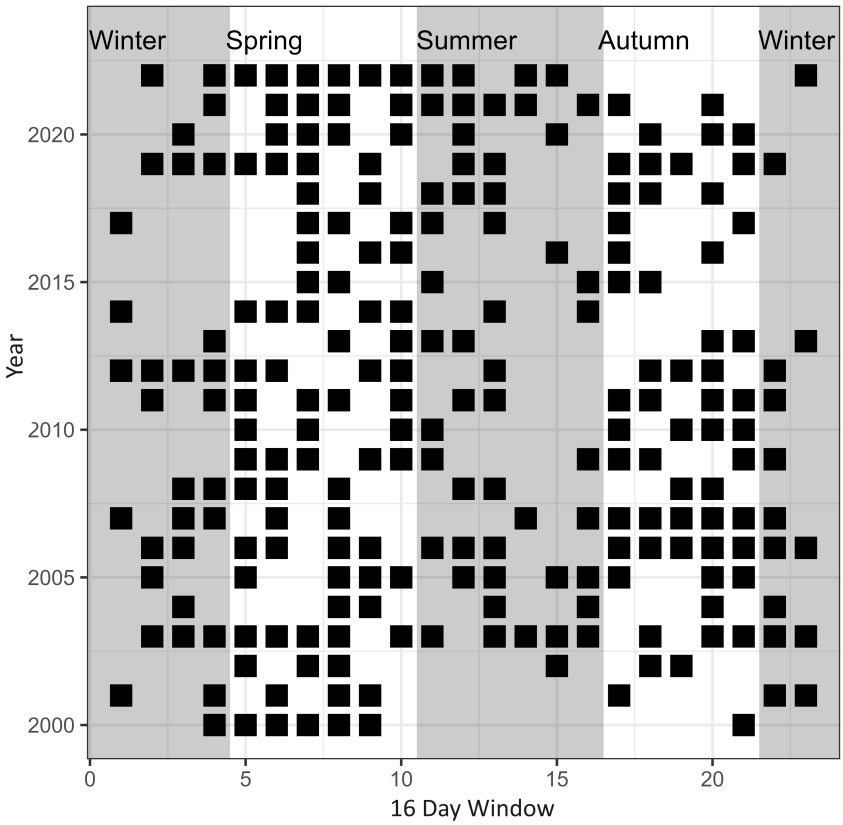

Figure A.5: The 16 day windows that include high quality MODIS observations. For each year between 2000 and 2022 dates were separated into 16 day windows (23 per year). The black squares represent a high quality observation was present (see Table A.1 for data filtering) in a specific 16 day window.

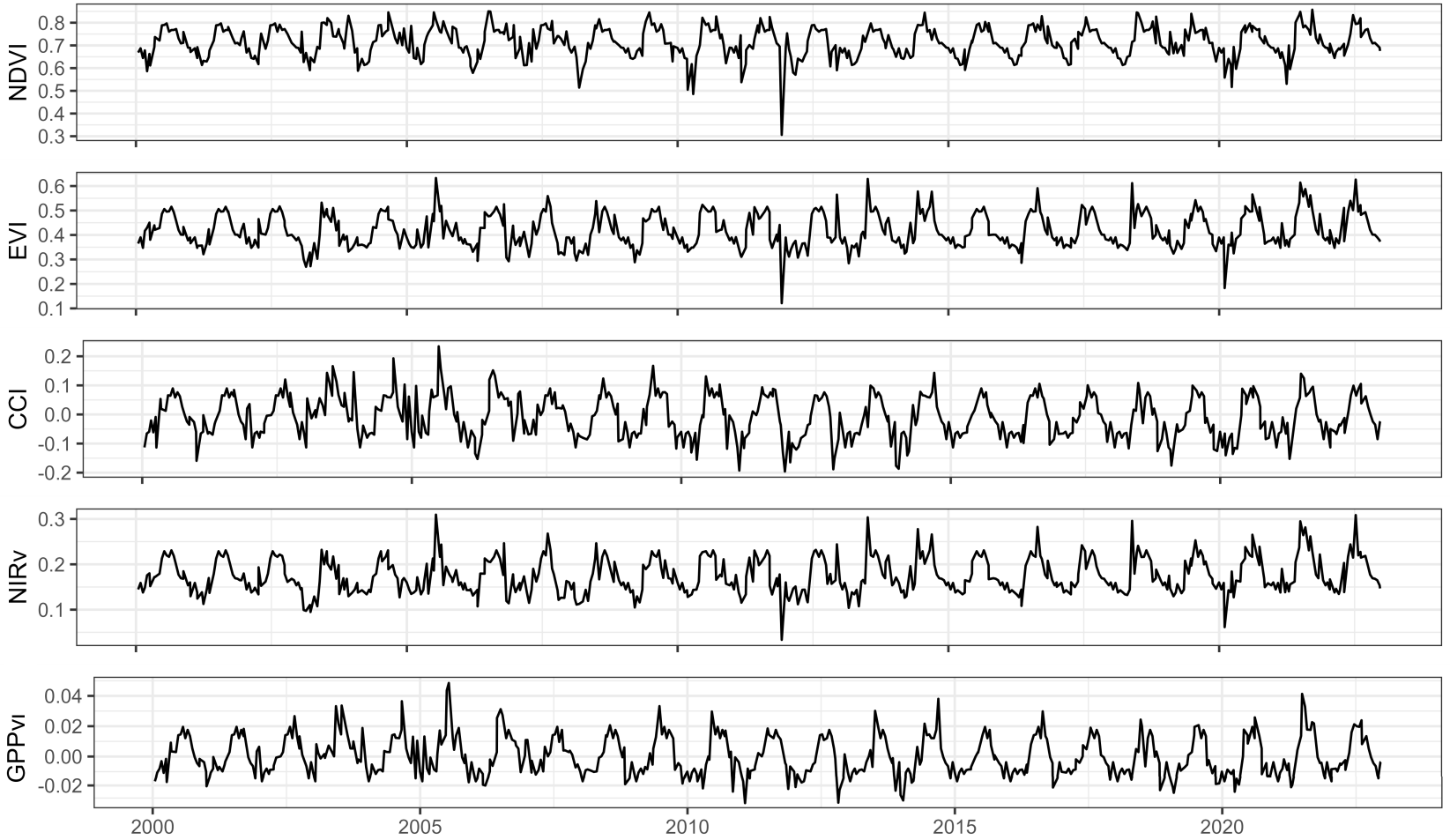

Figure A.6: The full VI_{16} time series 2000 - 2022. VI_{16} is processed using the CV-MVC method outlined in 2.4.5.2 (p.56) for each of the five Vegetation Indices (VI). The original data source is MAIAC-processed MODIS daily reflectance. For full VI names, formula and references see Table 2.2 (p.58).

A.3 Interpolation algorithms

Table A.2: Comparison of interpolation methods for gap filling MODIS time series. To create a continuous daily time series (VI_{day}) for five VI (NDVI, EVI, CCI, NIRv, GPP_{VI}) daily interpolation was conducted, using Decomposition and Analysis of Time Series software (DATimeS) (Belda et al., 2020), on quality filtered MAIAC observations. DATimeS is a stand-alone image processing GUI toolbox containing many mathematical fitting algorithms (fs). For each VI, five fitting algorithms (GPR = Gaussian Process Regression, KRR = Kernel Ridge Regression, LIN = Linear interpolation, FT = Fourier Transform, SIG = Sigmoid Function, WHIT = Whittaker smoothing) were run and the most appropriate selected by comparing each interpolated VI time series to flux tower GPP (ftGPP) using regression analysis. GPR was selected for all interpolations as for all VI, except NIRv, GPR was the best or joint best performing algorithm (highest R^2), and it is the only algorithm that produced uncertainty estimates.For full VI names, formula and references see Table 2.2 (p.58).

VI	fs	F-Statistic	df	p value	R^2
NDVI	GPR	705.22	1 1448	<0.001	0.33
	KRR	671.01	1 1448	<0.001	0.32
	LIN	492.36	1 1448	<0.001	0.25
	FT	709.92	1 1448	<0.001	0.33
	SIG	660.96	1 1448	<0.001	0.31
	WHIT	639.30	1 1448	<0.001	0.31
EVI	GPR	1221.25	1 1448	<0.001	0.46
	KRR	1248.58	1 1448	<0.001	0.46
	LIN	795.88	1 1448	<0.001	0.35
	FT	1244.88	1 1448	<0.001	0.46
	SIG	1045.47	1 1448	<0.001	0.42
	WHIT	1080.89	1 1448	<0.001	0.43
CCI	GPR	1693.84	1 1448	<0.001	0.54
	KRR	1657.21	1 1448	<0.001	0.53
	LIN	1294.04	1 1448	<0.001	0.47
	FT	1620.33	1 1448	<0.001	0.53
	SIG	1482.16	1 1448	<0.001	0.51
	WHIT	1495.74	1 1448	<0.001	0.51
NIRv	GPR	905.22	1 1448	<0.001	0.38
	KRR	904.17	1 1448	<0.001	0.38
	LIN	727.71	1 1448	<0.001	0.33
	FT	863.92	1 1448	<0.001	0.37
	SIG	975.53	1 1448	<0.001	0.40
	WHIT	830.67	1 1448	<0.001	0.36
GPP_{VI}	GPR	1702.42	1 1448	<0.001	0.54
	KRR	1656.50	1 1448	<0.001	0.53
	LIN	1317.57	1 1448	<0.001	0.48

Table A.2 continued on next page

Table A.2 continued from previous page

VI	fs	F-Statistic	df	p value	R^2
	FT	1602.13	1 1448	<0.001	0.52
	SIG	1592.45	1 1448	<0.001	0.52
	WHIT	1516.98	1 1448	<0.001	0.51

Appendix B

Supplementary material: Chapter 3

Evaluating the drought responses of Sitka spruce (*Picea sitchensis*) clones using Vegetation Indices (VI). Are genetic differences detectable with VI?

B.1 Estimated marginal means (EMM) contrasts

Table B.1: Estimated Marginal Means (EMM) to analyse the effects of drought on Vegetation Indices (VI) over an increasingly severe drought. For each VI, a mixed effect model was formulated where each individual plant was treated as a random effect. Time in days after drought treatment initiation (Time), watering regime (Treatment) and clonal group (Clone) were treated as main effects. Interactive effects of these main variables, including a three-way interaction, were also tested. When a significant Time: Treatment effect was detected, EMM contrasts between the control and drought groups were conducted at regular time points (results for a contrast every seven days are presented here) using the mixed effects models. DoD is the number of days since the initiation of the experimental drought. For full VI names, formula and references see Table 2.1 (p.43).

VI	DoD	Estimate	SE	*df*	t.ratio	*p* value
ARI	1	-0.092	0.083	104.777	-1.104	0.272
	7	-0.173	0.078	81.867	-2.213	0.030
	14	-0.267	0.073	63.902	-3.645	0.001
	21	-0.362	0.070	53.802	-5.149	<0.001
	28	-0.456	0.069	50.260	-6.604	<0.001
	35	-0.550	0.070	52.743	-7.875	<0.001
	42	-0.644	0.073	61.630	-8.871	<0.001
	49	-0.739	0.077	78.112	-9.573	<0.001
	56	-0.833	0.083	103.823	-10.018	<0.001
ARI2	1	-0.057	0.054	105.312	-1.073	0.286

Table B.1 continued on next page

Table B.1 continued from previous page

VI	DoD	Estimate	SE	*df*	t.ratio	*p* value
	7	-0.113	0.050	82.162	-2.254	0.027
	14	-0.178	0.047	64.016	-3.782	<0.001
	21	-0.243	0.045	53.820	-5.392	<0.001
	28	-0.308	0.044	50.246	-6.951	<0.001
	35	-0.373	0.045	52.752	-8.315	<0.001
	42	-0.438	0.047	61.722	-9.385	<0.001
	49	-0.502	0.050	78.369	-10.140	<0.001
	56	-0.567	0.053	104.347	-10.620	<0.001
CCI	1	-0.014	0.011	207.098	-1.332	0.184
	7	-0.007	0.009	106.790	-0.770	0.443
	14	0.003	0.009	114.671	0.301	0.764
	21	0.012	0.009	98.850	1.430	0.156
	28	0.021	0.008	81.830	2.600	0.011
	35	0.029	0.009	92.969	3.413	0.001
	42	0.035	0.009	110.651	3.875	<0.001
	49	0.037	0.009	104.534	4.227	<0.001
	56	0.036	0.011	210.583	3.343	0.001
CIgr	1	0.140	0.210	75.783	0.667	0.507
	7	-0.006	0.199	61.416	-0.033	0.974
	14	-0.144	0.200	62.395	-0.720	0.474
	21	-0.239	0.199	60.986	-1.202	0.234
	28	-0.285	0.198	59.626	-1.443	0.154
	35	-0.277	0.200	61.838	-1.385	0.171
	42	-0.206	0.201	63.673	-1.025	0.309
	49	-0.068	0.199	61.135	-0.341	0.734
	56	0.145	0.210	74.852	0.691	0.492
CIre	1	0.093	0.103	69.762	0.901	0.371
	7	0.091	0.099	59.334	0.916	0.364
	14	0.092	0.099	60.176	0.921	0.361
	21	0.100	0.099	58.470	1.008	0.318
	28	0.118	0.098	56.558	1.202	0.234
	35	0.150	0.098	57.820	1.520	0.134
	42	0.199	0.099	59.747	2.001	0.050
	49	0.268	0.099	59.092	2.707	0.009
	56	0.361	0.103	70.154	3.492	0.001
CRI1	1	0.051	0.347	368.671	0.147	0.883
	7	-0.642	0.263	179.511	-2.443	0.016
	14	-1.031	0.271	197.776	-3.808	<0.001
	21	-1.094	0.254	160.808	-4.302	<0.001
	28	-0.959	0.234	119.872	-4.100	<0.001
	35	-0.757	0.248	146.722	-3.060	0.003
	42	-0.619	0.267	188.535	-2.319	0.021
	49	-0.674	0.260	174.158	-2.587	0.011

Table B.1 continued on next page

Table B.1 continued from previous page

VI	DoD	Estimate	SE	*df*	t.ratio	*p* value
	56	-1.052	0.350	372.863	-3.005	0.003
MSI	1	-0.002	0.005	226.894	-0.316	0.752
	7	<0.001	0.004	114.029	0.033	0.974
	14	0.004	0.004	121.819	0.890	0.375
	21	0.007	0.004	110.429	1.775	0.079
	28	0.009	0.004	99.544	2.000	0.029
	35	0.007	0.004	116.618	1.589	0.115
	42	-0.001	0.004	131.451	-0.303	0.762
	49	-0.017	0.004	111.846	-4.080	<0.001
	56	-0.041	0.005	220.651	-8.258	<0.001
NDWI	1	0.003	0.003	211.788	1.014	0.312
	7	0.001	0.002	108.305	0.611	0.543
	14	-0.001	0.002	116.601	-0.493	0.623
	21	-0.004	0.002	106.341	-1.591	0.115
	28	-0.005	0.002	97.179	-2.226	0.028
	35	-0.004	0.002	114.603	-1.748	0.083
	42	<0.001	0.003	129.105	0.041	0.967
	49	0.009	0.002	110.095	3.748	<0.001
	56	0.024	0.003	215.490	8.029	<0.001
NDWI2	1	0.003	0.006	225.237	0.471	0.638
	7	<0.001	0.005	113.399	<0.001	1.000
	14	-0.005	0.005	121.106	-0.984	0.327
	21	-0.009	0.004	109.839	-1.958	0.053
	28	-0.011	0.004	99.075	-2.470	0.015
	35	-0.009	0.005	115.970	-1.879	0.063
	42	<0.001	0.005	130.644	-0.035	0.972
	49	0.016	0.005	111.239	3.641	<0.001
	56	0.043	0.006	219.035	7.805	<0.001
NDVIre	1	0.015	0.016	68.983	0.962	0.339
	7	0.015	0.015	58.975	0.980	0.331
	14	0.014	0.015	59.664	0.917	0.363
	21	0.014	0.015	58.674	0.896	0.374
	28	0.015	0.015	57.716	0.987	0.328
	35	0.019	0.015	59.275	1.257	0.214
	42	0.028	0.016	60.564	1.790	0.078
	49	0.041	0.015	58.778	2.692	0.009
	56	0.062	0.016	68.340	3.853	<0.001
PRI	1	-0.002	0.005	80.411	-0.286	0.776
	7	0.004	0.005	68.896	0.712	0.479
	14	0.010	0.005	59.551	1.959	0.055
	21	0.016	0.005	54.055	3.259	0.002
	28	0.022	0.005	51.997	4.554	<0.001

Table B.1 continued on next page

Table B.1 continued from previous page

VI	DoD	Estimate	SE	*df*	t.ratio	*p* value
	35	0.028	0.005	53.214	5.784	<0.001
	42	0.035	0.005	57.804	6.896	<0.001
	49	0.041	0.005	66.118	7.855	<0.001
	56	0.047	0.005	78.708	8.649	<0.001
SRWI	1	0.007	0.008	211.835	0.984	0.326
	7	0.003	0.006	108.323	0.555	0.580
	14	-0.003	0.006	116.621	-0.536	0.593
	21	-0.010	0.006	106.358	-1.606	0.111
	28	-0.013	0.006	97.193	-2.214	0.029
	35	-0.011	0.006	114.622	-1.733	0.086
	42	<0.001	0.007	129.128	0.019	0.985
	49	0.023	0.006	110.113	3.624	<0.001
	56	0.060	0.008	215.538	7.776	<0.001
WI	1	0.002	0.003	256.392	0.710	0.479
	7	<0.001	0.002	126.469	0.133	0.895
	14	-0.003	0.002	137.260	-1.107	0.270
	21	-0.005	0.002	115.533	-2.456	0.016
	28	-0.007	0.002	92.090	-3.506	0.001
	35	-0.007	0.002	107.444	-3.308	0.001
	42	-0.004	0.002	131.753	-1.773	0.079
	49	0.003	0.002	123.416	1.336	0.184
	56	0.015	0.003	260.934	5.264	<0.001
WI/NDVI	1	0.008	0.009	224.895	0.933	0.352
	7	0.012	0.007	113.289	1.578	0.117
	14	0.009	0.008	122.162	1.191	0.236
	21	0.003	0.007	104.351	0.354	0.724
	28	-0.004	0.007	85.203	-0.629	0.531
	35	-0.008	0.007	97.731	-1.169	0.245
	42	-0.006	0.007	117.637	-0.818	0.415
	49	0.006	0.007	110.747	0.763	0.447
	56	0.030	0.009	228.655	3.304	0.001

Table B.2: Estimated Marginal Means (EMM) to analyse the effects of drought and clonal group on Vegetation Indices (VI) over an increasingly severe drought. For each VI, a mixed effect model was formulated where each individual plant was treated as a random effect. Time in days after drought treatment initiation (Time), watering regime (Treatment) and clonal group (Clone) were treated as main effects. Interactive effects of these main variables, including a three-way interaction, were also tested. When a significant Time: Treatment: Clone effect was detected, EMM contrasts between the control and drought groups for each Clonal group were conducted at regular time points (results for a contrast every seven days are presented here) using the mixed effects models. DoD is the number of days since the initiation of the experimental drought. For full VI names, formula and references see Table 2.1 (p.43).

VI	Clone	DoD	Estimate	SE	*df*	t.ratio	*p* value
ARI	Clone 1	1	-0.088	0.083	104.928	-1.055	0.294
		7	-0.145	0.081	88.785	-1.785	0.078
		14	-0.211	0.085	90.122	-2.472	0.015
		21	-0.277	0.096	108.297	-2.888	0.005
		28	-0.344	0.111	137.254	-3.087	0.002
		35	-0.410	0.130	170.522	-3.164	0.002
		42	-0.476	0.150	202.976	-3.181	0.002
		49	-0.542	0.171	231.838	-3.171	0.002
		56	-0.608	0.193	256.259	-3.149	0.002
	Clone 2	1	-0.091	0.083	104.928	-1.093	0.277
		7	-0.167	0.081	88.785	-2.057	0.043
		14	-0.255	0.085	90.122	-2.990	0.004
		21	-0.344	0.096	108.297	-3.578	0.001
		28	-0.432	0.111	137.254	-3.881	<0.001
		35	-0.520	0.130	170.522	-4.017	<0.001
		42	-0.608	0.150	202.976	-4.066	<0.001
		49	-0.697	0.171	231.838	-4.075	<0.001
		56	-0.785	0.193	256.259	-4.064	<0.001
	Clone 3	1	-0.090	0.083	104.882	-1.081	0.282
		7	-0.160	0.081	88.737	-1.969	0.052
		14	-0.241	0.086	90.575	-2.816	0.006
		21	-0.322	0.097	109.558	-3.335	0.001
		28	-0.403	0.112	139.302	-3.592	<0.001
		35	-0.485	0.131	173.065	-3.700	<0.001
		42	-0.566	0.152	205.658	-3.734	<0.001
		49	-0.647	0.173	234.396	-3.733	<0.001
		56	-0.728	0.196	258.551	-3.717	<0.001
	Clone 4	1	-0.089	0.083	104.928	-1.071	0.287
		7	-0.154	0.081	88.785	-1.901	0.061
		14	-0.230	0.085	90.122	-2.694	0.008
		21	-0.306	0.096	108.297	-3.183	0.002

Table B.2 continued on next page

Table B.2 continued from previous page

VI	Clone	DoD	Estimate	SE	*df*	t.ratio	*p* value
		28	-0.381	0.111	137.254	-3.	0.001
		35	-0.457	0.130	170.522	-3.529	0.001
		42	-0.533	0.150	202.976	-3.559	<0.001
		49	-0.608	0.171	231.838	-3.557	<0.001
		56	-0.684	0.193	256.259	-3.540	<0.001
	Clone 5	1	-0.089	0.083	104.928	-1.066	0.289
		7	-0.151	0.081	88.785	-1.865	0.065
		14	-0.224	0.085	90.122	-2.626	0.010
		21	-0.297	0.096	108.297	-3.093	0.003
		28	-0.370	0.111	137.254	-3.323	0.001
		35	-0.443	0.130	170.522	-3.417	0.001
		42	-0.515	0.150	202.976	-3.444	0.001
		49	-0.588	0.171	231.838	-3.439	0.001
		56	-0.661	0.193	256.259	-3.421	0.001
	Clone 6	1	-0.105	0.083	104.910	-1.253	0.213
		7	-0.260	0.081	88.761	-3.209	0.002
		14	-0.442	0.085	90.338	-5.171	<0.001
		21	-0.624	0.096	108.862	-6.470	<0.001
		28	-0.805	0.112	137.995	-7.191	<0.001
		35	-0.987	0.131	171.089	-7.559	<0.001
		42	-1.169	0.151	203.056	-7.736	<0.001
		49	-1.350	0.173	231.268	-7.815	<0.001
		56	-1.532	0.195	255.008	-7.844	<0.001
ARI2	Clone 1	1	-0.055	0.054	105.462	-1.018	0.311
		7	-0.093	0.052	89.085	-1.779	0.079
		14	-0.137	0.055	90.259	-2.504	0.014
		21	-0.182	0.062	108.311	-2.947	0.004
		28	-0.226	0.072	137.110	-3.165	0.002
		35	-0.271	0.083	170.170	-3.253	0.001
		42	-0.315	0.096	202.390	-3.277	0.001
		49	-0.360	0.110	231.029	-3.272	0.001
		56	-0.404	0.124	255.259	-3.254	0.001
	Clone 2	1	-0.057	0.054	105.462	-1.057	0.293
		7	-0.108	0.052	89.085	-2.064	0.042
		14	-0.167	0.055	90.259	-3.045	0.003
		21	-0.226	0.062	108.311	-3.668	<0.001
		28	-0.286	0.072	137.110	-3.994	<0.001
		35	-0.345	0.083	170.170	-4.143	<0.001
		42	-0.404	0.096	202.390	-4.202	<0.001
		49	-0.464	0.110	231.029	-4.216	<0.001
		56	-0.523	0.124	255.259	-4.209	<0.001
	Clone 3	1	-0.056	0.054	105.416	-1.048	0.297

Table B.2 continued on next page

Table B.2 continued from previous page

VI	Clone	DoD	Estimate	SE	*df*	t.ratio	*p* value
		7	-0.104	0.052	89.037	-1.992	0.049
		14	-0.159	0.055	90.711	-2.901	0.005
		21	-0.215	0.062	109.569	-3.465	0.001
		28	-0.271	0.072	139.151	-3.750	<0.001
		35	-0.326	0.084	172.700	-3.875	<0.001
		42	-0.382	0.097	205.056	-3.919	<0.001
		49	-0.438	0.111	233.571	-3.925	<0.001
		56	-0.493	0.126	257.536	-3.913	<0.001
	Clone 4	1	-0.056	0.054	105.462	-1.049	0.297
		7	-0.104	0.052	89.085	-2.004	0.048
		14	-0.161	0.055	90.259	-2.930	0.004
		21	-0.217	0.062	108.311	-3.516	0.001
		28	-0.273	0.072	137.110	-3.819	<0.001
		35	-0.329	0.083	170.170	-3.955	<0.001
		42	-0.386	0.096	202.390	-4.007	<0.001
		49	-0.442	0.110	231.029	-4.017	<0.001
		56	-0.498	0.124	255.259	-4.007	<0.001
	Clone 5	1	-0.055	0.054	105.462	-1.033	0.304
		7	-0.098	0.052	89.085	-1.887	0.062
		14	-0.148	0.055	90.259	-2.708	0.008
		21	-0.199	0.062	108.311	-3.000	0.002
		28	-0.249	0.072	137.110	-3.478	0.001
		35	-0.299	0.083	170.170	-3.590	<0.001
		42	-0.349	0.096	202.390	-3.627	<0.001
		49	-0.399	0.110	231.029	-3.629	<0.001
		56	-0.449	0.124	255.259	-3.615	<0.001
	Clone 6	1	-0.066	0.054	105.445	-1.229	0.222
		7	-0.172	0.052	89.064	-3.296	0.001
		14	-0.295	0.055	90.478	-5.378	<0.001
		21	-0.419	0.062	108.877	-6.760	<0.001
		28	-0.542	0.072	137.848	-7.533	<0.001
		35	-0.666	0.084	170.730	-7.929	<0.001
		42	-0.789	0.097	202.464	-8.123	<0.001
		49	-0.912	0.111	230.455	-8.212	<0.001
		56	-1.036	0.126	254.005	-8.247	<0.001
MSI	Clone 1	1	-0.024	0.010	489.510	-2.531	0.012
		7	-0.007	0.007	387.796	-1.013	0.312
		14	0.005	0.007	411.116	0.772	0.440
		21	0.010	0.006	362.412	1.543	0.124
		28	0.008	0.005	280.512	1.512	0.132
		35	0.003	0.006	343.116	0.529	0.597
		42	-0.004	0.007	404.752	-0.576	0.565
		49	-0.011	0.006	379.380	-1.726	0.085

Table B.2 continued on next page

Table B.2 continued from previous page

VI	Clone	DoD	Estimate	SE	*df*	t.ratio	*p* value
		56	-0.017	0.010	489.521	-1.733	0.084
	Clone 2	1	0.007	0.010	489.647	0.736	0.462
		7	0.013	0.007	388.349	1.995	0.047
		14	0.020	0.007	410.830	2.881	0.004
		21	0.024	0.006	362.391	3.771	<0.001
		28	0.022	0.006	281.136	4.030	<0.001
		35	0.013	0.006	343.640	2.176	0.030
		42	-0.006	0.007	404.926	-0.890	0.374
		49	-0.038	0.006	379.435	-5.893	<0.001
		56	-0.085	0.010	489.516	-8.885	<0.001
	Clone 3	1	0.015	0.010	489.615	1.590	0.112
		7	0.006	0.007	387.565	0.934	0.351
		14	0.002	0.007	410.590	0.233	0.816
		21	0.001	0.006	362.964	0.170	0.865
		28	0.002	0.006	287.521	0.311	0.756
		35	0.001	0.006	351.919	0.130	0.896
		42	-0.005	0.007	408.046	-0.665	0.507
		49	-0.017	0.006	383.103	-2.629	0.009
		56	-0.039	0.010	490.611	-3.951	<0.001
	Clone 4	1	0.007	0.010	489.505	0.721	0.471
		7	0.002	0.007	387.148	0.312	0.755
		14	0.001	0.007	410.329	0.138	0.890
		21	0.002	0.006	361.857	0.389	0.698
		28	0.004	0.006	282.205	0.730	0.466
		35	0.003	0.006	346.341	0.543	0.588
		42	-0.002	0.007	406.912	-0.326	0.745
		49	-0.015	0.006	380.416	-2.324	0.021
		56	-0.037	0.010	489.513	-3.918	<0.001
	Clone 5	1	-0.018	0.010	489.589	-1.838	0.067
		7	-0.012	0.007	388.293	-1.770	0.078
		14	-0.003	0.007	411.037	-0.456	0.648
		21	0.005	0.006	362.284	0.789	0.431
		28	0.011	0.005	280.321	1.916	0.056
		35	0.012	0.006	342.850	1.942	0.053
		42	0.007	0.007	404.579	0.971	0.332
		49	-0.007	0.006	379.397	-1.106	0.270
		56	-0.031	0.010	489.527	-3.264	0.001
	Clone 6	1	0.003	0.010	489.738	0.307	0.759
		7	-0.002	0.007	396.359	-0.330	0.742
		14	-0.002	0.007	417.138	-0.280	0.780
		21	0.002	0.006	366.233	0.305	0.761
		28	0.006	0.006	281.360	1.105	0.270

Table B.2 continued on next page

Table B.2 continued from previous page

VI	Clone	DoD	Estimate	SE	*df*	t.ratio	*p* value
		35	0.007	0.006	347.259	1.198	0.232
		42	0.002	0.007	411.368	0.331	0.741
		49	-0.012	0.007	388.451	-1.879	0.061
		56	-0.040	0.010	489.607	-4.143	<0.001
NDWI	Clone 1	1	0.017	0.006	490.757	3.012	0.003
		7	0.006	0.004	381.754	1.618	0.106
		14	-0.002	0.004	406.306	-0.445	0.657
		21	-0.006	0.004	356.436	-1.535	0.126
		28	-0.006	0.003	274.975	-1.874	0.062
		35	-0.004	0.004	338.544	-1.076	0.283
		42	<0.001	0.004	401.283	0.090	0.928
		49	0.006	0.004	375.262	1.532	0.126
		56	0.012	0.006	490.939	2.093	0.037
	Clone 2	1	<0.001	0.006	490.794	0.045	0.965
		7	-0.007	0.004	381.876	-1.873	0.062
		14	-0.012	0.004	406.316	-3.134	0.002
		21	-0.014	0.004	356.814	-3.864	<0.001
		28	-0.012	0.003	275.904	-3.633	<0.001
		35	-0.005	0.004	339.	-1.443	0.150
		42	0.006	0.004	401.573	1.508	0.132
		49	0.022	0.004	375.470	5.785	<0.001
		56	0.043	0.006	490.925	7.626	<0.001
	Clone 3	1	-0.005	0.006	490.868	-0.938	0.349
		7	-0.002	0.004	382.185	-0.573	0.567
		14	-0.001	0.004	406.011	-0.206	0.837
		21	-0.001	0.004	357.099	-0.204	0.839
		28	-0.001	0.003	281.963	-0.253	0.801
		35	<0.001	0.004	347.184	0.020	0.984
		42	0.003	0.004	404.398	0.775	0.439
		49	0.009	0.004	379.069	2.462	0.014
		56	0.020	0.006	492.321	3.418	0.001
	Clone 4	1	-0.003	0.006	490.814	-0.622	0.534
		7	<0.001	0.004	382.278	0.113	0.910
		14	0.002	0.004	406.002	0.378	0.706
		21	<0.001	0.004	356.027	0.112	0.911
		28	-0.001	0.003	276.188	-0.378	0.705
		35	-0.002	0.004	341.195	-0.490	0.624
		42	<0.001	0.004	403.278	0.119	0.905
		49	0.007	0.004	376.471	1.875	0.062
		56	0.020	0.006	490.923	3.528	<0.001
	Clone 5	1	0.009	0.006	490.759	1.606	0.109
		7	0.005	0.004	381.757	1.345	0.180

Table B.2 continued on next page

Table B.2 continued from previous page

VI	Clone	DoD	Estimate	SE	*df*	t.ratio	*p* value
		14	<0.001	0.004	406.306	0.077	0.939
		21	-0.004	0.004	356.404	-1.065	0.288
		28	-0.006	0.003	274.812	-1.987	0.048
		35	-0.006	0.004	338.357	-1.750	0.081
		42	-0.002	0.004	401.214	-0.568	0.570
		49	0.007	0.004	375.304	1.736	0.083
		56	0.021	0.006	490.932	3.791	<0.001
	Clone 6	1	0.001	0.006	490.926	0.098	0.922
		7	0.006	0.004	390.266	1.653	0.099
		14	0.006	0.004	412.810	1.490	0.137
		21	0.001	0.004	360.512	0.306	0.760
		28	-0.005	0.003	275.955	-1.527	0.128
		35	-0.009	0.004	342.883	-2.452	0.015
		42	-0.007	0.004	408.225	-1.747	0.081
		49	0.004	0.004	384.634	0.972	0.332
		56	0.027	0.006	491.040	4.788	<0.001
NDWI2	Clone 1	1	0.028	0.010	489.328	2.634	0.009
		7	0.007	0.007	385.934	1.044	0.297
		14	-0.006	0.008	409.429	-0.858	0.391
		21	-0.012	0.007	360.438	-1.738	0.083
		28	-0.011	0.006	278.575	-1.811	0.071
		35	-0.006	0.007	341.106	-0.835	0.404
		42	0.002	0.007	403.017	0.311	0.756
		49	0.011	0.007	377.471	1.507	0.133
		56	0.017	0.010	489.339	1.663	0.097
	Clone 2	1	-0.006	0.011	489.475	-0.533	0.594
		7	-0.015	0.007	386.492	-2.076	0.039
		14	-0.023	0.007	409.140	-3.107	0.002
		21	-0.027	0.007	360.416	-3.968	<0.001
		28	-0.025	0.006	279.198	-4.090	<0.001
		35	-0.014	0.007	341.632	-2.108	0.036
		42	0.007	0.007	403.194	0.932	0.352
		49	0.040	0.007	377.526	5.665	<0.001
		56	0.087	0.010	489.334	8.310	<0.001
	Clone 3	1	-0.015	0.011	489.441	-1.000	0.154
		7	-0.006	0.007	385.701	-0.878	0.380
		14	-0.002	0.007	408.897	-0.318	0.750
		21	-0.002	0.007	360.993	-0.352	0.725
		28	-0.003	0.006	285.572	-0.565	0.572
		35	-0.003	0.007	349.940	-0.379	0.705
		42	0.003	0.007	406.345	0.432	0.666
		49	0.017	0.007	381.	2.368	0.018

Table B.2 continued on next page

Table B.2 continued from previous page

VI	Clone	DoD	Estimate	SE	*df*	t.ratio	*p* value
		56	0.041	0.011	490.525	3.757	<0.001
	Clone 4	1	-0.008	0.010	489.323	-0.800	0.424
		7	-0.002	0.007	385.281	-0.324	0.746
		14	-0.001	0.007	408.633	-0.086	0.932
		21	-0.002	0.007	359.880	-0.320	0.749
		28	-0.004	0.006	280.264	-0.700	0.485
		35	-0.004	0.007	344.340	-0.611	0.542
		42	0.001	0.007	405.198	0.136	0.892
		49	0.014	0.007	378.514	1.947	0.052
		56	0.037	0.010	489.331	3.521	<0.001
	Clone 5	1	0.019	0.011	489.413	1.853	0.065
		7	0.012	0.007	386.435	1.685	0.093
		14	0.002	0.008	409.349	0.309	0.757
		21	-0.007	0.007	360.308	-0.976	0.330
		28	-0.013	0.006	278.384	-2.125	0.034
		35	-0.014	0.007	340.839	-2.117	0.035
		42	-0.008	0.007	402.843	-1.116	0.265
		49	0.007	0.007	377.488	0.946	0.345
		56	0.033	0.010	489.345	3.131	0.002
	Clone 6	1	-0.002	0.011	489.573	-0.217	0.828
		7	0.004	0.007	394.574	0.542	0.588
		14	0.003	0.008	415.525	0.417	0.677
		21	-0.002	0.007	364.281	-0.343	0.731
		28	-0.009	0.006	279.421	-1.409	0.160
		35	-0.011	0.007	345.262	-1.669	0.096
		42	-0.006	0.008	409.704	-0.821	0.412
		49	0.011	0.007	386.612	1.479	0.140
		56	0.043	0.011	489.432	4.125	<0.001
PRI	Clone 1	1	-0.002	0.005	80.538	-0.374	0.710
		7	<0.001	0.005	74.293	0.066	0.947
		14	0.003	0.006	80.402	0.564	0.575
		21	0.006	0.006	100.246	0.976	0.332
		28	0.009	0.007	132.707	1.280	0.203
		35	0.012	0.008	174.525	1.494	0.137
		42	0.014	0.009	220.399	1.641	0.102
		49	0.017	0.010	264.985	1.744	0.082
		56	0.020	0.011	304.704	1.817	0.070
	Clone 2	1	-0.002	0.005	80.525	-0.318	0.751
		7	0.002	0.005	74.219	0.460	0.647
		14	0.007	0.006	80.300	1.321	0.190
		21	0.012	0.006	100.158	2.018	0.046
		28	0.017	0.007	132.673	2.520	0.013

Table B.2 continued on next page

Table B.2 continued from previous page

VI	Clone	DoD	Estimate	SE	*df*	t.ratio	*p* value
		35	0.022	0.008	174.568	2.863	0.005
		42	0.027	0.009	220.518	3.093	0.002
		49	0.032	0.010	265.156	3.249	0.001
		56	0.037	0.011	304.898	3.358	0.001
	Clone 3	1	-0.002	0.005	80.516	-0.309	0.758
		7	0.003	0.005	74.336	0.527	0.600
		14	0.008	0.006	80.917	1.447	0.152
		21	0.013	0.006	101.621	2.184	0.031
		28	0.019	0.007	135.183	2.710	0.008
		35	0.024	0.008	178.031	3.066	0.003
		42	0.029	0.009	224.552	3.304	0.001
		49	0.034	0.010	269.293	3.465	0.001
		56	0.040	0.011	308.775	3.575	<0.001
	Clone 4	1	-0.001	0.005	80.557	-0.215	0.831
		7	0.006	0.005	74.415	1.195	0.236
		14	0.015	0.006	80.622	2.735	0.008
		21	0.024	0.006	100.529	3.961	<0.001
		28	0.033	0.007	133.001	4.834	<0.001
		35	0.042	0.008	174.772	5.421	<0.001
		42	0.051	0.009	220.564	5.810	<0.001
		49	0.060	0.010	265.067	6.069	<0.001
		56	0.068	0.011	304.723	6.246	<0.001
	Clone 5	1	-0.001	0.005	80.523	-0.246	0.806
		7	0.005	0.005	74.202	0.973	0.334
		14	0.013	0.006	80.258	2.310	0.023
		21	0.021	0.006	100.086	3.378	0.001
		28	0.028	0.007	132.565	4.139	<0.001
		35	0.036	0.008	174.425	4.651	<0.001
		42	0.044	0.009	220.345	4.991	<0.001
		49	0.051	0.010	264.960	5.217	<0.001
		56	0.059	0.011	304.688	5.372	<0.001
	Clone 6	1	-0.001	0.005	80.486	-0.251	0.803
		7	0.005	0.005	74.097	0.941	0.350
		14	0.013	0.006	80.375	2.246	0.027
		21	0.020	0.006	100.692	3.282	0.001
		28	0.028	0.007	133.775	4.015	<0.001
		35	0.035	0.008	176.083	4.505	<0.001
		42	0.043	0.009	222.076	4.827	<0.001
		49	0.050	0.010	266.371	5.042	<0.001
		56	0.058	0.011	305.526	5.187	<0.001
SRWI	Clone 1	1	0.044	0.014	490.763	3.021	0.003
		7	0.016	0.010	381.812	1.578	0.115

Table B.2 continued on next page

Table B.2 continued from previous page

VI	Clone	DoD	Estimate	SE	*df*	t.ratio	*p* value
		14	-0.005	0.010	406.359	-0.504	0.614
		21	-0.015	0.009	356.496	-1.593	0.112
		28	-0.016	0.008	275.033	-1.914	0.057
		35	-0.010	0.009	338.605	-1.092	0.276
		42	0.001	0.010	401.336	0.078	0.938
		49	0.015	0.010	375.321	1.487	0.138
		56	0.029	0.015	490.945	2.009	0.045
	Clone 2	1	0.001	0.014	490.801	0.080	0.937
		7	-0.018	0.010	381.933	-1.865	0.063
		14	-0.032	0.010	406.368	-3.123	0.002
		21	-0.036	0.009	356.875	-3.820	<0.001
		28	-0.030	0.008	275.962	-3.549	<0.001
		35	-0.013	0.009	339.281	-1.371	0.171
		42	0.016	0.010	401.627	1.509	0.132
		49	0.055	0.010	375.529	5.625	<0.001
		56	0.106	0.015	490.932	7.324	<0.001
	Clone 3	1	-0.014	0.015	490.875	-0.996	0.320
		7	-0.006	0.010	382.242	-0.655	0.513
		14	-0.003	0.010	406.063	-0.263	0.793
		21	-0.002	0.009	357.159	-0.234	0.815
		28	-0.002	0.008	282.022	-0.252	0.801
		35	<0.001	0.009	347.244	0.039	0.969
		42	0.008	0.010	404.451	0.785	0.433
		49	0.024	0.010	379.127	2.431	0.016
		56	0.051	0.015	492.324	3.340	0.001
	Clone 4	1	-0.009	0.014	490.821	-0.654	0.513
		7	0.001	0.010	382.335	0.059	0.953
		14	0.004	0.010	406.054	0.347	0.729
		21	0.001	0.009	356.087	0.113	0.910
		28	-0.003	0.008	276.246	-0.342	0.733
		35	-0.004	0.009	341.256	-0.448	0.654
		42	0.001	0.010	403.331	0.128	0.898
		49	0.018	0.010	376.529	1.798	0.073
		56	0.049	0.015	490.929	3.367	0.001
	Clone 5	1	0.023	0.014	490.765	1.556	0.120
		7	0.013	0.010	381.815	1.283	0.200
		14	<0.001	0.010	406.358	0.043	0.965
		21	-0.010	0.009	356.464	-1.068	0.286
		28	-0.016	0.008	274.870	-1.961	0.051
		35	-0.016	0.009	338.418	-1.720	0.086
		42	-0.006	0.010	401.268	-0.566	0.572
		49	0.016	0.010	375.363	1.671	0.096

Table B.2 continued on next page

Table B.2 continued from previous page

VI	Clone	DoD	Estimate	SE	*df*	t.ratio	*p* value
		56	0.053	0.015	490.938	3.665	<0.001
	Clone 6	1	0.001	0.015	490.932	0.102	0.919
		7	0.017	0.010	390.322	1.672	0.095
		14	0.016	0.011	412.861	1.502	0.134
		21	0.003	0.010	360.572	0.295	0.769
		28	-0.013	0.008	276.013	-1.579	0.116
		35	-0.024	0.009	342.944	-2.533	0.012
		42	-0.019	0.010	408.277	-1.839	0.067
		49	0.009	0.010	384.690	0.874	0.383
		56	0.069	0.015	491.046	4.739	<0.001

Appendix C

Supplementary material: Chapter 4

The effect of canopy position on Vegetation Indices (VI) for Sitka spruce (*Picea sitchensis*) needles

C.1 Mixed effects model results

Table C.1: Results from the mixed effects models for Chapter 4. Mixed effects models were constructed for each VI where individual plants were treated as a random effect. The main effects modelled where: time in days after drought treatment initiation (Time); watering regime (Treatment); position of needles in the canopy (Position); and clonal group (Clone). Additional interaction effects for the main effects over Time (Time:Treatment (Time:Treat), Time:Position (Time:Pos) and Time:Clone, and three way interactions between Time:Treatment:Position (Time:Treat:Pos) and Time:Treatment:Clone (Time:Treat:Clone), were included in the model where this improved model fit. The marginal and conditional R^2 are presented. For full VI names, formula and references see Table 2.1 (p.43).

VI	Model Term	F value	*df*	R^2 Marg.	Cond.	*p* value
ARI	Time	140.12	1269.6, 1	0.35	0.38	<0.001
	Treatment	0.55	186.8, 1	0.35	0.38	0.460
	Position	27.88	1268.7, 2	0.35	0.38	<0.001
	Clone	6.64	186.9, 4	0.35	0.38	<0.001
	Time:Treat	15.94	1269.2, 1	0.35	0.38	<0.001
	Time:Pos	3.28	1269.2, 2	0.35	0.38	0.038
	Time:Clone	5.71	1269.6, 4	0.35	0.38	<0.001
	Time:Treat:Pos	6.30	1269.1, 2	0.35	0.38	0.002
ARI2	Time	162.96	1269.6, 1	0.37	0.40	<0.001
	Treatment	0.55	174.8, 1	0.37	0.40	0.458
	Position	28.86	1268.7, 2	0.37	0.40	<0.001

Table C.1 continued on next page

Table C.1 continued from previous page

VI	Model Term	F value	*df*	R^2 Marg.	Cond.	*p* value
	Clone	6.85	174.8, 4	0.37	0.40	<0.001
	Time:Treat	18.79	1269.1, 1	0.37	0.40	<0.001
	Time:Pos	3.40	1269.2, 2	0.37	0.40	0.034
	Time:Clone	5.99	1269.5, 4	0.37	0.40	<0.001
	Time:Treat:Pos	6.67	1269.1, 2	0.37	0.40	0.001
CCI	Time	82.36	1266.6, 3	0.47	0.55	<0.001
	Treatment	8.90	44.1, 1	0.47	0.55	0.005
	Position	366.18	1266.4, 2	0.47	0.55	<0.001
	Clone	14.02	44.1, 4	0.47	0.55	<0.001
	Time:Treat	10.50	1266.7, 3	0.47	0.55	<0.001
	Time:Treat:Position	3.81	1266.3, 6	0.47	0.55	0.001
CIgr	Time	3.38	1242.1, 3	0.40	0.69	0.018
	Treatment	0.92	44.0, 1	0.40	0.69	0.343
	Position	302.03	1242.1, 2	0.40	0.69	<0.001
	Clone	9.15	44.0, 4	0.40	0.69	<0.001
	Time:Treat	1.32	1242.1, 3	0.40	0.69	0.267
	Time:Pos	3.25	1242.1, 6	0.40	0.69	0.004
	Time:Clone	0.74	1242.1, 12	0.40	0.69	0.708
	Time:Treat:Clone	2.01	1242.2, 12	0.40	0.69	0.021
CIre	Time	15.05	1242.0, 3	0.41	0.75	<0.001
	Treatment	0.30	44.0, 1	0.41	0.75	0.588
	Position	404.10	1242.1, 2	0.41	0.75	<0.001
	Clone	7.06	44.0, 4	0.41	0.75	<0.001
	Time:Treat	3.48	1242.0, 3	0.41	0.75	0.015
	Time:Pos	2.25	1242.0, 6	0.41	0.75	0.036
	Time:Clone	1.02	1242.0, 12	0.41	0.75	0.427
	Time:Treat:Clone	2.81	1242.1, 12	0.41	0.75	0.001
CRI1	Time	9.65	1242.7, 3	0.41	0.43	<0.001
	Treatment	8.67	44.0, 1	0.41	0.43	0.005
	Position	265.04	1242.8, 2	0.41	0.43	<0.001
	Clone	28.15	44.0, 4	0.41	0.43	<0.001
	Time:Treat	1.71	1242.8, 3	0.41	0.43	0.163
	Time:Pos	9.14	1242.6, 6	0.41	0.43	<0.001
	Time:Clone	0.65	1242.6, 12	0.41	0.43	0.804
	Time:Treat:Clone	2.87	1243.6, 12	0.41	0.43	0.001
CRI2	Time	14.17	1267.3, 3	0.39	0.41	<0.001
	Treatment	9.47	44.0, 1	0.39	0.41	0.004
	Position	261.56	1266.8, 2	0.39	0.41	<0.001
	Clone	28.56	44.0, 4	0.39	0.41	<0.001
	Time:Treat	2.51	1267.5, 3	0.39	0.41	0.057
	Time:Pos	8.95	1266.5, 6	0.39	0.41	<0.001

Table C.1 continued on next page

Table C.1 continued from previous page

VI	Model Term	F value	*df*	R^2 Marg.	Cond.	*p* value
MSI	Time	11.59	1248.3, 3	0.40	0.52	<0.001
	Treatment	7.06	44.1, 1	0.40	0.52	0.011
	Position	97.87	1248.3, 2	0.40	0.52	<0.001
	Clone	7.32	44.1, 4	0.40	0.52	<0.001
	Time:Treat	5.22	1248.3, 3	0.40	0.52	0.001
	Time:Clone	0.56	1248.2, 12	0.40	0.52	0.877
	Time:Treat:Clone	5.98	1248.6, 12	0.40	0.52	<0.001
NDVI16	Time	9.64	1248.3, 3	0.39	0.50	<0.001
	Treatment	6.00	44.1, 1	0.39	0.50	0.018
	Position	104.54	1248.3, 2	0.39	0.50	<0.001
	Clone	9.00	44.1, 4	0.39	0.50	<0.001
	Time:Treat	5.24	1248.3, 3	0.39	0.50	0.001
	Time:Clone	0.60	1248.2, 12	0.39	0.50	0.845
	Time:Treat:Clone	5.13	1248.6, 12	0.39	0.50	<0.001
NDVI	Time	25.85	1269.8, 3	0.31	0.37	<0.001
	Treatment	2.60	44.0, 1	0.31	0.37	0.114
	Position	140.73	1269.5, 2	0.31	0.37	<0.001
	Clone	19.85	44.0, 4	0.31	0.37	<0.001
	Time:Pos	4.50	1269.3, 6	0.31	0.37	<0.001
NDWI	Time	4.75	1248.3, 3	0.36	0.47	0.003
	Treatment	6.66	44.1, 1	0.36	0.47	0.013
	Position	121.78	1248.3, 2	0.36	0.47	<0.001
	Clone	7.17	44.1, 4	0.36	0.47	<0.001
	Time:Treat	5.95	1248.3, 3	0.36	0.47	0.001
	Time:Clone	0.70	1248.3, 12	0.36	0.47	0.749
	Time:Treat:Clone	4.21	1248.6, 12	0.36	0.47	<0.001
NRre	Time	15.24	1242.0, 3	0.40	0.75	<0.001
	Treatment	0.62	44.0, 1	0.40	0.75	0.435
	Position	425.93	1242.1, 2	0.40	0.75	<0.001
	Clone	6.35	44.0, 4	0.40	0.75	<0.001
	Time:Treat	3.37	1242.0, 3	0.40	0.75	0.018
	Time:Pos	2.65	1242.0, 6	0.40	0.75	0.015
	Time:Clone	0.90	1242.0, 12	0.40	0.75	0.549
	Time:Treat:Clone	2.13	1242.1, 12	0.40	0.75	0.013
PRI	Time	11.75	1236.1, 3	0.41	0.61	<0.001
	Treatment	18.33	44.0, 1	0.41	0.61	<0.001
	Position	162.34	1236.1, 2	0.41	0.61	<0.001
	Clone	4.31	44.0, 4	0.41	0.61	0.005
	Time:Treat	2.56	1236.1, 3	0.41	0.61	0.054
	Time:Pos	2.11	1236.1, 6	0.41	0.61	0.049
	Time:Clone	1.06	1236.1, 12	0.41	0.61	0.388

Table C.1 continued on next page

Table C.1 continued from previous page

VI	Model Term	F value	*df*	R^2 Marg.	Cond.	*p* value
	Time:Treat:Pos	3.34	1236.1, 6	0.41	0.61	0.003
	Time:Treat:Clone	1.92	1236.3, 12	0.41	0.61	0.028
SR	Time	31.97	1269.9, 3	0.30	0.34	<0.001
	Treatment	3.93	43.9, 1	0.30	0.34	0.054
	Position	148.09	1269.5, 2	0.30	0.34	<0.001
	Clone	16.75	43.9, 4	0.30	0.34	<0.001
	Time:Pos	6.38	1269.3, 6	0.30	0.34	<0.001
SRWI	Time	4.74	1248.3, 3	0.36	0.47	0.003
	Treatment	6.41	44.1, 1	0.36	0.47	0.015
	Position	124.49	1248.3, 2	0.36	0.47	<0.001
	Clone	7.43	44.1, 4	0.36	0.47	<0.001
	Time:Treat	5.84	1248.3, 3	0.36	0.47	0.001
	Time:Clone	0.72	1248.3, 12	0.36	0.47	0.733
	Time:Treat:Clone	3.93	1248.6, 12	0.36	0.47	<0.001
WI	Time	4.03	1248.3, 3	0.36	0.45	0.007
	Treatment	0.15	44.0, 1	0.36	0.45	0.697
	Position	133.03	1248.4, 2	0.36	0.45	<0.001
	Clone	10.80	44.0, 4	0.36	0.45	<0.001
	Time:Treat	4.58	1248.3, 3	0.36	0.45	0.003
	Time:Clone	0.74	1248.3, 12	0.36	0.45	0.715
	Time:Treat:Clone	4.95	1248.7, 12	0.36	0.45	<0.001
WI/NDVI	Time	19.82	1254.7, 3	0.36	0.45	<0.001
	Treatment	1.84	44.1, 1	0.36	0.45	0.182
	Position	221.62	1254.4, 2	0.36	0.45	<0.001
	Clone	13.38	44.1, 4	0.36	0.45	<0.001
	Time:Treat	9.02	1254.7, 3	0.36	0.45	<0.001
	Time:Pos	5.35	1254.3, 6	0.36	0.45	<0.001
	Time:Clone	2.86	1254.7, 12	0.36	0.45	0.001

C.1.1 Estimated marginal means (EMM) contrasts

Table C.2: Estimated Marginal Means (EMM) contrasts of 17 Vegetation Indices (VI) between three canopy positions (Upr = Needles measured from the top 25% of the canopy (N^{upper}), Lwr = Needles measured from the bottom 25% of the canopy (N^{lower}), Old = Needles measured from the previous years growth (2020) (N^{old}). Upr and Lwr needles grew in 2021). Mixed effects model were constructed to evaluate the effects of time, drought treatment, position in the canopy and clonal group for each VI. The results here use EMM contrasts to compare if VI differ statistically between the canopy positions within the model.For full VI names, formula and references see Table 2.1 (p.43).

VI	Contrast	Estimate	SE	*df*	t.ratio	*p* value
ARI	Lwr - Old	-0.04	0.03	1268.93	-1.69	0.211
	Lwr - Upr	0.14	0.03	1268.47	5.56	<0.001
	Old - Upr	0.18	0.03	1268.69	7.26	<0.001
ARI2	Lwr - Old	-0.03	0.02	1268.87	-1.77	0.181
	Lwr - Upr	0.09	0.02	1268.44	5.58	<0.001
	Old - Upr	0.12	0.02	1268.64	7.36	<0.001
CCI	Lwr - Old	0.08	0.00	1266.17	19.48	<0.001
	Lwr - Upr	0.03	0.00	1266.08	7.82	<0.001
	Old - Upr	-0.05	0.00	1266.13	-11.73	<0.001
CIgr	Lwr - Old	0.13	0.07	1242.04	1.89	0.141
	Lwr - Upr	1.08	0.07	1242.02	15.53	<0.001
	Old - Upr	0.95	0.07	1242.03	13.64	<0.001
CIre	Lwr - Old	-0.17	0.03	1242.03	-6.38	<0.001
	Lwr - Upr	0.35	0.03	1242.01	13.37	<0.001
	Old - Upr	0.52	0.03	1242.02	19.78	<0.001
CRI1	Lwr - Old	3.35	0.19	1242.47	17.52	<0.001
	Lwr - Upr	2.19	0.19	1242.24	11.50	<0.001
	Old - Upr	-1.16	0.19	1242.37	-6.08	<0.001
CRI2	Lwr - Old	3.35	0.19	1266.47	17.40	<0.001
	Lwr - Upr	2.19	0.19	1266.24	11.42	<0.001
	Old - Upr	-1.16	0.19	1266.35	-6.04	<0.001
MSI	Lwr - Old	0.00	0.00	1248.32	2.46	0.037
	Lwr - Upr	0.02	0.00	1248.15	13.14	<0.001
	Old - Upr	0.02	0.00	1248.24	10.67	<0.001
NDVI16	Lwr - Old	-0.01	0.00	1248.34	-3.97	0.001
	Lwr - Upr	-0.02	0.00	1248.16	-14.02	<0.001
	Old - Upr	-0.02	0.00	1248.25	-10.03	<0.001
NDVI	Lwr - Old	0.03	0.00	1269.29	12.15	<0.001
	Lwr - Upr	0.02	0.00	1269.15	10.15	<0.001
	Old - Upr	0.00	0.00	1269.22	-2.04	0.104

Table C.2 continued on next page

Table C.2 continued from previous page

VI	Contrast	Estimate	SE	*df*	t.ratio	*p* value
NDWI	Lwr - Old	0.00	0.00	1248.35	-4.63	<0.001
	Lwr - Upr	-0.01	0.00	1248.17	-15.21	<0.001
	Old - Upr	-0.01	0.00	1248.26	-10.56	<0.001
NRre	Lwr - Old	-0.02	0.00	1242.03	-5.97	<0.001
	Lwr - Upr	0.05	0.00	1242.01	13.74	<0.001
	Old - Upr	0.07	0.00	1242.02	19.74	<0.001
PRI	Lwr - Old	0.00	0.00	1236.07	1.59	0.252
	Lwr - Upr	0.02	0.00	1236.03	10.92	<0.001
	Old - Upr	0.02	0.00	1236.05	9.34	<0.001
SR	Lwr - Old	3.48	0.28	1269.36	12.53	<0.001
	Lwr - Upr	2.94	0.28	1269.18	10.62	<0.001
	Old - Upr	-0.54	0.28	1269.27	-1.95	0.126
SRWI	Lwr - Old	-0.01	0.00	1248.35	-4.67	<0.001
	Lwr - Upr	-0.03	0.00	1248.17	-15.38	<0.001
	Old - Upr	-0.02	0.00	1248.26	-10.69	<0.001
WI	Lwr - Old	-0.01	0.00	1248.44	-6.07	<0.001
	Lwr - Upr	-0.01	0.00	1248.21	-16.14	<0.001
	Old - Upr	-0.01	0.00	1248.32	-10.04	<0.001
WI/	Lwr - Old	-0.05	0.00	1254.19	-13.79	<0.001
	Lwr - Upr	-0.05	0.00	1254.09	-14.27	<0.001
	Old - Upr	0.00	0.00	1254.15	-0.44	0.900

Table C.3: Estimated Marginal Means (EMM) contrasts of 12 Vegetation Indices (VI) between three canopy positions (Upr = Needles measured from the top 25% of the canopy (N^{upper}), Lwr = Needles measured from the bottom 25% of the canopy (N^{lower}), Old = Needles measured from the previous year's growth (2020) (N^{old}). Upr and Lwr needles grew in 2021). Mixed effects models were constructed to evaluate the effects of time, drought treatment, position in the canopy and clonal group for each VI. Where a significant interaction effect of canopy position over time was found, EMM contrasts were performed at regular (7 days) intervals to compare if VI differ statistically between the canopy positions within the model. DoD is Day of Drought and is the time in days since the initiation of the experimental drought. For full VI names, formula and references see Table 2.1 (p.43).

VI	DoD	Contrast	Estimate	SE	*df*	t.ratio	*p* value
ARI	0	Lwr - Old	-0.065	0.048	1268.882	-1.356	0.365
		Lwr - Upr	0.269	0.048	1268.629	5.653	<0.001
		Old - Upr	0.334	0.047	1268.257	7.039	<0.001
	7	Lwr - Old	-0.059	0.040	1268.856	-1.495	0.293
		Lwr - Upr	0.238	0.040	1268.644	6.001	<0.001
		Old - Upr	0.297	0.039	1268.194	7.532	<0.001
	14	Lwr - Old	-0.054	0.033	1268.834	-1.652	0.225
		Lwr - Upr	0.206	0.033	1268.644	6.319	<0.001
		Old - Upr	0.260	0.033	1268.173	8.009	<0.001
	21	Lwr - Old	-0.049	0.028	1268.845	-1.765	0.182
		Lwr - Upr	0.175	0.027	1268.599	6.357	<0.001
		Old - Upr	0.223	0.027	1268.295	8.155	<0.001
	28	Lwr - Old	-0.043	0.025	1268.925	-1.703	0.204
		Lwr - Upr	0.143	0.025	1268.484	5.660	<0.001
		Old - Upr	0.187	0.025	1268.650	7.376	<0.001
	35	Lwr - Old	-0.038	0.027	1269.040	-1.405	0.339
		Lwr - Upr	0.112	0.027	1268.359	4.167	<0.001
		Old - Upr	0.150	0.027	1269.059	5.567	<0.001
	42	Lwr - Old	-0.033	0.032	1269.115	-1.025	0.561
		Lwr - Upr	0.080	0.032	1268.299	2.548	0.029
		Old - Upr	0.113	0.032	1269.270	3.568	0.001
	49	Lwr - Old	-0.027	0.039	1269.143	-0.706	0.760
		Lwr - Upr	0.049	0.038	1268.292	1.278	0.408
		Old - Upr	0.076	0.038	1269.312	1.982	0.117
	56	Lwr - Old	-0.022	0.046	1269.148	-0.471	0.885
		Lwr - Upr	0.017	0.046	1268.305	0.377	0.925
		Old - Upr	0.039	0.046	1269.286	0.849	0.673
ARI2	0	Lwr - Old	-0.050	0.031	1268.824	-1.600	0.246
		Lwr - Upr	0.173	0.031	1268.587	5.601	<0.001
		Old - Upr	0.223	0.031	1268.239	7.234	<0.001
	7	Lwr - Old	-0.045	0.026	1268.799	-1.730	0.194
		Lwr - Upr	0.153	0.026	1268.601	5.956	<0.001
		Old - Upr	0.198	0.026	1268.181	7.723	<0.001

Table C.3 continued on next page

Table C.3 continued from previous page

VI	DoD	Contrast	Estimate	SE	*df*	t.ratio	*p* value
	14	Lwr - Old	-0.040	0.021	1268.779	-1.865	0.150
		Lwr - Upr	0.133	0.021	1268.601	6.286	<0.001
		Old - Upr	0.173	0.021	1268.161	8.190	<0.001
	21	Lwr - Old	-0.035	0.018	1268.790	-1.933	0.130
		Lwr - Upr	0.113	0.018	1268.559	6.343	<0.001
		Old - Upr	0.148	0.018	1268.275	8.309	<0.001
	28	Lwr - Old	-0.030	0.017	1268.865	-1.792	0.173
		Lwr - Upr	0.093	0.016	1268.452	5.673	<0.001
		Old - Upr	0.123	0.016	1268.608	7.478	<0.001
	35	Lwr - Old	-0.025	0.018	1268.974	-1.401	0.341
		Lwr - Upr	0.073	0.017	1268.335	4.204	<0.001
		Old - Upr	0.098	0.017	1268.991	5.601	<0.001
	42	Lwr - Old	-0.020	0.021	1269.044	-0.948	0.610
		Lwr - Upr	0.053	0.020	1268.279	2.602	0.025
		Old - Upr	0.073	0.021	1269.189	3.544	0.001
	49	Lwr - Old	-0.015	0.025	1269.071	-0.582	0.830
		Lwr - Upr	0.033	0.025	1268.273	1.341	0.373
		Old - Upr	0.048	0.025	1269.229	1.919	0.134
	56	Lwr - Old	-0.010	0.030	1269.075	-0.317	0.946
		Lwr - Upr	0.013	0.030	1268.285	0.444	0.897
		Old - Upr	0.023	0.030	1269.204	0.760	0.727
CCI	0	Lwr - Old	0.075	0.008	1266.319	9.595	<0.001
		Lwr - Upr	0.025	0.008	1266.149	3.229	0.004
		Old - Upr	-0.050	0.008	1266.150	-6.417	<0.001
	7	Lwr - Old	0.088	0.005	1266.330	18.148	<0.001
		Lwr - Upr	0.030	0.005	1266.271	6.269	<0.001
		Old - Upr	-0.057	0.005	1266.069	-11.978	<0.001
	14	Lwr - Old	0.091	0.005	1266.231	18.106	<0.001
		Lwr - Upr	0.033	0.005	1266.235	6.503	<0.001
		Old - Upr	-0.058	0.005	1266.024	-11.695	<0.001
	21	Lwr - Old	0.088	0.005	1266.190	19.034	<0.001
		Lwr - Upr	0.033	0.005	1266.173	7.177	<0.001
		Old - Upr	-0.055	0.005	1266.019	-11.938	<0.001
	28	Lwr - Old	0.080	0.004	1266.170	19.633	<0.001
		Lwr - Upr	0.032	0.004	1266.090	7.842	<0.001
		Old - Upr	-0.048	0.004	1266.116	-11.856	<0.001
	35	Lwr - Old	0.070	0.004	1266.218	15.813	<0.001
		Lwr - Upr	0.030	0.004	1266.077	6.705	<0.001
		Old - Upr	-0.041	0.004	1266.304	-9.177	<0.001
	42	Lwr - Old	0.062	0.005	1266.330	12.425	<0.001
		Lwr - Upr	0.027	0.005	1266.134	5.493	<0.001
		Old - Upr	-0.035	0.005	1266.443	-7.009	<0.001
	49	Lwr - Old	0.056	0.005	1266.526	11.766	<0.001
		Lwr - Upr	0.025	0.005	1266.178	5.175	<0.001

Table C.3 continued on next page

Table C.3 continued from previous page

VI	DoD	Contrast	Estimate	SE	*df*	t.ratio	*p* value
		Old - Upr	-0.032	0.005	1266.601	-6.679	<0.001
	56	Lwr - Old	0.058	0.007	1266.378	8.234	<0.001
		Lwr - Upr	0.023	0.007	1266.053	3.314	0.003
		Old - Upr	-0.035	0.007	1266.346	-4.950	<0.001
CIgr	0	Lwr - Old	0.089	0.134	1242.074	0.664	0.784
		Lwr - Upr	1.215	0.133	1242.034	9.149	<0.001
		Old - Upr	1.127	0.133	1242.035	8.488	<0.001
	7	Lwr - Old	0.214	0.083	1242.074	2.581	0.027
		Lwr - Upr	1.168	0.083	1242.060	14.105	<0.001
		Old - Upr	0.953	0.082	1242.016	11.578	<0.001
	14	Lwr - Old	0.251	0.086	1242.051	2.906	0.010
		Lwr - Upr	1.137	0.086	1242.051	13.165	<0.001
		Old - Upr	0.886	0.086	1242.005	10.324	<0.001
	21	Lwr - Old	0.220	0.079	1242.041	2.781	0.015
		Lwr - Upr	1.112	0.079	1242.037	14.075	<0.001
		Old - Upr	0.892	0.079	1242.004	11.362	<0.001
	28	Lwr - Old	0.140	0.070	1242.038	2.005	0.111
		Lwr - Upr	1.082	0.070	1242.019	15.546	<0.001
		Old - Upr	0.942	0.070	1242.027	13.553	<0.001
	35	Lwr - Old	0.031	0.076	1242.051	0.408	0.912
		Lwr - Upr	1.035	0.076	1242.017	13.669	<0.001
		Old - Upr	1.004	0.076	1242.072	13.199	<0.001
	42	Lwr - Old	-0.087	0.085	1242.078	-1.019	0.565
		Lwr - Upr	0.960	0.084	1242.030	11.386	<0.001
		Old - Upr	1.047	0.085	1242.105	12.350	<0.001
	49	Lwr - Old	-0.194	0.082	1242.125	-2.350	0.050
		Lwr - Upr	0.846	0.082	1242.040	10.366	<0.001
		Old - Upr	1.040	0.082	1242.143	12.680	<0.001
	56	Lwr - Old	-0.270	0.120	1242.091	-2.251	0.063
		Lwr - Upr	0.681	0.119	1242.012	5.711	<0.001
		Old - Upr	0.951	0.120	1242.083	7.936	<0.001
CIre	0	Lwr - Old	-0.102	0.050	1242.050	-2.029	0.106
		Lwr - Upr	0.366	0.050	1242.023	7.283	<0.001
		Old - Upr	0.468	0.050	1242.023	9.331	<0.001
	7	Lwr - Old	-0.095	0.031	1242.050	-3.040	0.007
		Lwr - Upr	0.344	0.031	1242.040	11.010	<0.001
		Old - Upr	0.440	0.031	1242.011	14.129	<0.001
	14	Lwr - Old	-0.108	0.033	1242.034	-3.296	0.003
		Lwr - Upr	0.340	0.033	1242.034	10.414	<0.001
		Old - Upr	0.448	0.032	1242.004	13.804	<0.001
	21	Lwr - Old	-0.133	0.030	1242.028	-4.456	<0.001
		Lwr - Upr	0.345	0.030	1242.025	11.536	<0.001
		Old - Upr	0.478	0.030	1242.003	16.092	<0.001
	28	Lwr - Old	-0.165	0.026	1242.025	-6.269	<0.001

Table C.3 continued on next page

Table C.3 continued from previous page

VI	DoD	Contrast	Estimate	SE	*df*	t.ratio	*p* value
		Lwr - Upr	0.351	0.026	1242.013	13.329	<0.001
		Old - Upr	0.516	0.026	1242.018	19.640	<0.001
	35	Lwr - Old	-0.198	0.029	1242.034	-6.867	<0.001
		Lwr - Upr	0.351	0.029	1242.011	12.252	<0.001
		Old - Upr	0.549	0.029	1242.048	19.081	<0.001
	42	Lwr - Old	-0.225	0.032	1242.052	-6.980	<0.001
		Lwr - Upr	0.337	0.032	1242.020	10.573	<0.001
		Old - Upr	0.561	0.032	1242.070	17.528	<0.001
	49	Lwr - Old	-0.239	0.031	1242.084	-7.665	<0.001
		Lwr - Upr	0.302	0.031	1242.027	9.793	<0.001
		Old - Upr	0.541	0.031	1242.096	17.454	<0.001
	56	Lwr - Old	-0.234	0.045	1242.061	-5.167	<0.001
		Lwr - Upr	0.238	0.045	1242.008	5.285	<0.001
		Old - Upr	0.472	0.045	1242.056	10.433	<0.001
CRI1	0	Lwr - Old	3.274	0.366	1242.912	8.942	<0.001
		Lwr - Upr	2.376	0.364	1242.422	6.523	<0.001
		Old - Upr	-0.898	0.364	1242.445	-2.466	0.037
	7	Lwr - Old	3.915	0.227	1242.917	17.209	<0.001
		Lwr - Upr	2.646	0.227	1242.743	11.658	<0.001
		Old - Upr	-1.269	0.226	1242.204	-5.618	<0.001
	14	Lwr - Old	4.070	0.237	1242.637	17.171	<0.001
		Lwr - Upr	2.671	0.237	1242.639	11.278	<0.001
		Old - Upr	-1.399	0.235	1242.074	-5.947	<0.001
	21	Lwr - Old	3.857	0.217	1242.520	17.789	<0.001
		Lwr - Upr	2.509	0.217	1242.473	11.577	<0.001
		Old - Upr	-1.348	0.215	1242.061	-6.259	<0.001
	28	Lwr - Old	3.393	0.191	1242.468	17.726	<0.001
		Lwr - Upr	2.218	0.191	1242.250	11.621	<0.001
		Old - Upr	-1.174	0.191	1242.328	-6.159	<0.001
	35	Lwr - Old	2.794	0.209	1242.616	13.357	<0.001
		Lwr - Upr	1.857	0.208	1242.217	8.942	<0.001
		Old - Upr	-0.936	0.209	1242.846	-4.488	<0.001
	42	Lwr - Old	2.177	0.233	1242.933	9.329	<0.001
		Lwr - Upr	1.484	0.231	1242.373	6.417	<0.001
		Old - Upr	-0.693	0.232	1243.235	-2.982	0.008
	49	Lwr - Old	1.661	0.226	1243.477	7.347	<0.001
		Lwr - Upr	1.157	0.224	1242.491	5.169	<0.001
		Old - Upr	-0.504	0.225	1243.678	-2.241	0.065
	56	Lwr - Old	1.361	0.329	1243.059	4.134	<0.001
		Lwr - Upr	0.934	0.327	1242.154	2.856	0.012
		Old - Upr	-0.427	0.329	1242.975	-1.300	0.396
CRI2	0	Lwr - Old	3.281	0.369	1266.871	8.897	<0.001
		Lwr - Upr	2.370	0.367	1266.408	6.458	<0.001
		Old - Upr	-0.911	0.367	1266.420	-2.483	0.035

Table C.3 continued on next page

Table C.3 continued from previous page

VI	DoD	Contrast	Estimate	SE	*df*	t.ratio	*p* value
	7	Lwr - Old	3.915	0.229	1266.904	17.078	<0.001
		Lwr - Upr	2.643	0.229	1266.744	11.555	<0.001
		Old - Upr	-1.272	0.228	1266.193	-5.588	<0.001
	14	Lwr - Old	4.068	0.239	1266.640	17.029	<0.001
		Lwr - Upr	2.670	0.239	1266.648	11.186	<0.001
		Old - Upr	-1.398	0.237	1266.071	-5.896	<0.001
	21	Lwr - Old	3.857	0.219	1266.525	17.648	<0.001
		Lwr - Upr	2.509	0.218	1266.481	11.488	<0.001
		Old - Upr	-1.347	0.217	1266.057	-6.206	<0.001
	28	Lwr - Old	3.396	0.193	1266.464	17.604	<0.001
		Lwr - Upr	2.219	0.192	1266.252	11.534	<0.001
		Old - Upr	-1.176	0.192	1266.313	-6.122	<0.001
	35	Lwr - Old	2.800	0.211	1266.588	13.287	<0.001
		Lwr - Upr	1.858	0.209	1266.214	8.877	<0.001
		Old - Upr	-0.942	0.210	1266.809	-4.481	<0.001
	42	Lwr - Old	2.187	0.235	1266.885	9.298	<0.001
		Lwr - Upr	1.485	0.233	1266.369	6.370	<0.001
		Old - Upr	-0.702	0.234	1267.178	-2.996	0.008
	49	Lwr - Old	1.669	0.228	1267.399	7.331	<0.001
		Lwr - Upr	1.157	0.226	1266.485	5.130	<0.001
		Old - Upr	-0.513	0.226	1267.592	-2.263	0.062
	56	Lwr - Old	1.364	0.332	1266.998	4.114	<0.001
		Lwr - Upr	0.933	0.329	1266.149	2.832	0.013
		Old - Upr	-0.431	0.331	1266.914	-1.303	0.394
NDVI	0	Lwr - Old	0.024	0.005	1269.534	5.239	<0.001
		Lwr - Upr	0.019	0.005	1269.252	4.110	<0.001
		Old - Upr	-0.005	0.005	1269.256	-1.155	0.480
	7	Lwr - Old	0.034	0.003	1269.561	11.710	<0.001
		Lwr - Upr	0.023	0.003	1269.463	7.927	<0.001
		Old - Upr	-0.011	0.003	1269.118	-3.828	<0.001
	14	Lwr - Old	0.037	0.003	1269.397	12.211	<0.001
		Lwr - Upr	0.025	0.003	1269.402	8.259	<0.001
		Old - Upr	-0.012	0.003	1269.042	-3.988	<0.001
	21	Lwr - Old	0.035	0.003	1269.325	12.672	<0.001
		Lwr - Upr	0.025	0.003	1269.298	9.204	<0.001
		Old - Upr	-0.010	0.003	1269.033	-3.495	0.001
	28	Lwr - Old	0.030	0.002	1269.290	12.328	<0.001
		Lwr - Upr	0.025	0.002	1269.155	10.171	<0.001
		Old - Upr	-0.005	0.002	1269.197	-2.191	0.073
	35	Lwr - Old	0.024	0.003	1269.369	8.930	<0.001
		Lwr - Upr	0.023	0.003	1269.130	8.782	<0.001
		Old - Upr	-0.001	0.003	1269.513	-0.207	0.977
	42	Lwr - Old	0.018	0.003	1269.553	6.037	<0.001
		Lwr - Upr	0.021	0.003	1269.226	7.216	<0.001

Table C.3 continued on next page

Table C.3 continued from previous page

VI	DoD	Contrast	Estimate	SE	*df*	t.ratio	*p* value
		Old - Upr	0.003	0.003	1269.747	1.120	0.502
	49	Lwr - Old	0.014	0.003	1269.873	4.959	<0.001
		Lwr - Upr	0.019	0.003	1269.298	6.718	<0.001
		Old - Upr	0.005	0.003	1270.008	1.703	0.204
	56	Lwr - Old	0.014	0.004	1269.626	3.465	0.002
		Lwr - Upr	0.017	0.004	1269.090	4.142	<0.001
		Old - Upr	0.003	0.004	1269.577	0.651	0.792
NRre	0	Lwr - Old	-0.011	0.007	1242.049	-1.638	0.230
		Lwr - Upr	0.051	0.007	1242.023	7.400	<0.001
		Old - Upr	0.063	0.007	1242.023	9.053	<0.001
	7	Lwr - Old	-0.012	0.004	1242.049	-2.737	0.017
		Lwr - Upr	0.047	0.004	1242.040	10.861	<0.001
		Old - Upr	0.059	0.004	1242.010	13.674	<0.001
	14	Lwr - Old	-0.014	0.005	1242.034	-3.103	0.006
		Lwr - Upr	0.046	0.005	1242.034	10.222	<0.001
		Old - Upr	0.060	0.004	1242.004	13.416	<0.001
	21	Lwr - Old	-0.017	0.004	1242.027	-4.202	<0.001
		Lwr - Upr	0.047	0.004	1242.025	11.500	<0.001
		Old - Upr	0.065	0.004	1242.003	15.801	<0.001
	28	Lwr - Old	-0.021	0.004	1242.025	-5.864	<0.001
		Lwr - Upr	0.050	0.004	1242.013	13.669	<0.001
		Old - Upr	0.071	0.004	1242.018	19.573	<0.001
	35	Lwr - Old	-0.026	0.004	1242.034	-6.419	<0.001
		Lwr - Upr	0.051	0.004	1242.011	13.007	<0.001
		Old - Upr	0.077	0.004	1242.048	19.384	<0.001
	42	Lwr - Old	-0.029	0.004	1242.052	-6.617	<0.001
		Lwr - Upr	0.051	0.004	1242.020	11.670	<0.001
		Old - Upr	0.081	0.004	1242.070	18.253	<0.001
	49	Lwr - Old	-0.032	0.004	1242.083	-7.524	<0.001
		Lwr - Upr	0.048	0.004	1242.026	11.313	<0.001
		Old - Upr	0.080	0.004	1242.095	18.826	<0.001
	56	Lwr - Old	-0.034	0.006	1242.060	-5.424	<0.001
		Lwr - Upr	0.040	0.006	1242.008	6.513	<0.001
		Old - Upr	0.074	0.006	1242.055	11.913	<0.001
PRI	0	Lwr - Old	0.009	0.003	1236.130	2.669	0.021
		Lwr - Upr	0.023	0.003	1236.060	7.089	<0.001
		Old - Upr	0.014	0.003	1236.063	4.410	<0.001
	7	Lwr - Old	0.006	0.002	1236.130	3.117	0.005
		Lwr - Upr	0.019	0.002	1236.105	9.390	<0.001
		Old - Upr	0.013	0.002	1236.028	6.298	<0.001
	14	Lwr - Old	0.005	0.002	1236.089	2.205	0.071
		Lwr - Upr	0.018	0.002	1236.089	8.225	<0.001
		Old - Upr	0.013	0.002	1236.009	6.058	<0.001
	21	Lwr - Old	0.004	0.002	1236.072	1.828	0.161

Table C.3 continued on next page

Table C.3 continued from previous page

VI	DoD	Contrast	Estimate	SE	*df*	t.ratio	*p* value
		Lwr - Upr	0.018	0.002	1236.065	9.016	<0.001
		Old - Upr	0.014	0.002	1236.008	7.231	<0.001
	28	Lwr - Old	0.003	0.002	1236.066	1.614	0.240
		Lwr - Upr	0.019	0.002	1236.034	10.843	<0.001
		Old - Upr	0.016	0.002	1236.048	9.237	<0.001
	35	Lwr - Old	0.002	0.002	1236.089	1.142	0.489
		Lwr - Upr	0.020	0.002	1236.030	10.676	<0.001
		Old - Upr	0.018	0.002	1236.125	9.484	<0.001
	42	Lwr - Old	0.001	0.002	1236.136	0.705	0.761
		Lwr - Upr	0.021	0.002	1236.053	10.020	<0.001
		Old - Upr	0.019	0.002	1236.183	9.262	<0.001
	49	Lwr - Old	0.001	0.002	1236.217	0.286	0.956
		Lwr - Upr	0.021	0.002	1236.071	10.240	<0.001
		Old - Upr	0.020	0.002	1236.249	9.906	<0.001
	56	Lwr - Old	-0.001	0.003	1236.157	-0.250	0.966
		Lwr - Upr	0.019	0.003	1236.021	6.304	<0.001
		Old - Upr	0.019	0.003	1236.144	6.522	<0.001
SR	0	Lwr - Old	3.197	0.532	1269.660	6.012	<0.001
		Lwr - Upr	2.623	0.529	1269.312	4.956	<0.001
		Old - Upr	-0.574	0.529	1269.318	-1.085	0.523
	7	Lwr - Old	4.257	0.331	1269.693	12.876	<0.001
		Lwr - Upr	3.101	0.330	1269.573	9.400	<0.001
		Old - Upr	-1.156	0.328	1269.147	-3.521	0.001
	14	Lwr - Old	4.527	0.345	1269.492	13.141	<0.001
		Lwr - Upr	3.276	0.344	1269.498	9.516	<0.001
		Old - Upr	-1.252	0.342	1269.053	-3.660	0.001
	21	Lwr - Old	4.219	0.315	1269.403	13.389	<0.001
		Lwr - Upr	3.210	0.315	1269.370	10.190	<0.001
		Old - Upr	-1.010	0.313	1269.042	-3.225	0.004
	28	Lwr - Old	3.543	0.278	1269.358	12.735	<0.001
		Lwr - Upr	2.965	0.277	1269.193	10.687	<0.001
		Old - Upr	-0.577	0.277	1269.243	-2.082	0.094
	35	Lwr - Old	2.706	0.304	1269.455	8.903	<0.001
		Lwr - Upr	2.605	0.302	1269.162	8.628	<0.001
		Old - Upr	-0.102	0.303	1269.631	-0.335	0.940
	42	Lwr - Old	1.920	0.339	1269.681	5.662	<0.001
		Lwr - Upr	2.190	0.336	1269.279	6.514	<0.001
		Old - Upr	0.269	0.338	1269.918	0.797	0.705
	49	Lwr - Old	1.395	0.328	1270.073	4.247	<0.001
		Lwr - Upr	1.783	0.325	1269.369	5.482	<0.001
		Old - Upr	0.388	0.327	1270.237	1.188	0.460
	56	Lwr - Old	1.339	0.478	1269.768	2.800	0.014
		Lwr - Upr	1.446	0.475	1269.113	3.044	0.007
		Old - Upr	0.107	0.477	1269.708	0.225	0.973

Table C.3 continued on next page

Table C.3 continued from previous page

VI	DoD	Contrast	Estimate	SE	*df*	t.ratio	*p* value
WI/NDVI	0	Lwr - Old	-0.043	0.007	1254.338	-6.083	<0.001
		Lwr - Upr	-0.046	0.007	1254.162	-6.425	<0.001
		Old - Upr	-0.002	0.007	1254.166	-0.314	0.947
	7	Lwr - Old	-0.057	0.004	1254.353	-12.758	<0.001
		Lwr - Upr	-0.050	0.004	1254.290	-11.301	<0.001
		Old - Upr	0.007	0.004	1254.076	1.493	0.295
	14	Lwr - Old	-0.061	0.005	1254.248	-13.204	<0.001
		Lwr - Upr	-0.053	0.005	1254.250	-11.405	<0.001
		Old - Upr	0.008	0.005	1254.027	1.823	0.163
	21	Lwr - Old	-0.059	0.004	1254.202	-13.913	<0.001
		Lwr - Upr	-0.054	0.004	1254.184	-12.702	<0.001
		Old - Upr	0.005	0.004	1254.021	1.225	0.439
	28	Lwr - Old	-0.052	0.004	1254.185	-13.947	<0.001
		Lwr - Upr	-0.053	0.004	1254.095	-14.271	<0.001
		Old - Upr	-0.001	0.004	1254.131	-0.289	0.955
	35	Lwr - Old	-0.043	0.004	1254.247	-10.493	<0.001
		Lwr - Upr	-0.051	0.004	1254.083	-12.612	<0.001
		Old - Upr	-0.008	0.004	1254.343	-2.037	0.104
	42	Lwr - Old	-0.033	0.005	1254.369	-7.285	<0.001
		Lwr - Upr	-0.048	0.005	1254.145	-10.564	<0.001
		Old - Upr	-0.014	0.005	1254.497	-3.196	0.004
	49	Lwr - Old	-0.025	0.004	1254.578	-5.720	<0.001
		Lwr - Upr	-0.043	0.004	1254.192	-9.828	<0.001
		Old - Upr	-0.018	0.004	1254.664	-4.032	<0.001
	56	Lwr - Old	-0.021	0.006	1254.414	-3.281	0.003
		Lwr - Upr	-0.037	0.006	1254.058	-5.787	<0.001
		Old - Upr	-0.016	0.006	1254.379	-2.472	0.036

Table C.4: Estimated Marginal Means (EMM) contrasts of nine Vegetation Indices (VI) between three canopy positions (Upr = Needles measured from the top 25% of the canopy (N^{upper}), Lwr = Needles measured from the bottom 25% of the canopy (N^{lower}), Old = Needles measured from the previous year's growth (2020) (N^{old}). Upr and Lwr needles grew in 2021). Mixed effects model were constructed to evaluate the effects of time, drought treatment, position in the canopy and clonal group for each VI. Where a significant three way interaction effect of drought effect and canopy position over time was found EMM, contrasts were performed at regular (7 days) intervals to compare if the drought response for each VI differ statistically between the canopy positions within the model. DoD is Day of Drought and is the time in days since the initiation of the experimental drought. For full VI names, formula and references see Table 2.1 (p.43).

VI	DoD	Contrast	Estimate	SE	*df*	t.ratio	*p* value
ARI	0	Lwr	-0.034	0.045	186.300	-0.741	0.460
		Old	-0.034	0.045	186.300	-0.741	0.460
		Upr	-0.034	0.045	186.300	-0.741	0.460
	7	Lwr	-0.074	0.040	120.205	-1.828	0.070
		Old	-0.095	0.040	119.988	-2.338	0.021
		Upr	-0.111	0.040	120.037	-2.746	0.007
	14	Lwr	-0.114	0.038	90.318	-3.039	0.003
		Old	-0.155	0.038	90.225	-4.136	<0.001
		Upr	-0.189	0.038	89.792	-5.022	<0.001
	21	Lwr	-0.155	0.037	87.755	-4.142	<0.001
		Old	-0.216	0.037	88.055	-5.792	<0.001
		Upr	-0.266	0.037	86.640	-7.149	<0.001
	28	Lwr	-0.195	0.040	111.598	-4.909	<0.001
		Old	-0.277	0.040	112.676	-6.965	<0.001
		Upr	-0.343	0.039	109.459	-8.693	<0.001
	35	Lwr	-0.235	0.044	169.410	-5.308	<0.001
		Old	-0.338	0.045	171.866	-7.599	<0.001
		Upr	-0.421	0.044	165.553	-9.557	<0.001
	42	Lwr	-0.275	0.051	272.361	-5.452	<0.001
		Old	-0.399	0.051	276.807	-7.853	<0.001
		Upr	-0.498	0.050	266.075	-9.927	<0.001
	49	Lwr	-0.316	0.058	424.276	-5.458	<0.001
		Old	-0.460	0.058	430.751	-7.899	<0.001
		Upr	-0.576	0.057	415.452	-10.019	<0.001
	56	Lwr	-0.356	0.066	610.464	-5.401	<0.001
		Old	-0.521	0.066	617.985	-7.848	<0.001
		Upr	-0.653	0.065	600.102	-9.977	<0.001
ARI2	0	Lwr	-0.022	0.030	174.229	-0.743	0.458
		Old	-0.022	0.030	174.229	-0.743	0.458
		Upr	-0.022	0.030	174.229	-0.743	0.458
	7	Lwr	-0.051	0.027	114.008	-1.889	0.061
		Old	-0.063	0.027	113.807	-2.355	0.020

Table C.4 continued on next page

Table C.4 continued from previous page

VI	DoD	Postion	Estimate	SE	*df*	t.ratio	*p* value
		Upr	-0.076	0.027	113.854	-2.816	0.006
	14	Lwr	-0.079	0.025	86.704	-3.162	0.002
		Old	-0.104	0.025	86.619	-4.161	<0.001
		Upr	-0.129	0.025	86.221	-5.156	<0.001
	21	Lwr	-0.107	0.025	84.357	-4.328	<0.001
		Old	-0.145	0.025	84.637	-5.829	<0.001
		Upr	-0.182	0.025	83.333	-7.352	<0.001
	28	Lwr	-0.136	0.026	106.154	-5.158	<0.001
		Old	-0.186	0.026	107.153	-7.034	<0.001
		Upr	-0.235	0.026	104.196	-8.974	<0.001
	35	Lwr	-0.164	0.029	158.839	-5.612	<0.001
		Old	-0.227	0.029	161.120	-7.710	<0.001
		Upr	-0.288	0.029	155.315	-9.915	<0.001
	42	Lwr	-0.193	0.033	252.837	-5.794	<0.001
		Old	-0.267	0.033	257.015	-8.002	<0.001
		Upr	-0.342	0.033	247.055	-10.346	<0.001
	49	Lwr	-0.221	0.038	393.267	-5.825	<0.001
		Old	-0.308	0.038	399.523	-8.076	<0.001
		Upr	-0.395	0.038	384.991	-10.480	<0.001
	56	Lwr	-0.249	0.043	569.701	-5.783	<0.001
		Old	-0.349	0.043	577.291	-8.043	<0.001
		Upr	-0.448	0.043	559.666	-10.464	<0.001
PRI	0	Lwr	0.001	0.006	244.795	0.198	0.843
		Old	0.008	0.006	243.983	1.361	0.175
		Upr	-0.008	0.006	239.182	-1.358	0.176
	7	Lwr	0.012	0.004	89.716	2.678	0.009
		Old	0.010	0.004	89.177	2.249	0.027
		Upr	0.004	0.004	88.234	0.902	0.369
	14	Lwr	0.016	0.004	96.843	3.591	0.001
		Old	0.010	0.004	95.807	2.269	0.026
		Upr	0.009	0.004	94.967	2.042	0.044
	21	Lwr	0.016	0.004	82.890	3.784	<0.001
		Old	0.010	0.004	82.073	2.276	0.025
		Upr	0.010	0.004	81.663	2.419	0.018
	28	Lwr	0.014	0.004	67.968	3.557	0.001
		Old	0.010	0.004	67.941	2.425	0.018
		Upr	0.010	0.004	67.624	2.549	0.013
	35	Lwr	0.013	0.004	77.316	3.093	0.003
		Old	0.012	0.004	77.995	2.770	0.007
		Upr	0.012	0.004	77.005	2.814	0.006
	42	Lwr	0.014	0.004	93.085	3.167	0.002
		Old	0.016	0.004	93.771	3.683	<0.001
		Upr	0.017	0.004	91.971	3.944	<0.001
	49	Lwr	0.019	0.004	88.174	4.487	<0.001

Table C.4 continued on next page

Table C.4 continued from previous page

VI	DoD	Postion	Estimate	SE	*df*	t.ratio	*p* value
		Old	0.025	0.004	88.410	5.701	<0.001
		Upr	0.029	0.004	86.717	6.822	<0.001
	56	Lwr	0.032	0.005	188.937	5.994	<0.001
		Old	0.038	0.005	192.432	7.199	<0.001
		Upr	0.051	0.005	187.938	9.631	<0.001

C.2 Treatment differences at t0

Figure C.1: Summary results from estimated marginal means (EMM) for drought and control groups contrasts at day 0. Estimated marginal means (EMM) are calculated on the VI-specific mixed effect models. p values are for drought - control contrast. The VI selected are those where a significant ($p < 0.05$) Treatment main effect was detected. Dashed line is $p = 0.05$. Values which are below this line indicate significant ($p < 0.05$) differences between the drought and control groups at t0. Crosses are top of the canopy, triangles are old needles and circles are bottom of the canopy. Full full results see Table C.5. For full VI names, formula and references see Table 2.1 (p.43).

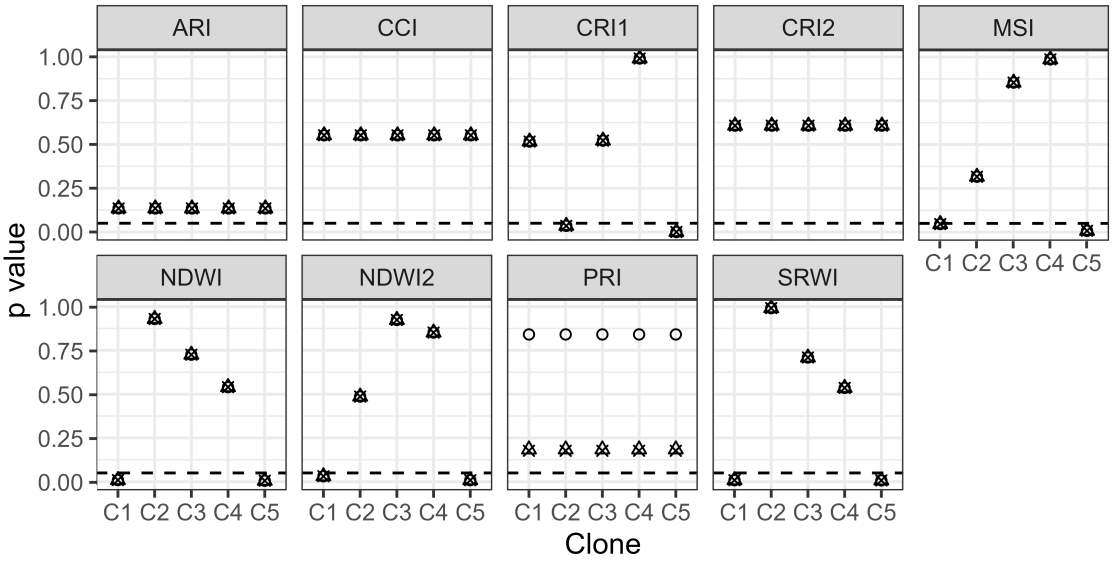

Table C.5: Estimated Marginal Mean (EMM) contrasts for drought and control group contrasts at day 0 (t0). Canopy Pos. is the canopy position (Upr = Needles measured from the top 25% of the canopy (N^{upper}), Lwr = Needles measured from the bottom 25% of the canopy (N^{lower}), Old = Needles measured from the previous year's growth (2020) (N^{old}). Upr and Lwr needles grew in 2021). Estimate is the estimated differences between the means of the groups in VI value. SE and *df* are the standard error and degrees of freedom of the estimate. * are when $p < 0.05$.

VI	Clone	Canopy Pos.	Estimate	SE	*df*	t.ratio	*p* value
ARI	Clone 1	BOC	-0.09	0.06	530.38	-1.50	0.13
		PYN	-0.09	0.06	530.38	-1.50	0.13
		TOC	-0.09	0.06	530.38	-1.50	0.13
	Clone 2	BOC	-0.09	0.06	530.38	-1.50	0.13
		PYN	-0.09	0.06	530.38	-1.50	0.13
		TOC	-0.09	0.06	530.38	-1.50	0.13
	Clone 3	BOC	-0.09	0.06	530.38	-1.50	0.13
		PYN	-0.09	0.06	530.38	-1.50	0.13
		TOC	-0.09	0.06	530.38	-1.50	0.13
	Clone 4	BOC	-0.09	0.06	530.38	-1.50	0.13

Table C.5 continued on next page

Table C.5 continued from previous page

VI	Clone	Canopy Pos.	Estimate	SE	*df*	t.ratio	*p* value
		PYN	-0.09	0.06	530.38	-1.50	0.13
		TOC	-0.09	0.06	530.38	-1.50	0.13
	Clone 5	BOC	-0.09	0.06	530.38	-1.50	0.13
		PYN	-0.09	0.06	530.38	-1.50	0.13
		TOC	-0.09	0.06	530.38	-1.50	0.13
CCI	Clone 1	BOC	0.00	0.01	211.17	-0.60	0.55
		PYN	0.00	0.01	211.17	-0.60	0.55
		TOC	0.00	0.01	211.17	-0.60	0.55
	Clone 2	BOC	0.00	0.01	211.17	-0.60	0.55
		PYN	0.00	0.01	211.17	-0.60	0.55
		TOC	0.00	0.01	211.17	-0.60	0.55
	Clone 3	BOC	0.00	0.01	211.17	-0.60	0.55
		PYN	0.00	0.01	211.17	-0.60	0.55
		TOC	0.00	0.01	211.17	-0.60	0.55
	Clone 4	BOC	0.00	0.01	211.17	-0.60	0.55
		PYN	0.00	0.01	211.17	-0.60	0.55
		TOC	0.00	0.01	211.17	-0.60	0.55
	Clone 5	BOC	0.00	0.01	211.17	-0.60	0.55
		PYN	0.00	0.01	211.17	-0.60	0.55
		TOC	0.00	0.01	211.17	-0.60	0.55
CRI1	Clone 1	BOC	-0.42	0.65	1272.00	-0.65	0.52
		PYN	-0.42	0.65	1272.00	-0.65	0.52
		TOC	-0.42	0.65	1272.00	-0.65	0.52
	Clone 2	BOC	-1.34	0.64	1268.67	-2.11	0.04*
		PYN	-1.34	0.64	1268.67	-2.11	0.04*
		TOC	-1.34	0.64	1268.67	-2.11	0.04*
	Clone 3	BOC	0.41	0.64	1268.53	0.64	0.52
		PYN	0.41	0.64	1268.53	0.64	0.52
		TOC	0.41	0.64	1268.53	0.64	0.52
	Clone 4	BOC	-0.01	0.64	1268.55	-0.01	0.99
		PYN	-0.01	0.64	1268.55	-0.01	0.99
		TOC	-0.01	0.64	1268.55	-0.01	0.99
	Clone 5	BOC	3.02	0.64	1268.62	4.75	<0.001*
		PYN	3.02	0.64	1268.62	4.75	<0.001*
		TOC	3.02	0.64	1268.62	4.75	<0.001*
CRI2	Clone 1	BOC	0.16	0.32	621.30	0.51	0.61
		PYN	0.16	0.32	621.30	0.51	0.61
		TOC	0.16	0.32	621.30	0.51	0.61
	Clone 2	BOC	0.16	0.32	621.30	0.51	0.61
		PYN	0.16	0.32	621.30	0.51	0.61
		TOC	0.16	0.32	621.30	0.51	0.61
	Clone 3	BOC	0.16	0.32	621.30	0.51	0.61
		PYN	0.16	0.32	621.30	0.51	0.61
		TOC	0.16	0.32	621.30	0.51	0.61

Table C.5 continued on next page

Table C.5 continued from previous page

VI	Clone	Canopy Pos.	Estimate	SE	*df*	t.ratio	*p* value
	Clone 4	BOC	0.16	0.32	621.30	0.51	0.61
		PYN	0.16	0.32	621.30	0.51	0.61
		TOC	0.16	0.32	621.30	0.51	0.61
	Clone 5	BOC	0.16	0.32	621.30	0.51	0.61
		PYN	0.16	0.32	621.30	0.51	0.61
		TOC	0.16	0.32	621.30	0.51	0.61
MSI	Clone 1	BOC	-0.02	0.01	850.03	-2.00	0.05*
		PYN	-0.02	0.01	850.03	-2.00	0.05*
		TOC	-0.02	0.01	850.03	-2.00	0.05*
	Clone 2	BOC	0.01	0.01	815.77	1.00	0.32
		PYN	0.01	0.01	815.77	1.00	0.32
		TOC	0.01	0.01	815.77	1.00	0.32
	Clone 3	BOC	0.00	0.01	817.22	0.18	0.85
		PYN	0.00	0.01	817.22	0.18	0.85
		TOC	0.00	0.01	817.22	0.18	0.85
	Clone 4	BOC	0.00	0.01	814.66	-0.02	0.99
		PYN	0.00	0.01	814.66	-0.02	0.99
		TOC	0.00	0.01	814.66	-0.02	0.99
	Clone 5	BOC	-0.02	0.01	815.41	-2.67	0.01*
		PYN	-0.02	0.01	815.41	-2.67	0.01*
		TOC	-0.02	0.01	815.41	-2.67	0.01*
NDWI	Clone 1	BOC	0.01	0.00	903.11	2.61	0.01*
		PYN	0.01	0.00	903.11	2.61	0.01*
		TOC	0.01	0.00	903.11	2.61	0.01*
	Clone 2	BOC	0.00	0.00	869.95	-0.09	0.93
		PYN	0.00	0.00	869.95	-0.09	0.93
		TOC	0.00	0.00	869.95	-0.09	0.93
	Clone 3	BOC	0.00	0.00	871.32	-0.35	0.73
		PYN	0.00	0.00	871.32	-0.35	0.73
		TOC	0.00	0.00	871.32	-0.35	0.73
	Clone 4	BOC	0.00	0.00	868.87	0.61	0.54
		PYN	0.00	0.00	868.87	0.61	0.54
		TOC	0.00	0.00	868.87	0.61	0.54
	Clone 5	BOC	0.01	0.00	869.59	2.78	0.01*
		PYN	0.01	0.00	869.59	2.78	0.01*
		TOC	0.01	0.00	869.59	2.78	0.01*
NDWI2	Clone 1	BOC	0.02	0.01	884.52	2.16	0.03*
		PYN	0.02	0.01	884.52	2.16	0.03*
		TOC	0.02	0.01	884.52	2.16	0.03*
	Clone 2	BOC	-0.01	0.01	850.90	-0.70	0.49
		PYN	-0.01	0.01	850.90	-0.70	0.49
		TOC	-0.01	0.01	850.90	-0.70	0.49
	Clone 3	BOC	0.00	0.01	852.31	-0.10	0.92
		PYN	0.00	0.01	852.31	-0.10	0.92

Table C.5 continued on next page

Table C.5 continued from previous page

VI	Clone	Canopy Pos.	Estimate	SE	*df*	t.ratio	*p* value
		TOC	0.00	0.01	852.31	-0.10	0.92
	Clone 4	BOC	0.00	0.01	849.81	0.19	0.85
		PYN	0.00	0.01	849.81	0.19	0.85
		TOC	0.00	0.01	849.81	0.19	0.85
	Clone 5	BOC	0.02	0.01	850.54	2.64	0.01*
		PYN	0.02	0.01	850.54	2.64	0.01*
		TOC	0.02	0.01	850.54	2.64	0.01*
PRI	Clone 1	BOC	0.00	0.01	247.18	0.20	0.84
		PYN	0.01	0.01	246.38	1.33	0.18
		TOC	-0.01	0.01	241.72	-1.36	0.18
	Clone 2	BOC	0.00	0.01	247.18	0.20	0.84
		PYN	0.01	0.01	246.38	1.33	0.18
		TOC	-0.01	0.01	241.72	-1.36	0.18
	Clone 3	BOC	0.00	0.01	247.18	0.20	0.84
		PYN	0.01	0.01	246.38	1.33	0.18
		TOC	-0.01	0.01	241.72	-1.36	0.18
	Clone 4	BOC	0.00	0.01	247.18	0.20	0.84
		PYN	0.01	0.01	246.38	1.33	0.18
		TOC	-0.01	0.01	241.72	-1.36	0.18
	Clone 5	BOC	0.00	0.01	247.18	0.20	0.84
		PYN	0.01	0.01	246.38	1.33	0.18
		TOC	-0.01	0.01	241.72	-1.36	0.18
SRWI	Clone 1	BOC	0.03	0.01	906.99	2.64	0.01*
		PYN	0.03	0.01	906.99	2.64	0.01*
		TOC	0.03	0.01	906.99	2.64	0.01*
	Clone 2	BOC	0.00	0.01	873.93	-0.01	0.99
		PYN	0.00	0.01	873.93	-0.01	0.99
		TOC	0.00	0.01	873.93	-0.01	0.99
	Clone 3	BOC	0.00	0.01	875.29	-0.37	0.71
		PYN	0.00	0.01	875.29	-0.37	0.71
		TOC	0.00	0.01	875.29	-0.37	0.71
	Clone 4	BOC	0.01	0.01	872.85	0.62	0.54
		PYN	0.01	0.01	872.85	0.62	0.54
		TOC	0.01	0.01	872.85	0.62	0.54
	Clone 5	BOC	0.03	0.01	873.57	2.69	0.01*
		PYN	0.03	0.01	873.57	2.69	0.01*
		TOC	0.03	0.01	873.57	2.69	0.01*

Appendix D

Supplementary material: Chapter 5

Evaluating five MODIS Vegetation Indices (VI) for tracking GPP seasonal dynamics in a UK mature Sitka spruce (*Picea sitchensis*) plantation. Are effects of the 2018 drought detectable from space?

D.1 Regression analyses

D.1.1 Validation results

Table D.1: Statistics for the leave-one year-out validation models. Using the 16 day timeseries one year of data was removed (Test data) and models built using the equations outlined in Section 5.2.2 (p.123) using the remaining three years' data (Training data). The coefficients from the training models were then used to predict GPP using the removed Test data. Model performance evaluations (coefficient of determination (R^2) and Root Mean Square Error (RMSE)) were carried out for each of the four study years (2015-2018) and averaged. For every model formulation, the coefficients from each of the four training models (one for each year) were averaged. These averaged coefficients were then used to construct models for further analysis at all three time intervals. The VI are NDVI = Normalised Difference Vegetation Index, EVI = Enhanced Vegetation Index, CCI = Chlorophyll/ Carotenoid Index, NIRv = Near-infrared radiation from vegetation, GPP_{VI} = Gross Primary Productivity Vegetation Index. For VI formula and reference see Table 2.2 (p.58).

Model	Year	Slope	Intercept	R^2	RMSE
NDVI	2015	-17.68	34.02	0.24	3.00
	2016	-15.73	30.98	0.38	3.04
	2017	-16.57	32.12	0.24	3.40

Table D.1 continued on next page

Table D.1 continued from previous page

Model	Year	Slope	Intercept	R^2	RMSE
	2018	-19.91	37.18	0.22	3.15
NDVI × PAR × ε_{MODIS}	2015	2.09	13075.98	0.89	1.17
	2016	1.89	12779.99	0.82	1.64
	2017	1.92	12562.10	0.89	1.30
	2018	1.63	14207.50	0.79	1.63
NDVI × PAR × ε_{CCI}	2015	2.17	23676.57	0.92	0.96
	2016	1.98	23163.25	0.87	1.42
	2017	1.95	22999.89	0.88	1.33
	2018	1.60	26431.98	0.75	1.80
EVI	2015	-9.08	37.64	0.64	2.08
	2016	-11.55	42.94	0.38	3.06
	2017	-9.75	38.45	0.45	2.88
	2018	-11.48	43.38	0.42	2.71
EVI × PAR × ε_{MODIS}	2015	2.42	20126.23	0.92	0.98
	2016	2.20	19587.98	0.86	1.46
	2017	2.24	19189.40	0.93	1.00
	2018	1.77	23040.07	0.73	1.85
NDVI × PAR × ε_{CCI}	2015	2.53	35949.36	0.94	0.83
	2016	2.28	35524.96	0.85	1.51
	2017	2.32	34526.06	0.93	1.03
	2018	1.85	41630.34	0.70	1.96
CCI	2015	7.68	47.05	0.78	1.63
	2016	7.45	50.05	0.65	2.29
	2017	7.45	46.74	0.64	2.34
	2018	7.56	51.24	0.59	2.28
NIRv	2015	-4.62	63.82	0.60	2.19
	2016	-6.28	71.83	0.38	3.06
	2017	-5.16	65.03	0.43	2.95
	2018	-6.52	74.63	0.40	2.78
GPP_{VI}	2015	7.13	252.52	0.78	1.63
	2016	6.95	272.36	0.67	2.22
	2017	6.89	250.05	0.65	2.29

Table D.1 continued on next page

Table D.1 continued from previous page

Model	Year	Slope	Intercept	R^2	RMSE
	2018	7.00	279.38	0.57	2.36
NIRv × ε_{MODIS}	2015	-2.03	55.09	0.63	2.10
	2016	-2.63	56.86	0.58	2.52
	2017	-2.05	53.07	0.63	2.36
	2018	-3.05	61.03	0.55	2.41

D.1.2 Model statistics

Table D.2: Statistics for 10 Gross Primary Productivity (GPP) models for the relationship between modelled GPP (mGPP) and Flux Tower GPP (ftGPP) at different temporal resolutions. The slope and intercept are generated from averaging coefficients from the leave-one year-out procedure see in Figure D.1. The summary statistics are the coefficient of determination (R^2) and Root Mean Square Error (RMSE). For VI abbreviations see Figure D.1. For VI formula and reference see Table 2.2 (p.58).

Model	Year	Slope	Intercept	R^2	RMSE
CCI	16 Day	7.53	48.77	0.67	2.13
	Month	7.53	48.77	0.52	2.47
	Day	7.53	48.77	0.53	2.76
EVI	16 Day	-10.46	40.60	0.47	2.68
	Month	-10.46	40.60	0.43	2.68
	Day	-10.46	40.60	0.43	3.03
EVI × PAR × ε_{MODIS}	16 Day	2.16	20485.92	0.86	1.32
	Month	2.16	20485.92	0.88	1.23
	Day	2.16	20485.92	0.75	2.02
EVI × PAR × ε_{CCI}	16 Day	2.25	36907.68	0.86	1.33
	Month	2.25	36907.68	0.89	1.18
	Day	2.25	36907.68	0.75	1.99
NDVI	16 Day	-17.47	33.57	0.27	3.15
	Month	-17.47	33.57	0.23	3.13
	Day	-17.47	33.57	0.22	3.53

Table D.2 continued on next page

Table D.2 continued from previous page

Model	Year	Slope	Intercept	R^2	RMSE
NDVI × PAR × ε_{MODIS}	16 Day	1.89	13156.39	0.85	1.44
	Month	1.89	13156.39	0.89	1.18
	Day	1.89	13156.39	0.74	2.04
NDVI × PAR × ε_{CCI}	16 Day	1.93	24067.92	0.85	1.38
	Month	1.93	24067.92	0.91	1.08
	Day	1.93	24067.92	0.75	2.00
NIRv	16 Day	-5.64	68.83	0.45	2.74
	Month	-5.64	68.83	0.43	2.67
	Day	-5.64	68.83	0.42	3.04
GPP_{VI}	16 Day	6.99	263.58	0.67	2.12
	Month	6.99	263.58	0.53	2.43
	Day	6.99	263.58	0.55	2.69
NIRv × ε_{MODIS}	16 Day	-2.44	56.51	0.60	2.35
	Month	-2.44	56.51	0.60	2.26
	Day	-2.44	56.51	0.55	2.68

D.2 Annual Totals

Table D.3: Annual estimated Gross Primary Productivity (GPP) totals for Sitka spruce from 10 GPP models at three temporal resolutions across the study period (2015 - 2018). Annual Totals are the cumulative sum (tC ha^{-1} yr^{-1}) of GPP across a given year. Difference is the difference in GPP (tC ha^{-1} yr^{-1}) between modelled GPP (mGPP) and flux tower GPP (ftGPP). For VI abbreviations see Figure D.1. For VI formula and reference see Table 2.2 (p.58).

Model	Time Interval	Year	Annual Total	Difference
CCI	Day	2015	23.94	1.79
		2016	23.59	-1.37
		2017	24.49	-1.01
		2018	20.63	-2.33
	16 Day	2015	24.37	2.22
		2016	23.36	-1.60

Table D.3 continued on next page

Table D.3 continued from previous page

Model	Time Interval	Year	Annual Total	Difference
		2017	24.99	-0.51
		2018	23.01	0.05
	Month	2015	24.66	2.51
		2016	22.94	-2.02
		2017	24.63	-0.87
		2018	21.58	-1.38
EVI	Day	2015	22.89	0.74
		2016	24.35	-0.61
		2017	23.35	-2.15
		2018	24.94	1.98
	16 Day	2015	24.05	1.90
		2016	23.47	-1.49
		2017	22.86	-2.64
		2018	25.64	2.68
	Month	2015	23.28	1.13
		2016	24.17	-0.79
		2017	23.32	-2.18
		2018	25.32	2.36
EVI $\times$ PAR $\times$ $\varepsilon_{\text{MODIS}}$	Day	2015	28.19	6.04
		2016	28.55	3.59
		2017	29.36	3.86
		2018	30.72	7.76
	16 Day	2015	24.59	2.44
		2016	22.97	-1.99
		2017	22.76	-2.74
		2018	25.78	2.82
		2015	23.71	1.56
		2016	23.26	-1.70
		2017	23.47	-2.03
		2018	25.03	2.07
EVI $\times$ PAR $\times$ ε_{CCI}	Day	2015	27.85	5.70
		2016	28.45	3.49
		2017	28.91	3.41
		2018	29.76	6.80

Table D.3 continued on next page

Table D.3 continued from previous page

Model	Time Interval	Year	Annual Total	Difference
	16 Day	2015	24.43	2.28
		2016	23.26	-1.70
		2017	22.67	-2.83
		2018	25.74	2.78
	Month	2015	23.84	1.69
		2016	23.52	-1.44
		2017	23.41	-2.09
		2018	24.61	1.65
NDVI	Day	2015	22.47	0.32
		2016	24.02	-0.94
		2017	23.81	-1.69
		2018	24.59	1.63
	16 Day	2015	23.33	1.18
		2016	23.51	-1.45
		2017	23.66	-1.84
		2018	25.46	2.50
	Month	2015	22.61	0.46
		2016	23.84	-1.12
		2017	24.17	-1.33
		2018	25.09	2.13
NDVI $\times$ PAR $\times$ $\varepsilon_{\text{MODIS}}$	Day	2015	28.37	6.22
		2016	29.17	4.21
		2017	30.07	4.57
		2018	30.59	7.63
	16 Day	2015	24.48	2.33
		2016	23.22	-1.74
		2017	23.08	-2.42
		2018	25.18	2.22
	Month	2015	23.61	1.46
		2016	23.46	-1.50
		2017	23.64	-1.86
		2018	24.37	1.41
NDVI $\times$ PAR $\times$ ε_{CCI}	Day	2015	28.02	5.87
		2016	28.89	3.93

Table D.3 continued on next page

Table D.3 continued from previous page

Model	Time Interval	Year	Annual Total	Difference
		2017	29.70	4.20
		2018	29.65	6.69
	16 Day	2015	24.33	2.18
		2016	23.39	-1.57
		2017	23.02	-2.48
		2018	25.24	2.28
	Month	2015	23.72	1.57
		2016	23.45	-1.51
		2017	23.61	-1.89
		2018	23.98	1.02
NIRv	Day	2015	22.85	0.70
		2016	24.89	-0.07
		2017	23.52	-1.98
		2018	25.32	2.36
	16 Day	2015	23.92	1.77
		2016	23.52	-1.44
		2017	22.91	-2.59
		2018	25.70	2.74
	Month	2015	23.16	1.01
		2016	24.62	-0.34
		2017	23.60	-1.90
		2018	25.62	2.66
GPP_{VI}	Day	2015	23.82	1.67
		2016	24.70	-0.26
		2017	23.75	-1.75
		2018	20.42	-2.54
	16 Day	2015	24.10	1.95
		2016	24.16	-0.80
		2017	24.41	-1.09
		2018	23.11	0.15
	Month	2015	24.32	2.17
		2016	23.93	-1.03
		2017	24.00	-1.50
		2018	21.07	-1.89

Table D.3 continued on next page

Table D.3 continued from previous page

Model	Time Interval	Year	Annual Total	Difference
NIRv × $\varepsilon_{\text{MODIS}}$	Day	2015	23.01	0.86
		2016	24.91	-0.05
		2017	23.73	-1.77
		2018	23.98	1.02
	16 Day	2015	24.51	2.36
		2016	23.09	-1.87
		2017	23.34	-2.16
		2018	24.97	2.01
	Month	2015	23.61	1.46
		2016	24.02	-0.94
		2017	23.94	-1.56
		2018	24.91	1.95

Table D.4: Average annual estimated Gross Primary Productivity (GPP) differences for Sitka spruce from 10 GPP models at three temporal resolutions across the study period (2015 - 2018). Average Annual Total Diff. is the difference in mean annual GPP (tC ha^{-1} yr^{-1}) between modelled GPP (mGPP) and flux tower GPP (ftGPP). For VI abbreviations see Figure D.1. For VI formula and reference see Table 2.2 (p.58).

Model	Time Interval	Annual Total Diff.
CCI	Day	1.63
	16 Day	1.10
	Month	1.69
EVI	Day	1.37
	16 Day	2.18
	Month	1.62
EVI × PAR × $\varepsilon_{\text{MODIS}}$	Day	5.31
	16 Day	2.50
	Month	1.84
EVI × PAR × ε_{CCI}	Day	4.85
	16 Day	2.40
	Month	1.72

Table D.4 continued on next page

Table D.4 continued from previous page

Model	Time Interval	Annual Total Diff.
NDVI	Day	1.14
	16 Day	1.74
	Month	1.26
NDVI × PAR × $\varepsilon_{\text{MODIS}}$	Day	5.66
	16 Day	2.18
	Month	1.56
NDVI × PAR × ε_{CCI}	Day	5.17
	16 Day	2.13
	Month	1.50
NIRv	Day	1.28
	16 Day	2.13
	Month	1.48
GPP_{VI}	Day	1.56
	16 Day	0.99
	Month	1.65
NIRv × $\varepsilon_{\text{MODIS}}$	Day	0.93
	16 Day	2.10
	Month	1.48

D.3 The 2018 drought

Table D.5: Annual 2018 Gross Primary Productivity (GPP) anomalies estimated from 10 GPP models at three temporal resolutions. The 2018 anomalies (Difference, tC ha^{-1} yr^{-1}) are calculated as the difference (%) between the average total annual GPP (Average Total, tC ha^{-1} yr^{-1}) of 2015 - 2017 and the total annual GPP (tC ha^{-1} yr^{-1}) in 2018 (2018 Total). For VI abbreviations see Figure D.1. For VI formula and reference see Table 2.2 (p.58).

Model	Time Interval	Average Total	2018 Total	Difference
CCI	Day	24.01	20.63	-14.05
	16 Day	24.24	23.01	-5.10

Table D.5 continued on next page

Table D.5 continued from previous page

Model	Time Interval	Average Total	2018 Total	Difference
	Month	24.08	21.58	-10.38
EVI	Day	23.53	24.94	5.99
	16 Day	23.46	25.64	9.27
	Month	23.59	25.32	7.35
EVI × PAR × $\varepsilon_{\text{MODIS}}$	Day	28.70	30.72	7.07
	16 Day	23.44	25.78	9.99
	Month	23.48	25.03	6.62
EVI × PAR × ε_{CCI}	Day	28.40	29.76	4.77
	16 Day	23.45	25.74	9.75
	Month	23.59	24.61	4.31
NDVI	Day	23.43	24.59	4.94
	16 Day	23.50	25.46	8.34
	Month	23.54	25.09	6.56
NDVI × PAR × $\varepsilon_{\text{MODIS}}$	Day	29.20	30.59	4.77
	16 Day	23.59	25.18	6.72
	Month	23.57	24.37	3.37
NDVI × PAR × ε_{CCI}	Day	28.87	29.65	2.70
	16 Day	23.58	25.24	7.02
	Month	23.60	23.98	1.62
NIRv	Day	23.76	25.32	6.61
	16 Day	23.45	25.70	9.56
	Month	23.79	25.62	7.66
GPP_{VI}	Day	24.09	20.42	-15.25
	16 Day	24.22	23.11	-4.62
	Month	24.08	21.07	-12.50
NIRv × $\varepsilon_{\text{MODIS}}$	Day	23.89	23.98	0.41
	16 Day	23.65	24.97	5.56
	Month	23.85	24.91	4.43

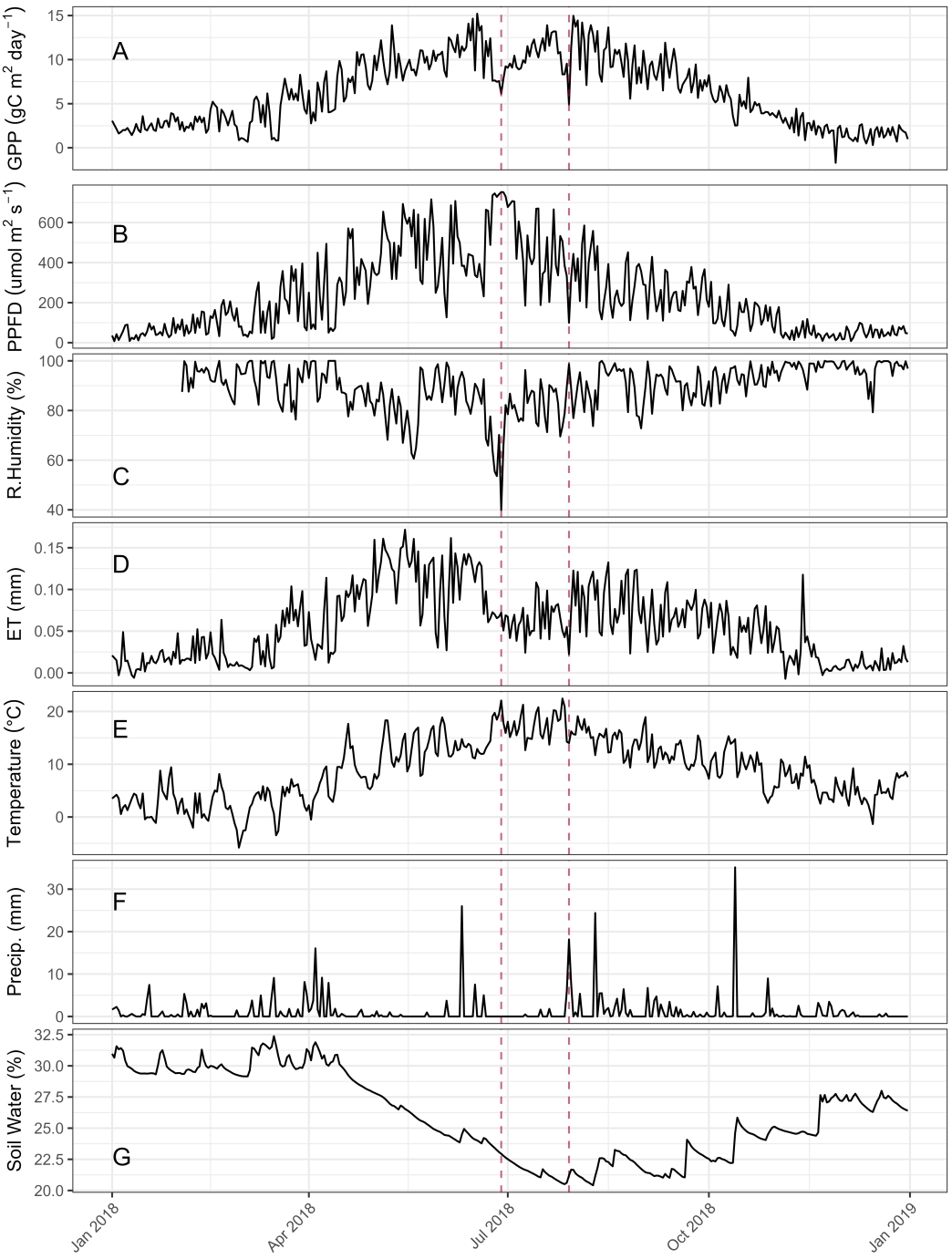

Figure D.1: Time series of flux tower Gross Primary Productivity (ftGPP) (Panel A) meteorological variables (Panels B to G), measured by (Xenakis et al., 2021), across 2018. A, ftGPP (gC m^2 day^{-1}) B, Photosynthetic Photon Flux Density Total (µmol m^2 s^{-1}), C, Mean daily relative humidity (%), D, mean daily evapotranspiration (mm), E, mean daily temperature (°C), F, daily precipitation (mm) and G, mean daily soil water content (%) at an average depth of 30 cm. The red dashed vertical lines correspond to two points during the drought where ftGPP reached particularly low values due to drought stress. These occurred after rapid drops in ftGPP and were followed by recovery. Note: very limited rain fell between these two dates, and soil moisture continued to fall, so they are considered to be within the same drought period, despite temporary recovery of ftGPP.

D.4 $\varepsilon_{\text{MODIS}}$ scalars

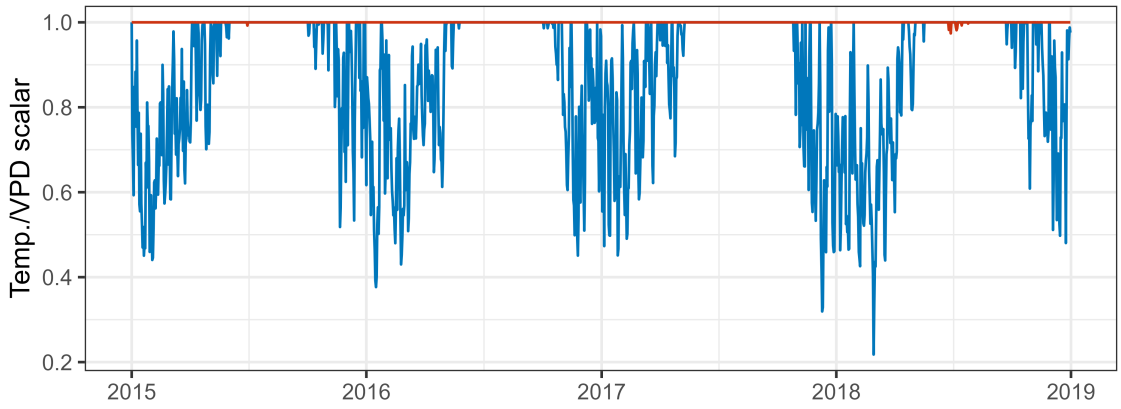

Figure D.2: Time series of $\varepsilon_{\text{MODIS}}$ scalars used to limit ε_{max} in Equation 5.2 (p.124). The red line is $\text{VPD}_{\text{scalar}}$ and the blue line is T_{scalar}. VPD refers to Vapour Pressure Deficit. Temperature limits are imposed on modelled GPP in non-summer months seen when the blue line < 1. Very little VPD limits (red line) are imposed across the whole time series. See Section 5.2.2.2 (p.123) for calculation of the scalars.

Appendix E

Supplementary material: Chapter 6

Testing the Simple Biosphere Model (SiB) for GPP retrieval in a UK mature Sitka spruce (*Picea sitchensis*) plantation. Can new VI improve the model and are effects of the 2018 drought detectable with SiB?

E.1 SiBx model runs

E.1.1 Static Vcmax

Table E.1: Results from iterative runs of the Simple Biosphere model (SiBx) with different Vcmax values. The SiBx model was run over the study period (2015 - 2018) for a series of Vcmax values (20 to 200 µmol m^2 s^{-1} at 20 µmol m^2 s^{-1} intervals) for five Vegetation Indices (VI) (NDVI, EVI, CCI, NIRv GPP_{VI}). The leaf level gross photosynthesis (A) and the canopy level gross photosynthesis (CAg) were compared to Flux Tower Gross Primary Productivity (ftGPP) using liner regression analysis to give R^2 and RMSE (tC ha^{-1} yr^{-1}). Over the full study period, total gross primary productivity (GPP or CAg) was calculated for each SiBx run and is presented (Total, tC ha^{-1} yr^{-1}). The difference between SiBx total GPP and ftGPP total GPP across the four years is presented (Difference, tC ha^{-1} yr^{-1}). For full VI names, formula and references see Table 2.2 (p.58).

		A		CAg			
VI	Vcmax	R^2	RMSE	R^2	RMSE	Total	Difference
NDVI	20	0.60	2.54	0.67	2.29	60.80	-60.80
	40	0.65	2.37	0.72	2.14	29.72	-29.72
	60	0.66	2.34	0.74	2.06	3.29	-3.29
	80	0.68	2.25	0.76	1.95	20.35	20.35
	100	0.70	2.20	0.78	1.87	41.55	41.55
	120	0.70	2.18	0.79	1.84	60.25	60.25

Table E.1 continued on next page

Table E.1 continued from previous page

VI	Vcmax	A R^2	RMSE	CAg R^2	RMSE	Total	Difference
	140	0.70	2.17	0.79	1.81	76.74	76.74
	160	0.70	2.19	0.79	1.82	90.93	90.93
	180	0.69	2.22	0.79	1.82	102.80	102.80
	200	0.68	2.27	0.79	1.85	112.91	112.91
EVI	20	0.60	2.53	0.69	2.24	62.04	-62.04
	40	0.65	2.36	0.73	2.08	32.00	-32.00
	60	0.66	2.34	0.75	2.01	6.43	-6.43
	80	0.68	2.25	0.77	1.91	16.51	16.51
	100	0.70	2.20	0.79	1.84	37.11	37.11
	120	0.70	2.18	0.80	1.81	55.20	55.20
	140	0.70	2.18	0.80	1.79	71.16	71.16
	160	0.70	2.20	0.80	1.80	85.01	85.01
	180	0.69	2.23	0.80	1.81	96.73	96.73
	200	0.68	2.27	0.79	1.84	106.47	106.47
CCI	20	0.60	2.53	0.70	2.20	61.91	-61.91
	40	0.65	2.37	0.74	2.05	31.75	-31.75
	60	0.66	2.34	0.76	1.97	6.06	-6.06
	80	0.68	2.26	0.78	1.88	16.99	16.99
	100	0.70	2.20	0.80	1.81	37.66	37.66
	120	0.70	2.18	0.80	1.78	55.96	55.96
	140	0.70	2.18	0.80	1.77	72.07	72.07
	160	0.70	2.20	0.80	1.79	86.03	86.03
	180	0.69	2.22	0.80	1.80	97.87	97.87
	200	0.68	2.27	0.79	1.83	107.70	107.70
NIRv	20	0.60	2.53	0.69	2.23	62.21	-62.21
	40	0.65	2.36	0.73	2.08	32.31	-32.31
	60	0.66	2.34	0.75	2.01	6.85	-6.85
	80	0.68	2.25	0.77	1.91	15.99	15.99
	100	0.70	2.20	0.79	1.84	36.48	36.48
	120	0.70	2.18	0.80	1.80	54.48	54.48
	140	0.70	2.18	0.80	1.79	70.39	70.39
	160	0.70	2.20	0.80	1.80	84.15	84.15
	180	0.69	2.23	0.80	1.81	95.85	95.85
	200	0.68	2.27	0.79	1.84	105.51	105.51
GPP_{VI}	20	0.60	2.53	0.70	2.18	62.64	-62.64
	40	0.65	2.36	0.74	2.04	33.11	-33.11
	60	0.66	2.34	0.76	1.96	7.94	-7.94
	80	0.68	2.26	0.78	1.87	14.70	14.70
	100	0.70	2.20	0.80	1.81	35.02	35.02
	120	0.70	2.18	0.80	1.78	52.89	52.89
	140	0.70	2.18	0.80	1.77	68.69	68.69
	160	0.70	2.20	0.80	1.78	82.45	82.45

Table E.1 continued on next page

Table E.1 continued from previous page

VI	Vcmax	A R^2	RMSE	CAg R^2	RMSE	Total	Difference
	180	0.69	2.23	0.80	1.81	94.15	94.15
	200	0.68	2.27	0.79	1.84	103.70	103.70

E.1.2 All years

Table E.2: Results from iterative runs of the Simple Biosphere model (SiBx) with different Vcmax (vm60 = Static Vcmax value of 60 µmol m^2 s^{-1}, vmCCI = dynamic Vcmax derived from CCI time series, vmGPP = dynamic Vcmax derived from GPP_{VI} time series, vmDy = dynamic Vcmax time series derived from model optimisation (for development of dynamic Vcmax see Section 2.6.2)) and Vegetation Index (VI) (NDVI, EVI, CCI, NIRv GPP_{VI}) inputs, with and without a drought stress term (S_d) over the total study period (2015 - 2018). The S_d was derived from VPD (see Section 2.5.2.1 (p.63)). For each model run, the leaf level gross photosynthesis (A) and the canopy level gross photosynthesis (CAg) were compared to Flux Tower Gross Primary Productivity (ftGPP) using liner regression analysis to give R^2 and RMSE (tC ha^{-1} yr^{-1}). Over the full study period, total gross primary productivity (GPP or CAg) was calculated for each SiBx run and is presented (Total, tC ha^{-1} yr^{-1}). The difference between SiBx total GPP and ftGPP total GPP across the four years is presented (Diff., tC ha^{-1} yr^{-1}). For full VI names, formula and references see Table 2.2 (p.58).

VI	Vcmax		A R^2	RMSE	CAg R^2	RMSE	Total	Diff.
NDVI	vm60	S_d	0.63	2.44	0.74	2.06	90.55	-5.02
		-	0.66	2.34	0.74	2.06	92.29	-3.29
	vmCCI	S_d	0.68	2.25	0.73	2.09	94.70	-0.88
		-	0.70	2.20	0.73	2.09	96.64	1.06
	vmDy	S_d	0.73	2.06	0.79	1.82	94.35	-1.23
		-	0.74	2.02	0.78	1.87	96.35	0.77
	vmGPP	S_d	0.69	2.23	0.73	2.09	95.36	-0.21
		-	0.71	2.17	0.73	2.09	97.32	1.74
EVI	vm60	S_d	0.63	2.44	0.75	2.01	90.87	-4.70
		-	0.66	2.34	0.75	2.01	92.61	-2.97
	vmCCI	S_d	0.68	2.26	0.74	2.04	94.99	-0.58
		-	0.70	2.20	0.74	2.05	96.93	1.36
	vmDy	S_d	0.73	2.07	0.80	1.81	94.86	-0.72
		-	0.74	2.03	0.79	1.85	96.86	1.29
	vmGPP	S_d	0.69	2.23	0.74	2.05	95.69	0.12
		-	0.71	2.17	0.74	2.05	97.65	2.07

Table E.2 continued on next page

Table E.2 continued from previous page

VI	Vcmax		A R^2	RMSE	CAg R^2	RMSE	Total	Diff.
NIRv	vm60	S_d	0.63	2.44	0.75	2.01	90.87	-4.71
		-	0.66	2.34	0.75	2.01	92.61	-2.97
	vmCCI	S_d	0.68	2.26	0.74	2.04	94.97	-0.60
		-	0.70	2.20	0.74	2.04	96.91	1.34
	vmDy	S_d	0.73	2.06	0.80	1.81	94.87	-0.70
		-	0.74	2.03	0.79	1.85	96.88	1.30
	vmGPP	S_d	0.69	2.23	0.74	2.04	95.67	0.10
		-	0.71	2.17	0.74	2.05	97.63	2.06
GPP	vm60	S_d	0.63	2.44	0.76	1.97	90.68	-4.90
		-	0.66	2.34	0.76	1.95	92.36	-3.22
	vmCCI	S_d	0.68	2.26	0.74	2.02	94.74	-0.84
		-	0.70	2.20	0.75	2.02	96.62	1.05
	vmDy	S_d	0.73	2.07	0.79	1.81	94.72	-0.86
		-	0.74	2.03	0.79	1.83	96.65	1.08
	vmGPP	S_d	0.69	2.23	0.74	2.04	95.45	-0.12
		-	0.71	2.17	0.74	2.03	97.35	1.78
Static	vm60	S_d	0.63	2.43	0.74	2.03	92.09	-3.48
		-	0.66	2.33	0.75	2.00	93.73	-1.84
	vmDy	S_d	0.68	2.26	0.76	1.97	95.55	-0.02
		-	0.70	2.20	0.76	1.97	97.38	1.81
	vmCCI	S_d	0.74	2.06	0.78	1.88	95.88	0.31
		-	0.75	2.02	0.78	1.89	97.77	2.19
	vmGPP	S_d	0.69	2.23	0.76	1.97	96.18	0.60
		-	0.70	2.17	0.76	1.96	98.03	2.45

E.1.3 Individual years

Table E.3: Results from iterative runs of the Simple Biosphere model (SiBx) with different Vcmax (vm60 = Static Vcmax value of 60 µmol m^2 s^{-1}, vmCCI = dynamic Vcmax derived from CCI time series, vmGPP = dynamic Vcmax derived from GPP_{VI} time series, vmDy = dynamic Vcmax time series derived from model optimisation (for development of dynamic Vcmax see Section 2.6.2)) and Vegetation Index (VI) (NDVI, EVI, CCI, NIRv GPP_{VI}) inputs, with and without a drought stress term (S_d) for each study year (2015 - 2018). The S_d was derived from VPD (see Section 2.5.2.1 (p.63)). For each model run, the leaf level gross photosynthesis (A) and the canopy level gross photosynthesis (CAg) were compared to Flux Tower Gross Primary Productivity (ftGPP) using liner regression analysis to give R^2 and RMSE (tC ha^{-1} yr^{-1}). Over each study year, total gross primary productivity (GPP or CAg) was calculated for each SiBx run and is presented (Total, tC ha^{-1} yr^{-1}). The difference between SiBx total GPP and ftGPP total GPP for each year is presented (Diff., tC ha^{-1} yr^{-1}). For full VI names, formula and references see Table 2.2 (p.58).

				A		CAg			
VI	Vcmax	Year		R^2	RMSE	R^2	RMSE	Total	Diff.
NDVI	vm60	2015	S_d	0.67	2.10	0.77	1.74	21.84	-0.32
			-	0.67	2.10	0.77	1.76	21.98	-0.18
		2016	S_d	0.63	2.51	0.72	2.17	23.34	-1.62
			-	0.65	2.45	0.73	2.13	23.45	-1.51
		2017	S_d	0.62	2.64	0.72	2.26	23.31	-2.19
			-	0.63	2.61	0.72	2.26	23.51	-1.99
		2018	S_d	0.61	2.41	0.73	1.98	22.06	-0.90
			-	0.71	2.08	0.74	1.94	23.35	0.39
	vmCCI	2015	S_d	0.73	1.91	0.76	1.80	23.20	1.05
			-	0.73	1.92	0.75	1.82	23.36	1.21
		2016	S_d	0.69	2.29	0.73	2.13	24.63	-0.33
			-	0.71	2.24	0.74	2.10	24.76	-0.20
		2017	S_d	0.66	2.50	0.71	2.30	24.72	-0.78
			-	0.66	2.48	0.71	2.30	24.94	-0.56
		2018	S_d	0.67	2.21	0.73	2.01	22.16	-0.81
			-	0.71	2.06	0.71	2.06	23.58	0.62
	vmDy	2015	S_d	0.77	1.76	0.83	1.53	22.85	0.70
			-	0.76	1.78	0.82	1.57	23.01	0.86
		2016	S_d	0.71	2.22	0.77	1.97	24.31	-0.65
			-	0.72	2.17	0.78	1.93	24.44	-0.52
		2017	S_d	0.73	2.20	0.78	2.00	24.25	-1.25
			-	0.74	2.20	0.78	2.02	24.47	-1.03
		2018	S_d	0.74	1.98	0.80	1.70	22.94	-0.02
			-	0.78	1.80	0.78	1.78	24.42	1.46
	vmGPP	2015	S_d	0.74	1.87	0.76	1.80	23.43	1.27
			-	0.73	1.89	0.75	1.82	23.59	1.44
		2016	S_d	0.71	2.21	0.74	2.09	25.21	0.25

Table E.3 continued on next page

Table E.3 continued from previous page

VI	Vcmax	Year		A R^2	A RMSE	CAg R^2	CAg RMSE	Total	Diff.
			-	0.72	2.17	0.75	2.06	25.35	0.39
		2017	S_d	0.65	2.52	0.70	2.35	24.74	-0.76
			-	0.66	2.50	0.70	2.34	24.96	-0.54
		2018	S_d	0.69	2.14	0.74	1.98	21.99	-0.97
			-	0.72	2.02	0.72	2.04	23.42	0.46
EVI	vm60	2015	S_d	0.67	2.10	0.80	1.65	21.95	-0.21
			-	0.67	2.10	0.79	1.67	22.09	-0.07
		2016	S_d	0.63	2.51	0.72	2.19	23.30	-1.66
			-	0.65	2.45	0.73	2.14	23.41	-1.55
		2017	S_d	0.62	2.65	0.73	2.21	23.40	-2.10
			-	0.63	2.61	0.73	2.21	23.61	-1.89
		2018	S_d	0.61	2.41	0.75	1.91	22.22	-0.74
			-	0.71	2.08	0.77	1.85	23.50	0.54
	vmCCI	2015	S_d	0.73	1.91	0.78	1.70	23.27	1.12
			-	0.72	1.93	0.78	1.73	23.44	1.28
		2016	S_d	0.69	2.28	0.72	2.17	24.60	-0.36
			-	0.71	2.24	0.73	2.13	24.74	-0.22
		2017	S_d	0.66	2.50	0.72	2.27	24.84	-0.66
			-	0.66	2.48	0.72	2.27	25.07	-0.43
		2018	S_d	0.67	2.21	0.75	1.91	22.28	-0.69
			-	0.71	2.06	0.74	1.97	23.70	0.73
	vmDy	2015	S_d	0.77	1.75	0.83	1.51	23.03	0.87
			-	0.77	1.77	0.82	1.55	23.19	1.04
		2016	S_d	0.71	2.23	0.77	1.96	24.26	-0.70
			-	0.72	2.18	0.78	1.92	24.39	-0.57
		2017	S_d	0.73	2.20	0.78	1.99	24.40	-1.10
			-	0.73	2.20	0.78	2.01	24.63	-0.87
		2018	S_d	0.74	1.98	0.81	1.69	23.17	0.21
			-	0.78	1.80	0.80	1.74	24.65	1.69
	vmGPP	2015	S_d	0.74	1.88	0.78	1.70	23.51	1.35
			-	0.73	1.89	0.78	1.73	23.67	1.52
		2016	S_d	0.71	2.21	0.73	2.13	25.21	0.25
			-	0.72	2.17	0.74	2.10	25.34	0.38
		2017	S_d	0.65	2.53	0.71	2.31	24.86	-0.64
			-	0.66	2.51	0.71	2.32	25.09	-0.41
		2018	S_d	0.69	2.14	0.76	1.88	22.12	-0.84
			-	0.72	2.02	0.74	1.95	23.54	0.58
CCI	vm60	2015	S_d	0.67	2.10	0.80	1.64	22.40	0.25
			-	0.67	2.10	0.79	1.67	22.55	0.39
		2016	S_d	0.63	2.52	0.75	2.07	23.27	-1.69
			-	0.65	2.46	0.76	2.03	23.38	-1.58
		2017	S_d	0.62	2.64	0.73	2.22	23.58	-1.92
			-	0.63	2.61	0.73	2.22	23.78	-1.72

Table E.3 continued on next page

Table E.3 continued from previous page

VI	Vcmax	Year		A R^2	A RMSE	CAg R^2	CAg RMSE	Total	Diff.
		2018	S_d	0.61	2.41	0.76	1.88	21.49	-1.47
			-	0.71	2.08	0.77	1.83	22.73	-0.23
	vmCCI	2015	S_d	0.73	1.91	0.78	1.71	23.78	1.63
			-	0.72	1.93	0.77	1.74	23.95	1.80
		2016	S_d	0.69	2.29	0.75	2.05	24.56	-0.40
			-	0.71	2.24	0.76	2.02	24.69	-0.27
		2017	S_d	0.66	2.50	0.71	2.29	25.01	-0.49
			-	0.66	2.48	0.71	2.28	25.24	-0.26
		2018	S_d	0.67	2.21	0.75	1.90	21.53	-1.43
			-	0.71	2.06	0.74	1.97	22.90	-0.06
	vmDy	2015	S_d	0.77	1.76	0.83	1.51	23.52	1.37
			-	0.76	1.78	0.82	1.55	23.69	1.54
		2016	S_d	0.71	2.23	0.78	1.93	24.31	-0.65
			-	0.72	2.18	0.79	1.90	24.44	-0.52
		2017	S_d	0.73	2.21	0.78	1.99	24.56	-0.94
			-	0.73	2.20	0.78	2.01	24.79	-0.71
		2018	S_d	0.73	1.98	0.81	1.67	22.39	-0.57
			-	0.78	1.79	0.80	1.73	23.81	0.85
	vmGPP	2015	S_d	0.74	1.88	0.78	1.71	24.02	1.86
			-	0.73	1.89	0.77	1.74	24.19	2.03
		2016	S_d	0.71	2.22	0.76	2.02	25.16	0.20
			-	0.72	2.17	0.77	1.99	25.30	0.34
		2017	S_d	0.65	2.52	0.70	2.33	25.05	-0.45
			-	0.66	2.50	0.70	2.33	25.27	-0.23
		2018	S_d	0.69	2.14	0.76	1.87	21.38	-1.58
			-	0.72	2.01	0.74	1.96	22.77	-0.20
NIRv	vm60	2015	S_d	0.67	2.10	0.80	1.65	21.87	-0.28
			-	0.67	2.10	0.79	1.68	22.01	-0.14
		2016	S_d	0.63	2.51	0.72	2.19	23.38	-1.58
			-	0.65	2.45	0.73	2.15	23.49	-1.47
		2017	S_d	0.62	2.65	0.73	2.20	23.38	-2.12
			-	0.63	2.61	0.73	2.20	23.58	-1.91
		2018	S_d	0.61	2.41	0.76	1.90	22.24	-0.72
			-	0.71	2.08	0.77	1.85	23.52	0.56
	vmCCI	2015	S_d	0.73	1.91	0.79	1.70	23.19	1.04
			-	0.72	1.92	0.78	1.73	23.35	1.20
		2016	S_d	0.69	2.28	0.72	2.17	24.68	-0.28
			-	0.71	2.24	0.73	2.14	24.81	-0.15
		2017	S_d	0.66	2.50	0.72	2.25	24.81	-0.69
			-	0.66	2.48	0.72	2.26	25.04	-0.46
		2018	S_d	0.67	2.21	0.75	1.91	22.29	-0.67
			-	0.71	2.06	0.74	1.96	23.71	0.75
	vmDy	2015	S_d	0.77	1.75	0.83	1.51	22.95	0.80

Table E.3 continued on next page

Table E.3 continued from previous page

VI	Vcmax	Year		A R^2	A RMSE	CAg R^2	CAg RMSE	Total	Diff.
			-	0.76	1.78	0.82	1.55	23.12	0.96
		2016	S_d	0.71	2.23	0.77	1.96	24.34	-0.62
			-	0.72	2.18	0.78	1.93	24.47	-0.49
		2017	S_d	0.73	2.20	0.78	1.98	24.39	-1.11
			-	0.74	2.20	0.78	2.00	24.63	-0.87
		2018	S_d	0.74	1.98	0.81	1.69	23.19	0.23
			-	0.78	1.80	0.80	1.74	24.67	1.71
	vmGPP	2015	S_d	0.74	1.88	0.79	1.70	23.42	1.27
			-	0.73	1.89	0.78	1.73	23.59	1.43
		2016	S_d	0.71	2.21	0.73	2.14	25.28	0.32
			-	0.72	2.16	0.74	2.10	25.42	0.46
		2017	S_d	0.65	2.53	0.71	2.30	24.84	-0.66
			-	0.66	2.50	0.71	2.30	25.06	-0.43
		2018	S_d	0.69	2.14	0.76	1.88	22.13	-0.83
			-	0.72	2.02	0.74	1.95	23.56	0.60
GPP	vm60	2015	S_d	0.67	2.10	0.80	1.63	22.36	0.21
			-	0.67	2.10	0.79	1.66	22.51	0.35
		2016	S_d	0.63	2.52	0.75	2.06	23.45	-1.51
			-	0.65	2.45	0.76	2.02	23.57	-1.39
		2017	S_d	0.62	2.64	0.73	2.22	23.42	-2.08
			-	0.63	2.61	0.73	2.22	23.62	-1.88
		2018	S_d	0.61	2.41	0.76	1.86	21.45	-1.52
			-	0.71	2.07	0.78	1.80	22.67	-0.29
	vmCCI	2015	S_d	0.73	1.91	0.79	1.69	23.72	1.56
			-	0.72	1.92	0.78	1.72	23.88	1.73
		2016	S_d	0.69	2.29	0.76	2.03	24.73	-0.23
			-	0.71	2.24	0.77	2.00	24.86	-0.10
		2017	S_d	0.66	2.50	0.71	2.29	24.83	-0.67
			-	0.66	2.48	0.71	2.29	25.05	-0.45
		2018	S_d	0.67	2.21	0.76	1.87	21.46	-1.50
			-	0.71	2.06	0.75	1.94	22.82	-0.14
	vmDy	2015	S_d	0.77	1.76	0.83	1.51	23.48	1.32
			-	0.76	1.78	0.82	1.55	23.65	1.49
		2016	S_d	0.71	2.23	0.78	1.93	24.51	-0.45
			-	0.72	2.18	0.79	1.90	24.65	-0.31
		2017	S_d	0.73	2.20	0.78	1.99	24.38	-1.12
			-	0.73	2.20	0.78	2.01	24.61	-0.89
		2018	S_d	0.73	1.98	0.81	1.69	22.34	-0.62
			-	0.78	1.79	0.80	1.73	23.75	0.79
	vmGPP	2015	S_d	0.74	1.88	0.79	1.69	23.95	1.79
			-	0.73	1.89	0.78	1.72	24.12	1.96
		2016	S_d	0.71	2.22	0.76	2.01	25.33	0.37
			-	0.72	2.17	0.77	1.98	25.47	0.51

Table E.3 continued on next page

Table E.3 continued from previous page

VI	Vcmax	Year		A R^2	A RMSE	CAg R^2	CAg RMSE	Total	Diff.
		2017	S_d	0.65	2.52	0.70	2.34	24.86	-0.64
			-	0.66	2.50	0.70	2.34	25.09	-0.41
		2018	S_d	0.69	2.14	0.77	1.85	21.31	-1.65
			-	0.72	2.02	0.75	1.92	22.68	-0.28
Static		2015	S_d	0.67	2.10	0.79	1.70	22.52	0.37
	vm60		-	0.67	2.09	0.78	1.72	22.66	0.50
		2016	S_d	0.63	2.51	0.72	2.17	23.47	-1.49
			-	0.65	2.45	0.74	2.12	23.57	-1.39
		2017	S_d	0.62	2.63	0.73	2.21	23.63	-1.87
			-	0.63	2.60	0.73	2.21	23.82	-1.68
		2018	S_d	0.61	2.41	0.74	1.97	22.48	-0.48
			-	0.71	2.07	0.78	1.80	23.68	0.71
	vmCCI	2015	S_d	0.73	1.92	0.80	1.65	23.70	1.55
			-	0.72	1.93	0.79	1.68	23.86	1.70
		2016	S_d	0.69	2.29	0.76	2.03	24.54	-0.42
			-	0.70	2.24	0.77	2.00	24.67	-0.29
		2017	S_d	0.66	2.50	0.73	2.21	24.91	-0.59
			-	0.66	2.48	0.73	2.21	25.12	-0.38
		2018	S_d	0.67	2.21	0.76	1.88	22.40	-0.56
			-	0.71	2.06	0.76	1.88	23.73	0.77
	vmDy	2015	S_d	0.77	1.74	0.81	1.58	23.56	1.40
			-	0.77	1.76	0.80	1.62	23.72	1.56
		2016	S_d	0.71	2.22	0.75	2.07	24.44	-0.52
			-	0.72	2.17	0.76	2.02	24.56	-0.40
		2017	S_d	0.73	2.20	0.78	1.99	24.51	-0.99
			-	0.74	2.19	0.78	2.01	24.73	-0.77
		2018	S_d	0.73	1.98	0.79	1.78	23.38	0.42
			-	0.78	1.79	0.80	1.72	24.76	1.79
	vmGPP	2015	S_d	0.74	1.88	0.80	1.64	23.90	1.75
			-	0.73	1.89	0.79	1.67	24.06	1.91
		2016	S_d	0.71	2.22	0.77	1.99	25.12	0.16
			-	0.72	2.17	0.77	1.96	25.25	0.29
		2017	S_d	0.65	2.53	0.72	2.25	24.91	-0.59
			-	0.65	2.51	0.72	2.25	25.13	-0.37
		2018	S_d	0.69	2.14	0.77	1.84	22.25	-0.71
			-	0.72	2.02	0.77	1.86	23.59	0.63

E.1.4 Seasonal runs

Table E.4: Results from iterative runs of the Simple Biosphere model (SiBx) with different Vcmax (vm60 = Static Vcmax value of 60 µmol m^2 s^{-1}, vmCCI = dynamic Vcmax derived from CCI time series, vmGPP = dynamic Vcmax derived from GPP_{VI} time series, vmDy = dynamic Vcmax time series derived from model optimisation (for development of dynamic Vcmax see Section 2.6.2)) and Vegetation Index (VI) (NDVI, EVI, CCI, NIRv GPP_{VI}) inputs, with and without a drought stress term (S_d) for each season (Winter = December - February, Spring = March - May, Summer = June - August, Autumn = September - November) acorss the study period (2015 - 2018). The S_d was derived from VPD (see Section 2.5.2.1 (p.63)). For each model run, the leaf level gross photosynthesis (A) and the canopy level gross photosynthesis (CAg) were compared to Flux Tower Gross Primary Productivity (ftGPP) using liner regression analysis to give R^2 and RMSE (tC ha^{-1} yr^{-1}). For each season, total gross primary productivity (GPP or CAg) was calculated for each SiBx run and is presented (Total, tC ha^{-1} yr^{-1}). The difference between SiBx total GPP and ftGPP total GPP for each season is presented (Diff., tC ha^{-1} yr^{-1}). For full VI names, formula and references see Table 2.2 (p.58).

				A		CAg			
VI	Vcmax	Season		R^2	RMSE	R^2	RMSE	Total	Diff.
NDVI	vm60	Autumn	S_d	0.53	1.85	0.66	1.58	22.68	3.69
			-	0.53	1.85	0.66	1.58	22.68	3.69
		Spring	S_d	0.42	2.04	0.51	1.87	22.03	-4.61
			-	0.42	2.05	0.51	1.88	22.09	-4.56
		Summer	S_d	0.09	2.49	0.12	2.44	35.33	-6.16
			-	0.03	2.57	0.05	2.54	37.01	-4.48
		Winter	S_d	0.31	0.90	0.29	0.91	10.39	1.93
			-	0.31	0.90	0.29	0.91	10.39	1.93
	vmCCI	Autumn	S_d	0.60	1.70	0.68	1.52	23.64	4.65
			-	0.60	1.70	0.68	1.52	23.64	4.65
		Spring	S_d	0.46	1.98	0.51	1.89	20.64	-6.01
			-	0.46	1.98	0.50	1.90	20.69	-5.95
		Summer	S_d	0.16	2.39	0.18	2.36	40.41	-1.08
			-	0.12	2.45	0.12	2.44	42.30	0.81
		Winter	S_d	0.28	0.92	0.26	0.93	9.89	1.43
			-	0.28	0.92	0.26	0.93	9.89	1.43
	vmDy	Autumn	S_d	0.63	1.64	0.69	1.50	20.86	1.87
			-	0.63	1.64	0.69	1.50	20.86	1.87
		Spring	S_d	0.47	1.96	0.53	1.85	24.82	-1.82
			-	0.46	1.97	0.52	1.86	24.89	-1.76
		Summer	S_d	0.11	2.46	0.15	2.40	39.69	-1.79
			-	0.04	2.55	0.06	2.53	41.63	0.14
		Winter	S_d	0.37	0.85	0.38	0.85	8.85	0.40
			-	0.37	0.85	0.38	0.85	8.85	0.40
	vmGPP	Autumn	S_d	0.62	1.67	0.68	1.52	23.48	4.50
			-	0.62	1.67	0.68	1.52	23.48	4.50

Table E.4 continued on next page

Table E.4 continued from previous page

VI	Vcmax	Season		A R^2	A RMSE	CAg R^2	CAg RMSE	Total	Diff.
		Spring	S_d	0.44	2.00	0.49	1.91	20.51	-6.14
			-	0.44	2.01	0.49	1.92	20.56	-6.08
		Summer	S_d	0.17	2.38	0.19	2.35	41.45	-0.04
			-	0.14	2.42	0.14	2.42	43.35	1.86
		Winter	S_d	0.29	0.91	0.27	0.92	9.80	1.35
			-	0.29	0.91	0.27	0.92	9.80	1.35
EVI	vm60	Autumn	S_d	0.53	1.85	0.66	1.56	22.26	3.27
			-	0.53	1.85	0.66	1.56	22.26	3.27
		Spring	S_d	0.42	2.04	0.50	1.90	22.56	-4.09
			-	0.42	2.05	0.50	1.90	22.61	-4.04
		Summer	S_d	0.09	2.49	0.13	2.43	35.61	-5.87
			-	0.03	2.56	0.06	2.52	37.29	-4.19
		Winter	S_d	0.31	0.90	0.31	0.90	10.33	1.87
			-	0.31	0.90	0.31	0.90	10.33	1.87
	vmCCI	Autumn	S_d	0.60	1.70	0.69	1.50	23.22	4.23
			-	0.60	1.70	0.69	1.50	23.22	4.23
		Spring	S_d	0.46	1.98	0.50	1.90	21.10	-5.55
			-	0.46	1.98	0.50	1.91	21.15	-5.49
		Summer	S_d	0.16	2.39	0.18	2.35	40.73	-0.75
			-	0.11	2.45	0.13	2.43	42.62	1.13
		Winter	S_d	0.28	0.92	0.28	0.92	9.83	1.37
			-	0.28	0.92	0.28	0.92	9.83	1.37
	vmDy	Autumn	S_d	0.63	1.64	0.69	1.49	20.49	1.51
			-	0.63	1.64	0.69	1.49	20.49	1.51
		Spring	S_d	0.47	1.96	0.51	1.87	25.42	-1.23
			-	0.46	1.97	0.51	1.88	25.49	-1.16
		Summer	S_d	0.11	2.46	0.16	2.39	40.01	-1.48
			-	0.04	2.56	0.07	2.51	41.94	0.46
		Winter	S_d	0.37	0.85	0.38	0.85	8.82	0.36
			-	0.37	0.85	0.38	0.85	8.82	0.36
	vmGPP	Autumn	S_d	0.61	1.67	0.69	1.51	23.08	4.09
			-	0.61	1.67	0.69	1.51	23.08	4.09
		Spring	S_d	0.44	2.00	0.49	1.92	20.98	-5.66
			-	0.44	2.01	0.49	1.93	21.04	-5.61
		Summer	S_d	0.17	2.38	0.19	2.34	41.77	0.29
			-	0.14	2.42	0.15	2.40	43.67	2.19
		Winter	S_d	0.29	0.91	0.29	0.91	9.74	1.28
			-	0.29	0.91	0.29	0.91	9.74	1.28
CCI	vm60	Autumn	S_d	0.53	1.84	0.66	1.56	21.73	2.74
			-	0.53	1.84	0.66	1.56	21.73	2.74
		Spring	S_d	0.42	2.04	0.50	1.89	22.62	-4.02
			-	0.42	2.04	0.50	1.90	22.67	-3.97
		Summer	S_d	0.09	2.49	0.13	2.43	35.73	-5.76

Table E.4 continued on next page

Table E.4 continued from previous page

VI	Vcmax	Season		A R^2	A RMSE	CAg R^2	CAg RMSE	Total	Diff.
			-	0.03	2.56	0.08	2.50	37.37	-4.11
		Winter	S_d	0.31	0.90	0.34	0.88	10.55	2.09
			-	0.31	0.90	0.34	0.88	10.55	2.09
	vmCCI	Autumn	S_d	0.60	1.70	0.68	1.53	22.66	3.68
			-	0.60	1.70	0.68	1.53	22.66	3.68
		Spring	S_d	0.46	1.98	0.49	1.91	21.17	-5.48
			-	0.46	1.98	0.49	1.92	21.22	-5.43
		Summer	S_d	0.16	2.39	0.18	2.36	40.90	-0.59
			-	0.12	2.45	0.14	2.42	42.75	1.26
		Winter	S_d	0.28	0.92	0.31	0.90	10.04	1.58
			-	0.28	0.92	0.31	0.90	10.04	1.58
	vmDy	Autumn	S_d	0.63	1.64	0.69	1.51	20.01	1.02
			-	0.63	1.64	0.69	1.51	20.01	1.02
		Spring	S_d	0.47	1.96	0.51	1.87	25.47	-1.17
			-	0.46	1.97	0.51	1.88	25.53	-1.11
		Summer	S_d	0.11	2.46	0.15	2.40	40.14	-1.35
			-	0.04	2.55	0.08	2.50	42.03	0.55
		Winter	S_d	0.37	0.85	0.39	0.85	9.04	0.58
			-	0.37	0.85	0.39	0.85	9.04	0.58
	vmGPP	Autumn	S_d	0.62	1.67	0.68	1.53	22.54	3.56
			-	0.62	1.67	0.68	1.53	22.54	3.56
		Spring	S_d	0.44	2.00	0.48	1.93	21.04	-5.61
			-	0.44	2.01	0.48	1.94	21.09	-5.55
		Summer	S_d	0.17	2.38	0.18	2.35	41.96	0.47
			-	0.14	2.42	0.15	2.40	43.82	2.34
		Winter	S_d	0.29	0.91	0.32	0.89	9.95	1.50
			-	0.29	0.91	0.32	0.89	9.95	1.50
NIRv	vm60	Autumn	S_d	0.53	1.85	0.66	1.56	22.22	3.24
			-	0.53	1.85	0.66	1.56	22.22	3.24
		Spring	S_d	0.42	2.04	0.50	1.89	22.61	-4.04
			-	0.42	2.05	0.50	1.90	22.67	-3.98
		Summer	S_d	0.09	2.49	0.13	2.43	35.59	-5.90
			-	0.03	2.57	0.06	2.53	37.27	-4.22
		Winter	S_d	0.31	0.90	0.31	0.90	10.33	1.87
			-	0.31	0.90	0.31	0.90	10.33	1.87
	vmCCI	Autumn	S_d	0.60	1.70	0.69	1.50	23.18	4.19
			-	0.60	1.70	0.69	1.50	23.18	4.19
		Spring	S_d	0.46	1.98	0.50	1.90	21.15	-5.49
			-	0.46	1.98	0.50	1.91	21.21	-5.44
		Summer	S_d	0.16	2.39	0.19	2.35	40.70	-0.79
			-	0.11	2.45	0.13	2.43	42.58	1.10
		Winter	S_d	0.28	0.92	0.28	0.92	9.83	1.37
			-	0.28	0.92	0.28	0.92	9.83	1.37

Table E.4 continued on next page

Table E.4 continued from previous page

VI	Vcmax	Season		A R^2	A RMSE	CAg R^2	CAg RMSE	Total	Diff.
	vmDy	Autumn	S_d	0.63	1.64	0.69	1.49	20.46	1.47
			-	0.63	1.64	0.69	1.49	20.46	1.47
		Spring	S_d	0.47	1.96	0.51	1.87	25.48	-1.16
			-	0.46	1.97	0.51	1.88	25.55	-1.10
		Summer	S_d	0.11	2.46	0.16	2.39	39.99	-1.50
			-	0.04	2.56	0.07	2.52	41.93	0.45
		Winter	S_d	0.37	0.85	0.38	0.85	8.82	0.37
			-	0.37	0.85	0.38	0.85	8.82	0.37
	vmGPP	Autumn	S_d	0.62	1.67	0.69	1.51	23.04	4.05
			-	0.62	1.67	0.69	1.51	23.04	4.05
		Spring	S_d	0.44	2.00	0.49	1.92	21.04	-5.61
			-	0.44	2.01	0.49	1.92	21.09	-5.55
		Summer	S_d	0.17	2.38	0.19	2.34	41.74	0.25
			-	0.13	2.42	0.15	2.40	43.64	2.16
		Winter	S_d	0.29	0.91	0.29	0.91	9.74	1.29
			-	0.29	0.91	0.29	0.91	9.74	1.29
GPP	vm60	Autumn	S_d	0.53	1.85	0.66	1.56	21.52	2.53
			-	0.53	1.85	0.66	1.56	21.52	2.53
		Spring	S_d	0.42	2.04	0.49	1.92	22.86	-3.79
			-	0.42	2.04	0.49	1.92	22.91	-3.73
		Summer	S_d	0.09	2.49	0.13	2.43	35.57	-5.92
			-	0.03	2.56	0.08	2.50	37.20	-4.29
		Winter	S_d	0.31	0.90	0.35	0.87	10.61	2.15
			-	0.31	0.90	0.35	0.87	10.61	2.15
	vmCCI	Autumn	S_d	0.60	1.70	0.68	1.52	22.46	3.47
			-	0.60	1.70	0.68	1.52	22.46	3.47
		Spring	S_d	0.46	1.97	0.49	1.92	21.37	-5.27
			-	0.46	1.98	0.49	1.92	21.43	-5.22
		Summer	S_d	0.16	2.39	0.18	2.36	40.70	-0.79
			-	0.12	2.45	0.14	2.41	42.52	1.04
		Winter	S_d	0.28	0.92	0.32	0.89	10.09	1.64
			-	0.28	0.92	0.32	0.89	10.09	1.64
	vmDy	Autumn	S_d	0.63	1.64	0.69	1.50	19.82	0.83
			-	0.63	1.64	0.69	1.50	19.82	0.83
		Spring	S_d	0.47	1.96	0.51	1.89	25.74	-0.90
			-	0.46	1.97	0.50	1.90	25.81	-0.84
		Summer	S_d	0.11	2.46	0.15	2.41	39.94	-1.55
			-	0.04	2.55	0.08	2.49	41.81	0.32
		Winter	S_d	0.37	0.85	0.39	0.84	9.10	0.64
			-	0.37	0.85	0.39	0.84	9.10	0.64
	vmGPP	Autumn	S_d	0.62	1.67	0.68	1.53	22.33	3.34
			-	0.62	1.67	0.68	1.53	22.33	3.34
		Spring	S_d	0.44	2.00	0.48	1.95	21.25	-5.40

Table E.4 continued on next page

Table E.4 continued from previous page

VI	Vcmax	Season		A R^2	A RMSE	CAg R^2	CAg RMSE	Total	Diff.
			-	0.44	2.01	0.47	1.95	21.30	-5.35
		Summer	S_d	0.17	2.38	0.18	2.36	41.75	0.26
			-	0.14	2.42	0.15	2.40	43.60	2.11
		Winter	S_d	0.29	0.91	0.33	0.89	10.01	1.55
			-	0.29	0.91	0.33	0.89	10.01	1.55
Static	vm60	Autumn	S_d	0.53	1.84	0.64	1.62	21.95	2.96
			-	0.53	1.84	0.64	1.62	21.95	2.96
		Spring	S_d	0.42	2.04	0.49	1.93	24.73	-1.92
			-	0.42	2.05	0.48	1.93	24.78	-1.86
		Summer	S_d	0.09	2.49	0.10	2.48	33.76	-7.72
			-	0.03	2.56	0.03	2.56	35.34	-6.14
		Winter	S_d	0.31	0.90	0.34	0.88	11.52	3.07
			-	0.31	0.90	0.34	0.88	11.52	3.07
	vmCCI	Autumn	S_d	0.60	1.69	0.67	1.54	22.85	3.87
			-	0.60	1.69	0.67	1.54	22.85	3.87
		Spring	S_d	0.46	1.98	0.50	1.90	23.09	-3.56
			-	0.45	1.98	0.49	1.91	23.15	-3.50
		Summer	S_d	0.15	2.39	0.17	2.38	38.52	-2.97
			-	0.11	2.45	0.12	2.45	40.29	-1.19
		Winter	S_d	0.28	0.92	0.32	0.89	10.96	2.51
			-	0.28	0.92	0.32	0.89	10.96	2.51
	vmDy	Autumn	S_d	0.63	1.64	0.68	1.53	20.14	1.15
			-	0.63	1.64	0.68	1.53	20.14	1.15
		Spring	S_d	0.47	1.96	0.51	1.89	27.84	1.19
			-	0.47	1.96	0.50	1.89	27.90	1.25
		Summer	S_d	0.11	2.46	0.11	2.46	37.91	-3.58
			-	0.04	2.55	0.04	2.56	39.73	-1.76
		Winter	S_d	0.37	0.85	0.39	0.84	9.87	1.42
			-	0.37	0.85	0.39	0.84	9.87	1.42
	vmGPP	Autumn	S_d	0.62	1.66	0.68	1.53	22.71	3.73
			-	0.62	1.66	0.68	1.53	22.71	3.73
		Spring	S_d	0.44	2.00	0.48	1.93	22.95	-3.69
			-	0.44	2.01	0.48	1.94	23.01	-3.64
		Summer	S_d	0.17	2.38	0.18	2.36	39.51	-1.97
			-	0.14	2.42	0.14	2.42	41.31	-0.18
		Winter	S_d	0.29	0.91	0.32	0.89	10.87	2.41
			-	0.29	0.91	0.32	0.89	10.87	2.41

E.2 Additional VI figures

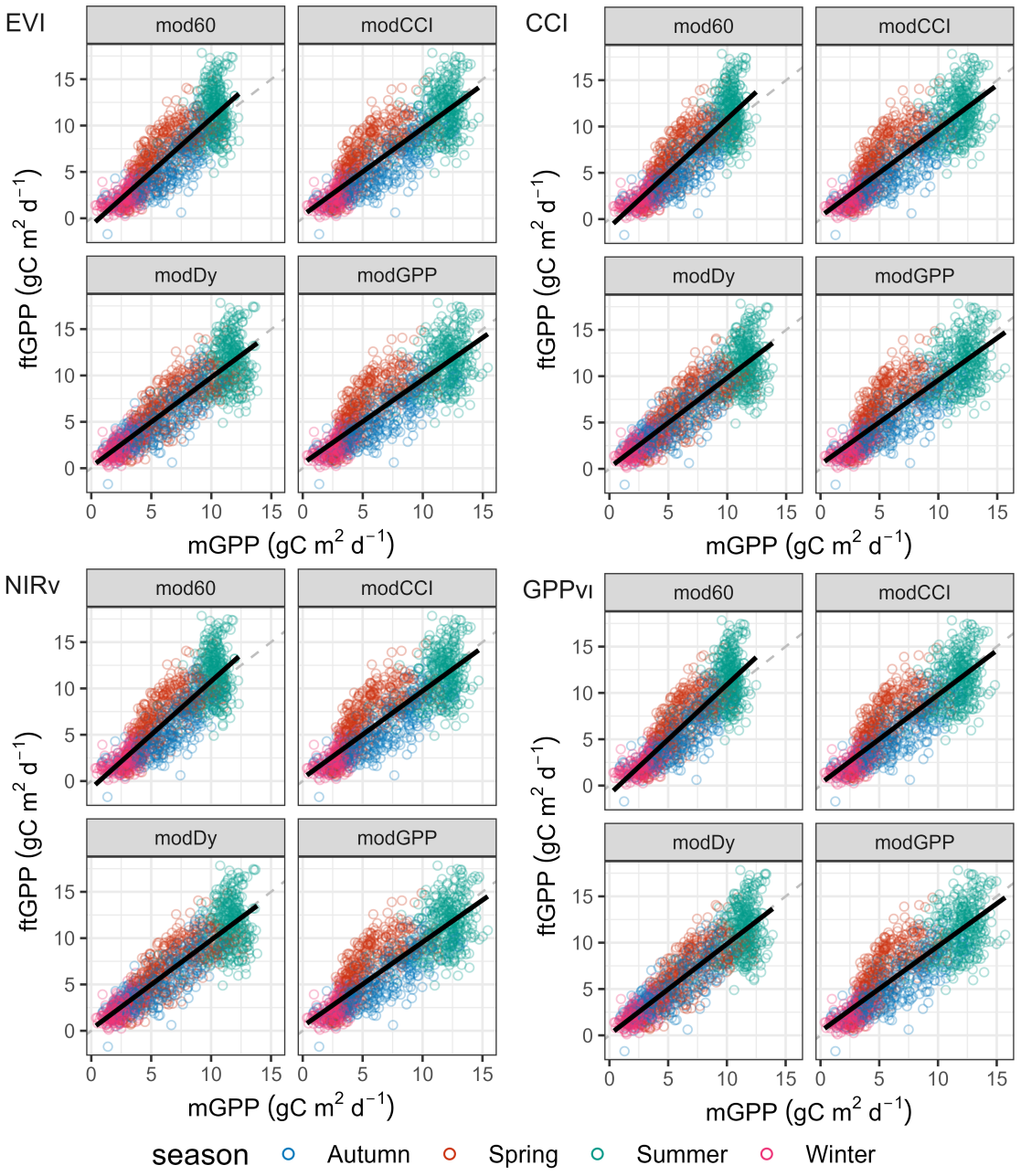

Figure E.1: Relationship between mGPP and ftGPP (gC m^2 d^{-1}) for four Vegetation Indcies (VI) (EVI, CCI, NIRv, GPP_{VI}, for NDVI results see Figure 6.9). The black solid line is the regression line between the two variables. For full VI names, formula and references see Table 2.2 (p.58).

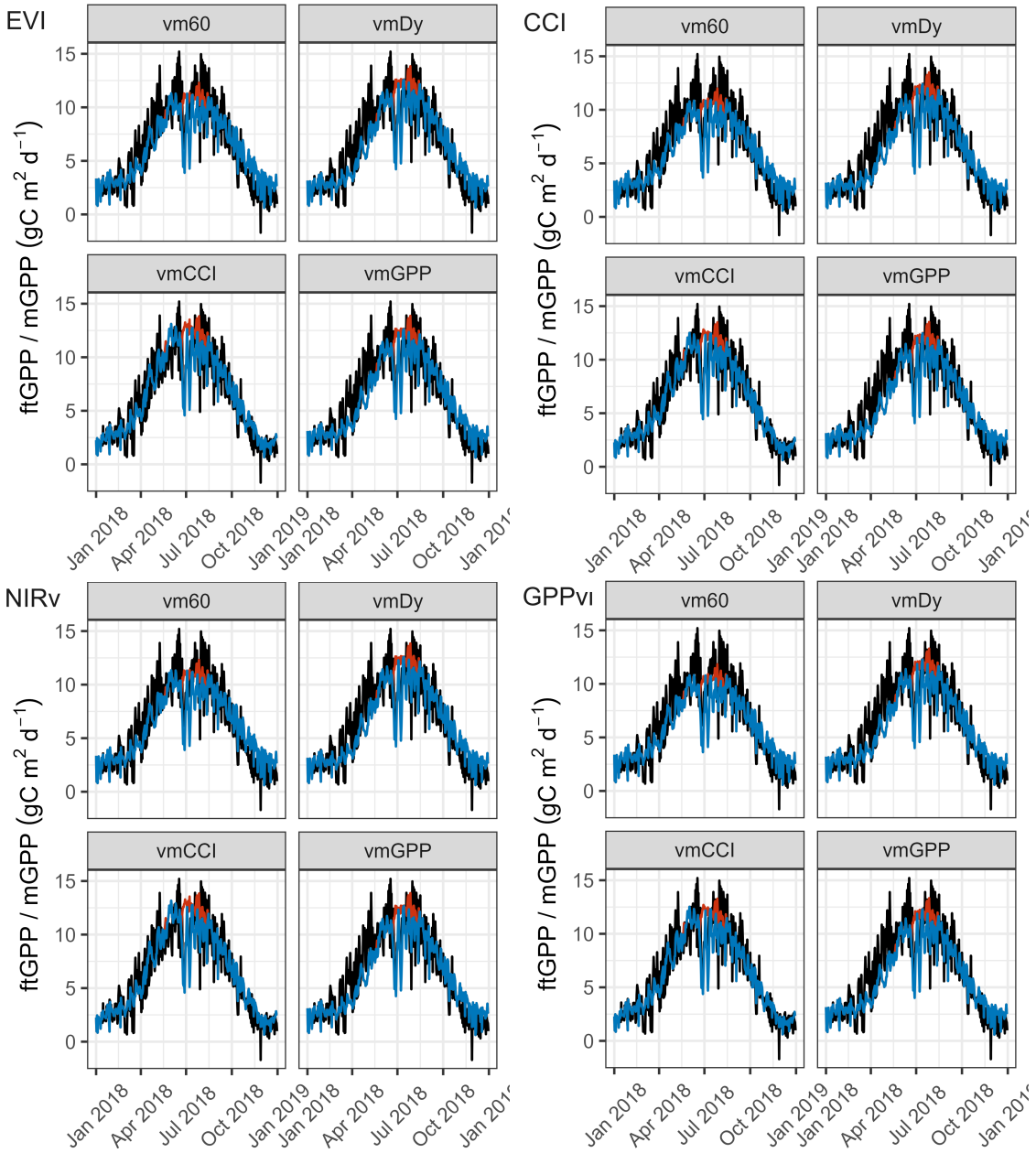

Figure E.2: Time series of flux tower Gross Primary Productivity (ftGPP, gC $m^2\,d^{-1}$) and the SiBx modelled Gross Primary Productivity (mGPP, gC $m^2\,d^{-1}$) across 2018. The black line is ftGPP. Red and blue lines are mGPP from SiBx model runs using Vegetation Indices (VI) (EVI, CCI, NIRv GPP_{VI}, for NDVI results see 6.11) separated by choice of Vcmax. Red line is the original model formulation while the blue line includes a drought stress term (S_d) based on vapour pressure deficit (VPD). For full VI names, formula and references see Table 2.2 (p.58).

References

AghaKouchak, A., Farahmand, A., Melton, F. S., Teixeira, J., Anderson, M. C., Wardlow, B. D., & Hain, C. R. (2015). Remote sensing of drought: Progress, challenges and opportunities. *Reviews of Geophysics*, *53*(2), 452–480.

Ahl, D. E., Gower, S. T., Burrows, S. N., Shabanov, N. V., Myneni, R. B., & Knyazikhin, Y. (2006). Monitoring spring canopy phenology of a deciduous broadleaf forest using MODIS. *Remote Sensing of Environment*, *104*(1), 88–95.

Alduchov, O. A., & Eskridge, R. E. (1996). Improved Magnus Form Approximation of Saturation Vapor Pressure. *Journal of Applied Meteorology*, *35*(4), 601–609.

Allen, C. D., Macalady, A. K., Chenchouni, H., Bachelet, D., McDowell, N., Vennetier, M., Kitzberger, T., Rigling, A., Breshears, D. D., Hogg, E. H., Gonzalez, P., Fensham, R., Zhang, Z., Castro, J., Demidova, N., Lim, J. H., Allard, G., Running, S. W., Semerci, A., & Cobb, N. (2010). A global overview of drought and heat-induced tree mortality reveals emerging climate change risks for forests. *Forest Ecology and Management*, *259*(4), 660–684.

Altemus Cullen, K. (2023). A review of applications of remote sensing for drought studies in the Andes region. *Journal of Hydrology: Regional Studies*, *49*, 101483.

Alton, P. B., & Bodin, P. (2010). A comparative study of a multilayer and a productivity (light-use) efficiency land-surface model over different temporal scales. *Agricultural and Forest Meteorology*, *150*(2), 182–195.

Alton, P. B., Ellis, R., Los, S. O., & North, P. R. (2007). Improved global simulations of gross primary product based on a separate and explicit treatment of diffuse and direct sunlight. *Journal of Geophysical Research: Atmospheres*, *112*(D7), 1–12.

Alton, P. B., North, P. R., & Los, S. O. (2007). The impact of diffuse sunlight on canopy light-use efficiency, gross photosynthetic product and net ecosystem exchange in three forest biomes. *Global Change Biology*, *13*(4), 776–787.

Alton, P. B. (2016). Agricultural and Forest Meteorology The sensitivity of models of gross primary productivity to meteorological and leaf area forcing : A comparison between a Penman – Monteith ecophysiological approach and the MODIS Light-Use Efficiency algorithm. *Agricultural and Forest Meteorology*, *218-219*, 11–24.

Alton, P. B. (2017). Retrieval of seasonal Rubisco-limited photosynthetic capacity at global FLUXNET sites from hyperspectral satellite remote sensing: Impact on carbon modelling. *Agricultural and Forest Meteorology*, *232*, 74–88.

Anderegg, W. R. L., Kane, J. M., & Anderegg, L. D. L. (2013). Consequences of widespread tree mortality triggered by drought and temperature stress. *Nature Climate Change*, *3*(1), 30–36.

Anderegg, W. R., Anderegg, L. D., Kerr, K. L., & Trugman, A. T. (2019). Widespread drought-induced tree mortality at dry range edges indicates that climate stress exceeds species' compensating mechanisms. *Global Change Biology*, *25*(11), 3793–3802.

Anderegg, W. R., Berry, J. A., Smith, D. D., Sperry, J. S., Anderegg, L. D., & Field, C. B. (2012). The roles of hydraulic and carbon stress in a widespread climate-induced forest die-off. *Proceedings of the National Academy of Sciences of the United States of America*, *109*(1), 233–237.

Anderegg, W. R., Klein, T., Bartlett, M., Sack, L., Pellegrini, A. F., Choat, B., & Jansen, S. (2016). Meta-analysis reveals that hydraulic traits explain cross-species patterns of drought-induced tree mortality across the globe. *Proceedings of the National Academy of Sciences of the United States of America*, *113*(18), 5024–5029.

Andrews, S. F., Flanagan, L. B., Sharp, E. J., & Cai, T. (2012). Variation in water potential, hydraulic characteristics and water source use in montane Douglas-fir and lodgepole pine trees in southwestern Alberta and consequences for seasonal changes in photosynthetic capacity. *Tree Physiology*, *32*(2), 146–160.

Anjum, S. A., Xie, X.-Y., Wang, L.-C., Saleem, M. F., Man, C., & Lei, W. (2011). Morphological, physiological and biochemical responses of plants to drought stress. *African Journal of Agricultural Research*, *6*(9), 2026–2032.

Anyamba, A., & Tucker, C. J. (2012). Historical perspectives on AVHRR NDVI and vegetation drought monitoring. In *Remote sensing of drought: Innovative monitoring approaches* (pp. 23–49). NASA Publications.

Aranda, I., Alía, R., Ortega, U., Dantas, Â. K., & Majada, J. (2010). Intra-specific variability in biomass partitioning and carbon isotopic discrimination under moderate drought stress in seedlings from four Pinus pinaster populations. *Tree Genetics and Genomes*, *6*(2), 169–178.

Armitage, R. P., Alberto Ramirez, F., Mark Danson, F., & Ogunbadewa, E. Y. (2013). Probability of cloud-free observation conditions across great britain estimated using MODIS cloud mask. *Remote Sensing Letters*, *4*(5), 427–435.

Ashraf, M., & Foolad, M. R. (2007). Roles of glycine betaine and proline in improving plant abiotic stress resistance. *Environmental and Experimental Botany*, *59*(2), 206–216.

Atkinson, P. M., Jeganathan, C., Dash, J., & Atzberger, C. (2012). Inter-comparison of four models for smoothing satellite sensor time-series data to estimate vegetation phenology. *Remote Sensing of Environment*, *123*, 400–417.

Aussenac, G. (2000). Interactions between forest stands and microclimate: Ecophysiological aspects and consequences for silviculture. *Annals of Forest Science*, *57*(3), 287–301.

Aznar-Sánchez, J., Belmonte-Ureña, L., López-Serrano, M., & Velasco-Muñoz, J. (2018). Forest Ecosystem Services: An Analysis of Worldwide Research. *Forests*, *9*(8), 453.

Badgley, G., Anderegg, L. D. L., Berry, J. A., & Field, C. B. (2019). Terrestrial gross primary production: Using NIRv to scale from site to globe. *Global Change Biology*, *25*(11), 3731–3740.

Badgley, G., Field, C. B., & Berry, J. A. (2017). Canopy near-infrared reflectance and terrestrial photosynthesis. *Science Advances*, *3*(3), 1–6.

Baker, I. T., Prihodko, L., Denning, A. S., Goulden, M., Miller, S., & da Rocha, H. R. (2008). Seasonal drought stress in the Amazon: Reconciling models and observations. *Journal of Geophysical Research: Biogeosciences*, *113*(G1), 1–10.

Baker, I., Denning, A. S., Hanan, N., Prihodko, L., Uliasz, M., Vidale, P. L., Davis, K., & Bakwin, P. (2003). Simulated and observed fluxes of sensible and latent heat and CO2 at the WLEF-TV tower using SiB2.5. *Global Change Biology*, *9*(9), 1262–1277.

Baker, N. R., & Rosenqvist, E. (2004). Applications of chlorophyll fluorescence can improve crop production strategies: An examination of future possibilities. *Journal of Experimental Botany*, *55*(403), 1607–1621.

Baldi, P., & La Porta, N. (2022). Toward the Genetic Improvement of Drought Tolerance in Conifers: An Integrated Approach. *Forests*, *13*(12), 1–21.

Baldocchi, D. D. (2003). Assessing the eddy covariance technique for evaluating carbon dioxide exchange rates of ecosystems: past, present and future. *Global Change Biology*, *9*(4), 479–492.

Baldocchi, D. D., Falge, E., Gu, L., Olson, R., Hollinger, D., Running, S., Anthoni, P., Bernhofer, C., Davis, K., Evans, R., Fuentes, J., Goldstein, A., Katul, G., Law, B., Lee, X., Malhi, Y., Meyers, T., Munger, W., Oechel, W., ... Wofsy,

S. (2001). FLUXNET: A New Tool to Study the Temporal and Spatial Variability of Ecosystem–Scale Carbon Dioxide, Water Vapor, and Energy Flux Densities. *Bulletin of the American Meteorological Society*, *82*(11), 2415–2434.

Baldocchi, D. D., Ryu, Y., Dechant, B., Eichelmann, E., Hemes, K., Ma, S., Sanchez, C. R., Shortt, R., Szutu, D., Valach, A., Verfaillie, J., Badgley, G., Zeng, Y., & Berry, J. A. (2020). Outgoing Near-Infrared Radiation From Vegetation Scales With Canopy Photosynthesis Across a Spectrum of Function, Structure, Physiological Capacity, and Weather. *Journal of Geophysical Research: Biogeosciences*, *125*(7), 1–17.

Balekoglu, S., Caliskan, S., Dirik, H., & Rosner, S. (2023). Response to drought stress differs among Pinus pinea provenances. *Forest Ecology and Management*, *531*, 120779.

Ball, M., Cowan, I., & Farquhar, G. (1988). Maintenance of Leaf Temperature and the Optimisation of Carbon Gain in Relation to Water Loss in a Tropical Mangrove Forest. *Functional Plant Biology*, *15*(2), 263.

Barakat, M., El-Hendawy, S., Al-Suhaibani, N., Elshafei, A., Al-Doss, A., Al-Ashkar, I., Ahmed, E., & Al-Gaadi, K. (2016). The genetic basis of spectral reflectance indices in drought-stressed wheat. *Acta Physiologiae Plantarum*, *38*(9), 227.

Barnes, M. L., Breshears, D. D., Law, D. J., Leeuwen, W. J. D. V., Monson, R. K., Fojtik, A. C., Barron-gafford, G. A., & Moore, D. J. P. (2017). Beyond greenness : Detecting temporal changes in photosynthetic capacity with hyperspectral reflectance data. *PLoS ONE*, *12*(12), 1–17.

Barton, C. V., & North, P. R. (2001). Remote sensing of canopy light use efficiency using the photochemical reflectance index model and sensitivity analysis. *Remote Sensing of Environment*, *78*(3), 264–273.

Bates, D., Mächler, M., Bolker, B., & Walker, S. (2015). Fitting Linear Mixed-Effects Models Using lme4. *Journal of Statistical Software*, *67*(1).

Bauman, D., Fortunel, C., Delhaye, G., Malhi, Y., Cernusak, L. A., Bentley, L. P., Rifai, S. W., Aguirre-Gutiérrez, J., Menor, I. O., Phillips, O. L., McNellis, B. E., Bradford, M., Laurance, S. G. W., Hutchinson, M. F., Dempsey, R., Santos-Andrade, P. E., Ninantay-Rivera, H. R., Chambi Paucar, J. R., & McMahon, S. M. (2022). Tropical tree mortality has increased with rising atmospheric water stress. *Nature*, *608*(7923), 528–533.

Bayle, A., Carlson, B., Thierion, V., Isenmann, M., & Choler, P. (2019). Improved Mapping of Mountain Shrublands Using the Sentinel-2 Red-Edge Band. *Remote Sensing*, *11*(23), 2807.

Beer, C., Reichstein, M., Tomelleri, E., Ciais, P., Jung, M., Carvalhais, N., Rödenbeck, C., Arain, M. A., Baldocchi, D., Bonan, G. B., Bondeau, A., Cescatti,

A., Lasslop, G., Lindroth, A., Lomas, M., Luyssaert, S., Margolis, H., Oleson, K. W., Roupsard, O., & Papale, D. (2010). Terrestrial Gross Carbon Dioxide Uptake: Global Distribution and Covariation with Climate. *Science*, *329*(5993), 834–838.

Belda, S., Pipia, L., Morcillo-Pallarés, P., Rivera-Caicedo, J. P., Amin, E., De Grave, C., & Verrelst, J. (2020). DATimeS: A machine learning time series GUI toolbox for gap-filling and vegetation phenology trends detection. *Environmental Modelling & Software*, *127*, 104666.

Bennett, A. C., McDowell, N. G., Allen, C. D., & Anderson-Teixeira, K. J. (2015). Larger trees suffer most during drought in forests worldwide. *Nature Plants*, *1*(10), 15139.

Berard, G. M., Cloutis, E. A., & Mann, P. (2017). Leaf reflectance and transmission properties (350-2500 nm): Implications for vegetation indices. *Journal of Near Infrared Spectroscopy*, *25*(2), 138–144.

Berry, P., & Brown, I. (2021). Natural environment and assets. *The Third UK Climate Change Risk Assessment Technical Report*.

Betts, R. A., & Brown, K. (2021). The Third UK Climate Change Risk Assessment (CCRA3) Technical Reportduction. *UK Climate Risk*.

Bi, W., He, W., Zhou, Y., Ju, W., Liu, Y., Liu, Y., Zhang, X., Wei, X., & Cheng, N. (2022). A global 0.05° dataset for gross primary production of sunlit and shaded vegetation canopies from 1992 to 2020. *Scientific Data*, *9*(1), 213.

Bigras, F. J. (2005). Photosynthetic response of white spruce families to drought stress. *New Forests*, *29*(2), 135–148.

Biswal, B., Joshi, P. N., Raval, M. K., & Biswal, U. C. (2011). Photosynthesis, a global sensor of environmental stress in green plants: Stress signalling and adaptation. *Current Science*, *101*(1), 47–56.

Black, K., Philk, D., Mc Grath, J., Doherty, P., & Bruce, O. (2005). Interactive effects of irradiance and water availability on the photosynthetic performance of Picea sitchensis seedlings: implications for seedling establishment under different management practices. *Annals of Forest Science*, *64*, 219–228.

Blackburn, G. A. (1998). Spectral indices for estimating photosynthetic pigment concentrations: A test using senescent tree leaves. *International Journal of Remote Sensing*, *19*(4), 657–675.

Blackburn, G. A. (2007). Hyperspectral remote sensing of plant pigments. *Journal of Experimental Botany*, *58*(4), 855–867.

Blum, A. (2017). Osmotic adjustment is a prime drought stress adaptive engine in support of plant production. *Plant, Cell & Environment*, *40*(1), 4–10.

Bonan, G. B. (2008). Forests and Climate Change: Forcings, Feedbacks, and the Climate Benefits of Forests. *Science*, *320*(5882), 1444–1449.

Bonan, G. B., Patton, E. G., Finnigan, J. J., Baldocchi, D. D., & Harman, I. N. (2021). Moving beyond the incorrect but useful paradigm: reevaluating big-leaf and multilayer plant canopies to model biosphere-atmosphere fluxes – a review. *Agricultural and Forest Meteorology*, *306*, 108435.

Bounoua, L., Collatz, G. J., Los, S. O., Sellers, P. J., Dazlich, D. A., Tucker, C. J., & Randall, D. A. (2000). Sensitivity of Climate to Changes in NDVI. *Journal of Climate*, *13*(13), 2277–2292.

Box, G. (1979). Robustness in the Strategy of Scientific Model Building. In *Robustness in statistics* (pp. 201–236). Elsevier.

Brodersen, C. R., & Vogelmann, T. C. (2010). Do changes in light direction affect absorption profiles in leaves? *Functional Plant Biology*, *37*(5), 403–412.

Brown, J. F., Wardlow, B. D., Tadesse, T., Hayes, M. J., & Reed, B. C. (2008). The Vegetation Drought Response Index (VegDRI): A new integrated approach for monitoring drought stress in vegetation. *GIScience and Remote Sensing*, *45*(1), 16–46.

Burke, E. J., Perry, R. H., & Brown, S. J. (2010). An extreme value analysis of UK drought and projections of change in the future. *Journal of Hydrology*, *388*(1-2), 131–143.

Cai, W., Ullah, S., Yan, L., & Lin, Y. (2021). Remote sensing of ecosystem water use efficiency: A review of direct and indirect estimation methods. *Remote Sensing*, *13*(12), 1–20.

Cai, W., & Prentice, I. C. (2020). Recent trends in gross primary production and their drivers: analysis and modelling at flux-site and global scales. *Environmental Research Letters*, *15*(12), 124050.

Cameron, A. D. (2015). Building resilience into sitka spruce (Picea sitchensis (Bong.) Carr.) forests in Scotland in response to the threat of climate change. *Forests*, *6*(2), 398–415.

Canadell, J. G., Mooney, H. A., Baldocchi, D. D., Berry, J. A., Ehleringer, J. R., Field, C. B., Gower, S. T., Hollinger, D. Y., Hunt, J. E., Jackson, R. B., Running, S. W., Shaver, G. R., Steffen, W., Trumbore, S. E., Valentini, R., & Bond, B. Y. (2000). Carbon metabolism of the terrestrial biosphere: A multitechnique approach for improved understanding. *Ecosystems*, *3*(2), 115–130.

Cavender-Bares, J., & Bazzaz, F. A. (2000). Changes in drought response strategies with ontogeny in quercus rubra: Implications for scaling from seedlings to mature trees. *Oecologia*, *124*(1), 8–18.

Ceccato, P., Flasse, S., & Grégoire, J. M. (2002). Designing a spectral index to estimate vegetation water content from remote sensing data: Part 1: Theoretical approach. *Remote Sensing of Environment*, *82*(2-3), 188–197.

Čepl, J., Holá, D., Stejskal, J., Korecký, J., Kočová, M., Lhotáková, Z., Tomášková, I., Palovská, M., Rothová, O., Whetten, R. W., Kaňák, J., Albrechtová, J., & Lstibůrek, M. (2016). Genetic variability and heritability of chlorophyll a fluorescence parameters in Scots pine (Pinus sylvestris L.) (J.-P. Schnitzler, Ed.). *Tree Physiology*, *36*(7), 883–895.

Čepl, J., Stejskal, J., Lhotáková, Z., Holá, D., Korecký, J., Lstibůrek, M., Tomášková, I., Kočová, M., Rothová, O., Palovská, M., Hejtmánek, J., Krejzková, A., Gezan, S., Whetten, R., & Albrechtová, J. (2018). Heritable variation in needle spectral reflectance of Scots pine (Pinus sylvestris L.) peaks in red edge. *Remote Sensing of Environment*, *219*(September), 89–98.

Chalker-Scott, L. (1999). Environmental significance of anthocyanins in plant stress responses. *Photochemistry and Photobiology*, *70*(1), 1–9.

Chaves, M. M., Maroco B, J. P., & Pereira, J. S. (2003). Understanding plant responses to drought-from genes to the whole plant. *Functional Plant Biology*, *30*, 239–264.

Cheeseman, J. M. (2007). Hydrogen Peroxide and Plant Stress: A Challenging Relationship. *Plant Stress*, *1*(1), 4–15.

Chen, B., Black, T. A., Coops, N. C., Hilker, T., Trofymow, J. A., & Morgenstern, K. (2009). Assessing tower flux footprint climatology and scaling between remotely sensed and eddy covariance measurements. *Boundary-Layer Meteorology*, *130*(2), 137–167.

Chen, D., Huang, J., & Jackson, T. J. (2005). Vegetation water content estimation for corn and soybeans using spectral indices derived from MODIS near- and short-wave infrared bands. *Remote Sensing of Environment*, *98*(2-3), 225–236.

Chen, H., Zhu, G., Zhang, K., Bi, J., Jia, X., Ding, B., Zhang, Y., Shang, S., Zhao, N., & Qin, W. (2020). Evaluation of evapotranspiration models using different LAI and meteorological forcing data from 1982 to 2017. *Remote Sensing*, *12*(15), 1–20.

Chen, X., & Vierling, L. (2007). International Journal of Remote Monitoring boreal forest leaf area index across a Siberian burn chronosequence : a MODIS validation study. (October 2014), 37–41.

Chin, A. R., & Sillett, S. C. (2017). Leaf acclimation to light availability supports rapid growth in tall Picea sitchensis trees. *Tree Physiology*, *37*(10), 1352–1366.

Choat, B., Brodribb, T. J., Brodersen, C. R., Duursma, R. A., López, R., & Medlyn, B. E. (2018). Triggers of tree mortality under drought. *Nature*, *558*(7711), 531–539.

Chou, S., Chen, B., Chen, J., Wang, M., Wang, S., Croft, H., & Shi, Q. (2020). Estimation of leaf photosynthetic capacity from the photochemical reflectance index and leaf pigments. *Ecological Indicators*, *110*, 105867.

Chou, S., Chen, J. M., Yu, H., Chen, B., Zhang, X., Croft, H., Khalid, S., Li, M., & Shi, Q. (2017). Canopy-level photochemical reflectance index from hyperspectral remote sensing and leaf-level non-photochemical quenching as early indicators of water stress in maize. *Remote Sensing*, *9*(8), 1–17.

Chuine, I., Kramer, K., & Hänninen, H. (2003). Plant Development Models. In Schwartz (Ed.), *Phenology: An integrative environmental science* (pp. 217–235). Kluwer Academic Publishers.

Ciais, P., Reichstein, M., Viovy, N., Granier, A., Ogée, J., Allard, V., Aubinet, M., Buchmann, N., Bernhofer, C., Carrara, A., Chevallier, F., De Noblet, N., Friend, A. D., Friedlingstein, P., Grünwald, T., Heinesch, B., Keronen, P., Knohl, A., Krinner, G., & Valentini, R. (2005). Europe-wide reduction in primary productivity caused by the heat and drought in 2003. *Nature*, *437*(7058), 529–533.

Cifre, J., Bota, J., Escalona, J., Medrano, H., & Flexas, J. (2005). Physiological tools for irrigation scheduling in grapevine (Vitis vinifera L.) *Agriculture, Ecosystems & Environment*, *106*(2-3), 159–170.

Cirillo, V., D'Amelia, V., Esposito, M., Amitrano, C., Carillo, P., Carputo, D., & Maggio, A. (2021). Anthocyanins are key regulators of drought stress tolerance in tobacco. *Biology*, *10*(2), 1–15.

Clark, J. S., Iverson, L., Woodall, C. W., Allen, C. D., Bell, D. M., Bragg, D. C., D'Amato, A. W., Davis, F. W., Hersh, M. H., Ibanez, I., Jackson, S. T., Matthews, S., Pederson, N., Peters, M., Schwartz, M. W., Waring, K. M., & Zimmermann, N. E. (2016, July). The impacts of increasing drought on forest dynamics, structure, and biodiversity in the United States.

Clement, R. J., Burba, G. G., Grelle, A., Anderson, D. J., & Moncrieff, J. B. (2009). Improved trace gas flux estimation through IRGA sampling optimization. *Agricultural and Forest Meteorology*, *149*(3-4), 623–638.

Clevers, J. G., & Gitelson, A. A. (2013). Remote estimation of crop and grass chlorophyll and nitrogen content using red-edge bands on sentinel-2 and-3. *International Journal of Applied Earth Observation and Geoinformation*, *23*(1), 344–351.

Close, D. C., & Beadle, C. L. (2003). The Ecophysiology of Foliar Anthocyanin. *Botanical Review*, *69*(2), 149–161.

Collatz, G. J., Ball, J. T., Grivet, C., & Berry, J. A. (1991). Physiological and environmental regulation of stomatal conductance, photosynthesis and tran-

spiration: a model that includes a laminar boundary layer. *Agricultural and Forest Meteorology*, *54*(2-4), 107–136.

Coops, N. C., Hilker, T., Hall, F. G., Nichol, C. J., & Drolet, G. G. (2010). Estimation of light-use efficiency of terrestrial ecosystems from space: A status report. *BioScience*, *60*(10), 788–797.

Cowen, I., & Farquhar, G. D. (1977). Stomatal function in relation to leaf metabolism and environment: Stomatal function in the regulation of gas exchange. *Symposia of the Society for Experimental Biology*, *31*, 471–505.

Croft, H., & Chen, J. (2018). Leaf Pigment Content. In *Comprehensive remote sensing* (pp. 117–142, Vol. 1-9). Elsevier.

Dalal, V. K., & Tripathy, B. C. (2018). Water-stress induced downsizing of light-harvesting antenna complex protects developing rice seedlings from photo-oxidative damage. *Scientific Reports*, *8*(1), 1–16.

Dao, P. D., He, Y., & Proctor, C. (2021). Plant drought impact detection using ultra-high spatial resolution hyperspectral images and machine learning. *International Journal of Applied Earth Observation and Geoinformation*, *102*, 102364.

Davies, S., Bathgate, S., Petr, M., Gale, A., Patenaude, G., & Perks, M. (2020). Drought risk to timber production – A risk versus return comparison of commercial conifer species in Scotland. *Forest Policy and Economics*, *117*, 102189.

de Miguel, M., Cabezas, J. A., de María, N., Sánchez-Gómez, D., Guevara, M. Á., Vélez, M. D., Sáez-Laguna, E., Díaz, L. M., Mancha, J. A., Barbero, M. C., Collada, C., Díaz-Sala, C., Aranda, I., & Cervera, M. T. (2014). Genetic control of functional traits related to photosynthesis and water use efficiency in Pinus pinaster Ait. drought response: Integration of genome annotation, allele association and QTL detection for candidate gene identification. *BMC Genomics*, *15*(1), 1–19.

De Pue, J., Wieneke, S., Bastos, A., Barrios, J. M., Liu, L., Ciais, P., Arboleda, A., Hamdi, R., Maleki, M., Maignan, F., Gellens-Meulenberghs, F., Janssens, I., & Balzarolo, M. (2023). Temporal variability of observed and simulated gross primary productivity, modulated by vegetation state and hydrometeorological drivers. *Biogeosciences*, *20*(23), 4795–4818.

De Tomás Marín, S., Novák, M., Klančnik, K., & Gaberščik, A. (2016). Spectral signatures of conifer needles mainly depend on their physical traits. *Polish Journal of Ecology*, *64*(1), 1–13.

Dechant, B., Cuntz, M., Vohland, M., Schulz, E., & Doktor, D. (2017). Remote Sensing of Environment Estimation of photosynthesis traits from leaf re fl

ectance spectra : Correlation to nitrogen content as the dominant mechanism. *Remote Sensing of Environment*, *196*, 279–292.

Dechant, B., Ryu, Y., Badgley, G., Zeng, Y., Berry, J. A., Zhang, Y., Goulas, Y., Li, Z., Zhang, Q., Kang, M., Li, J., & Moya, I. (2020). Canopy structure explains the relationship between photosynthesis and sun-induced chlorophyll fluorescence in crops. *Remote Sensing of Environment*, *241*(February).

Demarez, V., Gastellu-Etchegorry, V., Mougin, E., Marty, G., Proisy, C., Dufrêne, E., & Ledantec, V. (1999). Seasonal variation of leaf chlorophyll content of a temperate forest. Inversion of the prospect model. *International Journal of Remote Sensing*, *20*(5), 879–894.

Demmig-Adams, B. (1998). Survey of thermal energy dissipation and pigment composition in sun and shade leaves. *Plant and Cell Physiology*, *39*(5), 474–482.

Demmig-Adams, B., & Adams, W. W. (1996). Chlorophyll and carotenoid composition in leaves of Euonymus kiautschovicus acclimated to different degrees of light stress in the field. *Australian Journal of Plant Physiology*, *23*(5), 649–659.

Deng, X., Zhang, Z., Hu, X., Li, J., Li, S., Su, C., Du, S., & Shi, L. (2024). Estimation of photosynthetic parameters from hyperspectral images using optimal deep learning architecture. *Computers and Electronics in Agriculture*, *216*, 108540.

Dengel, S., Grace, J., Aakala, T., Hari, P., Newberry, S. L., & Mizunuma, T. (2013). Spectral characteristics of pine needles at the limit of tree growth in subarctic Finland. *Plant Ecology and Diversity*, *6*(1), 31–44.

Didan, K., Munoz, A. B., Solano, R., & Huete, A. (2015). MODIS Vegetation Index User's Guide (MOD13 Series) Version 3.0 Ccollection 6).

Dillen, S. Y., Op, M., Beeck, D., Hufkens, K., Buonanduci, M., & Phillips, N. G. (2012). Agricultural and Forest Meteorology Seasonal patterns of foliar reflectance in relation to photosynthetic capacity and color index in two co-occurring tree species , Quercus rubra and Betula papyrifera. *Agricultural and Forest Meteorology*, *160*, 60–68.

D'Odorico, P., Gonsamo, A., Gough, C. M., Bohrer, G., Morison, J., Wilkinson, M., Hanson, P. J., Gianelle, D., Fuentes, J. D., & Buchmann, N. (2015). The match and mismatch between photosynthesis and land surface phenology of deciduous forests. *Agricultural and Forest Meteorology*, *214-215*, 25–38.

Donoghue, D. N., & Watt, P. J. (2006). Using LiDAR to compare forest height estimates from IKONOS and Landsat ETM+ data in Sitka spruce plantation forests. *International Journal of Remote Sensing*, *27*(11), 2161–2175.

Donoghue, D. N., Watt, P. J., Cox, N. J., Dunford, R. W., Wilson, J., Stables, S., & Smith, S. (2004). An evaluation of the use of satellite data for monitoring

early development of young Sitka spruce plantation forest growth. *Forestry*, *77*(5), 383–396.

Drolet, G. G., Middleton, E. M., Huemmrich, K. F., Hall, F. G., Amiro, B. D., Barr, A. G., Black, T. A., McCaughey, J. H., & Margolis, H. A. (2008). Regional mapping of gross light-use efficiency using MODIS spectral indices. *Remote Sensing of Environment*, *112*(6), 3064–3078.

Drolet, G. G., Huemmrich, K. F., Hall, F. G., Middleton, E. M., Black, T. A., Barr, A. G., & Margolis, H. A. (2005). A MODIS-derived photochemical reflectance index to detect inter-annual variations in the photosynthetic light-use efficiency of a boreal deciduous forest. *Remote Sensing of Environment*, *98*(2-3), 212–224.

Du, L., Tian, Q., Yu, T., Meng, Q., Jancso, T., Udvardy, P., & Huang, Y. (2013). A comprehensive drought monitoring method integrating MODIS and TRMM data. *International Journal of Applied Earth Observation and Geoinformation*, *23*(1), 245–253.

Eimil-Fraga, C., Sánchez-Rodríguez, F., Álvarez-Rodríguez, E., & Rodríguez-Soalleiro, R. (2015). Relationships between needle traits, needle age and site and stand parameters in Pinus pinaster. *Trees - Structure and Function*, *29*(4), 1103–1113.

El-Hendawy, S. E., Alotaibi, M., Al-Suhaibani, N., Al-Gaadi, K., Hassan, W., Dewir, Y. H., Emam, M. A. E.-G., Elsayed, S., & Schmidhalter, U. (2019). Comparative Performance of Spectral Reflectance Indices and Multivariate Modeling for Assessing Agronomic Parameters in Advanced Spring Wheat Lines Under Two Contrasting Irrigation Regimes. *Frontiers in Plant Science*, *10*, 1–20.

Ensminger, I., Sveshnikov, D., Campbell, D. A., Funk, C., Jansson, S., Lloyd, J., Shibistova, O., & Öquist, G. (2004). Intermittent low temperatures constrain spring recovery of photosynthesis in boreal Scots pine forests. *Global Change Biology*, *10*(6), 995–1008.

Ensminger, I., Yao-Yun Chang, C., & Bräutigam, K. (2015). Tree Responses to Environmental Cues. *Advances in Botanical Research*, *74*, 229–263.

Esteban, R., Becerril, J. M., & García-Plazaola, J. I. (2009). Lutein epoxide cycle, more than just a forest tale. *Plant Signaling and Behavior*, *4*(4), 342–344.

Estiarte, M., & Peñuelas, J. (2015). Alteration of the phenology of leaf senescence and fall in winter deciduous species by climate change: effects on nutrient proficiency. *Global Change Biology*, *21*(3), 1005–1017.

Fang, Y., & Xiong, L. (2015). General mechanisms of drought response and their application in drought resistance improvement in plants. *Cellular and Molecular Life Sciences*, *72*(4), 673–689.

Fang-yuan, Y., & Guy, R. D. (2004). Variable chlorophyll fluorescence in response to water plus heat stress treatments in three coniferous tree seedlings. *Journal of Forestry Research*, *15*(1), 24–28.

Farquhar, G. D., Caemmerer, S. V., & Berry, J. a. (1980). A biochemical model of photosynthesis CO2 fixation in leaves of C3 species. *Planta*, *149*, 78–90.

Feild, T. S., Lee, D. W., & Holbrook, N. M. (2001). Why leaves turn red in autumn. The role of anthocyanins in senescing leaves of red-osier dogwood. *Plant physiology*, *127*(2), 566–74.

Feng, H., Guo, Z., Yang, W., Huang, C., Chen, G., Fang, W., Xiong, X., Zhang, H., Wang, G., Xiong, L., & Liu, Q. (2017). An integrated hyperspectral imaging and genome-wide association analysis platform provides spectral and genetic insights into the natural variation in rice. *Scientific Reports*, *7*(1), 1–10.

Fernández-Martínez, M., Yu, R., Gamon, J., Hmimina, G., Filella, I., Balzarolo, M., Stocker, B., & Peñuelas, J. (2019). Monitoring spatial and temporal variabilities of gross primary production using MAIAC MODIS data. *Remote Sensing*, *11*(7).

Filella, I., Porcar-Castell, A., Munné-Bosch, S., Bäck, J., Garbulsky, M. F., & Peñuelas, J. (2009). PRI assessment of long-term changes in carotenoids/chlorophyll ratio and short-term changes in de-epoxidation state of the xanthophyll cycle. *International Journal of Remote Sensing*, *30*(17), 4443–4455.

Foley, J. A., DeFries, R., Asner, G. P., Barford, C., Bonan, G., Carpenter, S. R., Chapin, F. S., Coe, M. T., Daily, G. C., Gibbs, H. K., Helkowski, J. H., Holloway, T., Howard, E. A., Kucharik, C. J., Monfreda, C., Patz, J. A., Prentice, I. C., Ramankutty, N., & Snyder, P. K. (2005). Global consequences of land use. *Science*, *309*(5734), 570–574.

Foroutan-pour, K., Dutilleul, P., & Smith, D. L. (2001). Inclusion of the Fractal Dimension of Leafless Plant Structure in the Beer-Lambert Law. *Agronomy Journal*, *93*(2), 333–338.

Fu, Z., Stoy, P. C., Luo, Y., Chen, J., Sun, J., Montagnani, L., Wohlfahrt, G., Rahman, A. F., Rambal, S., Bernhofer, C., Wang, J., Shirkey, G., & Niu, S. (2017). Climate controls over the net carbon uptake period and amplitude of net ecosystem production in temperate and boreal ecosystems. *Agricultural and Forest Meteorology*, *243*(May), 9–18.

Gallé, A., & Feller, U. (2007). Changes of photosynthetic traits in beech saplings (Fagus sylvatica) under severe drought stress and during recovery. *Physiologia Plantarum*, *131*(3), 412–421.

Gamon, J. A., Serrano, L., & Surfus, J. S. (1997). The photochemical reflectance index: An optical indicator of photosynthetic radiation use efficiency across species, functional types, and nutrient levels. *Oecologia*, *112*(4), 492–501.

Gamon, J., Peñuelas, J., & Field, C. (1992). A narrow-waveband spectral index that tracks diurnal changes in photosynthetic efficiency. *Remote Sensing of Environment*, *41*(1), 35–44.

Gamon, J. A., & Berry, J. A. (2012). Facultative and constitutive pigment effects on the Photochemical Reflectance Index (PRI) in sun and shade conifer needles. *Israel Journal of Plant Sciences*, *60*(1-2), 85–95.

Gamon, J. A., Huemmrich, K. F., Wong, C. Y., Ensminger, I., Garrity, S., Hollinger, D. Y., Noormets, A., & Peñuelask, J. (2016). A remotely sensed pigment index reveals photosynthetic phenology in evergreen conifers. *Proceedings of the National Academy of Sciences of the United States of America*, *113*(46), 13087–13092.

Gao, B.-C. (1996). NDWI—A normalized difference water index for remote sensing of vegetation liquid water from space. *Remote Sensing of Environment*, *58*(3), 257–266.

Gao, Y., Quevedo, A., Szantoi, Z., & Skutsch, M. (2021). Monitoring forest disturbance using time-series MODIS NDVI in Michoacán, Mexico. *Geocarto International*, *36*(15), 1768–1784.

García-Mora, T. J., Mas, J. F., & Hinkley, E. A. (2012). Land cover mapping applications with MODIS: A literature review. *International Journal of Digital Earth*, *5*(1), 63–87.

García-Plazaola, J. I., Matsubara, S., & Osmond, C. B. (2007). The lutein epoxide cycle in higher plants: its relationships to other xanthophyll cycles and possible functions. *Functional Plant Biology*, *34*(9), 759.

García-Tejero, I., Gutiérrez-Gordillo, S., Ortega-Arévalo, C., Iglesias-Contreras, M., Moreno, J., Souza-Ferreira, L., & Durán-Zuazo, V. (2018). Thermal imaging to monitor the crop-water status in almonds by using the non-water stress baselines. *Scientia Horticulturae*, *238*, 91–97.

Gates, D. M., Keegan, H. J., Schleter, J. C., & Weidner, V. R. (1965). Spectral Properties of Plants. *Applied Optics*, *4*(1), 11.

Gauthier, S., Bernier, P., Kuuluvainen, T., Shvidenko, A. Z., & Schepaschenko, D. G. (2015). Boreal forest health and global change. *Science*, *349*(6250), 819–822.

Gerhards, M., Schlerf, M., Rascher, U., Udelhoven, T., Juszczak, R., Alberti, G., Miglietta, F., & Inoue, Y. (2018). Analysis of Airborne Optical and Thermal Imagery for Detection of Water Stress Symptoms. *Remote Sensing*, *10*(7), 1139.

Geßler, A., Keitel, C., Kreuzwieser, J., Matyssek, R., Seiler, W., & Rennenberg, H. (2006). Potential risks for European beech (Fagus sylvatica L.) in a changing climate. *Trees*, *21*(1), 1–11.

Gilabert, M., Sánchez-Ruiz, S., & Moreno, Á. (2017). Annual Gross Primary Production from Vegetation Indices: A Theoretically Sound Approach. *Remote Sensing*, *9*(3), 193.

Gitelson, A. A. (2020). Towards a generic approach to remote non-invasive estimation of foliar carotenoid-to-chlorophyll ratio. *Journal of Plant Physiology*, *252*, 153227.

Gitelson, A. A., & Merzlyak, M. N. (1994). Spectral Reflectance Changes Associated with Autumn Senescence of Aesculus hippocastanum L. and Acer platanoides L. Leaves. Spectral Features and Relation to Chlorophyll Estimation. *Journal of Plant Physiology*, *143*(3), 286–292.

Gitelson, A. A., Merzlyak, M. N., & Chivkunova, O. B. (2001). Optical Properties and Nondestructive Estimation of Anthocyanin Content in Plant Leaves. *Photochemistry and Photobiology*, *74*(1), 38.

Gitelson, A. A., Viña, A., Ciganda, V., Rundquist, D. C., & Arkebauer, T. J. (2005). Remote estimation of canopy chlorophyll content in crops. *Geophysical Research Letters*, *32*(8), 1–4.

Gitelson, A. A., Zur, Y., Chivkunova, O. B., & Merzlyak, M. N. (2002). Assessing Carotenoid Content in Plant Leaves with Reflectance Spectroscopy. *Photochemistry and Photobiology*, *75*(3), 272.

Goerner, A., Reichstein, M., Tomelleri, E., Hanan, N., Rambal, S., Papale, D., Dragoni, D., & Schmullius, C. (2011). Remote sensing of ecosystem light use efficiency with MODIS-based PRI. *Biogeosciences*, *8*(1), 189–202.

Gomes, M. d. M. d. A., Lagôa, A. M. M. A., Medina, C. L., Machado, E. C., & Machado, M. A. (2004). Interactions between leaf water potential, stomatal conductance and abscisic acid content of orange trees submitted to drought stress. *Brazilian Journal of Plant Physiology*, *16*(3), 155–161.

Gonsamo, A., Chen, J. M., & D'Odorico, P. (2013). Deriving land surface phenology indicators from CO2 eddy covariance measurements. *Ecological Indicators*, *29*, 203–207.

Gonzalez-Dugo, V., Zarco-Tejada, P., Berni, J. A., Suárez, L., Goldhamer, D., & Fereres, E. (2012). Almond tree canopy temperature reveals intra-crown variability that is water stress-dependent. *Agricultural and Forest Meteorology*, *154-155*, 156.

Gorelick, N., Hancher, M., Dixon, M., Ilyushchenko, S., Thau, D., & Moore, R. (2017). Google Earth Engine: Planetary-scale geospatial analysis for everyone. *Remote Sensing of Environment*, *202*, 18–27.

Gould, K. S. (2004). Nature's Swiss army knife: The diverse protective roles of anthocyanins in leaves. *Journal of Biomedicine and Biotechnology*, *2004*(5), 314–320.

Govender, M., Dye, P. J., Weiersbye, I. M., Witkowski, E. T. F., & Ahmed, F. (2009). Review of commonly used remote sensing and ground-based technologies to measure plant water stress. *35*(5), 741–752.

Goward, S. N., Tucker, C. J., & Dye, D. G. (1985). North American vegetation patterns observed with the NOAA-7 advanced very high resolution radiometer. *Vegetatio*, *64*(1), 3–14.

Grant, O. M., Montero Ribeiro, A. F., Glombik, P., & O'Reilly, C. (2018). Impact of limited water availability on growth and biomass production of a range of full-sibling Sitka spruce (Picea sitchensis (Bong.) Carr.) families. *Forestry*, *91*(1), 83–97.

Grant, O. M., & O'Reilly, C. (2017). Impact of genetic variation and long-term limited water availability on the ecophysiology of young Sitka spruce (Picea sitchensis (Bong.) Carr.) *Tree Physiology*, *37*(4), 536–549.

Grassi, G., Vicinelli, E., Ponti, F., Cantoni, L., & Magnani, F. (2005). Seasonal and interannual variability of photosynthetic capacity in relation to leaf nitrogen in a deciduous forest plantation in northern Italy. *Tree Physiology*, *25*(3), 349–360.

Green, S., Hendry, S., & Redfern, D. (2008). Drought damage to pole-stage Sitka in NE Scotland. *Scottish Forestry*, *62*, 10–18.

Green, S., & Ray, D. (2009). Potential impacts of drought and disease on forestry in Scotland. *Forest Research*, 1–8.

Grulke, N., Maxfield, J., Riggan, P., & Schrader-Patton, C. (2020). Pre-emptive detection of mature pine drought stress using multispectral aerial imagery. *Remote Sensing*, *12*(14), 1–23.

Guarini, R., Nichol, C., Clement, R., Loizzo, R., Grace, J., & Borghetti, M. (2014). The utility of MODIS-sPRI for investigating the photosynthetic light-use efficiency in a Mediterranean deciduous forest. *International Journal of Remote Sensing*, *35*(16), 6157–6172.

Guindin-Garcia, N., Gitelson, A. A., Arkebauer, T. J., Shanahan, J., & Weiss, A. (2012). An evaluation of MODIS 8- and 16-day composite products for monitoring maize green leaf area index. *Agricultural and Forest Meteorology*, *161*, 15–25.

Gulias, J., Flexas, J., Abadia, A., & Madrano, H. (2002). Photosynthetic responses to water deficit in six Mediterranean sclerophyll species: possible factors explaining the declining distribution of Rhamnus ludovici-salvatoris, an endemic Balearic species. *Tree Physiology*, *22*(10), 687–697.

Harrison, E. L., Arce Cubas, L., Gray, J. E., & Hepworth, C. (2020). The influence of stomatal morphology and distribution on photosynthetic gas exchange. *The Plant Journal*, *101*(4), 768–779.

Hasegawa, S. (1976). Metabolism of limonoids. Limonin D-ring lactone hydrolase activity in Pseudomonas. *Journal of Agricultural and Food Chemistry*, *24*(1), 24–26.

Hashimoto, H., Uragami, C., & Cogdell, R. J. (2016). Carotenoids and Photosynthesis. In C. Stange (Ed.), *Carotenoids in nature: Biosynthesis, regulation, and function* (pp. 111–139, Vol. 79). Springer International Publishing.

Hashimoto, H., Wang, W., Milesi, C., White, M. A., Ganguly, S., Gamo, M., Hirata, R., Myneni, R. B., & Nemani, R. R. (2012). Exploring simple algorithms for estimating gross primary production in forested areas from satellite data. *Remote Sensing*, *4*(1), 303–326.

Hatcher, P. E. (1990). Seasonal and age-related variation in the needle quality of five conifer species. *Oecologia*, *85*(2), 200–212.

Hauglin, M., & Ørka, H. (2016). Discriminating between Native Norway Spruce and Invasive Sitka Spruce—A Comparison of Multitemporal Landsat 8 Imagery, Aerial Images and Airborne Laser Scanner Data. *Remote Sensing*, *8*(5), 363.

Haynes, K. D., Baker, I. T., Denning, A. S., Stöckli, R., Schaefer, K., Lokupitiya, E. Y., & Haynes, J. M. (2019). Representing Grasslands Using Dynamic Prognostic Phenology Based on Biological Growth Stages: 1. Implementation in the Simple Biosphere Model (SiB4). *Journal of Advances in Modeling Earth Systems*, *11*(12), 4423–4439.

Haynes, K., Baker, I., & Denning, A. S. (2020). The Simple Biosphere Model, Version 4.2: SiB4 Technical description. *Colorado State University*, (February).

Heim, R. R. (2002). A Review of Twentieth-Century Drought Indices Used in the United States. *Bulletin of the American Meteorological Society*, *83*(8), 1149–1166.

Hejtmánek, J., Stejskal, J., Čepl, J., Lhotáková, Z., Korecký, J., Krejzková, A., Dvořák, J., & Gezan, S. A. (2022). Revealing the Complex Relationship Among Hyperspectral Reflectance, Photosynthetic Pigments, and Growth in Norway Spruce Ecotypes. *Frontiers in Plant Science*, *13*.

Hernández, I., Alegre, L., Van Breusegem, F., & Munné-Bosch, S. (2009). How relevant are flavonoids as antioxidants in plants? *Trends in Plant Science*, *14*(3), 125–132.

Hernández-Clemente, R., Hornero, A., Mottus, M., Penuelas, J., González-Dugo, V., Jiménez, J. C., Suárez, L., Alonso, L., & Zarco-Tejada, P. J. (2019). Early Diagnosis of Vegetation Health From High-Resolution Hyperspectral

and Thermal Imagery: Lessons Learned From Empirical Relationships and Radiative Transfer Modelling. *Current Forestry Reports*, *5*(3), 169–183.

Hernández-Clemente, R., Navarro-Cerrillo, R. M., Suárez, L., Morales, F., & Zarco-Tejada, P. J. (2011). Assessing structural effects on PRI for stress detection in conifer forests. *Remote Sensing of Environment*, *115*(9), 2360–2375.

Hersbach, H., Bell, B., Berrisford, P., Hirahara, S., Horányi, A., Muñoz-Sabater, J., Nicolas, J., Peubey, C., Radu, R., Schepers, D., Simmons, A., Soci, C., Abdalla, S., Abellan, X., Balsamo, G., Bechtold, P., Biavati, G., Bidlot, J., Bonavita, M., ... Thépaut, J. N. (2020). The ERA5 global reanalysis. *Quarterly Journal of the Royal Meteorological Society*, *146*(730), 1999–2049.

Hetherington, A. M., & Woodward, F. I. (2003). The role of stomata in sensing and driving environmental change. *Nature*, *424*(6951), 901–908.

Hmimina, G., Dufrêne, E., Pontailler, J. Y., Delpierre, N., Aubinet, M., Caquet, B., de Grandcourt, A., Burban, B., Flechard, C., Granier, A., Gross, P., Heinesch, B., Longdoz, B., Moureaux, C., Ourcival, J. M., Rambal, S., Saint André, L., & Soudani, K. (2013). Evaluation of the potential of MODIS satellite data to predict vegetation phenology in different biomes: An investigation using ground-based NDVI measurements. *Remote Sensing of Environment*, *132*, 145–158.

Holzwarth, S., Thonfeld, F., Abdullahi, S., Asam, S., Canova, E. D. P., Gessner, U., Huth, J., Kraus, T., Leutner, B., & Kuenzer, C. (2020). Earth observation based monitoring of forests in germany: A review. *Remote Sensing*, *12*(21), 1–43.

Homolová, L., Janoutová, R., Lukeš, P., Hanuš, J., Novotný, J., Brovkina, O., & Loayza Fernandez, R. R. (2017). In situ data supporting remote sensing estimation of spruce forest parameters at the ecosystem station Bílý Kříž. *Beskydy*, *10*(1-2), 75–86.

Homolová, L., Lukeš, P., Malenovský, Z., Lhotáková, Z., Kaplan, V., & Hanuš, J. (2013). Measurement methods and variability assessment of the Norway spruce total leaf area: Implications for remote sensing. *Trees - Structure and Function*, *27*(1), 111–121.

Homolová, L., Malenovský, Z., Lhotáková, Z., Kaplan, V., & Hanuš, J. (2007). Optical differences between sun exposed and shaded Norway spruce needles. *Proceedings 5th EARSeL Workshop on Imaging Spectroscopy*, (1), 1–10.

Horler, D., Dockray, H., & Barber, J. (1983). International Journal of Remote Sensing The red edge of plant leaf reflectance. *Remote Sensing*, *4*, 273–288.

Hovi, A., Forsström, P., Mõttus, M., & Rautiainen, M. (2017). Evaluation of Accuracy and Practical Applicability of Methods for Measuring Leaf Reflectance and Transmittance Spectra. *Remote Sensing*, *10*(1), 25.

Hovi, A., Raitio, P., & Rautiainen, M. (2017). A spectral analysis of 25 boreal tree species. *Silva Fennica*, *51*(4), 1–16.

Huang, K., Yi, C., Wu, D., Zhou, T., Zhao, X., Blanford, W. J., Wei, S., Wu, H., Ling, D., & Li, Z. (2015). Tipping point of a conifer forest ecosystem under severe drought. *Environmental Research Letters*, *10*(2), 024011.

Huang, L., Yuan, W., Zheng, Y., Zhou, Y., He, M., Jin, J., Huang, X., Chen, S., Liu, M., Guan, X., Jiang, S., Lin, X., Li, Z. L., & Tang, R. (2024). A dynamic-leaf light use efficiency model for improving gross primary production estimation. *Environmental Research Letters*, *19*(1).

Huang, W., Zhou, X., Kong, W., & Ye, H. (2018, September). Monitoring Crop Carotenoids Concentration by Remote Sensing. In *Progress in carotenoid research*. InTech.

Huang, X., Xiao, J., & Ma, M. (2019). Evaluating the Performance of Satellite-Derived Vegetation Indices for Estimating Gross Primary Productivity Using FLUXNET Observations across the Globe. *Remote Sensing*, *11*(15), 1823.

Huemmrich, K. F., Vargas Zesati, S., Campbell, P., & Tweedie, C. (2021). Canopy reflectance models illustrate varying NDVI responses to change in high latitude ecosystems. *Ecological Applications*, *31*(8), 1–13.

Huete, A. r., Didan, K., Miura, T., Rodriguez, E., Gao, X., & Ferreira, L. (2002). Overview of the radiometric and biophysical performance of the MODIS vegetation indices. *Remote Sensing of Environment*, *83*(1-2), 195–213.

Huete, A. R., Restrepo-Coupe, N., Ratana, P., Didan, K., Saleska, S. R., Ichii, K., Panuthai, S., & Gamo, M. (2008). Multiple site tower flux and remote sensing comparisons of tropical forest dynamics in Monsoon Asia. *Agricultural and Forest Meteorology*, *148*(5), 748–760.

Huete, A. R. (2012). Vegetation Indices, Remote Sensing and Forest Monitoring. *Geography Compass*, *6*(9), 513–532.

Hufkens, K., Friedl, M., Sonnentag, O., Braswell, B. H., Milliman, T., & Richardson, A. D. (2012). Linking near-surface and satellite remote sensing measurements of deciduous broadleaf forest phenology. *Remote Sensing of Environment*, *117*, 307–321.

Hunt, E. R., & Rock, B. N. (1989). Detection of changes in leaf water content using Near- and Middle-Infrared reflectances. *Remote Sensing of Environment*, *30*(1), 43–54.

Ida, K. (1981). Eco-physiological studies on the response of taxodiaceous conifers to shading with special reference to the behavior of leaf pigments. *The Botanical Magazine Tokyo*, *94*(3), 181–196.

Intergovernmental Panel on Climate Change (IPCC). (2021, July). *Climate Change 2021 – The Physical Science Basis* (Vol. 34). Cambridge University Press.

Irvine, J., Perks, M. P., Magnani, F., & Grace, J. (1998). The response of Pinus sylvestris to drought: Stomatal control of transpiration and hydraulic conductance. *Tree Physiology*, *18*(6), 393–402.

Janni, M., Coppede, N., Bettelli, M., Briglia, N., Petrozza, A., Summerer, S., Vurro, F., Danzi, D., Cellini, F., Marmiroli, N., Pignone, D., Iannotta, S., & Zappettini, A. (2019). In Vivo Phenotyping for the Early Detection of Drought Stress in Tomato. *Plant Phenomics*, *2019*, 6168209.

Jiang, C.-D., Gao, H.-Y., Zou, Q., Jiang, G.-M., & Li, L.-H. (2006). Leaf orientation, photorespiration and xanthophyll cycle protect young soybean leaves against high irradiance in field. *Environmental and Experimental Botany*, *55*, 87–96.

Jin, P., Wang, Q., Iio, A., & Tenhunen, J. (2012). Ecological Informatics Retrieval of seasonal variation in photosynthetic capacity from multi-source vegetation indices. *Ecological Informatics*, *7*(1), 7–18.

Joiner, J., & Yoshida, Y. (2020). Satellite-based reflectances capture large fraction of variability in global gross primary production (GPP) at weekly time scales. *Agricultural and Forest Meteorology*, *291*, 108092.

Joiner, J., Yoshida, Y., Zhang, Y., Duveiller, G., Jung, M., Lyapustin, A., Wang, Y., & Tucker, C. J. (2018). Estimation of terrestrial global gross primary production (GPP) with satellite data-driven models and eddy covariance flux data. *Remote Sensing*, *10*(9), 1–38.

Jubany-Marí, T., Munné-Bosch, S., & Alegre, L. (2010). Redox regulation of water stress responses in field-grown plants. Role of hydrogen peroxide and ascorbate. *Plant Physiology and Biochemistry*, *48*(5), 351–358.

Junttila, S., Ardö, J., Cai, Z., Jin, H., Kljun, N., Klemedtsson, L., Krasnova, A., Lange, H., Lindroth, A., Mölder, M., Noe, S. M., Tagesson, T., Vestin, P., Weslien, P., & Eklundh, L. (2023). Estimating local-scale forest GPP in Northern Europe using Sentinel-2: Model comparisons with LUE, APAR, the plant phenology index, and a light response function. *Science of Remote Sensing*, *7*(January).

Juvany, M., Müller, M., & Munné-Bosch, S. (2013). Photo-oxidative stress in emerging and senescing leaves: A mirror image. *Journal of Experimental Botany*, *64*(11), 3087–3098.

Kannenberg, S. A., Schwalm, C. R., & Anderegg, W. R. (2020). Ghosts of the past: how drought legacy effects shape forest functioning and carbon cycling. *Ecology Letters*, *23*(5), 891–901.

Kattenborn, T., & Schmidtlein, S. (2019). Radiative transfer modelling reveals why canopy reflectance follows function. *Scientific Reports*, *9*(1), 1–10.

Kattge, J., Knorr, W., Raddatz, T., & Wirth, C. (2009). Quantifying photosynthetic capacity and its relationship to leaf nitrogen content for global-scale terrestrial biosphere models. *Global Change Biology*, *15*(4), 976–991.

Khanna-Chopra, R. (2012). Leaf senescence and abiotic stresses share reactive oxygen species-mediated chloroplast degradation. *Protoplasma*, *249*(3), 469–481.

Kiang, N. Y., Segura, A., Tinetti, G., Govindjee, Blankenship, R. E., Cohen, M., Siefert, J., Crisp, D., & Meadows, V. S. (2007). Spectral signatures of photosynthesis. II. Coevolution with other stars and the atmosphere on extrasolar worlds. *Astrobiology*, *7*(1), 252–274.

Kierzkowski, D., Samardakiewicz, S., & Robakowski, P. (2007). Variation in ultrastructure of chloroplasts in needles of silver fir (Abies Alba Mill.) saplings growing under the canopies of diverse tree species. *Polish Journal of Ecology*, *55*(4), 821–825.

Kimball, J. S., McDonald, K. C., Running, S. W., & Frolking, S. E. (2004). Satellite radar remote sensing of seasonal growing seasons for boreal and subalpine evergreen forests. *Remote Sensing of Environment*, *90*(2), 243–258.

Klein, T., Cahanovitc, R., Sprintsin, M., Herr, N., & Schiller, G. (2019). A nationwide analysis of tree mortality under climate change: Forest loss and its causes in Israel 1948–2017. *Forest Ecology and Management*, *432*(October 2018), 840–849.

Kormann, R., & Meixner, F. X. (2001). An analytical footprint model for non-neutral stratification. *Boundary-Layer Meteorology*, *99*(2), 207–224.

Krakau, U.-K., Liesebach, M., Aronen, T., Lelu-Walter, M.-A., & Schneck, V. (2013). Scots Pine (Pinus sylvestris L.) In *Forest tree breeding in europe* (pp. 267–323).

Kramer, R. D., Sillett, S. C., & Van Pelt, R. (2018). Quantifying aboveground components of Picea sitchensis for allometric comparisons among tall conifers in North American rainforests. *Forest Ecology and Management*, *430*, 59–77.

Kreuzwieser, J., & Gessler, A. (2010). Global climate change and tree nutrition: influence of water availability. *Tree Physiology*, *30*(9), 1221–1234.

Krishnamurthy, P. K., Fisher, J. B., Schimel, D. S., & Kareiva, P. M. (2020). Applying Tipping Point Theory to Remote Sensing Science to Improve Early Warning Drought Signals for Food Security. *Earth's Future*, *8*(3), 1–14.

Kross, A., Fernandes, R., Seaquist, J., & Beaubien, E. (2011). The effect of the temporal resolution of NDVI data on season onset dates and trends across Canadian broadleaf forests. *Remote Sensing of Environment*, *115*(6), 1564–1575.

Kruk, J., Holländer-Czytko, H., Oettmeier, W., & Trebst, A. (2005). Tocopherol as singlet oxygen scavenger in photosystem II. *Journal of Plant Physiology*, *162*(7), 749–757.

Kumagai, E., Burroughs, C. H., Pederson, T. L., Montes, C. M., Peng, B., Kimm, H., Guan, K., Ainsworth, E. A., & Bernacchi, C. J. (2022). Predicting biochemical acclimation of leaf photosynthesis in soybean under in-field canopy warming using hyperspectral reflectance. *Plant, Cell & Environment*, *45*(1), 80–94.

Kuznetsova, A., Brockhoff, P. B., & Christensen, R. H. B. (2017). lmerTest Package: Tests in Linear Mixed Effects Models. *Journal of Statistical Software*, *82*(13).

Kyparissis, A., Grammatikopoulos, G., & Manetas, Y. (2007). Leaf morphological and physiological adjustments to the spectrally selective shade imposed by anthocyanins in Prunus cerasifera. *Tree Physiology*, *27*(6), 849–857.

Landi, M., Tattini, M., & Gould, K. S. (2015). Multiple functional roles of anthocyanins in plant-environment interactions. *Environmental and Experimental Botany*, *119*, 4–17.

Landsberg, J. J., Waring, R. H., & Williams, M. (2020). The assessment of NPP/GPP ratio. *Tree Physiology*, *40*(6), 695–699.

Lange, M., Dechant, B., Rebmann, C., Vohland, M., Cuntz, M., & Doktor, D. (2017). Validating MODIS and Sentinel-2 NDVI Products at a Temperate Deciduous Forest Site Using Two Independent Ground-Based Sensors. *Sensors*, *17*(8), 1855.

Lausch, A., Erasmi, S., King, D. J., Magdon, P., & Heurich, M. (2016). Understanding forest health with remote sensing-Part I-A review of spectral traits, processes and remote-sensing characteristics. *Remote Sensing*, *8*(12), 1–44.

Lawrence, D. M., Oleson, K. W., Flanner, M. G., Fletcher, C. G., Lawrence, P. J., Levis, S., Swenson, S. C., & Bonan, G. B. (2012). The CCSM4 land simulation, 1850-2005: Assessment of surface climate and new capabilities. *Journal of Climate*, *25*(7), 2240–2260.

Lazár, D., Sušila, P., & Nauš, J. (2006). Early detection of plant stress from changes in distributions of chlorophyll a fluorescence parameters measured with fluorescence imaging. *Journal of Fluorescence*, *16*(2), 173–176.

Le, T. S., Harper, R., & Dell, B. (2023). Application of Remote Sensing in Detecting and Monitoring Water Stress in Forests. *Remote Sensing*, *15*(13), 3360.

Lee, S. J. (1999). Improving the timber quality of Sitka spruce through selection and breeding. *Forestry*, *72*(2), 123–133.

León, M. A. P. D., & Bailey, B. N. (2019). Evaluating the use of Beer ' s law for estimating light interception in canopy architectures with varying heterogeneity and anisotropy. *Ecological Modelling*, *406*(April), 133–143.

Lewandowska, M., & Jarvis, P. G. (1977). Changes in Chlorophyll and Carotenoid Content, Specific Leaf Area and Dry Weight Fraction in Sitka Spruce, in Respose to 2Shading and Season. *New Phytologist*, *79*(2), 247–256.

Lewis, S. L., Edwards, D. P., & Galbraith, D. (2015). Increasing human dominance of tropical forests. *Science*, *349*(6250), 827–832.

Lhotáková, Z., Kopačková-Strnadová, V., Oulehle, F., Homolová, L., Neuwirthová, E., Švik, M., Janoutová, R., & Albrechtová, J. (2021). Foliage biophysical trait prediction from laboratory spectra in norway spruce is more affected by needle age than by site soil conditions. *Remote Sensing*, *13*(3), 1–24.

Li, M., Wu, P., & Ma, Z. (2020). A comprehensive evaluation of soil moisture and soil temperature from third-generation atmospheric and land reanalysis data sets. *International Journal of Climatology*, *40*(13), 5744–5766.

Li, Z., Zhang, Q., Li, J., Yang, X., Wu, Y., Zhang, Z., Wang, S., Wang, H., & Zhang, Y. (2020). Solar-induced chlorophyll fluorescence and its link to canopy photosynthesis in maize from continuous ground measurements. *Remote Sensing of Environment*, *236*, 111420.

Liang, S., & Wang, J. (2020). Estimate of vegetation production of terrestrial ecosystem. In *Advanced remote sensing: Terrestrial information extraction and applications* (pp. 581–620).

Lichtenthaler, H. K., Ač, A., Marek, M. V., Kalina, J., & Urban, O. (2007). Differences in pigment composition, photosynthetic rates and chlorophyll fluorescence images of sun and shade leaves of four tree species. *Plant Physiology and Biochemistry*, *45*(8), 577–588.

Lillesaeter, O. (1982). Spectral reflectance of partly transmitting leaves: Laboratory measurements and mathematical modeling. *Remote Sensing of Environment*, *12*(3), 247–254.

Liming, B., & Huichun, Z. (2020). Application of Phenotyping Techniques in Forest Tree Breeding and Precision Forestry. *56*(6), 113–126.

Liu, F., Wang, C., & Wang, X. (2021). Can vegetation index track the interannual variation in gross primary production of temperate deciduous forests? *Ecological Processes*, *10*(1), 51.

Liu, H. Q., & Huete, A. (1995). Feedback based modification of the NDVI to minimize canopy background and atmospheric noise. *IEEE Transactions on Geoscience and Remote Sensing*, *33*(2), 457–465.

Liu, J. F., Arend, M., Yang, W. J., Schaub, M., Ni, Y. Y., Gessler, A., Jiang, Z. P., Rigling, A., & Li, M. H. (2017). Effects of drought on leaf carbon source and growth of European beech are modulated by soil type. *Scientific Reports*, *7*(1), 1–9.

Liu, J., & van Iersel, M. W. (2021). Photosynthetic Physiology of Blue, Green, and Red Light: Light Intensity Effects and Underlying Mechanisms. *Frontiers in Plant Science*, *12*, 619987.

Locatelli, T., Beauchamp, K., Perks, M., Xenakis, G., Nicoll, B., & Morison, J. (2021). Drought risk in Scottish forests. *ClimateXChange*.

Lokupitiya, E., Denning, S., Paustian, K., Baker, I., Schaefer, K., Verma, S., Meyers, T., Bernacchi, C. J., Suyker, A., & Fischer, M. (2009). Incorporation of crop phenology in Simple Biosphere model (SiBcrop) to improve land-atmosphere carbon exchanges from croplands. *Biogeosciences*, *6*(6), 969–986.

Long, S. P., & Bernacchi, C. J. (2003). Gas exchange measurements , what can they tell us about the underlying limitations to photosynthesis ? Procedures and sources of error. *54*(392), 2393–2401.

Long, S. P., Humphries, S., & Falkowskim, P. G. (1994). Photoinhibition of Photosynthesis in Nature. *Annual Review Of Plant Physiology And Plant Molecular Biology*, *45*(1), 633.

López, R., Rodríguez-Calcerrada, J., & Gil, L. (2009). Physiological and morphological response to water deficit in seedlings of five provenances of Pinus canariensis: Potential to detect variation in drought-tolerance. *Trees - Structure and Function*, *23*(3), 509–519.

Los, S. O., Collatz, G. J., Sellers, P. J., Malmström, C. M., Pollack, N. H., DeFries, R. S., Bounoua, L., Parris, M. T., Tucker, C. J., & Dazlich, D. A. (2000). A global 9-yr biophysical land surface dataset from NOAA AVHRR data. *Journal of Hydrometeorology*, *1*(2), 183–199.

Lukeš, P., Stenberg, P., Rautiainen, M., Mõttus, M., & Vanhatalo, K. M. (2013). Optical properties of leaves and needles for boreal tree species in Europe. *Remote Sensing Letters*, *4*(7), 667–676.

Luo, X., Chen, J. M., Liu, J., Black, A., Croft, H., Staebler, R., He, L., Arain, M. A., Bin, C., Gang, M., Gonsamo, A., & Mccaughey, H. (2018). Comparison of Big-Leaf, Two-Big-Leaf, and Two-Leaf Upscaling Schemes for Evapotranspiration Estimation Using Coupled Carbon-Water Modeling, 207–225.

Lüttge, U., Escher, P., Paluch, R., Pfanz, H., Wittmann, C., Rennenberg, H., & Rakowski, K. (2011). Variability of photosynthetic capacity and water relations of Pinus sylvestris L. in the field. *Biologia Plantarum*, *55*(1), 90–98.

Lyapustin, A., Wang, Y., Laszlo, I., Kahn, R., Korkin, S., Remer, L., Levy, R., & Reid, J. S. (2011). Multiangle implementation of atmospheric correction (MAIAC): 2. Aerosol algorithm. *Journal of Geophysical Research Atmospheres*, *116*(3), 1–15.

Lyapustin, A., Wang, Y., & Frey, R. (2008). An automatic cloud mask algorithm based on time series of MODIS measurements. *Journal of Geophysical Research Atmospheres*, *113*(16), 1–15.

Lyapustin, A., Wang, Y., Korkin, S., & Huang, D. (2018). MODIS Collection 6 MAIAC algorithm. *Atmospheric Measurement Techniques*, *11*(10), 5741–5765.

Lyapustin, A., Wang, Y., Laszlo, I., Hilker, T., G.Hall, F., Sellers, P. J., Tucker, C. J., & Korkin, S. V. (2012). Multi-angle implementation of atmospheric correction for MODIS (MAIAC): 3. Atmospheric correction. *Remote Sensing of Environment*, *127*, 385–393.

Ma, Y., Wu, H., Wang, L., Huang, B., Ranjan, R., Zomaya, A., & Jie, W. (2015). Remote sensing big data computing: Challenges and opportunities. *Future Generation Computer Systems*, *51*, 47–60.

MacAllister, S., Mencuccini, M., Sommer, U., Engel, J., Hudson, A., Salmon, Y., & Dexter, K. G. (2019). Drought-induced mortality in Scots pine: opening the metabolic black box. *Tree Physiology*, *39*(8), 1358–1370.

Marron, N., Dreyer, E., Boudouresque, E., Delay, D., Petit, J. M., Delmotte, F. M., & Brignolas, F. (2003). Impact of successive drought and re-watering cycles on growth and specific leaf area of two Populus x canadensis (Moench) clones, 'Dorskamp' and 'Luisa_Avanzo'. *Tree Physiology*, *23*(18), 1225–1235.

Matisons, R., Krišāns, O., Jansons, Ā., Kondratovičs, T., Elferts, D., & Ievinsh, G. (2021). Norway spruce seedlings from an eastern baltic provenance show tolerance to simulated drought. *Forests*, *12*(1), 1–16.

McCallum, I., Wagner, W., Schmullius, C., Shvidenko, A., Obersteiner, M., Fritz, S., & Nilsson, S. (2009). Satellite-based terrestrial production efficiency modeling. *Carbon Balance and Management*, *4*(1), 8.

McDowell, N. G., Beerling, D. J., Breshears, D. D., Fisher, R. A., Raffa, K. F., & Stitt, M. (2011). The interdependence of mechanisms underlying climate-driven vegetation mortality. *Trends in Ecology & Evolution*, *26*(10), 523–532.

McDowell, N. G. (2011). Mechanisms Linking Drought, Hydraulics, Carbon Metabolism, and Vegetation Mortality. *Plant Physiology*, *155*(3), 1051–1059.

McDowell, N. G., & Allen, C. D. (2015). Darcy's law predicts widespread forest mortality under climate warming. *Nature Climate Change*, *5*(7), 669–672.

Meir, P., Kruijt, B., Broadmeadow, M., Barbosa, E., Kull, O., Carswell, F., Nobre, A., & Jarvis, P. G. (2002). Acclimation of photosynthetic capacity to irradiance in tree canopies in relation to leaf nitrogen concentration and leaf mass per unit area. *Plant, Cell and Environment*, *25*(3), 343–357.

Mena-Petite, A., González-Moro, B., González-Murua, C., Lacuesta, M., & Rueda, A. M. (2000). Sequential effects of acidic precipitation and drought on pho-

tosynthesis and chlorophyll fluorescence parameters of Pinus radiata D. Don seedlings. *Journal of Plant Physiology*, *156*(1), 84–92.

Merilo, E., Tulva, I., Räim, O., Kükit, A., Sellin, A., & Kull, O. (2009). Changes in needle nitrogen partitioning and photosynthesis during 80 years of tree ontogeny in Picea abies. *Trees - Structure and Function*, *23*(5), 951–958.

Merlin, M., Perot, T., Perret, S., Korboulewsky, N., & Vallet, P. (2015). Effects of stand composition and tree size on resistance and resilience to drought in sessile oak and Scots pine. *Forest Ecology and Management*, *339*, 22–33.

Met Office. (2021). UK Climate Projections: Headline Findings. (September), 1–12.

Middleton, E. M., Chan, S. S., Rusin, R. I., & Mitchell, S. K. (1997). Optical properties of black spruce and jack pine needles at BOREAS Sites in saskatchewan, Canada. *Canadian Journal of Remote Sensing*, *23*(2), 108–119.

Middleton, E. M., Huemmrich, K. F., Landis, D. R., Black, T. A., Barr, A. G., & McCaughey, J. H. (2016). Photosynthetic efficiency of northern forest ecosystems using a MODIS-derived Photochemical Reflectance Index (PRI). *Remote Sensing of Environment*, *187*, 345–366.

Middleton, E. M., Cheng, Y. B., Hilker, T., Black, T. A., Krishnan, P., Coops, N. C., & Huemmrich, K. F. (2009). Linking foliage spectral responses to canopy-level ecosystem photosynthetic light-use efficiency at a douglas-fir forest in canada. *Canadian Journal of Remote Sensing*, *35*(2), 166–188.

Millar, C. I., & Stephenson, N. L. (2015). Temperate forest health in an era of emerging megadisturbance. *Science*, *349*(6250), 823–826.

Miller, G., Shulaev, V., & Mittler, R. (2008). Reactive oxygen signaling and abiotic stress. *Physiologia Plantarum*, *133*(3), 481–489.

Miller, G., Suzuki, N., Ciftci-Yilmaz, S., & Mittler, R. (2010). Reactive oxygen species homeostasis and signalling during drought and salinity stresses. *Plant, Cell & Environment*, *33*(4), 453–467.

Miller, J. R., Wu, J., Boyer, M. G., Belanger, M., & Hare, E. W. (1991). Seasonal patterns in leaf reflectance red-edge characteristics. *International Journal of Remote Sensing*, *12*(7), 1509–1523.

Mittler, R. (2002). Oxidative stress, antioxidants and stress tolerance. *Trends in Plant Science*, *7*(9), 405–410.

Mittler, R., Vanderauwera, S., Gollery, M., & Van Breusegem, F. (2004). Reactive oxygen gene network of plants. *Trends in Plant Science*, *9*(10), 490–498.

Monsi, M., Saeki, T., & Schortemeyer, M. (2005). On the factor light in plant communities and its importance for matter production (Originally published in: Japanese Journal of Botany 14: 22–52)). *Annals of Botany*, *95*(3), 549–567.

Monteith, J. (1977). Climate and the efficiency of crop production in Britain. *Philosophical Transactions of the Royal Society of London. B, Biological Sciences*, *281*(980), 277–294.

Mõttus, M., Aragao, L., Back, J., Hernandez-Clemente, R., Maeda, E. E., Markiet, V., Nichol, C., De Oliveira, R. C., & Restrepo-Coupe, N. (2019). Diurnal changes in leaf photochemical reflectance index in two evergreen forest canopies. *IEEE Journal of Selected Topics in Applied Earth Observations and Remote Sensing*, *12*(7), 2236–2243.

Mõttus, M., Hernández-Clemente, R., Perheentupa, V., & Markiet, V. (2017). In situ measurement of Scots pine needle PRI. *Plant Methods*, *13*(1), 1–8.

Mõttus, M., Rautiainen, M., & Schaepman, M. E. (2012). Shoot scattering phase function for Scots pine and its effect on canopy reflectance. *Agricultural and Forest Meteorology*, *154-155*, 67.

Mõttus, M., Sulev, M., & Hallik, L. (2014). Seasonal course of the spectral properties of alder and birch leaves. *IEEE Journal of Selected Topics in Applied Earth Observations and Remote Sensing*, *7*(6), 2496–2505.

Mullen, K. M., Ardia, D., Gil, D. L., & Cline, J. (2011). DEoptim : An R Package for Global Optimization by Differential Evolution. *40*(6).

Muñoz Sabater, J. (2021). ERA5-Land monthly averaged data from 1981 to present. *Earth System Science Data*, *13*(9), 4349–4383.

Munson, S. M., Reed, S. C., Peñuelas, J., McDowell, N. G., & Sala, O. E. (2018). Ecosystem thresholds, tipping points, and critical transitions. *New Phytologist*, *218*(4), 1315–1317.

Murchie, E. H., & Lawson, T. (2013). Chlorophyll fluorescence analysis: A guide to good practice and understanding some new applications. *Journal of Experimental Botany*, *64*(13), 3983–3998.

Nadal-Sala, D., Grote, R., Birami, B., Knüver, T., Rehschuh, R., Schwarz, S., & Ruehr, N. K. (2021). Leaf Shedding and Non-Stomatal Limitations of Photosynthesis Mitigate Hydraulic Conductance Losses in Scots Pine Saplings During Severe Drought Stress. *Frontiers in Plant Science*, *12*, 715127.

Nagai, S., Saigusa, N., Muraoka, H., & Nasahara, K. N. (2010). What makes the satellite-based EVI-GPP relationship unclear in a deciduous broad-leaved forest? *Ecological Research*, *25*(2), 359–365.

Nemani, R. R., Keeling, C. D., Hashimoto, H., Jolly, W. M., Piper, S. C., Tucker, C. J., Myneni, R. B., & Running, S. W. (2003). Climate-driven increases in global terrestrial net primary production from 1982 to 1999. *Science*, *300*(5625), 1560–1563.

Niinemets, Ü., Kollist, H., García-Plazaola, J. I., Hernández, A., & Becerril, J. M. (2003). Do the capacity and kinetics for modification of xanthophyll cycle

pool size depend on growth irradiance in temperate trees? *Plant, Cell and Environment*, *26*(10), 1787–1801.

Nishiyama, Y., Allakhverdiev, S. I., & Murata, N. (2006). A new paradigm for the action of reactive oxygen species in the photoinhibition of photosystem II. *Biochimica et Biophysica Acta (BBA) - Bioenergetics*, *1757*(7), 742–749.

Norman, J. M., Kucharik, C. J., Gower, S. T., Baldocchi, D. D., Crill, P. M., Rayment, M., Savage, K., & Striegl, R. G. (1997). A comparison of six methods for measuring soil-surface carbon dioxide fluxes. *Journal of Geophysical Research: Atmospheres*, *102*(D24), 28771–28777.

Noumonvi, K. D., & Ferlan, M. (2020). Empirical vs. light-use efficiency modelling for estimating carbon fluxes in a mid-succession ecosystem developed on abandoned karst grassland. *PLoS ONE*, *15*(8 August), 1–18.

Olascoaga, B., Juurola, E., Lukeš, P., Nikinmaa, E., Bäck, J., Porcar-Castell, A., Juurola, E., Pinho, P., & Halonen, L. (2014). Seasonal variation in the reflectance of photosynthetically active radiation from epicuticular waxes of Scots pine (Pinus sylvestris) needles. *Boreal Environment Research*, *19*(August), 132–141.

Ollinger, S., Reich, P., S, F., LC, L., Hollinger, D. Y., & AD, R. (2013). Nitrogen cycling , forest canopy re fl ectance , and emergent properties of ecosystems. *110*(27), 2437.

O'Neill, A. L., Kupiec, J. A., & Curran, P. J. (2002). Biochemical and reflectance variation throughout a sitka spruce canopy. *Remote Sensing of Environment*, *80*(1), 134–142.

Ørka, H. O., & Hauglin, M. (2016). Use of remote sensing for mapping of non-native conifer species. *INA fagrapport*, *33*.

Oyama, M. D., & Nobre, C. a. (2004). A simple potential vegetation model for coupling with the Simple Biosphere Model (SiB). *Rev. Bras. Meteorol.*, *19*, 203–216.

Pacheco-Labrador, J., Perez-Priego, O., El-Madany, T. S., Julitta, T., Rossini, M., Guan, J., Moreno, G., Carvalhais, N., Martín, M. P., Gonzalez-Cascon, R., Kolle, O., Reischtein, M., van der Tol, C., Carrara, A., Martini, D., Hammer, T. W., Moossen, H., & Migliavacca, M. (2019). Multiple-constraint inversion of SCOPE. Evaluating the potential of GPP and SIF for the retrieval of plant functional traits. *Remote Sensing of Environment*, *234*, 111362.

Pantin, F., Monnet, F., Jannaud, D., Costa, J. M., Renaud, J., Muller, B., Simonneau, T., & Genty, B. (2013). The dual effect of abscisic acid on stomata. *New Phytologist*, *197*(1), 65–72.

Patel, R., Rinker, L., Peng, J., & Chilian, W. M. (2018, May). Reactive Oxygen Species: The Good and the Bad. In *Reactive oxygen species (ros) in living cells*. InTech.

Peguero-Pina, J. J., Camarero, J. J., Abadía, A., Martín, E., González-Cascón, R., Morales, F., & Gil-Pelegrín, E. (2007). Physiological performance of silver-fir (Abies alba Mill.) populations under contrasting climates near the south-western distribution limit of the species. *Flora: Morphology, Distribution, Functional Ecology of Plants*, *202*(3), 226–236.

Peguero-Pina, J. J., Morales, F., Flexas, J., Gil-Pelegrín, E., & Moya, I. (2008). Photochemistry, remotely sensed physiological reflectance index and de-epoxidation state of the xanthophyll cycle in Quercus coccifera under intense drought. *Oecologia*, *156*(1), 1–11.

Peltier, D. M., & Ogle, K. (2019). Legacies of more frequent drought in ponderosa pine across the western United States. *Global Change Biology*, *25*(11), 3803–3816.

Penuelas, J., Filella, I., Biel, C., Serrano, L., & Save, R. (1993). The reflectance at the 950-970 nm region as an indicator of plant water status. *International Journal of Remote Sensing*, *14*(10), 1887–1905.

Peñuelas, J., Piñol, J., Ogaya, R., & Filella, I. (1997). International Journal of Remote Estimation of plant water concentration by the reflectance Water Index WI (R900 / R970). *International Journal of Remote*, *18*(13), 2869–2875.

Pessarakli, M. (2018). Plant signaling pathways involved in stomatal movement under drought stress conditions. *Advances in Plants & Agriculture Research*, *8*(3), 290–297.

Petr, M., Boerboom, L. G., van der Veen, A., & Ray, D. (2014). A spatial and temporal drought risk assessment of three major tree species in Britain using probabilistic climate change projections. *Climatic Change*, *124*(4), 791–803.

Phillips, O., Malhi, Y., Roberts, J. T., Betts, R. A., Killeen, T. J., Li, W., & Nobre, C. A. (2008). Drought sensitivity of the Amazon Rainforest. *Science*, *319*(5860), 169–172.

Pintó-Marijuan, M., & Munné-Bosch, S. (2014). Photo-oxidative stress markers as a measure of abiotic stress-induced leaf senescence: advantages and limitations. *Journal of Experimental Botany*, *65*(14), 3845–3857.

Plesa, I. M., Al Hassan, M., González-Orenga, S., Sestras, A. F., Vicente, O., Prohens, J., Boscaiu, M., & Sestras, R. E. (2019). Responses to drought in seedlings of European larch (Larix decidua Mill.) from several Carpathian provenances. *Forests*, *10*(6).

Pompa-García, M., Camarero, J. J., Colangelo, M., & González-Cásares, M. (2021). Inter and intra-annual links between climate, tree growth and NDVI: improving the resolution of drought proxies in conifer forests. *International Journal of Biometeorology*, *65*(12), 2111–2121.

Poorter, L., & Markesteijn, L. (2008). Seedling traits determine drought tolerance of tropical tree species. *Biotropica*, *40*(3), 321–331.

Porcar-Castell, A., Peñuelas, J., Owen, S. M., Llusià, J., Munné-Bosch, S., & Bäck, J. (2009). Leaf carotenoid concentrations and monoterpene emission capacity under acclimation of the light reactions of photosynthesis. *Boreal Environment Research*, *14*(4), 794–806.

Potithep, S., Nagai, S., Nishida, K., Muraoka, H., & Suzuki, R. (2013). Agricultural and Forest Meteorology Two separate periods of the LAI – VIs relationships using in situ measurements in a deciduous broadleaf forest. *Agricultural and Forest Meteorology*, *169*, 148–155.

Potůčková, M., Červená, L., Kupková, L., Lhotáková, Z., Lukeš, P., Hanuš, J., Novotný, J., & Albrechtová, J. (2016). Comparison of Reflectance Measurements Acquired with a Contact Probe and an Integration Sphere: Implications for the Spectral Properties of Vegetation at a Leaf Level. *Sensors*, *16*(11), 1801.

Powell, T. L., Galbraith, D. R., Christoffersen, B. O., Harper, A., Imbuzeiro, H. M. A., Rowland, L., Almeida, S., Brando, P. M., da Costa, A. C. L., Costa, M. H., Levine, N. M., Malhi, Y., Saleska, S. R., Sotta, E., Williams, M., Meir, P., & Moorcroft, P. R. (2013). Confronting model predictions of carbon fluxes with measurements of Amazon forests subjected to experimental drought. *New Phytologist*, *200*(2), 350–365.

Prentice, I. C., Balzarolo, M., Bloomfield, K. J., Chen, J. M., Dechant, B., Ghent, D., Janssens, I. A., Luo, X., Morfopoulos, C., Ryu, Y., Vicca, S., & van Hoolst, R. (2024). Principles for satellite monitoring of vegetation carbon uptake. *Nature Reviews Earth and Environment*, *5*(November).

Prieto, I., Querejeta, J. I., Segrestin, J., Volaire, F., & Roumet, C. (2018). Leaf carbon and oxygen isotopes are coordinated with the leaf economics spectrum in Mediterranean rangeland species (R. Oliveira, Ed.). *Functional Ecology*, *32*(3), 612–625.

Qi, Y., Dennison, P. E., Jolly, W. M., Kropp, R. C., & Brewer, S. C. (2014). Spectroscopic analysis of seasonal changes in live fuel moisture content and leaf dry mass. *Remote Sensing of Environment*, *150*, 198–206.

Qian, X., Liu, L., Chen, X., & Zarco-tejada, P. J. (2021). Assessment of Satellite Chlorophyll-Based Leaf Maximum Carboxylation Rate (Vcmax) Using Flux Observations at Crop and Grass Sites. *14*, 5352–5360.

Qiao, K., Zhu, W., Xie, Z., & Li, P. (2019). Estimating the Seasonal Dynamics of the Leaf Area Index Using Piecewise LAI-VI Relationships Based on Phenophases. *Remote Sensing*, *11*(6), 689.

Rahman, A. F., Cordova, V. D., Gamon, J. A., Schmid, H. P., & Sims, D. A. (2004). Potential of MODIS ocean bands for estimating CO2 flux from terrestrial vegetation: A novel approach. *Geophysical Research Letters*, *31*(10), 3–6.

Rahman, A. F., Sims, D. A., Cordova, V. D., & El-Masri, B. Z. (2005). Potential of MODIS EVI and surface temperature for directly estimating per-pixel ecosystem C fluxes. *Geophysical Research Letters*, *32*(19), 1–4.

Rasheed, F., Gondal, A., Kudus, K. A., Zafar, Z., Nawaz, M. F., Khan, W. R., Abdullah, M., Ibrahim, F. H., Depardieu, C., Pazi, A. M. M., Anjum, K., Afzal, S., Akram, S., & Nazre, M. (2021). Effects of Soil Water Deficit on Three Tree Species of the Arid Environment: Variations in Growth, Physiology, and Antioxidant Enzyme Activities. *Sustainability*, *13*(6), 3336.

Rautiainen, M., Heiskanen, J., & Korhonen, L. (2012). Seasonal changes in canopy leaf area index and MODIS vegetation products for a boreal forest site in central Finland. *Boreal Environment Research*, *17*(1), 72–84.

Rautiainen, M., Lukeš, P., Homolová, L., Hovi, A., Pisek, J., & Mõttus, M. (2018). Spectral properties of coniferous forests: A review of in situ and laboratory measurements. *Remote Sensing*, *10*(2), 1–28.

Rautiainen, M., & Stenberg, P. (2005). Application of photon recollision probability in coniferous canopy reflectance simulations. *Remote Sensing of Environment*, *96*(1), 98–107.

Reichstein, M., Ciais, P., Papale, D., Valentini, R., Running, S., Viovy, N., Cramer, W., Granier, A., Ogée, J., Allard, V., Aubinet, M., Bernhofer, C., Buchmann, N., Carrara, A., Grünwald, T., Heimann, M., Heinesch, B., Knohl, A., Kutsch, W., & Zhao, M. (2007). Reduction of ecosystem productivity and respiration during the European summer 2003 climate anomaly: A joint flux tower, remote sensing and modelling analysis. *Global Change Biology*, *13*(3), 634–651.

Richardson, A. D., Berlyn, G. P., & Gregoire, T. G. (2001). Spectral reflectance of Picea rubens (pinaceae) and Abies balsamea (Pinaceae) needles along an elevational gradient, Mt. Moosilauke, New Hampshire, USA. *American Journal of Botany*, *88*(4), 667–676.

Robakowski, P., & Bielinis, E. (2017). Needle age dependence of photosynthesis along a light gradient within an Abies alba crown. *Acta Physiologiae Plantarum*, *39*(3), 83.

Rogers, A. (2014). The use and misuse of Vc,max in Earth System Models. *Photosynthesis Research*, *119*(1-2), 15–29.

RStudio Team. (2020). RStudio: Integrated Development for R. RStudio.

Running, S. W., Nemani, R. R., Heinsch, F. A., Zhao, M., Reeves, M., & Hashimoto, H. (2004). A Continuous Satellite-Derived Measure of Global Terrestrial Primary Production. *BioScience*, *54*(6), 547–560.

Running, S. W., Nemani, R. R., Peterson, D. L., Band, L. E., Potts, D. F., Pierce, L. L., & Spanner, M. A. (1989). Mapping Regional Forest Evapotranspiration and Photosynthesis by Coupling Satellite Data with Ecosystem Simulation. *70*(4), 1090–1101.

Running, S. W., & Zhao, M. (2015). Daily GPP and Annual NPP (MOD17A2/A3) products NASA Earth Observing System MODIS Land Algorithm (User's guide V3). *User Guide*, 28.

Saibo, N. J. M., Lourenço, T., & Oliveira, M. M. (2009). Transcription factors and regulation of photosynthetic and related metabolism under environmental stresses. *Annals of Botany*, *103*(4), 609–623.

Salomonson, V. V., Barnes, W., & Masuoka, E. J. (2006). Introduction to MODIS and an overview of associated activities. *Earth Science Satellite Remote Sensing: Science and Instruments*, *1*, 12–32.

Samuel, C., Fletcher, A., & Lines, R. (2007). *Choice of Sitka Spruce Seed Origins for Use in British Forests* (Vol. 127).

Sánchez-Gómez, D., Velasco-Conde, T., Cano-Martín, F. J., Ángeles Guevara, M., Teresa Cervera, M., & Aranda, I. (2011). Inter-clonal variation in functional traits in response to drought for a genetically homogeneous Mediterranean conifer. *Environmental and Experimental Botany*, *70*(2-3), 104–109.

Schickling, A., Matveeva, M., Damm, A., Schween, J. H., Wahner, A., Graf, A., Crewell, S., & Rascher, U. (2016). Combining sun-induced chlorophyll fluorescence and photochemical reflectance index improves diurnal modeling of gross primary productivity. *Remote Sensing*, *8*(7).

Schiop, S. T., Al Hassan, M., Sestras, A. F., Boscaiu, M., Sestras, R. E., & Vicente, O. (2017). Biochemical responses to drought, at the seedling stage, of several Romanian Carpathian populations of Norway spruce (Picea abies L. Karst). *Trees - Structure and Function*, *31*(5), 1479–1490.

Schmid, H. P. (1994). Source areas for scalars and scalar fluxes. *Boundary-Layer Meteorology*, *67*(3), 293–318.

Schönbeck, L., Gessler, A., Hoch, G., McDowell, N. G., Rigling, A., Schaub, M., & Li, M. H. (2018). Homeostatic levels of nonstructural carbohydrates after 13 yr of drought and irrigation in Pinus sylvestris. *New Phytologist*, *219*(4), 1314–1324.

Schönbeck, L. C., Schuler, P., Lehmann, M. M., Mas, E., Mekarni, L., Pivovaroff, A. L., Turberg, P., & Grossiord, C. (2022). Increasing temperature and

vapour pressure deficit lead to hydraulic damages in the absence of soil drought. (July), 3275–3289.

Schuldt, B., Buras, A., Arend, M., Vitasse, Y., Beierkuhnlein, C., Damm, A., Gharun, M., Grams, T. E., Hauck, M., Hajek, P., Hartmann, H., Hiltbrunner, E., Hoch, G., Holloway-Phillips, M., Körner, C., Larysch, E., Lübbe, T., Nelson, D. B., Rammig, A., ... Kahmen, A. (2020). A first assessment of the impact of the extreme 2018 summer drought on Central European forests. *Basic and Applied Ecology*, *45*, 86–103.

Sellers, P. J., Berry, J. A., Collatz, G. J., Field, C. B., & Hall, F. G. (1992). Canopy reflectance, photosynthesis, and transpiration. III. A reanalysis using impr oved leaf models and a new canopy integration scheme. *Remote Sensing of Environment*, *42*(3), 187–216.

Sellers, P. J. (1987). Canopy reflectance, photosynthesis, and transpiration, II. The role of biophysics in the linearity of their interdependence. *Remote Sensing of Environment*, *21*, 143.

Sellers, P. J., Randall, D., Collatz, G., Berry, J., Field, C., Dazlich, D., Zhang, C., Collelo, G., & Bounoua, L. (1996). A Revised Land Surface Parameterization (SiB2) for Atmospheric GCMS. Part I: Model Formulation. *Journal of Climate*, *9*, 676–705.

Sellers, P. J., Tucker, C. J., Collatz, G. J., Los, S. O., Justice, C. O., Dazlich, D. A., & Randall, D. A. (1996). A Revised Land Surface Parameterization (SiB2) for Atmospheric GCMS. Part II: The Generation of Global Fields of Terrestrial Biophysical Parameters from Satellite Data. *Journal of Climate*, *9*(4), 706–737.

Sellers, P., & Mintz, Y. (1989). A Simple Biosphere Model (SiB) for use withing general circulation models. *J. Atmos*, *43*(6), 505–531.

Sellin, A., & Kupper, P. (2004). Within-crown variation in leaf conductance of Norway spruce: effects of irradiance, vapour pressure deficit, leaf water status and plant hydraulic constraints. *Annals of Forest Science*, *61*(5), 419–429.

Serbin, S. P., Dillaway, D. N., Kruger, E. L., & Townsend, P. A. (2012). Leaf optical properties reflect variation in photosynthetic metabolism and its sensitivity to temperature. *63*(1), 489–502.

Serbin, S. P., Singh, A., McNeil, B. E., Kingdon, C. C., & Townsend, P. A. (2014). Spectroscopic determination of leaf morphological and biochemical traits for northern temperate and boreal tree species. *Ecological Applications*, *24*(7), 1651–1669.

Shi, L., Li, X., Fu, Y., & Li, C. (2023). Environmental Stimuli and Phytohormones in Anthocyanin Biosynthesis: A Comprehensive Review. *International Journal of Molecular Sciences*, *24*(22), 1–17.

Silva-Perez, V., Molero, G., Serbin, S. P., Condon, A. G., Reynolds, M. P., Furbank, R. T., & Evans, J. R. (2018). Hyperspectral reflectance as a tool to measure biochemical and physiological traits in wheat. *Journal of Experimental Botany*, *69*(3), 483–496.

Simkin, A. J., Kapoor, L., Doss, C. G. P., Hofmann, T. A., Lawson, T., & Ramamoorthy, S. (2022). The role of photosynthesis related pigments in light harvesting, photoprotection and enhancement of photosynthetic yield in planta. *Photosynthesis Research*, *152*(1), 23–42.

Sims, D. A., & Gamon, J. A. (2003). Estimation of vegetation water content and photosynthetic tissue area from spectral reflectance: A comparison of indices based on liquid water and chlorophyll absorption features. *Remote Sensing of Environment*, *84*(4), 526–537.

Sims, D. A., Rahman, A. F., Cordova, V. D., El-Masri, B. Z., Baldocchi, D. D., Bolstad, P. V., Flanagan, L. B., Goldstein, A. H., Hollinger, D. Y., Misson, L., Monson, R. K., Oechel, W. C., Schmid, H. P., Wofsy, S. C., & Xu, L. (2008). A new model of gross primary productivity for North American ecosystems based solely on the enhanced vegetation index and land surface temperature from MODIS. *Remote Sensing of Environment*, *112*(4), 1633–1646.

Smith, M. L., Ollinger, S. V., Martin, M. E., Aber, J. D., Hallett, R. A., & Goodale, C. L. (2002). Direct estimation of aboveground forest productivity through hyperspectral remote sensing of canopy nitrogen. *Ecological Applications*, *12*(5), 1286–1302.

Smith, M. N., Stark, S. C., Taylor, T. C., Ferreira, M. L., de Oliveira, E., Restrepo-Coupe, N., Chen, S., Woodcock, T., dos Santos, D. B., Alves, L. F., Figueira, M., de Camargo, P. B., de Oliveira, R. C., Aragão, L. E., Falk, D. A., McMahon, S. M., Huxman, T. E., & Saleska, S. R. (2019). Seasonal and drought-related changes in leaf area profiles depend on height and light environment in an Amazon forest. *New Phytologist*, *222*(3), 1284–1297.

Somers, B., & Asner, G. P. (2012). Hyperspectral time series analysis of native and invasive species in Hawaiian rainforests. *Remote Sensing*, *4*(9), 2510–2529.

Song, Y., Sterck, F., Zhou, X., Liu, Q., Kruijt, B., & Poorter, L. (2022). Drought resilience of conifer species is driven by leaf lifespan but not by hydraulic traits. *New Phytologist*, *235*(3), 978–992.

Song, Y., Njoroge, J. B., & Morimoto, Y. (2013). Drought impact assessment from monitoring the seasonality of vegetation condition using long-term time-series satellite images: A case study of Mt. Kenya region. *Environmental Monitoring and Assessment*, *185*(5), 4117–4124.

Sonobe, R., Yamashita, H., Mihara, H., Morita, A., & Ikka, T. (2020). Estimation of leaf chlorophyll a, b and carotenoid contents and their ratios using hyperspectral reflectance. *Remote Sensing*, *12*(19), 1–19.

Spruce, Hicke, Hargrove, Grulke, & Meddens. (2019). Use of MODIS NDVI Products to Map Tree Mortality Levels in Forests Affected by Mountain Pine Beetle Outbreaks. *Forests*, *10*(9), 811.

Spruce, J. P., Sader, S., Ryan, R. E., Smoot, J., Kuper, P., Ross, K., Prados, D., Russell, J., Gasser, G., McKellip, R., & Hargrove, W. (2011). Assessment of MODIS NDVI time series data products for detecting forest defoliation by gypsy moth outbreaks. *Remote Sensing of Environment*, *115*(2), 427–437.

Sri Rahayu Romadhoni, L., As-syakur, A. R., Hidayah, Z., Budi Wiyanto, D., Safitri, R., Yusuf Satriyana Utama, R., Made Sara Wijana, I., Putra Anugrah, A., & Made Oka Guna Antara, I. (2022). Annual characteristics of gross primary productivity (GPP) in mangrove forest during 2016-2020 as revealed by Sentinel-2 remote sensing imagery. *IOP Conference Series: Earth and Environmental Science*, *1016*, 012051.

Steyn, W. J., Wand, S. J. E., Holcroft, D. M., & Jacobs, G. (2002). Anthocyanins in vegetative tissues: a proposed unified function in photoprotection. *New Phytologist*, *155*, 349–361.

Stimson, H. C., Breshears, D. D., Ustin, S. L., & Kefauver, S. C. (2005). Spectral sensing of foliar water conditions in two co-occurring conifer species: Pinus edulis and Juniperus monosperma. *Remote Sensing of Environment*, *96*(1), 108–118.

Stovall, A. E., Shugart, H., & Yang, X. (2019). Tree height explains mortality risk during an intense drought. *Nature Communications*, *10*(1), 1–6.

Stoy, P. C., Richardson, A. D., Baldocchi, D. D., Katul, G. G., Stanovick, J., Mahecha, M. D., Reichstein, M., Detto, M., Law, B. E., Wohlfahrt, G., Arriga, N., Campos, J., McCaughey, J. H., Montagnani, L., Paw U, K. T., Sevanto, S., & Williams, M. (2009). Biosphere-atmosphere exchange of CO2 in relation to climate: A cross-biome analysis across multiple time scales. *Biogeosciences*, *6*(10), 2297–2312.

Sun, S., & Xue, Y. (2001). Implementing a New Snow Scheme in Simplified Simple Biosphere Model. *Advances in Atmospheric Sciences*, *18*(3), 335–353.

Taïbi, K., Del Campo, A. D., Vilagrosa, A., Bellés, J. M., López-Gresa, M. P., Pla, D., Calvete, J. J., López-Nicolás, J. M., & Mulet, J. M. (2017). Drought tolerance in pinus halepensis seed sources as identified by distinctive physiological and molecular markers. *Frontiers in Plant Science*, *8*(July), 1–13.

Takahashi, S., & Badger, M. R. (2011). Photoprotection in plants: A new light on photosystem II damage. *Trends in Plant Science*, *16*(1), 53–60.

Tang, Y., Xu, X., Zhou, Z., Qu, Y., & Sun, Y. (2021). Estimating global maximum gross primary productivity of vegetation based on the combination of MODIS greenness and temperature data. *Ecological Informatics*, *63*, 101307.

Taylor, A. H. (1990). Disturbance and Persistence of Sitka Spruce (Picea sitchensis (Bong) Carr.) in Coastal Forests of the Pacific Northwest, North America. *Journal of Biogeography*, *17*(1), 47.

Tegischer, K., Tausz, M., Wieser, G., & Grill, D. (2002). Tree- and needle-age-dependent variations in antioxidants and photoprotective pigments in Norway spruce needles at the alpine timberline. *Tree Physiology*, *22*(8), 591–596.

Testa, S., Soudani, K., Boschetti, L., & Borgogno Mondino, E. (2018). MODIS-derived EVI, NDVI and WDRVI time series to estimate phenological metrics in French deciduous forests. *International Journal of Applied Earth Observation and Geoinformation*, *64*(July 2017), 132–144.

Testa, S., Mondino, E. C., & Pedroli, C. (2014). Correcting MODIS 16-day composite NDVI time-series with actual acquisition dates. *European Journal of Remote Sensing*, *47*(1), 285–305.

Tombesi, S., Nardini, A., Frioni, T., Soccolini, M., Zadra, C., Farinelli, D., Poni, S., & Palliotti, A. (2015). Stomatal closure is induced by hydraulic signals and maintained by ABA in drought-stressed grapevine. *Scientific Reports*, *5*(1), 12449.

Torres, M. A., & Dangl, J. L. (2005). Functions of the respiratory burst oxidase in biotic interactions, abiotic stress and development. *Current Opinion in Plant Biology*, *8*(4), 397–403.

Tucker, C. J. (1979). Red and photographic infrared linear combinations for monitoring vegetation. *Remote Sensing of Environment*, *8*(2), 127–150.

Turner, D. P., Ritts, W. D., Cohen, W. B., Maeirsperger, T. K., Gower, S. T., Kirschbaum, A. A., Running, S. W., Zhao, M., Wofsy, S. C., Dunn, A. L., Law, B. E., Campbell, J. L., Oechel, W. C., Kwon, H. J., Meyers, T. P., Small, E. E., Kurc, S. A., & Gamon, J. A. (2005). Site-level evaluation of satellite-based global terrestrial gross primary production and net primary production monitoring. *Global Change Biology*, *11*(4), 666–684.

Van Pelt, R. (2007). Identifying mature and old forests in western Washington. *Washington State Department of Natural Resources*, 1–104.

Vanino, S., Nino, P., De Michele, C., Falanga Bolognesi, S., D'Urso, G., Di Bene, C., Pennelli, B., Vuolo, F., Farina, R., Pulighe, G., & Napoli, R. (2018). Capability of Sentinel-2 data for estimating maximum evapotranspiration and irrigation requirements for tomato crop in Central Italy. *Remote Sensing of Environment*, *215*, 452–470.

Verbesselt, J., Hyndman, R., Zeileis, A., & Culvenor, D. (2010). Phenological change detection while accounting for abrupt and gradual trends in satellite image time series. *Remote Sensing of Environment*, *114*(12), 2970–2980.

Verma, M., Friedl, M. A., Law, B. E., Bonal, D., Kiely, G., Black, T. A., Wohlfahrt, G., Moors, E. J., Montagnani, L., Marcolla, B., Toscano, P., Varlagin, A., Roupsard, O., Cescatti, A., Arain, M. A., & D'Odorico, P. (2015). Improving the performance of remote sensing models for capturing intra- and inter-annual variations in daily GPP: An analysis using global FLUXNET tower data. *Agricultural and Forest Meteorology*, *214-215*, 416–429.

Vermote, E. F., Roger, J. C., & Ray, J. P. (2015). MYD09GA MODIS/Aqua Surface Reflectance Daily L2G Global 1kmand 500m SIN Grid V006. *NASA EOSDIS Land Processes DAAC*, 1–35.

Verrelst, J., Alonso, L., Camps-valls, G., Member, S., Delegido, J., & Moreno, J. (2011). Retrieval of Vegetation Biophysical Parameters Using Gaussian Process Techniques. *IEEE Transactions on Geoscience and Remote Sensing*, *50*(5), 1–12.

Verrelst, J., Malenovský, Z., Van der Tol, C., Camps-Valls, G., Gastellu-Etchegorry, J. P., Lewis, P., North, P., & Moreno, J. (2019). Quantifying Vegetation Biophysical Variables from Imaging Spectroscopy Data: A Review on Retrieval Methods. *Surveys in Geophysics*, *40*(3), 589–629.

Vicente-Serrano, S. M. (2007). Evaluating the impact of drought using remote sensing in a Mediterranean, Semi-arid Region. *Natural Hazards*, *40*(1), 173–208.

Viña, A., & Gitelson, A. A. (2011). Sensitivity to foliar anthocyanin content of vegetation indices using green reflectance. *IEEE Geoscience and Remote Sensing Letters*, *8*(3), 464–468.

Vinod, N., Slot, M., McGregor, I. R., Ordway, E. M., Smith, M. N., Taylor, T. C., Sack, L., Buckley, T. N., & Anderson-Teixeira, K. J. (2022). Thermal sensitivity across forest vertical profiles: patterns, mechanisms, and ecological implications. *New Phytologist*, 22–47.

Vorobiova, N., & Chernov, A. (2017). Curve fitting of MODIS NDVI time series in the task of early crops identification by satellite images. *Procedia Engineering*, *201*, 184–195.

Walshe, D., McInerney, D., De Kerchove, R. V., Goyens, C., Balaji, P., & Byrne, K. A. (2020). Detecting nutrient deficiency in spruce forests using multispectral satellite imagery. *International Journal of Applied Earth Observation and Geoinformation*, *86*, 101975.

Wang, L., Koike, T., Yang, D., & Yang, K. (2009). Amélioration de l'hydrologie du Modèle Simple de Biosphère 2 et son évaluation dans le cadre d'un modèle hydrologique distribué. *Hydrological Sciences Journal*, *54*(6), 989–1006.

Wang, Q., Tenhunen, J., Dinh, N. Q., Reichstein, M., Vesala, T., & Keronen, P. (2004). Similarities in ground- and satellite-based NDVI time series and their relationship to physiological activity of a Scots pine forest in Finland. *Remote Sensing of Environment*, *93*(1-2), 225–237.

Wang, R., Gamon, J. A., Emmerton, C. A., Springer, K. R., Yu, R., & Hmimina, G. (2020). Detecting intra- and inter-annual variability in gross primary productivity of a North American grassland using MODIS MAIAC data. *Agricultural and Forest Meteorology*, *281*, 107859.

Wang, S., Zhang, Y., Ju, W., Qiu, B., & Zhang, Z. (2021). Tracking the seasonal and inter-annual variations of global gross primary production during last four decades using satellite near-infrared reflectance data. *Science of the Total Environment*, *755*, 142569.

Wang, X., Chen, J. M., & Ju, W. (2020a). Photochemical reflectance index (PRI) can be used to improve the relationship between gross primary productivity (GPP) and sun-induced chlorophyll fluorescence (SIF). *Remote Sensing of Environment*, *246*, 111888.

Wang, X., Chen, J. M., & Ju, W. (2020b). Photochemical reflectance index (PRI) can be used to improve the relationship between gross primary productivity (GPP) and sun-induced chlorophyll fluorescence (SIF). *Remote Sensing of Environment*, *246*(November 2019), 111888.

Wang, X., Du, T., Huang, J., Peng, S., & Xiong, D. (2018). Leaf hydraulic vulnerability triggers the decline in stomatal and mesophyll conductance during drought in rice. *Journal of Experimental Botany*, *69*(16), 4033–4045.

Warren, C. R. (2006). Why does photosynthesis decrease with needle age in Pinus pinaster? *Trees - Structure and Function*, *20*(2), 157–164.

West, H., Quinn, N., & Horswell, M. (2019). Remote sensing for drought monitoring & impact assessment: Progress, past challenges and future opportunities. *Remote Sensing of Environment*, *232*, 111291.

Wilson, K. B., Baldocchi, D. D., & Hanson, P. J. (2000). Spatial and seasonal variability of photosynthetic parameters and their relationship to leaf nitrogen in a deciduous forest. *Tree Physiology*, *20*(9), 565–578.

Wingfield, M. J., Brockerhoff, E. G., Wingfield, B. D., & Slippers, B. (2015). Planted forest health: The need for a global strategy. *Science*, *349*(6250), 832–836.

Wong, C. Y., D'Odorico, P., Arain, M. A., & Ensminger, I. (2020). Tracking the phenology of photosynthesis using carotenoid-sensitive and near-infrared reflectance vegetation indices in a temperate evergreen and mixed deciduous forest. *New Phytologist*, *226*(6), 1682–1695.

Wong, C. Y., & Gamon, J. A. (2015a). The photochemical reflectance index provides an optical indicator of spring photosynthetic activation in evergreen conifers. *New Phytologist*, *206*(1), 196–208.

Wong, C. Y., & Gamon, J. A. (2015b). Three causes of variation in the photochemical reflectance index (PRI) in evergreen conifers. *New Phytologist*, *206*(1), 187–195.

Wong, C. Y., Mercado, L. M., Arain, M. A., & Ensminger, I. (2022). Remotely sensed carotenoid dynamics improve modelling photosynthetic phenology in conifer and deciduous forests. *Agricultural and Forest Meteorology*, *321*, 108977.

Wu, C., Niu, Z., & Gao, S. (2012). The potential of the satellite derived green chlorophyll index for estimating midday light use efficiency in maize, coniferous forest and grassland. *Ecological Indicators*, *14*(1), 66–73.

Wu, J., Kobayashi, H., Stark, S. C., Meng, R., Guan, K., Tran, N. N., Gao, S., Yang, W., Restrepo-Coupe, N., Miura, T., Oliviera, R. C., Rogers, A., Dye, D. G., Nelson, B. W., Serbin, S. P., Huete, A. R., & Saleska, S. R. (2018). Biological processes dominate seasonality of remotely sensed canopy greenness in an Amazon evergreen forest. *New Phytologist*, *217*(4), 1507–1520.

Wu, Q., Song, C., Song, J., Wang, J., Chen, S., Yang, L., Xiang, W., Zhao, Z., & Jiang, J. (2021). Effects of leaf age and canopy structure on gross ecosystem production in a subtropical evergreen Chinese fir forest. *Agricultural and Forest Meteorology*, *310*, 108618.

Wu, Q., Song, C., Song, J., Wang, J., Chen, S., & Yu, B. (2018). Impacts of Leaf Age on Canopy Spectral Signature Variation in Evergreen Chinese Fir Forests. *Remote Sensing*, *10*(2), 262.

Wu, Q., Song, J., Wang, J., Song, C., Chen, S., & Yang, L. (2020). Leaf Aging Affects the Variability of Canopy Reflectance with Stand Development in Evergreen Chinese FIR Plantation. *International Geoscience and Remote Sensing Symposium (IGARSS)*, 4826–4829.

Wu, X., Liu, H., Li, X., Ciais, P., Babst, F., Guo, W., Zhang, C., Magliulo, V., Pavelka, M., Liu, S., Huang, Y., Wang, P., Shi, C., & Ma, Y. (2018). Differentiating drought legacy effects on vegetation growth over the temperate Northern Hemisphere. *Global Change Biology*, *24*(1), 504–516.

Xenakis, G., Ash, A., Siebicke, L., Perks, M., & Morison, J. I. (2021). Comparison of the carbon, water, and energy balances of mature stand and clear-fell stages in a British Sitka spruce forest and the impact of the 2018 drought. *Agricultural and Forest Meteorology*, *306*, 108437.

Xiao, J., Chevallier, F., Gomez, C., Guanter, L., Hicke, J. A., Huete, A. R., Ichii, K., Ni, W., Pang, Y., Rahman, A. F., Sun, G., Yuan, W., Zhang, L., & Zhang, X.

(2019). Remote sensing of the terrestrial carbon cycle: A review of advances over 50 years. *Remote Sensing of Environment*, *233*, 111383.

Xiao, X., Hollinger, D., Aber, J., Goltz, M., Davidson, E. A., Zhang, Q., & Moore, B. (2004). Satellite-based modeling of gross primary production in an evergreen needleleaf forest. *Remote Sensing of Environment*, *89*(4), 519–534.

Xue, J., & Su, B. (2017). Significant Remote Sensing Vegetation Indices: A Review of Developments and Applications. *Journal of Sensors*, *2017*(1), 1–17.

Yan, D., Scott, R. L., Moore, D. J., Biederman, J. A., & Smith, W. K. (2019). Understanding the relationship between vegetation greenness and productivity across dryland ecosystems through the integration of PhenoCam, satellite, and eddy covariance data. *Remote Sensing of Environment*, *223*(December 2018), 50–62.

Yan, J., Zhang, X., Liu, J., Li, H., & Ding, G. (2020). MODIS-Derived estimation of soil respiration within five cold temperate coniferous forest sites in the eastern Loess Plateau, China. *Forests*, *11*(2).

Yan, K., Zou, D., Yan, G., Fang, H., Weiss, M., Rautiainen, M., Knyazikhin, Y., & Myneni, R. B. (2021). A Bibliometric Visualization Review of the MODIS LAI/FPAR Products from 1995 to 2020. *Journal of Remote Sensing*, *2021*(1), 1–19.

Yan, Z., Bond-Lamberty, B., Todd-Brown, K. E., Bailey, V. L., Li, S., Liu, C., & Liu, C. (2018). A moisture function of soil heterotrophic respiration that incorporates microscale processes. *Nature Communications*, *9*(1), 1–10.

Yanez-Rausell, L., Schaepman, M. E., Clevers, J. G., & Malenovsky, Z. (2014). Minimizing measurement uncertainties of coniferous needle-leaf optical properties, part i: Methodological review. *IEEE Journal of Selected Topics in Applied Earth Observations and Remote Sensing*, *7*(2), 399–405.

Yang, B., Hanson, P. J., Riggs, J. S., Pallardy, S. G., Heuer, M., Hosman, K. P., Meyers, T. P., Wullschleger, S. D., & Gu, L. H. (2007). Biases of CO2 storage in eddy flux measurements in a forest pertinent to vertical configurations of a profile system and CO2 density averaging. *Journal of Geophysical Research Atmospheres*, *112*(20), 1–15.

Yang, H., Yang, X., Heskel, M., Sun, S., & Tang, J. (2017). Seasonal variations of leaf and canopy properties tracked by ground-based NDVI imagery in a temperate forest. *Scientific Reports*, *7*(1), 1–10.

Yang, J. C., Magney, T. S., Yan, D., Knowles, J. F., Smith, W. K., Scott, R. L., & Barron-Gafford, G. A. (2020). The Photochemical Reflectance Index (PRI) Captures the Ecohydrologic Sensitivity of a Semiarid Mixed Conifer Forest. *Journal of Geophysical Research: Biogeosciences*, *125*(11), 1–18.

Yin, G., Verger, A., Descals, A., Filella, I., & Peñuelas, J. (2022). A Broadband Green-Red Vegetation Index for Monitoring Gross Primary Production Phenology. *Journal of Remote Sensing*, *2022*.

Yuan, W., Liu, S., Zhou, G., Zhou, G., Tieszen, L. L., Baldocchi, D., Bernhofer, C., Gholz, H., Goldstein, A. H., Goulden, M. L., Hollinger, D. Y., Hu, Y., Law, B. E., Stoy, P. C., Vesala, T., & Wofsy, S. C. (2007). Deriving a light use efficiency model from eddy covariance flux data for predicting daily gross primary production across biomes. *Agricultural and Forest Meteorology*, *143*(3-4), 189–207.

Zarco-Tejada, P. J., Miller, J. R., Noland, T. L., Mohammed, G. H., & Sampson, P. H. (2001). Scaling-up and model inversion methods with narrowband optical indices for chlorophyll content estimation in closed forest canopies with hyperspectral data. *IEEE Transactions on Geoscience and Remote Sensing*, *39*(7), 1491–1507.

Zeng, Y., Hao, D., Huete, A., Dechant, B., Berry, J., Chen, J. M., Joiner, J., Frankenberg, C., Bond-Lamberty, B., Ryu, Y., Xiao, J., Asrar, G. R., & Chen, M. (2022). Optical vegetation indices for monitoring terrestrial ecosystems globally. *Nature Reviews Earth & Environment*, *3*(7), 477–493.

Zhang, F., & Zhou, G. (2019). Estimation of vegetation water content using hyperspectral vegetation indices: A comparison of crop water indicators in response to water stress treatments for summer maize. *BMC Ecology*, *19*(1), 1–12.

Zhang, H., Bai, J., Sun, R., Wang, Y., Pan, Y., McGuire, P. C., & Xiao, Z. (2023). Improved Global Gross Primary Productivity Estimation by Considering Canopy Nitrogen Concentrations and Multiple Environmental Factors. *Remote Sensing*, *15*(3), 1–29.

Zhang, J., Zhao, T., Li, Z., Li, C., & Li, Z. (2021). Evaluation of Surface Relative Humidity in China from the CRA-40 and Current Reanalyses. *38*, 1958–1976.

Zhang, L.-X., Zhou, D.-C., Fan, J.-W., & Hu, Z.-M. (2015). Comparison of four light use efficiency models for estimating terrestrial gross primary production. *Ecological Modelling*, *300*, 30–39.

Zhang, Q., Cheng, Y. B., Lyapustin, A. I., Wang, Y., Gao, F., Suyker, A., Verma, S., & Middleton, E. M. (2014). Estimation of crop gross primary production (GPP): fAPARchl versus MOD15A2 FPAR. *Remote Sensing of Environment*, *153*, 1–6.

Zhang, X., Friedl, M. A., & Schaaf, C. B. (2009). Sensitivity of vegetation phenology detection to the temporal resolution of satellite data. *International Journal of Remote Sensing*, *30*(8), 2061–2074.

Zhang, Y., Xiao, X., Wu, X., Zhou, S., Zhang, G., Qin, Y., & Dong, J. (2017). A global moderate resolution dataset of gross primary production of vegetation for 2000-2016. *Scientific data*, *4*, 170165.

Zhao, D., Hou, Y., Zhang, Z., Wu, Y., Zhang, X., Wu, L., Zhu, X., & Zhang, Y. (2022). Temporal resolution of vegetation indices and solar-induced chlorophyll fluorescence data affects the accuracy of vegetation phenology estimation: A study using in-situ measurements. *Ecological Indicators*, *136*, 108673.

Zhao, M., & Running, S. W. (2010). Drought-induced reduction in global terrestrial net primary production from 2000 through 2009. *Science*, *329*(5994), 940–943.

Zhou, S., Zhang, Y., Caylor, K. K., Luo, Y., Xiao, X., Ciais, P., Huang, Y., & Wang, G. (2016). Explaining inter-annual variability of gross primary productivity from plant phenology and physiology. *Agricultural and Forest Meteorology*, *226-227*, 246–256.

Zhou, S.-x., Prentice, I. C., & Medlyn, B. E. (2019). Bridging Drought Experiment and Modeling: Representing the Differential Sensitivities of Leaf Gas Exchange to Drought. *Frontiers in Plant Science*, *9*, 1–12.

Zhu, H., Zhang, T., Zhang, P., & Peng, C. (2016). Pigment patterns and photoprotection of anthocyanins in the young leaves of four dominant subtropical forest tree species in two successional stages under contrasting light conditions (J.-P. Schnitzler, Ed.). *Tree Physiology*, *36*(9), 1092–1104.

Zhu, X., Wang, T., Skidmore, A. K., Darvishzadeh, R., Niemann, K. O., & Liu, J. (2017). Canopy leaf water content estimated using terrestrial LiDAR. *Agricultural and Forest Meteorology*, *232*, 152–162.

Zhuang, J., Wang, Y., Chi, Y., Zhou, L., Chen, J., Zhou, W., Song, J., Zhao, N., & Ding, J. (2020). Drought stress strengthens the link between chlorophyll fluorescence parameters and photosynthetic traits. *PeerJ*, *8*, 1–20.

Zuzana, L., Lukáš, B., Lucie, K., Kopačková, V., Markéta, P., Jan, M., Aleš, K., Monika, K., & Jana, A. (2013). Detection of multiple stresses in Scots pine growing at post-mining sites using visible to near-infrared spectroscopy. *Environmental Sciences: Processes and Impacts*, *15*(11), 2004–2015.